A SOLAR EXTREME ULTRAVIOLET FLUX MODEL

by

William Kent Tobiska

B.A., University of Colorado, 1972

M.S., University of Colorado, 1985

A thesis submitted to the

Faculty of the Graduate School of the

University of Colorado in partial fulfillment

of the requirements for the degree of

Doctor of Philosophy

Department of Aerospace Engineering Sciences

1988

This thesis for the Doctor of Philosophy degree by

William Kent Tobiska

has been approved for the

Department of

Aerospace Engineering Sciences

by

Robert D. Culp

Charles A. Barth

C.Y. Chow

George W. Rosborough

A. Ian F. Stewart

Gary J. Rottman

Date September 20, 1988

Tobiska, William Kent (Ph.D., Aerospace Engineering Sciences)

A Solar Extreme Ultraviolet Flux Model

Thesis directed by Professor Charles A. Barth

Solar extreme ultraviolet (EUV) flux for 37 discrete wavelengths or wavelength intervals is modeled during the decline of solar cycle 21. The primary modeling input parameters are the two indices of the filtered daily values of solar Lyman-α photon flux and the natural logarithm of solar 1-8 Å X-ray energy flux. These two emissions have been measured on a daily basis by the Solar Mesosphere Explorer (SME) and Geostationary Operational Environmental Satellites (GOES), respectively.

The EUV data from the Atmosphere Explorer E (AE-E) satellite is correlated with AE-E Lyman-α flux, Ottawa 10.7 cm flux ($F_{10.7}$), and GOES 1-8 Å X-ray flux. Linear relations are established between the EUV and Lyman-α emissions and between the EUV and the natural logarithm of 1-8 Å X-ray emissions during the rising phase of cycle 21. Nine dominant EUV energy emissions are detailed which contribute nearly 50% of the thermospheric heating for solar minimum and maximum conditions.

These EUV emissions are used as energy inputs into a one-dimensional, time-dependent thermospheric model to solve for temperatures and constituent densities. The resulting densities are compared with satellite-derived densities and MSIS 83 modeled densities for the period between January 1982 and May 1983. The two-indices method of modeling EUV flux is validated by this comparison although the 1-8 Å X-ray index tends to overestimate the energy flux during certain time periods. It is shown that chromospheric emissions contribute the 27-day variability in atmospheric density at satellite altitudes during high solar activity. Through the use of a long-term orbit

predictor, the two-indices method of modeling EUV flux is further validated by a comparison of the modeled orbit decay to the actual satellite orbit decay. In the orbit decay calculation, it is additionally suggested that the satellite drag coefficient, C_d, has a small variation due to the long-term solar EUV flux variation and its effects upon neutral thermospheric gas temperatures.

DEDICATION

This dissertation is dedicated to those individuals with the vision of building a future where humans will prosper in peace in space. This vision is tempered by the tragic loss of life among the *Challenger* crew in 1986 which poignantly demonstrated our fragility while traveling through our planet's thin atmosphere to reach space. May our efforts substantially improve in the coming years.

ACKNOWLEDGMENTS

Data from several separate sources are used in this study, spanning nearly a decade from 1977 through 1987. Three particular satellites, the AE-E, SME, and GOES have taken observations used in this work. The exerimenters, referenced in the text but including H.E. Hinteregger and G.J. Rottman, have made valuable contributions with their experiment designs as well as in the collection and organization of these data. Their efforts are deeply appreciated and acknowledged. Ground observatories have also contributed important data used in this study for the same decade. The staff at the Ottawa observatory and the World Data Center at NOAA have monitored and assembled a tremendous database which deserves special recognition.

The Laboratory for Atmospheric and Space Physics (LASP) at the University of Colorado in Boulder, through its research associates, staff, graduate students, and facilities, has provided the means for carrying out this research. Professor Charles Barth (LASP), as my thesis advisor, has provided invaluable theoretical and research support. Professor Robert Culp of Aerospace Engineering Sciences (AES) has provided continual advice and support as my graduate advisor. I would like to extend my deepest appreciation to both of them. Dr. Ian Stewart (LASP) and Dr. Gary Rottman (LASP) have held useful discussions and posed important questions regarding aeronomy and solar flux measurements at several points during this study. Dr. Oran White, Dr. Richard Donnelly (NOAA), Dr. Raymond Roble (NCAR), Dr. Paul Simon (Belgium), Professor C.Y. Chow (AES), and Dean Richard Seebass (College of Engineering) have also provided valuable insights and contributed to impor-

tant discussions ranging from solar physics, atmospheric physics, and orbital dynamics to gas dynamics for hypersonic flight regimes. Roy Barnes (NCAR) skillfully applied his knowledge of programming on the IBM interface machine with the NCAR CRAY so that the GOES X-ray data used in this thesis could be processed. I thank him.

Fellow graduate students have made this work much more pleasant and enjoyable than it ought to be. Dr. David Siskind, who inspired me with healthy competition as we both simultaneously finished our dissertations, provided the service of my sounding board. Alan Stern gave many useful comments on the draft versions of early chapters. Eric Jensen and Frank Eparvier both contributed to a stimulating office environment and rich discussions.

The staff at LASP provided support in ways far too numerous to list. However, the assistance with several figures in this work by Lynn Laubisch, the review of the technical writing by Rionda Osman-Jouchoux, and the assistance in obtaining the SME Lyman-α data by Barry Knapp deserve special recognition.

The unwavering support of my wife Susan, and two daughters Elizabeth and Catherine, helped me through several years of graduate work. Without their constant positive support, this research period would not have been possible. I am deeply indebted to them for their sacrifices during the 1980s. My parents, Aron and Barbara Tobiska, and my mother-in-law, Sally Romayne, also provided continual encouragement and welcome financial support at critical points which also made these years bearable. Thank you.

CONTENTS

CHAPTER PAGE

TABLES

TABLE PAGE

TABLE PAGE

FIGURES

FIGURE PAGE

FIGURE PAGE

CHAPTER I

INTRODUCTION

The upper atmosphere of the Earth is of great interest to a number of scientific and engineering communities. The atmosphere's structure between 100 and 500 km is particularly interesting as it changes in response to tides, solar energy, and auroral energy. The net result of numerous chemical, conduction, kinetic, and radiation processes is atmospheric heating.

Figure 1.1 outlines important components of the energy balance in the terrestrial atmosphere, including solar EUV flux penetration, typical densities, an average temperature structure, major thermal and kinetic processes, and atmospheric regions. The five temperature regions above the Earth's surface, i.e., the troposphere, stratosphere, mesosphere, thermosphere, and exosphere, reflect markedly different thermal processes. These result from the particular kinetic processes and gas properties which dominate each layer. In the thermosphere, the kinetic motion of neutral gases is mainly influenced by the Earth's gravitational field. They settle in separate density distributions according to their species weight. The subsequent exponential distribution of a gas is said to be in diffusive equilibrium and is located above the lower layers where turbulence and eddies mix the gases. This region is also known as the heterosphere. Kinetically defined molecular diffusion in the heterosphere complements the thermally defined region of molecular conduction in the upper atmosphere which is noted in Figure 1.1. The primary parameters describing the structure of the heterosphere are density, which is measured as a concen-

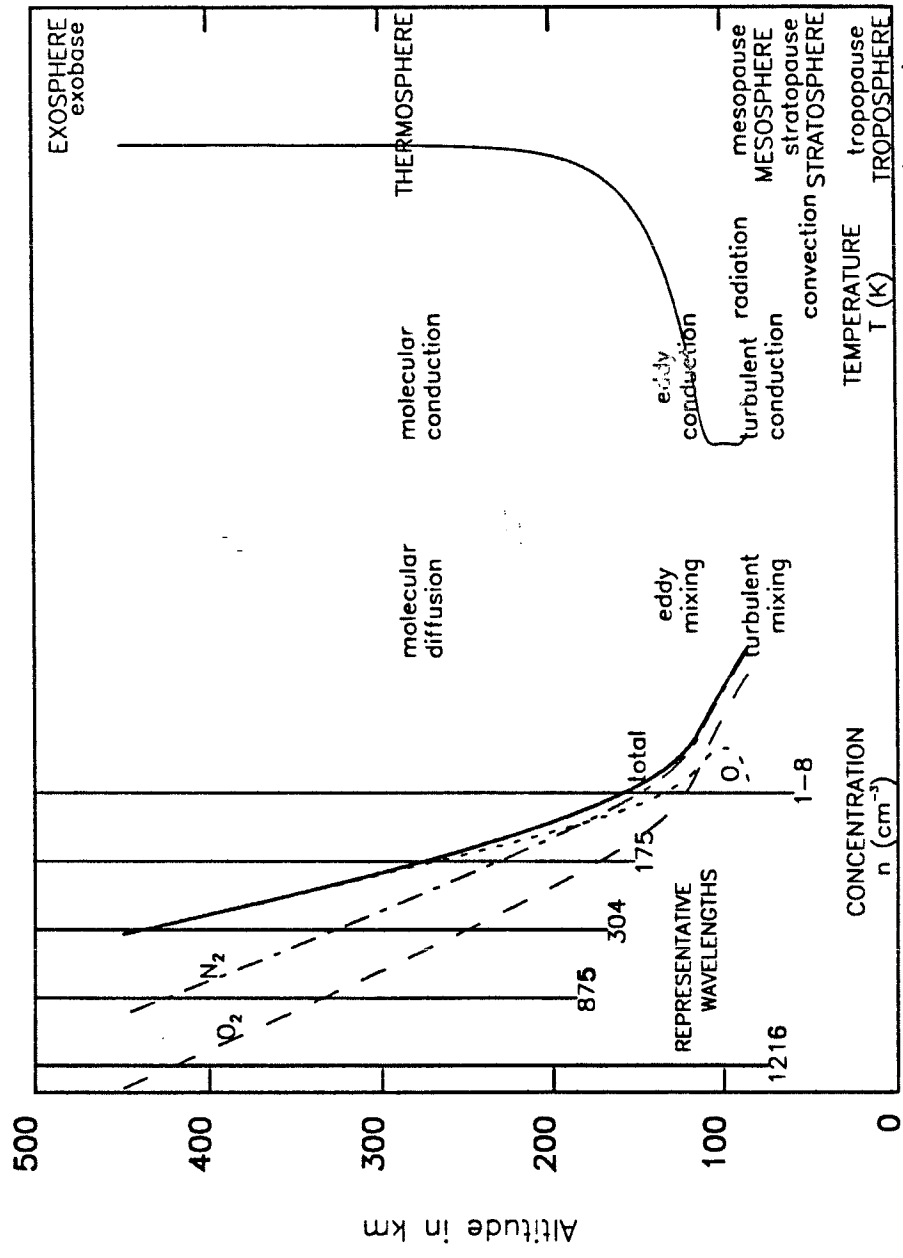

Figure 1.1 **Atmospheric processes and regions.** Unit optical depth penetration by representative wavelengths, major constituent concentrations, and the temperature profile for the terrestrial neutral thermosphere are shown. The kinetic processes, thermal processes, and temperature regions are also labeled.

tration in units of gas particles per cubic centimeter, and temperature, which is measured in degrees Kelvin.

It is possible to represent the thermosphere in a simple model with only three gas species: atomic oxygen, O, molecular nitrogen, N_2, and molecular oxygen, O_2. O is the dominant gas from the exobase at the top of the thermosphere, where the mean free path between atoms equals their density scale height, down to approximately 200 km. N_2 then achieves supremacy as the most abundant gas down to the planetary surface where the gases are thoroughly mixed.

Because of the lack of turbulence and resultant eddies in much of the thermosphere, molecular conduction is the primary means of heat transport from hot upper levels to cool lower levels. Thermal convection is nonexistent at high altitudes and only becomes an important thermal process in the lower thermosphere and below 100 km. Molecular radiation plays an increasingly important role in the lower thermosphere where concentrations of heteronuclear molecules rise.

The most important component in global thermospheric heating is the introduction of energy from extreme ultraviolet (EUV) wavelengths in the solar electromagnetic spectrum. This flux, consisting of wavelengths shorter than 1027 Å down to the X-rays, is absorbed in the upper atmosphere by the major constituents. Figure 1.1 also illustrates some important and representative EUV fluxes as well as Far UV (1216 Å) and X-ray (1-8 Å) fluxes which affect the thermospheric gases. The penetration lines stop at the point of unit optical depth, above which the atmosphere is increasingly transparent at that wavelength (λ) and below which most of the solar radiation at that wavelength has been absorbed. Hence, solar EUV heating occurs along the full range of altitudes of these lines of penetration, but maximizes the energy

deposition at certain altitudes.

From this brief description of the thermosphere, it is understood that the operation of low Earth orbiting spacecraft is significantly affected by a changing thermospheric structure. For example, long-term variations in atmospheric density dramatically affect satellite lifetimes, and large short-term perturbations occur along the orbit track during geomagnetic storms. Density variations affect the rate at which space debris "rains" out of orbit; additionally, gas particles undergo a variety of interactions with spacecraft surfaces depending upon density and temperature variations. For low Earth orbiting spacecraft, the principal perturbation is atmospheric drag. In predicting this perturbation, the predominant uncertainty is the atmospheric density, which varies with the temperature of the atmosphere. For these reasons, the atmospheric and astronautical communities have devoted considerable efforts in experimental studies and theoretical modeling to better understand and predict the behavior of this region of the atmosphere.

In the future, direct and instantaneous measurements of thermospheric density, composition, and temperature may become regularly available. However, until consistent monitoring can take place, modeling of the thermosphere will be the primary means of determining and predicting variations in the fundamental characteristics of temperature and density. The current problem of accurately modeling the density and temperature of the thermosphere as it varies with solar activity partially results from the lack of consistently measured solar EUV and soft X-ray fluxes.

Figure 1.2 shows the scale of these wavelengths in the electromagnetic spectrum and the relative magnitudes of the solar energy flux. One notes that EUV fluxes cover nearly a decade of wavelengths. The solar wavelengths in the part of the electromagnetic spectrum illustrated in Figure 1.2 range from

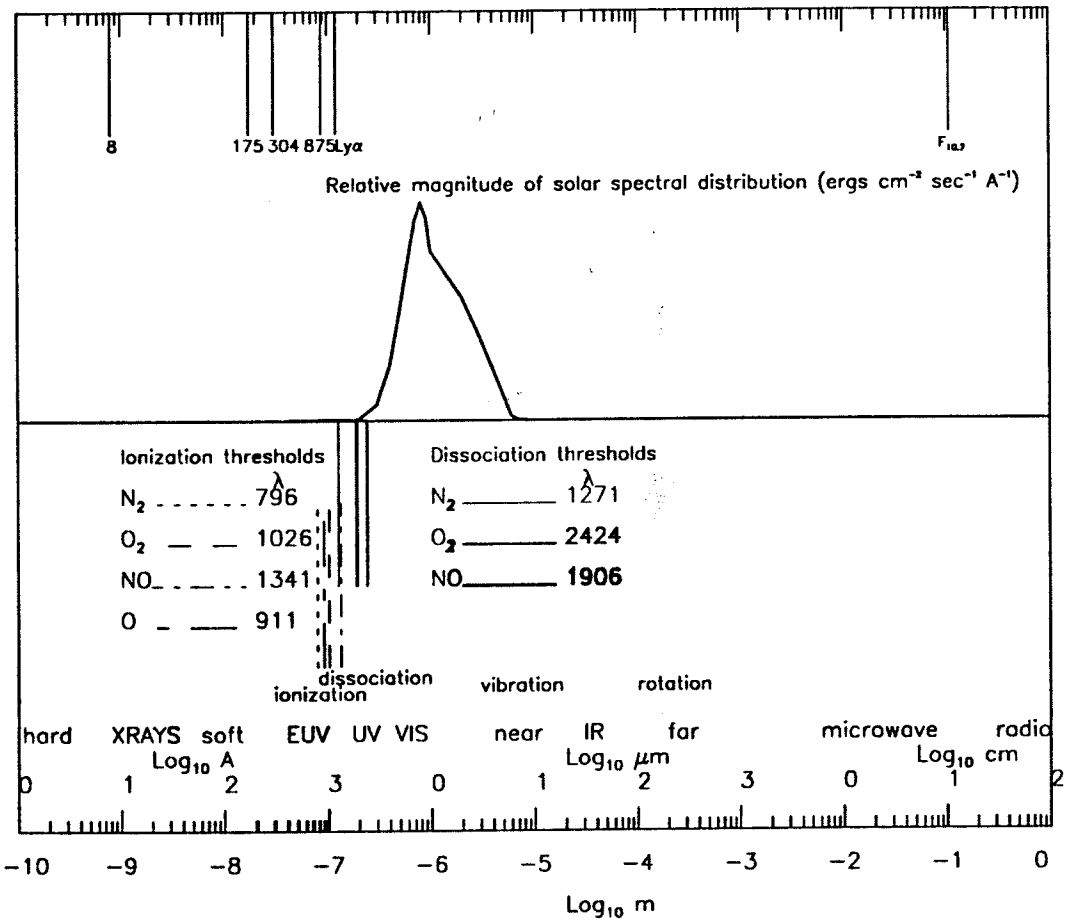

Figure 1.2 **Characteristics of the solar electromagnetic spectrum.** Example wavelengths in the X-rays, EUV, and radio spectra are shown, as is the relative magnitude of solar energy flux which peaks in the visible. Important ionization and dissociation thresholds are listed and shown graphically along with the spectral ranges for these processes. The names of various spectral regions are shown with the wavelength range they encompass, where the numbers are the $\log_{10}$ of the wavelength.

the hard X-rays (highly energetic) to the radio (low energy) fluxes, or from 1×10^{-10} to 1 meter in SI units on the bottom scale. The second scale indicates the conversion from SI units to other commonly used units in $\log_{10}$, including Ångströms (Å), microns (μm), and centimeters (cm). In addition, common labels for each part of the spectrum are included for reference. The solar spectrum spans these ten decades and more, but the relative magnitude of the energy flux is most strongly represented in the visible light (VIS), the near infrared (NIR), the ultraviolet (UV), and the EUV, in that order. Energy flux is measured in ergs cm^{-2} sec^{-1}.

Two comparative tables, displayed in Figure 1.2, contain information important to the study of solar effects upon the atmosphere. The vertical lines and table entries for N_2, O_2, nitric oxide (NO), and O are the energies at which these species are either ionized or dissociated. These two actions contribute to changes in the thermal balance of the atmosphere as a result of the absorption of photons by these gas particles. Wavelengths shortward of these values will affect these constituents. Thus, the importance of 150-1027 Å EUV fluxes for heating through a variety of photoabsorption processes is clear, even though the total EUV energy input is much less than the energy available at visible wavelengths.

Since EUV wavelengths are entirely absorbed prior to reaching the ground, the only methods of measuring them to the present have been rocket flights and satellite observations. Neither of these have been conducted on a daily basis except for the data collected in the late 1970s by the NASA Atmosphere Explorer (AE) series satellites. As a result, these fluxes have been parameterized by indices of solar activity which may be observed at the Earth's surface. Zurich sunspot numbers, R_z, and 10.7 cm solar radio flux, $F_{10.7}$, have historically been used as indicators of the general level of solar EUV

flux, although neither has any direct influence on the terrestrial atmosphere.

1.1 Predicting and Modeling the Solar Cycle EUV Flux

The widely used parameters for estimating solar EUV energy deposition in the thermosphere, R_z and $F_{10.7}$, have shown daily and long-term variations. Solar cycles were originally defined as the time between minimum points in the record of observed sunspots on the solar disk. These records have been maintained since the mid-1700s, and within them cycle 22 is now beginning. Daily R_z is derived from a combination of observed sunspots and sunspot groups. For $F_{10.7}$, over 40 years of daily observations have now been taken. $F_{10.7}$ daily variations were first reported by Covington [1948] and now provide a valuable record spanning nearly four solar cycles with approximately 11 years per cycle.

Predictions of $F_{10.7}$ have been improved in recent years by Sargent [1977] and Ohl and Ohl [1979], and by Schatten *et al.* [1978] and Brown [1979] who predicted sunspot activity for solar cycle 21 using an analysis of secular variations and a solar dynamo theory, respectively. Euler and Holland [1982] gave an empirical relationship between R_z and $F_{10.7}$. More recently, Schatten and Hedin [1984] predicted R_z and $F_{10.7}$ for solar cycle 22 using solar dynamo theory. Their results are shown in Figure 1.3 with a lower maximum value for $F_{10.7}$ (and therefore lower EUV energy input) available for heating in cycle 22 than in cycle 21. This work was extended by Schatten and Sofia [1987] and is shown in Figure 1.4. They used the same theory with updated solar magnetic field information to predict a slightly later maximum of $F_{10.7}$ with a significantly higher magnitude. Their $F_{10.7} \approx 200$ compared to the Schatten and Hedin value of 150.

Sargent [1984; personal communication, 1987] predicted the length and

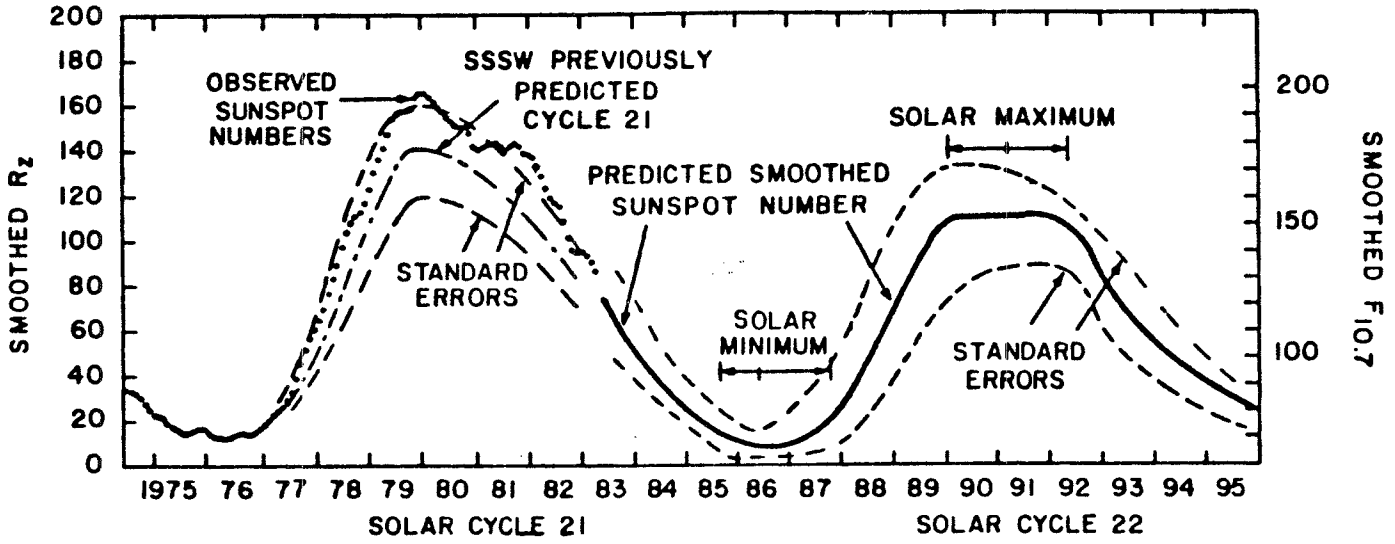

Figure 1.3 **Observed and predicted smoothed sunspot number and radio flux.** This plot is reproduced from Schatten and Hedin [1984] and shows both the observed and predicted smoothed sun-spot numbers and $F_{10.7}$ for solar cycles 21 and 22.

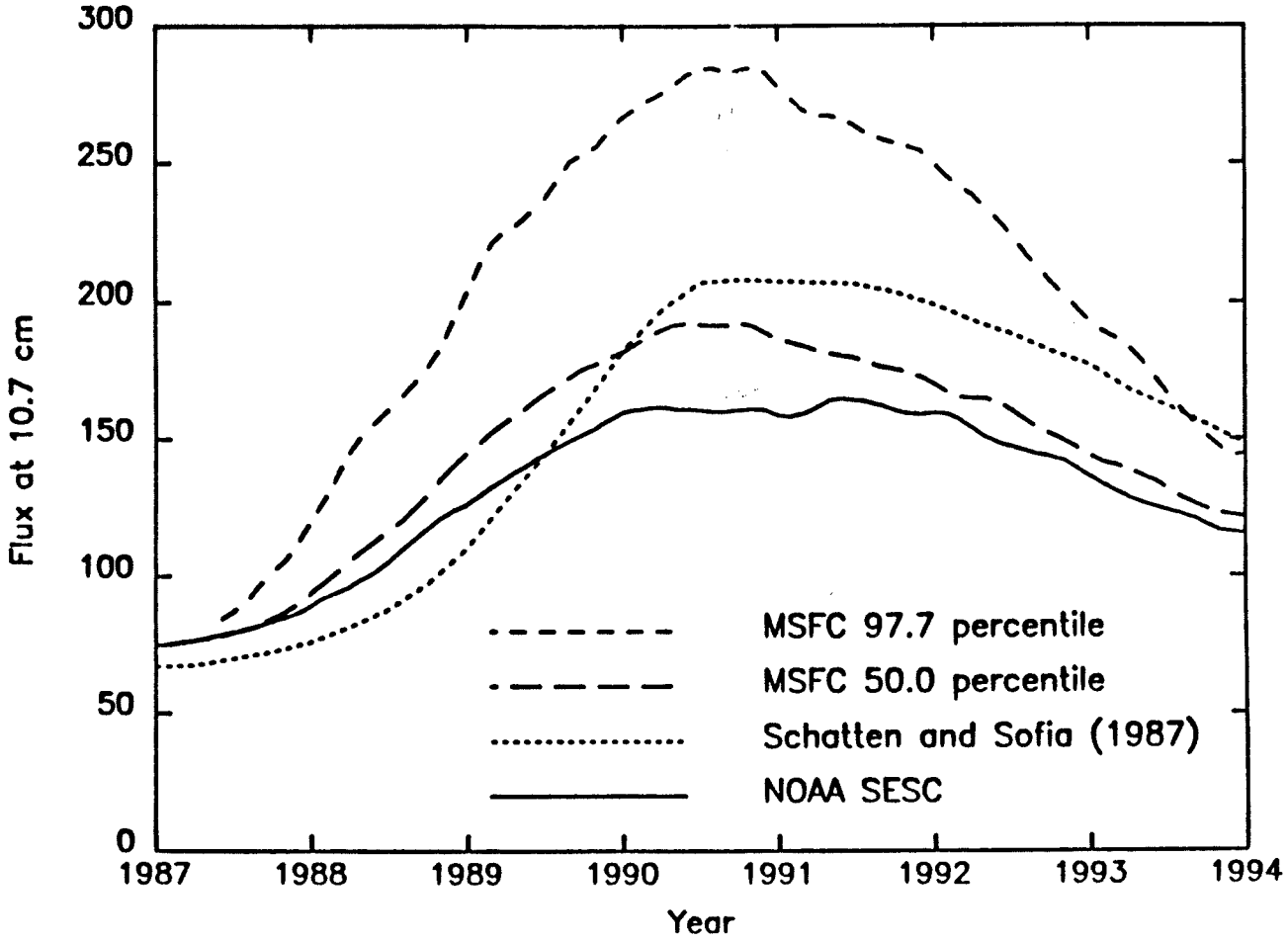

Figure 1.4 **Cycle 22 predictions.** This plot is reproduced from a private communication by J.B. Gurman to C.A. Barth in July 1987. The $F_{10.7}$ predictions from various sources for cycle 22 are discussed in the text.

amplitude of cycle 22 R_z using an observation of even/odd cycle characteristics. Tobiska [1985] extended the Sargent [1984] method to $F_{10.7}$. Figure 1.5 shows this extension. The peak of $F_{10.7}$ occurs a year later (1991) than the Schatten and Hedin prediction. The magnitude is also slightly lower, with $F_{10.7} \approx 140$. The observed monthly mean of $F_{10.7}$ is overplotted in Figure 1.5 through May 1988. It follows the best estimate values through mid-1985, the $+1\sigma$ line in 1986, and the $+4\sigma$ line in 1987-88. Minimum is in September 1986.

Figure 1.4 also shows the Sargent (personal communication, 1987) revised prediction, labeled as National Oceanic and Atmospheric Administration (NOAA) Space Environment Services Center (SESC) curve. It still reveals a relatively low predicted cycle maximum occurring near 1990-1991 with $F_{10.7} \approx 160$. Smith [1985] outlined a solar activity prediction technique based on Lagrangian smoothing combined with a linear regression of several solar cycle datasets. The results of that method are shown in Figure 1.4 as the Marshall Space Flight Center (MSFC) 97.7 and 50.0 percentile profiles. These predictions call for an extremely large maximum for cycle 22, with $F_{10.7} \approx 275$ and a maximum occurring in mid-1990.

There is a factor of 2 disagreement for possible $F_{10.7}$ values in these solar cycle maximum predictions. All predictions, however, agree that the time of maximum will occur in the 1990-1991 timeframe.

Proceeding beyond the predictions to direct modeling of the solar EUV flux, Hinteregger *et al.* [1981] provided two methods: a two-variable $F_{10.7}$ *association* formula, using daily $F_{10.7}$ and its 81-day average, and an *EUV class* model. The $F_{10.7}$ association model is given for the EUV flux, I, at a wavelength, λ

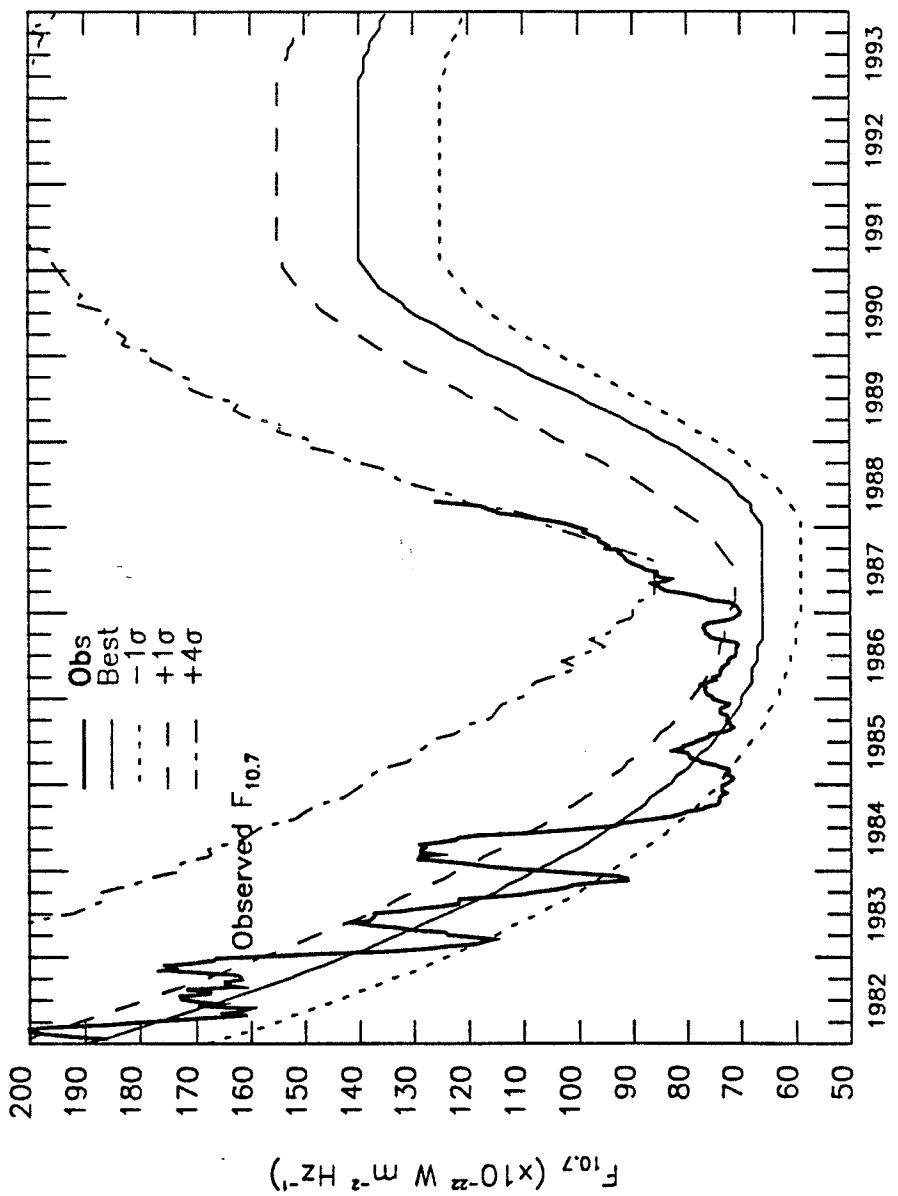

Figure 1.5 Predicted $F_{10.7}$. The overplotted monthly observed $F_{10.7}$ is the heavy line and is compared to the Sargent [1984] prediction, as extended by Tobiska [1985]. The light solid line is the best estimated flux, the dotted line is the -1σ estimated flux, the dashed line is the $+1\sigma$ estimated flux, and the dot-dash line is the $+4\sigma$ estimated flux.

$$I_\lambda = A_\lambda F^*_{10.7} + B_\lambda (F_{10.7} - F^*_{10.7}) + C_\lambda \quad \text{photons cm}^{-2}\ \text{sec}^{-1} \qquad (1.1)$$

where $F_{10.7}$ is the daily value and $F^*_{10.7}$ is the 81-day mean. A_λ, B_λ, and C_λ are obtained from a least squares fit to the AE-E EUV data. However, a more accurate representation, especially during shorter time periods over the AE-E time frame, is given by I_λ in the EUV class model

$$I_\lambda = I_{\lambda\text{ref}} + I_{\lambda\text{ref}}(R_k - 1)C_\lambda \quad \text{photons cm}^{-2}\ \text{sec}^{-1} \qquad (1.2)$$

where $I_{\lambda\text{ref}}$ is the EUV flux at solar cycle 21 minimum given by Hinteregger *et al.* [1981]. R_k is the ratio for a specific date of a key EUV flux to the solar minimum value. C_λ is a wavelength dependent scaling parameter for each EUV wavelength.

Equation (1.1) models the EUV flux and is called SERF1 by the Solar Electromagnetic Radiation Flux Study subgroup of the World Ionosphere - Thermosphere Study (WITS) under the auspices of the Committee on Space Research (COSPAR). Chapter II describes the equation (1.2) model in more detail. In brief, Hinteregger *et al.* [1981] developed this latter method by first obtaining three years of daily EUV fluxes using narrow bandwidth, full solar disk emissions measured by the AE-E satellite. A chromospheric emission, Lyman-β (1026 Å), and a coronal emission, Fe XVI (335 Å), were then used to reduce the volume of data into a more manageable set. They developed a time series of ratios to solar minimum for Lyman-β (1026 Å) and Fe XVI (335 Å), along with the $I_{\lambda\text{ref}}$ values for all EUV emissions at solar minimum. Schmidtke [1984] further discusses this method. Equation (1.2) represents the most accurate EUV modeling efforts to date.

1.2 Modeling Thermospheric Density

1.2.1 Empirical Thermospheric Modeling

Much effort has been placed on developing accurate empirical atmospheric density models since the late 1950s. Jacchia [1959] and others first found that thermospheric densities generally vary like $F_{10.7}$. An analytic expression for temperature was derived by Bates [1959]. Bates' thermospheric temperature equation at an altitude z is written as

$$T(z) = T_\infty - (T_\infty - T_0)e^{-\sigma(z-z_0)} \quad ^\circ\mathrm{K} \tag{1.3}$$

for an exospheric temperature, T_∞, a temperature T_0 at a reference altitude, z_0, and a shaping parameter

$$\sigma = \frac{\frac{\partial T}{\partial z}|_{z=z_0}}{T_\infty - T_0}. \quad \mathrm{cm}^{-1} \tag{1.4}$$

Harris and Priester [1962] developed a linear relation between $F_{10.7}$ and the minimum and maximum exospheric temperatures, i.e., those temperatures at the top of the thermosphere. They solved the heat conduction equation under quasi-hydrostatic conditions and represented the diurnal exospheric temperature minimum and maximum (in degrees Kelvin) by

$$T_{min} = 4.5S + 275^\circ\mathrm{K} \tag{1.5}$$

$$T_{max} = 7.1S + 372^\circ\mathrm{K} \tag{1.6}$$

where the solar flux, S, is the monthly $F_{10.7}$ average in units of 10^{-22} W m^{-2} Hz^{-1}. This work was incorporated into the COSPAR International Reference Atmosphere [1965] (CIRA 65).

Jacchia [1965] developed improved temperature profiles which were approximated by equation (1.3) in his second model thermosphere (J65). Jacchia [1971] further developed his upper atmosphere model by including solar,

geomagnetic, temporal, and geographic parameters represented by empirical equations. His work (J71) was adopted in the CIRA 72 model atmosphere. Jacchia obtained his results by comparing full solar disk $F_{10.7}$ with the terrestrial thermospheric and exospheric temperature variations. The exospheric temperature, T_∞, of the J71 model is

$$T_\infty = 379^\circ + 3.24(\bar{F}_{10.7}) + 1.3(F_{10.7} - \bar{F}_{10.7}) \quad ^\circ\text{K} \tag{1.7}$$

where $\bar{F}_{10.7}$ is the average over three solar rotations (81 days). This equation represents the night global average temperatures, while the day temperatures are given by $T_{\infty_D} = 1.3T_\infty$.

Hedin *et al.* [1977] and Hedin [1983] used mass spectrometer data from five satellites and incoherent scatter radar measurements from four ground stations to develop thermospheric temperature and density models based on the mass spectrometer and incoherent scatter radar information (MSIS), MSIS 77 and MSIS 83, in which the quantities were empirically represented by expansions of spherical harmonics. These empirical measurements included diurnal variations for different levels of geomagnetic activity and were combined with temperature profiles based on the J65 profiles.

The temperature formulation of Hedin's MSIS 83 model were written as a function of altitude, latitude, longitude, time of day, daily $F_{10.7}$, its 81-day average, and the geomagnetic index A_p

$$T(z) = T_\infty - (T_\infty - T_\ell)\exp[-\sigma\xi(z, z_\ell)] \qquad z \geq z_a \quad ^\circ\text{K} \tag{1.8a}$$

$$T(z) = 1/(1/T_0 + T_B x^2 + T_C x^4 + T_D x^6) \qquad z < z_a \quad ^\circ\text{K} \tag{1.8b}$$

and similarly, the density was given by

$$n(z, M) = [n_d(z, M)^A + n_m(z, M)^A]^{\frac{1}{A}} C_1(z) \ldots C_n(z) \quad \text{cm}^{-3} \tag{1.9a}$$

$$A = M_h/(\overline{M}_0 - M). \qquad (1.9b)$$

T_ℓ is the reference temperature at 120 km, σ is defined in equation (1.4), $\xi(z, z_\ell)$ is an altitude parameter, z_a is the altitude of the temperature profile junction (116.5 km), T_0 is the mesopause temperature, T_B, T_C, T_D are the lower thermosphere temperature parameters, and x is the lower thermosphere altitude parameter. M is the molecular weight of a gas species, $M_h = 28$, $\overline{M}_0 = 28.95$, n_d is the diffusive profile, n_m is the mixing profile, and C_n are coefficients which parameterize the chemistry and dynamic flow effects. Figures 1.6a-1.6d show typical density and temperature profiles generated by the MSIS 83 model for solar minimum (76200) and solar maximum (79050) conditions. 76200 refers to July 18, 1976 (day 200) while 79050 refers to February 19, 1979 (day 50). The total density at the top of the thermosphere ranges over a factor of twenty-five from 8×10^6 to 2×10^8 particles cm^{-3} from solar minimum to maximum conditions. This phenomenon is largely a function of the EUV energy variation. Lower altitude thermospheric concentrations vary slightly between 3.7×10^{11} to 4.9×10^{11} cm^{-3} at 120 km over this time period. The T_∞ varies from 750-1350 K from low to high solar activity while the temperature at 120 km varies slightly from 360 - 400 K.

Recent work by Hedin [1987], MSIS 86, extends MSIS 83. Additional data from the Dynamics Explorer (DE) satellite is included to improve the representation of the polar regions. MSIS 86 is a candidate for inclusion in the CIRA 86 model atmosphere. Hedin [1985] recently outlined in Figure 1.7 the historical development of empirical model thermospheres and discussed their relative advantages and disadvantages. He indicates that there have been two approaches to the development of the empirical models. First, several models have been based upon total derived density from satellite drag data,

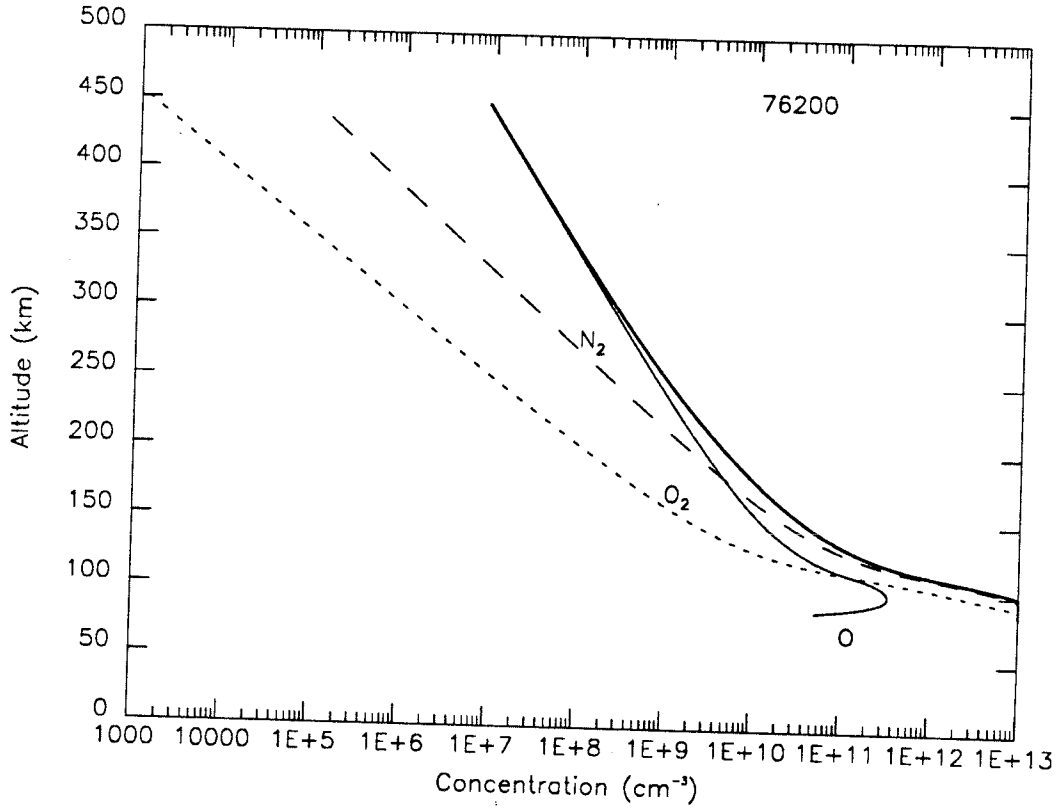

Figure 1.6 (a) **Solar minimum thermospheric concentrations.**

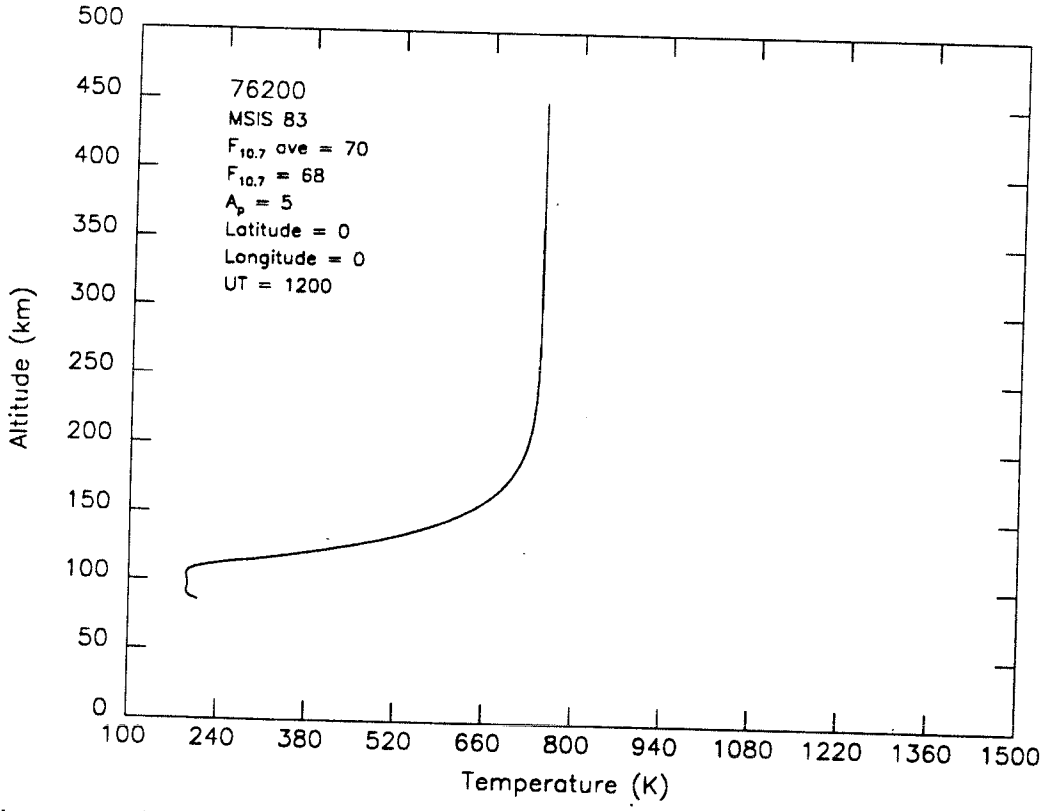

Figure 1.6 (b) **Solar minimum thermospheric temperatures.**

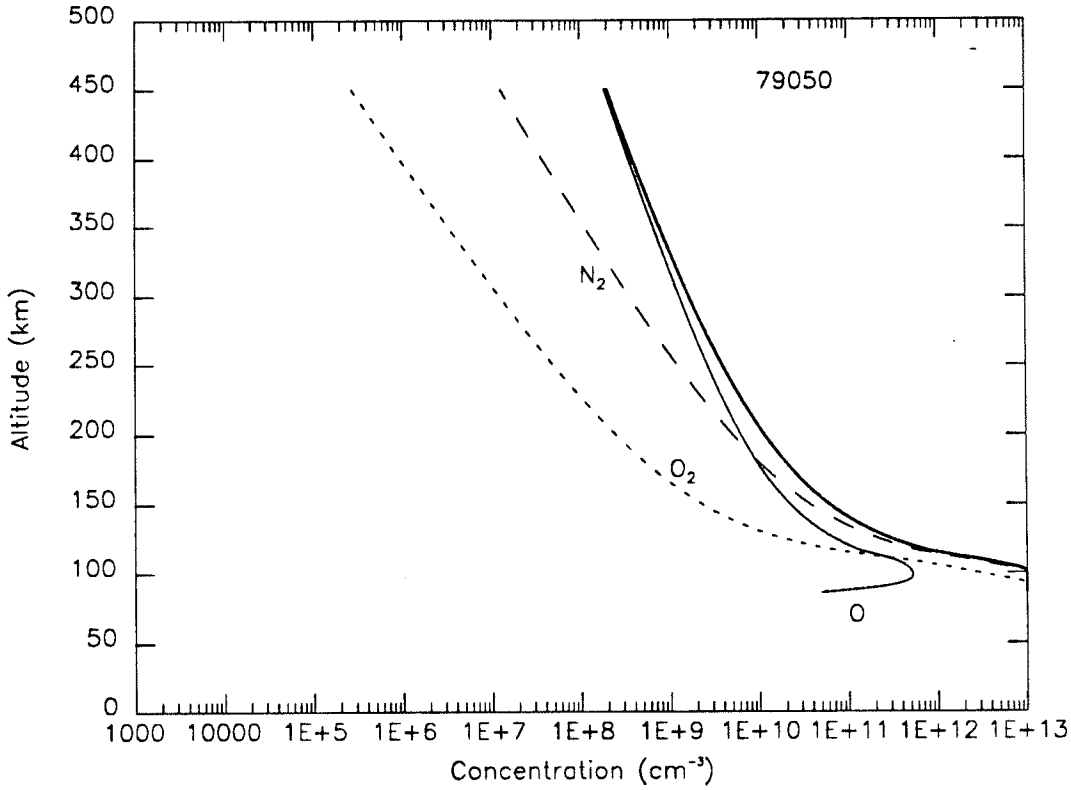

Figure 1.6 (c) **Solar maximum thermospheric concentrations.**

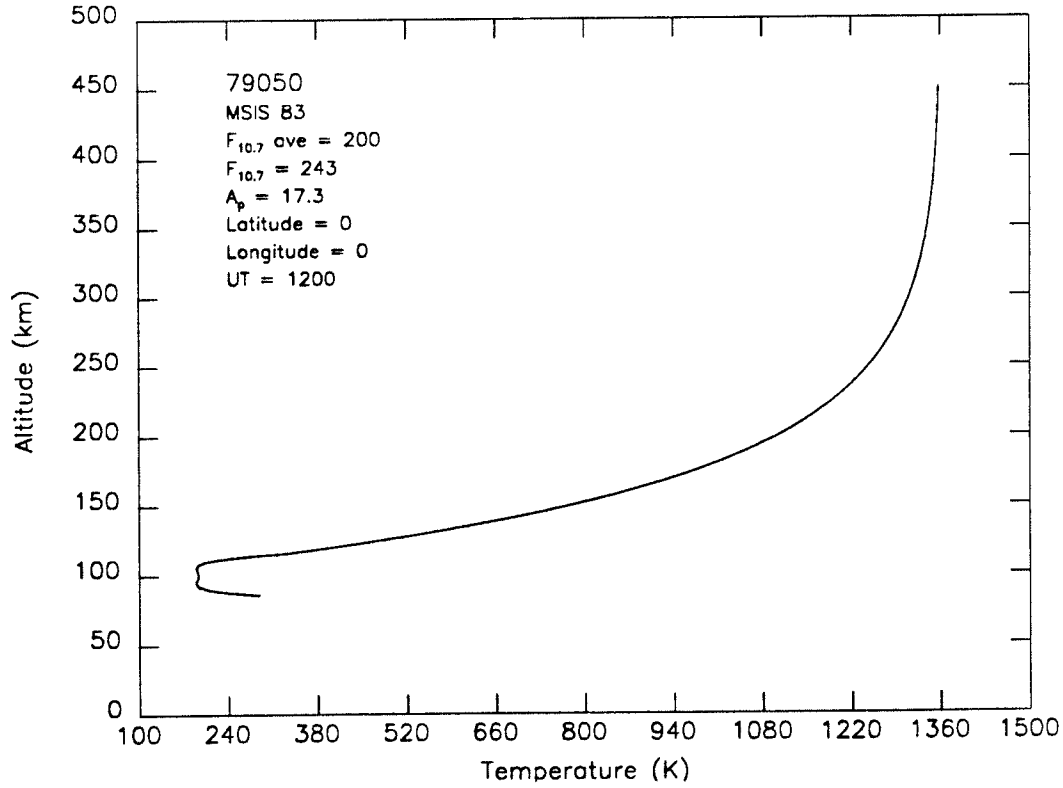

Figure 1.6 (d) **Solar maximum thermospheric temperatures.**

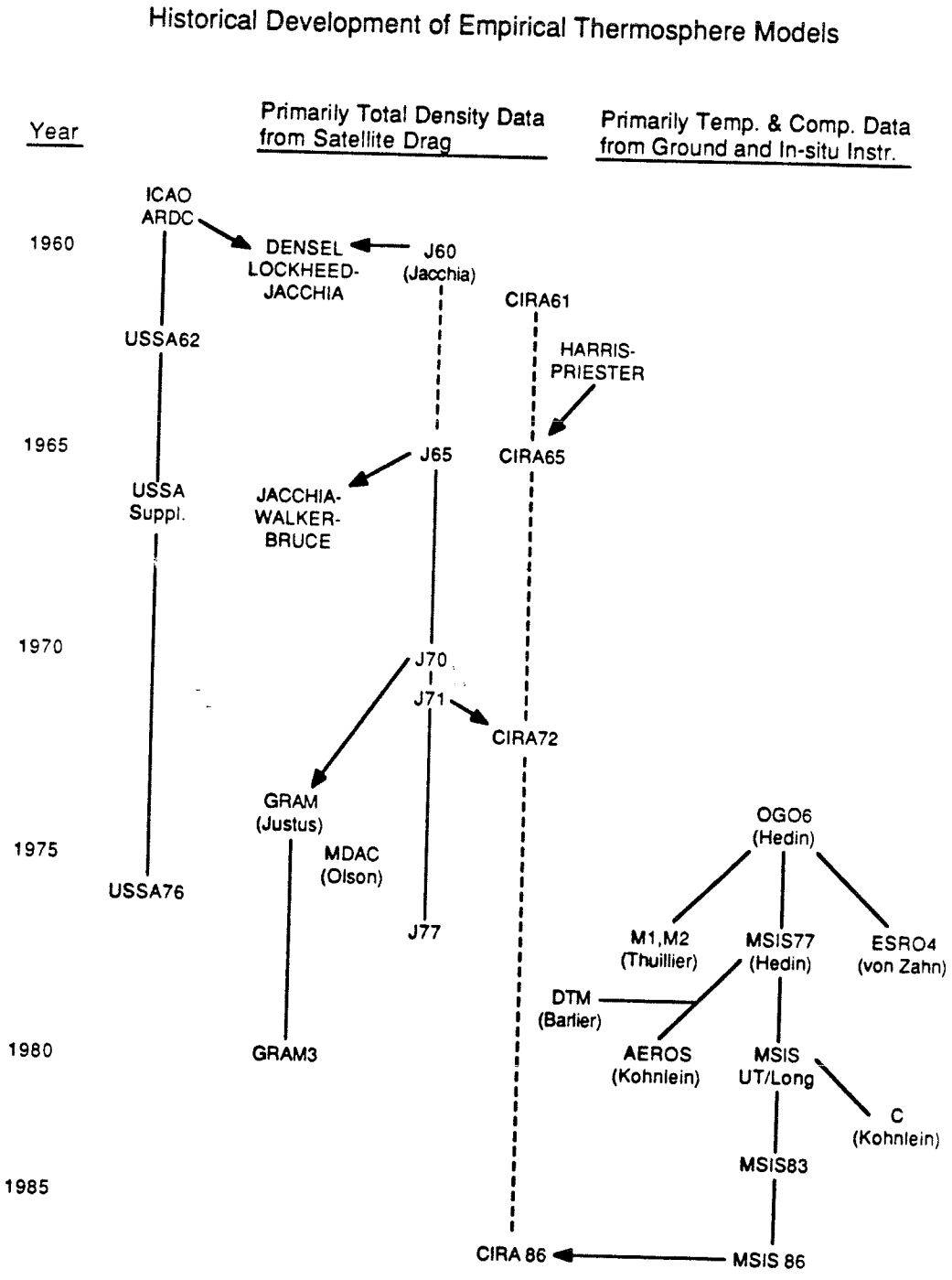

Figure 1.7 **Historical development of empirical thermosphere models.** This figure is reproduced from an original by Hedin [1985].

as in the Jacchia series models. Second, other models have been based upon temperature and compositional data from ground and in-situ observations, where MSIS is the prime example. The CIRA models have borrowed from both approaches.

1.2.2 Numerical Thermospheric Modeling

One-dimensional (altitude-varying) thermospheric models have been developed extensively since the early 1950s. S. Chapman, D.R. Bates, and M. Nicolet have contributed significantly to understanding the physics of the upper atmosphere. Using the principles of energy and momentum conservation and mass continuity in the thermosphere, several authors have analyzed steady state conditions for the one-dimensional model. Banks and Kockarts [1973] summarized much of this early work and reviewed the details of the conservation and continuity equations. The atmospheric model described in Chapter IV of this thesis is a one-dimensional numerical model based on the Banks and Kockarts summary. It combines the basic physics and chemistry of the thermosphere with a numerical technique for solving the temperature from the energy equation. This method of modeling is adequate for demonstrating the parameterization of solar EUV energy input on a global and climatic scale.

The full solutions of the conservation and continuity equations outlined in Banks and Kockarts require a three-dimensional, time-dependent model which is beyond the scope of this thesis. However, there are a few three-dimensional models currently in development. The National Center for Atmospheric Research (NCAR) Thermospheric Global Circulation Model (TGCM), as outlined by Roble *et al.* [1987], is an example of a self-consistent global numerical model with a fully coupled thermosphere and ionosphere. Global dynamics as a function of altitude, latitude, and longitude are included in that

model.

1.3 Modeling of Satellite Orbit Perturbations

In the last three decades, there has been extensive work conducted on the problem of satellite orbit perturbations. Both analytical and numerical approaches have shed new light on the behavior of low-Earth orbiting satellites. The history of orbit determination followed from Newton, where, in *Philosophiae Naturalis Principia Mathematica* (1686), he gave generalized results for circular orbits from his three laws of motion. Euler in 1744 was the first to propose a purely analytical method for determining parabolic orbits which was applicable to comets. Lambert extended Euler's equations to elliptical and hyperbolic orbits. However, it was Lagrange in 1788 who formulated a complete solution for the two-body problem, and his work as used today is termed Lagrange's planetary equations.

In modern times, methods for estimating orbit parameters have been developed with analytic solutions for circular orbits first, then elliptical orbits. Numerical solutions based on the classical equations were also devised, particularly by Sterne [1960] and King-Hele [1964]. For example, King-Hele used formulations which accounted for oblateness and rotation of the atmosphere to evaluate the effects upon one orbit revolution only. He integrated the single orbit revolution result over thousands of revolutions and thereby provided an analytic solution of the periapsis radius, $r_p(e)$, and the eccentricity, $e(t)$. This is an example of the drag-only problem.

The next level of sophistication in orbit determination methods used either analytic or semi-analytic methods to describe satellite behavior. These differ from the drag-only solutions by including solar-lunar perturbations and nonspherical gravitational attractions along with atmospheric density pertur-

bations. This is called the drag-coupled problem and has been reviewed by Liu [1983] in a tutorial paper. Both drag-only and drag-coupled methods are based on numerical or empirical models of atmospheric density as outlined in section 1.2.

For this study, a relatively accurate and rapid means of long-term orbit determination is accomplished using a semi-analytic drag-coupled method which numerically solves Lagrange's planetary equations of motion. The Long-term Orbit Predictor (LOP) program developed by Kwok [1986] embodies this method. This program is used and briefly described in Chapter V.

1.4 Thesis Objectives

This study follows the spirit of work summarized in three recent meetings: the NOAA satellite drag workshop in 1982, the Marshall Space Flight Center (MSFC) upper atmosphere modeling workshop in 1985, and the Air Force Geophysics Laboratory (AFGL) density workshop in 1987. This thesis is aimed at improving thermospheric density predictions. A common theme in the above workshops suggests bringing the empirical and numerical global thermospheric density models closer to the physics of the upper atmosphere in both structure and dynamics. A general goal of the community is to reduce the density uncertainty from a current 15-30% level to a 5-10% level over the next few years. One method of doing this, as addressed in this thesis, is to replace R_z and $F_{10.7}$ with indices more closely related to EUV flux variation. Eventually, of course, one hopes that EUV fluxes will be measured on a regular basis.

This work introduces Lyman-α (1216 Å) and 1-8 Å X-ray flux as indices for the solar EUV fluxes in lieu of the daily observations. The hypothesis is presented that the solar Lyman-α and 1-8 Å X-ray emissions, measured on

a daily basis by the Solar Mesosphere Explorer (SME) and Geostationary Operational Environmental Satellites (GOES), respectively, are superior indices for modeling the dominant EUV and soft X-ray fluxes and subsequent thermospheric heating. Solar Lyman-α is shown to be an effective EUV parameter comparable to $F_{10.7}$ during periods of high solar activity at high thermospheric altitudes for certain important fluxes. The 1-8 Å X-ray flux is shown to be useful in solar maximum conditions for portraying the activity of other important EUV fluxes. This two-indices EUV flux model enables the uncertainty to be narrowed in estimating the solar energy input. It is suggested that the uncertainty in the density and temperature variations may be likewise narrowed during periods of low solar activity.

The modeling method used is the following. Lyman-α is correlated to solar chromospheric region EUV fluxes and 1-8 Å X-rays are correlated to solar coronal region EUV fluxes. The two-indices set of modeled EUV fluxes is then used as the main energy input into a one-dimensional, time-dependent model of the thermosphere which solves for temperature and composition. The kinetic processes of molecular diffusion as well as eddy and turbulent mixing and the thermal processes of molecular, eddy, and turbulent conduction and radiative cooling are included in the model along with heating resulting from photoabsorption processes. The modeled densities at the top of the thermosphere over the decline of cycle 21 are then compared with the derived mass density from satellite orbit decay and MSIS 83 modeled density for the same time period. A separate test of this thermospheric density model is then made where it is used as an input for solving the problem of atmospheric drag and long-term orbit prediction on a low Earth orbiting spacecraft.

The results indicate that the modeled EUV flux in the one-dimensional thermospheric model leads to agreement with satellite derived densities during

solar maximum. These modeled densities have a comparable error margin as the MSIS 83 model which is based on the $F_{10.7}$ EUV parameter.

1.5 Thesis Outline

Chapter II (Observational Data) references the seven datasets used in this study. They include 1) the collection of solar Lyman-α and EUV emissions observed by AE-E, 2) the Lyman-α, 3) nitric oxide density, and 4) orbit period rate change data and derived mass density calculations from SME, 5) the World Data Center (WDC) $F_{10.7}$ data and 6) A_p data, and 7) the GOES 1-8 Å X-ray data.

Chapter III (Solar Flux - Terrestrial Thermosphere Coupling) outlines the current state of solar EUV monitoring. The heating of the thermosphere by EUV flux is examined and the details of the correlations between solar EUV flux and the indices of Lyman-α, $F_{10.7}$, and 1-8 Å X-rays are discussed. The dominant emissions and the relevant indices are then described. The A_p index is introduced for modeling auroral region temperatures, the derivation of the mass density from the SME orbit period rate change data is summarized, and the variation of equatorial nitric oxide in the lower thermosphere is reviewed.

Chapter IV (Thermospheric Modeling) contains two parts. First, a review of thermospheric structure and dynamics includes the basic principles of mass continuity, conservation of momentum, and conservation of energy. The solution of the latter time-dependent equation is discussed. The Crank-Nicolson numerical technique combined with the Thomas algorithm for the temperature calculation is introduced and is discussed in detail in Appendix A. The one-dimensional thermosphere model used in this study is detailed, including the initial and boundary conditions, the constituent densities, the EUV, dissociation, Joule, and particle precipitation heating and the heat

transfer processes of radiative cooling as well as molecular, eddy, and turbulent thermal conduction. Second, the model results for the above processes are validated for solar maximum and minimum conditions by comparison to MSIS 83. The results for modeling the declining phase of solar cycle 21 are also discussed in detail with conclusions drawn in the comparisons of this model's densities to MSIS and SME derived densities.

Chapter V (Modeling Thermosphere - Satellite Orbit Interactions) outlines a long-term orbit predictor (LOP) and its application to this problem of drag-coupled orbit prediction. The semi-analytic orbit predictor's theoretical basis is described along with the initial condition input parameters. The elimination of the J_2 and m-daily geopotential terms is justified. The drag coefficient, C_d, is described in great detail to justify the value used in this analysis. After the input modeled thermospheric density time series are outlined, comparisons are made of the final results of altitude decay for SME using different density inputs.

Chapter VI (Summary) reviews the work in this thesis and summarizes the significant and new contributions in the areas of observational data processing and analysis, EUV emission modeling, thermospheric modeling, and orbit lifetime modeling. Future work is outlined which will extend or improve upon the results of this dissertation.

CHAPTER II

OBSERVATIONAL DATA

Data from four separate sources, comprising seven datasets and spanning nearly a decade between 1977 and 1986, are used in this study. Three particular satellites, the AE-E, SME, and GOES series have taken observations which are used in this work. In addition, solar geophysical data from the World Data Center (WDC) are also used. Sections 2.1 - 2.4 detail the features of the datasets from these four sources. Further interpretations are left to Chapter III.

Figure 2.1 outlines on a relative scale, organized by wavelength, several of the solar cycle 21 fluxes used in this study between January 1, 1977 and December 31, 1986. They include daily $F_{10.7}$, adjusted to 1 AU, from the WDC for the dates January 1, 1977 through December 31, 1986. Daily-averaged and filtered SME H Lyman-α (1216 Å) adjusted to 1 AU is shown for the period January 1, 1982 through December 31, 1986. AE-E H Lyman-α emissions for the dates July 1, 1977 through December 30, 1980, which are interpolated over missing data, are shown along with H Lyman-β (1026 Å), 850-900 Å (dominated by H Lyman continuum), O V (630 Å), He I (584 Å), He II (304 Å), and 150-200 Å (dominated by Fe VIII (168 Å) among the chromospheric fluxes and by Fe IX (171 Å) among the coronal fluxes). The GOES 1-8 Å X-ray background data, as modeled by Bouwer [1983], are shown between the dates of March 21, 1977 through December 31, 1980. GOESS 1-8 Å data, supplied by the National Space Science Data Center (NSSDC) and condensed to a daily

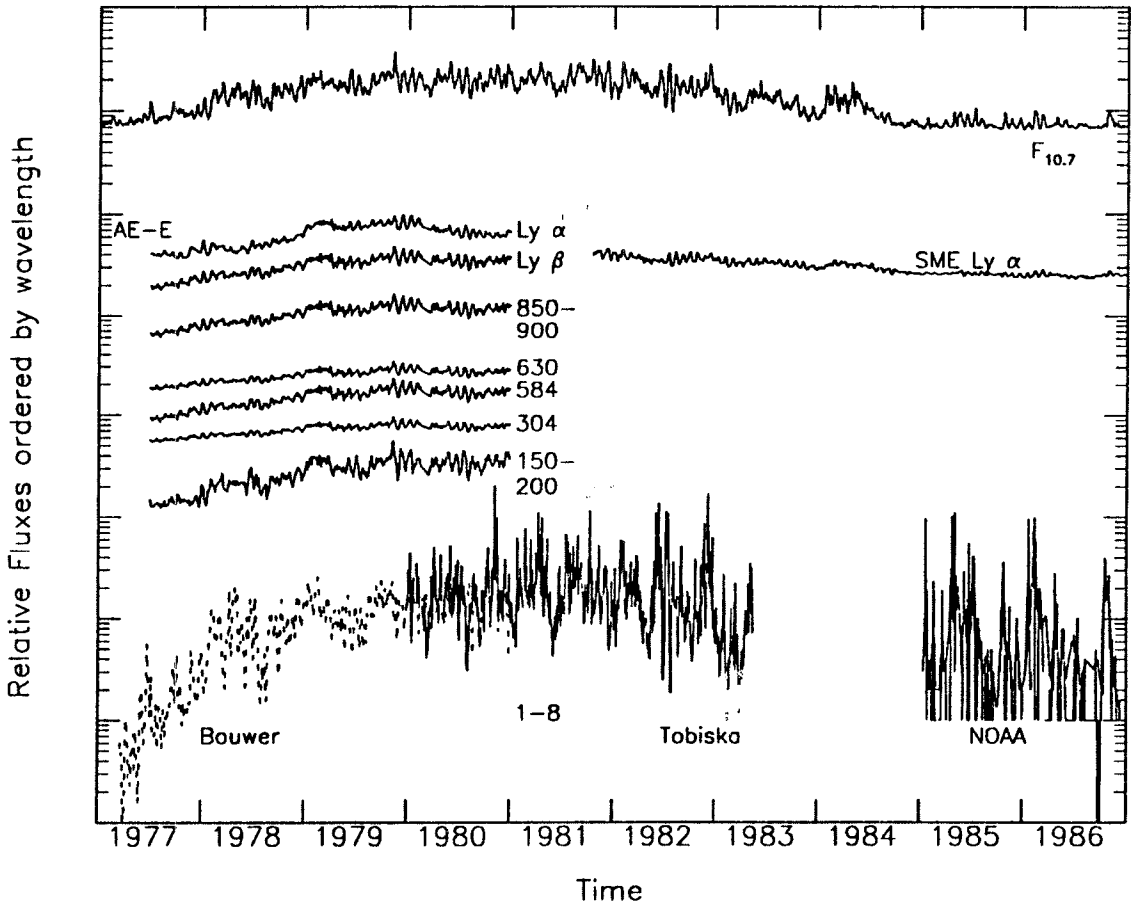

Figure 2.1 **Cycle 21 solar datasets.** The solar datasets of the $F_{10.7}$, SME Lyman-α, AE-E Lyman-α, Lyman-β, 850-900 Å, 630 Å, 584 Å, 304 Å(chromospheric), 150-200 Å(cool corona), and 1-8 Å X-rays (corona) are shown with their relative variations. The Bouwer [1983] and Tobiska (Appendix B) datasets are distinct from the NOAA dataset. The latter dataset has a lower threshold value below which there is little or no information.

background flux, are shown for January 1, 1980 through May 19, 1983. The January 1, 1985 through December 31, 1986 X-ray background data comes from the NOAA *Solar-Geophysical Data Comprehensive Reports*. The emissions are plotted by wavelength and not by comparative magnitudes with each other. The important feature in all the emissions is the consistent rise from solar minimum to maximum combined with solar rotational features superimposed upon the time series.

Figure 2.2 shows the relative variations of terrestrial data used in this study. The data are plotted with a relative scale according to observation height in the atmosphere for January 1, 1977 through December 31, 1986. The SME daily-averaged orbit period rate change data, dP/dt, are shown between January 1, 1982 and December 31, 1986. The daily-averaged, equatorial region, lower thermospheric nitric oxide (NO) γ-band (1,0) emission between $\pm 30^{\circ}$ latitude at 110 km altitude is shown between the dates of January 6, 1982 through August 25, 1986. The daily mean A_p geomagnetic index is given between January 1, 1977 and December 31, 1986. The relationships between the solar and terrestrial datasets are explained in fuller detail in Chapter III; however, some detailed information about each dataset is useful.

2.1 Atmosphere Explorer-E (AE-E) Data

Since rockets were first used for observing solar EUV, there have been a number of short duration observational flights. Hinteregger [1961], Neupert *et al.* [1964], Hinteregger *et al.* [1965], Hall and Hinteregger [1970], Timothy and Timothy [1970], and Schmidtke [1978] have all made early rocket observations or have interpreted data from the Orbiting Solar Observatory (OSO) or AEROS satellite series. These studies gave a first look at the order of magnitude of emissions in the EUV. Hinteregger *et al.* [1965] tabulated

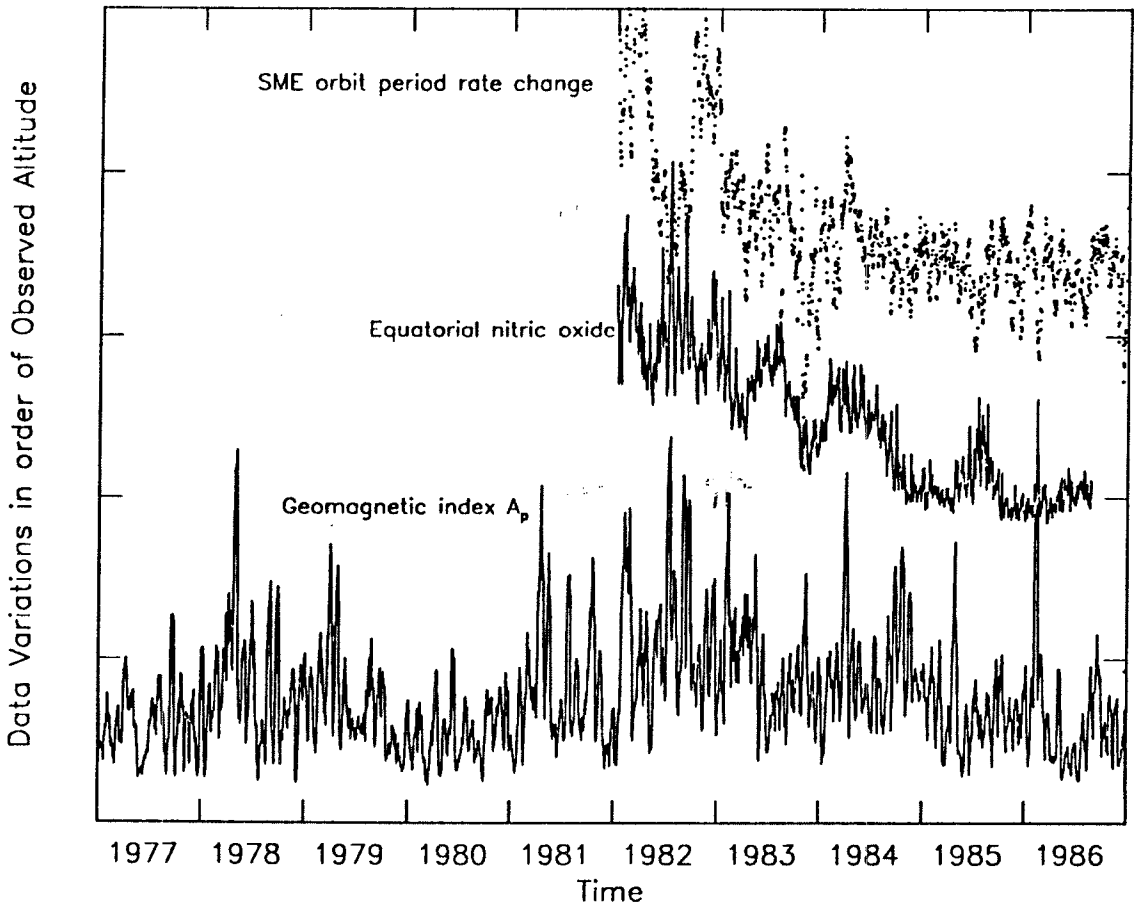

Figure 2.2 **Cycle 21 terrestrial datasets.** The terrestrial datasets of the SME orbit period rate change data, the equatorial nitric oxide density, and the A_p geomagnetic index are shown with their relative variations.

emission lines or ranges of line groups and these were widely considered the "EUV standard flux" for many years. A major step forward in the systematic observations of EUV flux occurred with the successful AE series of satellites in the 1970s. Data provided by AE-E in particular, and analyzed by Hinteregger *et al.* [1981], is the only contiguous, long-term solar EUV dataset available. It covers the rising portion and maximum period of solar cycle 21 (1977-1980) and is not corrected to 1 AU. This is helpful for comparison with other datasets. Approximately one-third of the data exists in each wavelength or wavelength group for that time period. Hence, the best resolution which may be obtained is the 27-day solar rotational periodicity in the data. There have been no comparable datasets developed since the cycle 21 maximum.

Since these data are the basis for EUV flux in SERF1 and are extensively referenced in this study, a brief discussion of collection and organization is appropriate. The AE-E satellite carried an EUV spectrophotometer. This instrument was composed of 24 monochromators, some operating at fixed wavelengths and others possessing a scanning capability. The spectrophotometer was nearly identical to those instruments flown on the AE-C and AE-D missions. Hinteregger *et al.* [1973] describes the operation of this instrument and the experiment objectives. Especially important to the study of EUV emissions were five monochromators, including a fixed wavelength monochromator (#22) sensitive to full-disk Lyman-α and the scanning monochromators (#1, #2, #5, and #9) for much of the wavelength range between 142-1049 Å. Table 2.1, which was provided in the AE-E dataset file SC#21OBS.EUVS obtained from the NSSDC, outlines 15 important wavelength groups as defined by Hinteregger. The monochromator number, the scan steps, and the nominal wavelength range are given for each wavelength group. The data under the headings WLG# RFJUL76 are the absolute fluxes for each wavelength group

TABLE 2.1. AE-E SC#21OBS.EUVS EUV IRRADIANCE OBSERVATIONS

DESIGNATION	SCAN MN#	FROM STEP	TO STEP	WAVELENGTH RANGE (NOM.)
WAVELENGTH GROUP # 1	1	57	93	168 Å — 190 Å
WAVELENGTH GROUP # 2	1	97	124	190 Å — 206 Å
WAVELENGTH GROUP # 3	2	1	61	206 Å — 255 Å
WAVELENGTH GROUP # 4	2	62	119	255 Å — 300 Å
WAVELENGTH GROUP # 5	2	125	127	304 Å (He II + Si XI)
WAVELENGTH GROUP # 6	5	1	56	510 Å — 580 Å
WAVELENGTH GROUP # 7	5	64	65	584 Å (He I)
WAVELENGTH GROUP # 8	5	72	128	590 Å — 660 Å
WAVELENGTH GROUP # 9	9	107	108	1026 Å (H Lyman-β)
WAVELENGTH GROUP #10	9	88	89	"KEY" for Class 1 335 Å (Fe XVI)
WAVELENGTH GROUP #11	2	100	101	"KEY" for Class 2 284 Å (Fe XV)
WAVELENGTH GROUP #12	1	118	119	200 Å — 204 Å (DOMINATED BY Fe XIII)
WAVELENGTH GROUP #13	1	76	77	178 Å — 183 Å (DOMINATED BY Fe XI)
WAVELENGTH GROUP #14	1	57	59	169 Å — 173 Å (DOMINATED BY Fe IX)
WAVELENGTH GROUP #15	22	64	64	1216 Å (H Lyman-α)

Flux reference values for July 13-28, 1976 given below are 10^9 photons cm^{-2} sec^{-1}.
In SC#21OBS, R = (Flux at given time)/(Flux Reference for 13-28 July, 1976).

WLG#	R FJUL76	WLG#	R FJUL76	WLG#	R FJUL76	WLG#	R FJUL76	WLG#	R FJUL76
1	1.38	**2**	.49	**3**	.85	**4**	1.16	**5**	6.24
6	1.44	**7**	1.58	**8**	2.36	**9**	4.41	**10**	.034
11	.114	**12**	.122	**13**	.265	**14**	.342	**15**	300.

in units of 10^9 photons cm^{-2} sec^{-1} for the July 13-28, 1976 cycle 21 minimum reference period. This table serves as a header for the daily absolute values in each wavelength group. They are given as a ratio to the solar minimum flux at that wavelength for the time period between July 1, 1977 through December 30, 1980, where this ratio is written as

$$R = (\text{Flux at given time})/(\text{Flux Reference for } 13-28 \text{ July}, 1976). \quad (2.1)$$

The July 13-28, 1976 period is considered the solar minimum reference period since there were no sunspots on the solar disk during that time, i.e., $R_z = 0$, and $F_{10.7}$ was constant at $68 \pm 1\%$. Figure 2.3 shows two representative AE-E EUV and the Lyman-α emissions where approximately two-thirds of the data are missing. A printed version of the dataset is listed by Schmidtke [1984].

A useful presentation of the AE-E EUV data is given by Torr *et al.* [1979] who have divided the wavelengths into 37 groups. These groups range from 50 Å to 1050 Å and include discrete lines as well as 50 Å intervals. The compilation of the EUV flux in 38 wavelength groups in Tables 2.2 and 2.3 follows the Torr *et al.* format with some changes. Wavelength lines at 787.71 and 790.15 Å for O IV, the interval 750-800 Å, and the interval 1000-1050 Å are corrected in Table 2.2 and Table 2.3 from the Torr *et al.* data. Additionally, the FeXVI (335.41 Å) and Lyman-α (1215.7 Å) lines are added. Table 2.2, combined with Figure 2.4, shows the emissions for solar minimum. The data are located in the NSSDC file SC#21REFW. Table 2.2 lists the wavelength group interval in Å, the flux in 10^9 photons cm^{-2} sec^{-1}, the source of the emission, the chromospheric or coronal key (explained below), and the wavelength dependent scaling parameter. Lyman-α flux and $F_{10.7}$ are also listed for comparison. The immediate observation of the solar minimum EUV spectrum in Figure 2.4 is that there are three distinct features. First, there

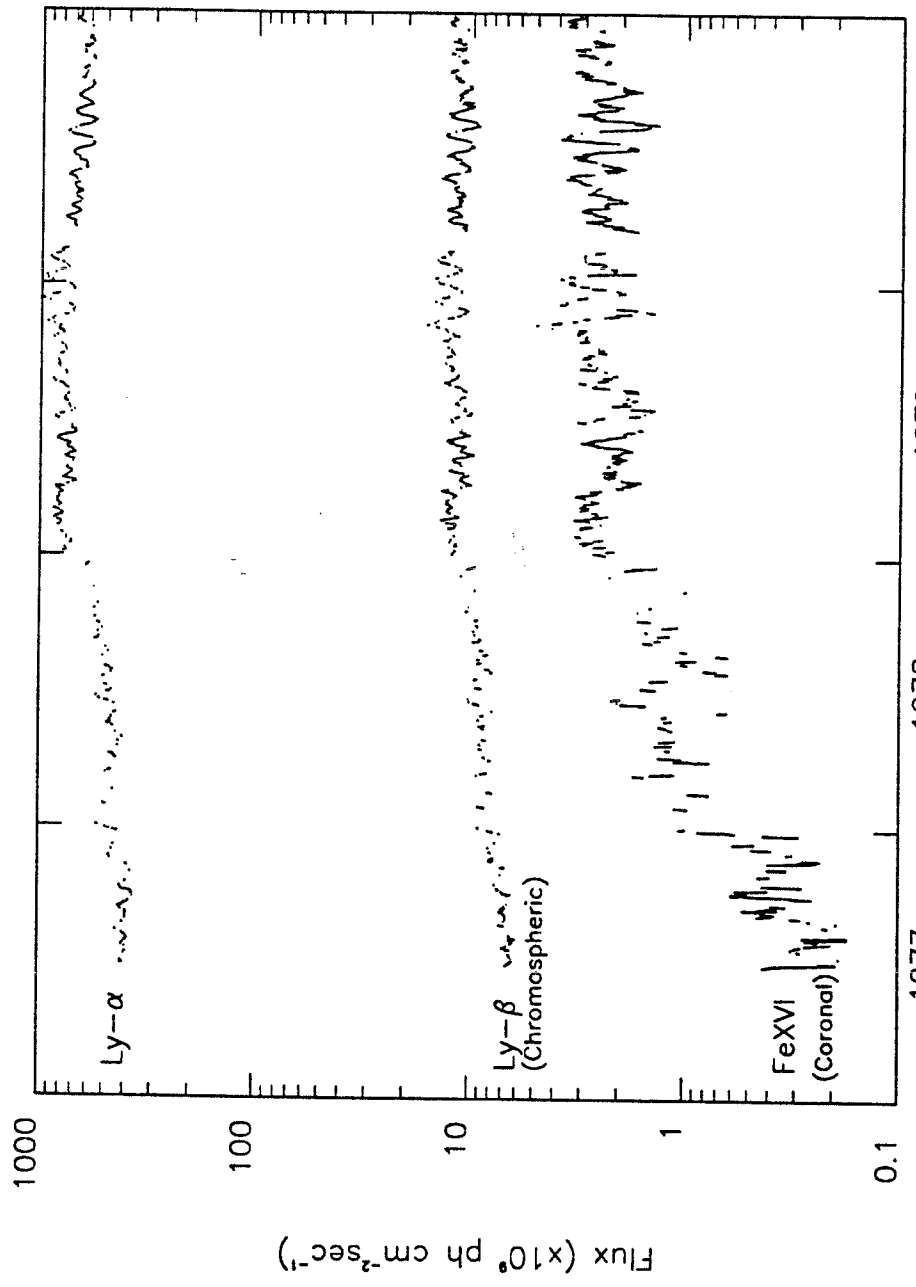

Figure 2.3 Representative AE-E EUV fluxes. Three representative AE-E datasets are shown from July 1, 1977 through December 30, 1980, demonstrating the chromospheric and coronal emissions along with the missing data.

TABLE 2.2. EUV WAVELENGTH INTERVALS - SOLAR MINIMUM

Interval	Wavelength (Å)		SC#21REFW	Ion Source	Key	C
1	50.000	100.00	0.3834		2	0.418
2	100.00	150.00	0.1346		1	0.473
3	150.00	200.00	1.8418		2	0.221
4	200.00	250.00	0.9235		2	0.324
5	256.32	256.32	0.2713	He II Si X	1	0.203
6	284.15	284.15	0.1000	Fe XV	2	0.408
7	250.00	300.00	0.8405		2	0.197
8	303.31	303.31	0.2350	Si XI	2	0.120
9	303.78	303.78	6.0000	He II	1	0.370
10	335.41	335.41	0.0340	Fe XVI	2	1.000
11	300.00	350.00	0.8321		2	0.254
12	368.07	368.07	0.7394	Mg IX	2	0.011
13	350.00	400.00	0.2121		2	0.392
14	400.00	450.00	0.3926		2	0.312
15	465.22	465.22	0.1800	Ne VII	2	0.013
16	450.00	500.00	0.3063		1	0.806
17	500.00	550.00	0.5085		1	0.606
18	554.37	554.37	0.7992	O IV G	1	0.460
19	584.33	584.33	1.5800	He I	1	0.988
20	550.00	600.00	0.4843		1	0.612
21	609.76	609.76	0.4500	Mg X	2	0.028
22	629.73	629.73	1.5000	O V	1	0.473
23	600.00	650.00	0.1746		1	0.420
24	650.00	700.00	0.2223		1	0.503
25	703.36	703.36	0.3915	O III G	1	0.415
26	700.00	750.00	0.1667		1	0.979
27	765.15	765.15	0.1997	N IV	1	0.581
28	770.41	770.41	0.2425	Ne VIII	2	0.022
29	787.71	790.15	0.7548	O IV O IV	1	0.460
30	750.00	800.00	0.9011		1	0.917
31	800.00	850.00	1.9311		1	0.989
32	850.00	900.00	4.4325		1	1.000
33	900.00	950.00	4.2170		1	0.665
34	977.02	977.02	5.9570	C III	1	0.608
35	950.00	1000.0	1.7850		1	0.508
36	1025.7	1025.7	4.3750	H Ly-β	1	1.000
37	1031.9	1031.9	3.1840	O VI	1	1.041
38	1000.0	1050.0	3.6284		1	0.508
	Total intensity		51.312	$\times 10^9$ ph cm^{-2}s^{-1}		
	1215.7	1215.7	300.0	H Ly-α	1	0.830
	$F_{10.7}$		68.0	$\times 10^{-22}$ W m^{-2}Hz^{-1}		

TABLE 2.3. EUV WAVELENGTH INTERVALS - SOLAR MAXIMUM

Interval	Wavelength (Å)		F79050N	Ion Source
1	50.000	100.00	1.1487	
2	100.00	150.00	0.3433	
3	150.00	200.00	4.8498	
4	200.00	250.00	3.7013	
5	256.32	256.32	0.5947	He II Si X
6	284.15	284.15	3.1675	Fe XV
7	250.00	300.00	4.1358	
8	303.31	303.31	2.4995	Si XI
9	303.78	303.78	11.2800	He II
10	335.41	335.41	2.7642	Fe XVI
11	300.00	350.00	2.8684	
12	368.07	368.07	1.3949	Mg IX
13	350.00	400.00	2.1965	
14	400.00	450.00	0.9932	
15	465.22	465.22	0.3621	Ne VII
16	450.00	500.00	1.6716	
17	500.00	550.00	1.5468	
18	554.37	554.37	1.5904	O IV G
19	584.33	584.33	4.8664	He I
20	550.00	600.00	1.0213	
21	609.76	609.76	1.4621	Mg X
22	629.73	629.73	3.0180	O V
23	600.00	650.00	0.4820	
24	650.00	700.00	0.4554	
25	703.36	703.36	0.7165	O III G
26	700.00	750.00	0.4256	
27	765.15	765.15	0.4318	N IV
28	770.41	770.41	0.6709	Ne VIII
29	787.71	790.15	1.5020	O IV O IV
30	750.00	800.00	2.2658	
31	800.00	850.00	5.0135	
32	850.00	900.00	13.2980	
33	900.00	950.00	12.0340	
34	977.02	977.02	13.1770	C III
35	950.00	1000.0	4.4204	
36	1025.7	1025.7	13.1250	H Ly-β
37	1031.9	1031.9	9.0426	O VI
38	1000.0	1050.0	8.6788	
	Total intensity		143.22	$\times 10^{9}$ ph cm^{-2}s^{-1}
	1215.7	1215.7	864.01	H Ly-α
	$F_{10.7}$		243.0	$\times 10^{-22}$ W m^{-2}Hz^{-1}

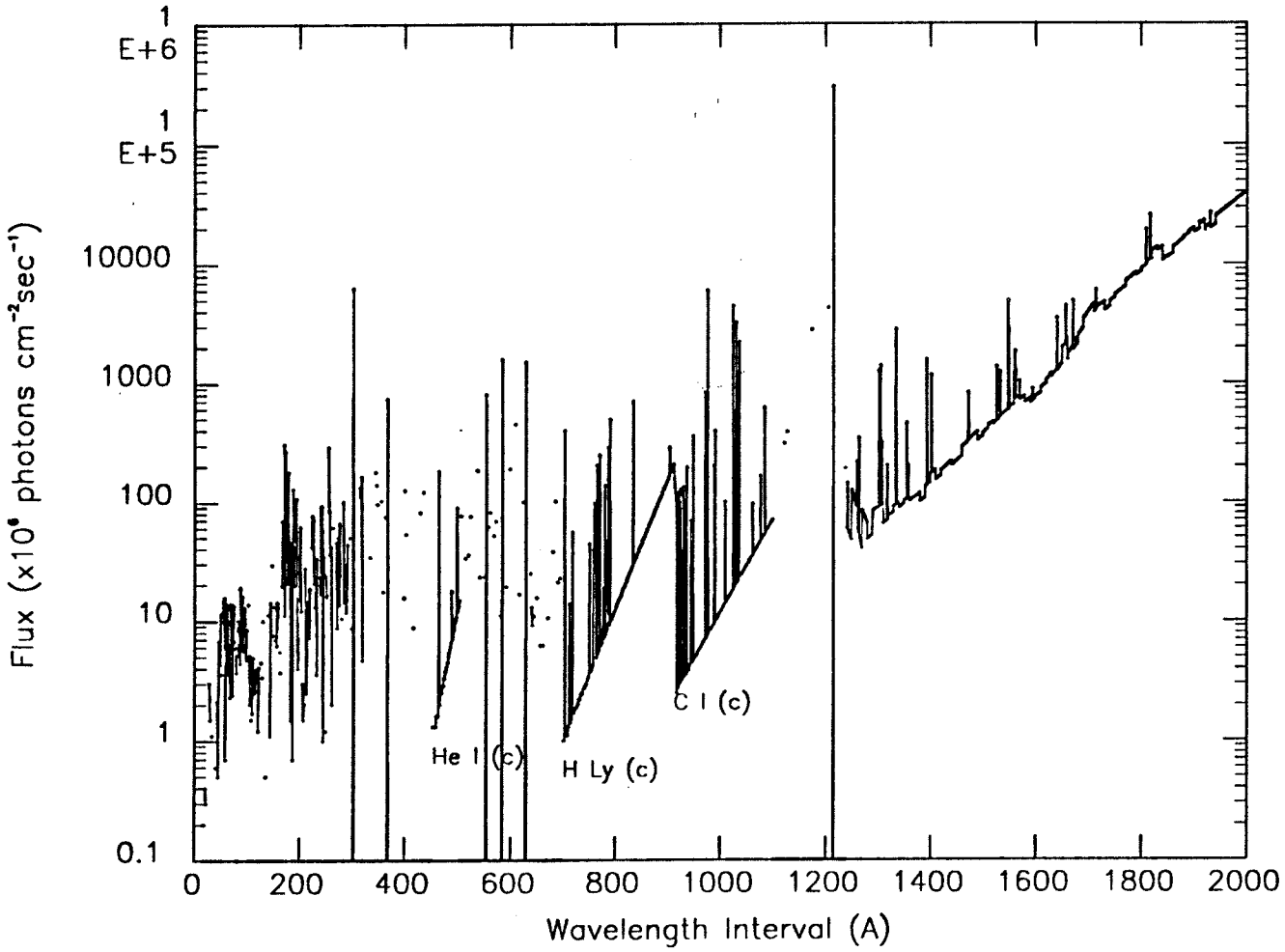

Figure 2.4 SC#21REFW reference spectrum for July 1976. This solar minimum dataset is described by Hinteregger *et al.* [1981].

are several lines which have high emissions compared to the others. These include He II, Mg IX, O IV, He I, O V, C III, H Lyman-β in the EUV and H Lyman-α in the far ultraviolet (FUV). Second, there are three distinct continuum features between 453-504 Å (He I continuum), 700-912 Å (H Lyman continuum), and 913-1100 Å (C I continuum). Third, the EUV part of the spectrum has significantly less flux than the longer UV wavelengths. The actual magnitudes of these emissions are listed in Table 2.2. For solar maximum conditions, or NSSDC file F79050N, Table 2.3 and Figure 2.5 show the same features but with larger magnitudes. The total EUV flux for solar minimum is 51.312×10^9 photons cm^{-2} sec^{-1} while solar maximum flux is 2.8 times larger at 143.22×10^9 photons cm^{-2} sec^{-1}. He II, C III, Lyman-β, 850-900 Å, and 900-950 Å emissions contribute the largest amount of flux in the EUV. These two AE-E datasets were released June 16, 1981 and represent the updated July 1976 and February 1979 solar EUV flux conditions.

Although the NSSDC EUV data cover the wavelength range from 18-1050 Å, AE-E only measured the solar spectrum greater than 142 Å. The NSSDC dataset from 18-142 Å is based on an Air Force Geophysics Laboratory (AFGL) rocket measurements supplied to Hinteregger by Heroux. This dataset is not yet published in a separate report. The AFGL rocket of August 14, 1979, referenced by Hinteregger *et al.* [1981] and Torr and Torr [1985], provided absolute intensity information for these shorter wavelengths. A separate file, F79226, has been provided by NSSDC corresponding to the date of the rocket flight. This 18-142 Å dataset is subject to further analysis and interpretation. It is used here as the best available, and the only pseudo-long-term, information for that wavelength range. Along with the AE-E absolute intensities, which are provided in the NSSDC files SC#21REFW and F79050N, these values should be considered no more than "typical" for a date and used only for

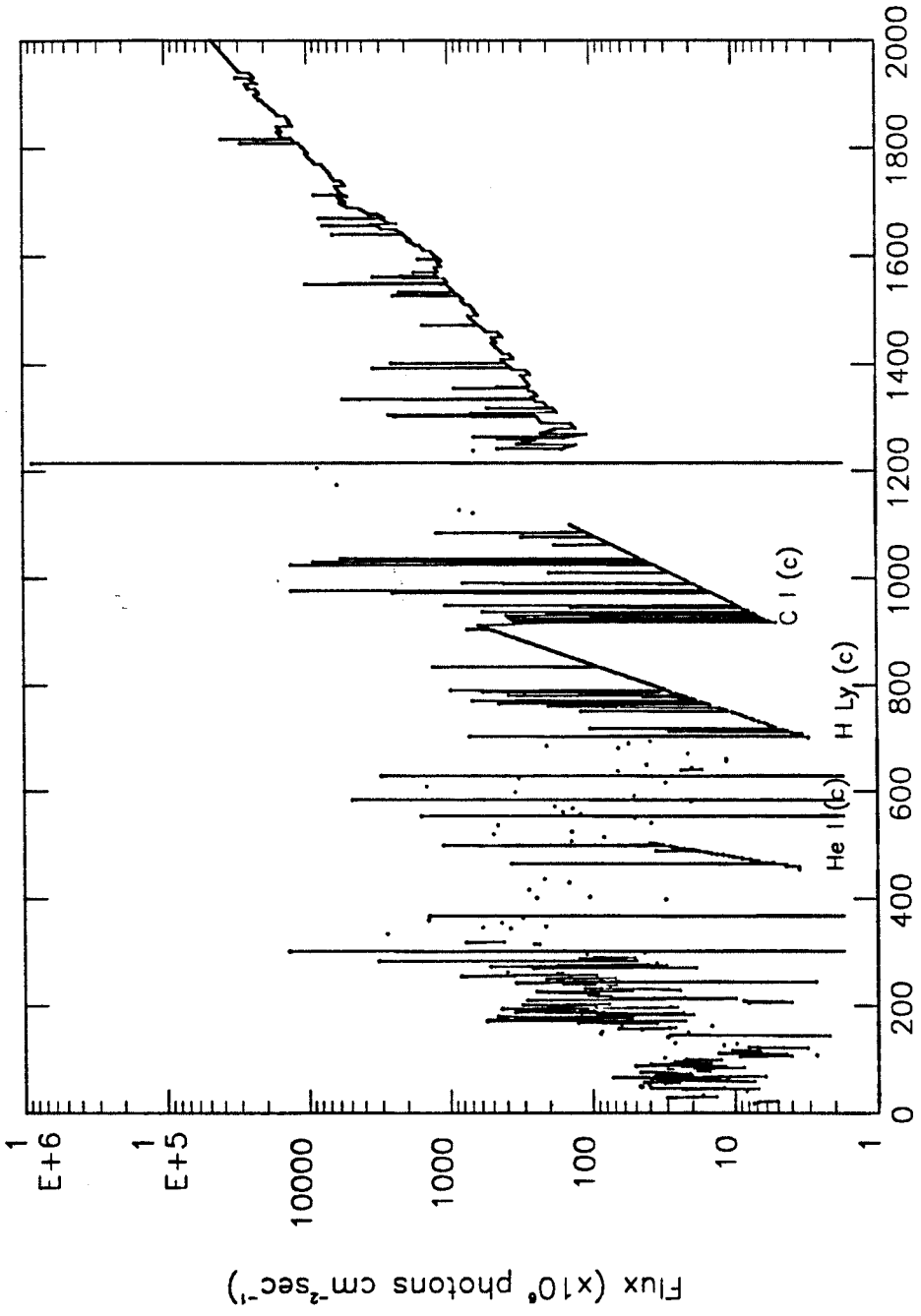

Figure 2.5 F79050N reference spectrum for February 1979. This solar maximum dataset is described by Hinteregger *et al.* [1981].

long-term trend analysis.

The use of Hinteregger's "key" and "C" items in Table 2.2 are explained more fully in Chapter III. They enable the approximate determination of an EUV flux for a given date during the AE-E time period. Each EUV flux is keyed to a chromospheric (Lyman-β, K=1) or coronal (Fe XVI, K=2) emission. The C value is an empirical scaling parameter for each wavelength. Using as R_k the data in wavelength group (WLG) 9 (Lyman-β) and WLG 10 (Fe XVI) from the SC#21OBS.EUVS file, the EUV flux on a given date is calculated using equation (1.2) with a wavelength dependent accuracy of 5 to 35%.

Table 2.4 adapted from Donnelly [1987a] gives additional source characteristics of the solar EUV. Ion sources are listed by wavelength and source region. The $\log_{10}$ peak temperature is also listed. The table indicates that there are three distinct regions in the solar atmosphere, two of which are shown in Chapter III to have an important effect upon the terrestrial thermosphere. In conjunction with explaining Table 2.4, Figure 2.6 is a diagram of the solar atmosphere adapted from Brasseur and Solomon [1984] showing these solar regions. The photosphere is often considered the "surface" of the sun, even though the entire star is in a gaseous state. It is a thin layer about 1000 km thick and is the visible disk. Most of the energy reaching the Earth, shown in Figure 1.2, comes from the photosphere which has relatively cool temperatures between 3000 and 6000 K. Granular cells, or granules, are distributed over the solar disk in the photosphere and are thought to be associated with strong convective processes. Sunspots are recorded on the photosphere as cool, dark regions as compared to faculae, which are bright features associated with active regions. Photospheric solar fluxes penetrate the middle and lower terrestrial atmosphere, with the visible wavelengths reaching the Earth's surface. Above the photosphere is the chromosphere, a layer approximately

TABLE 2.4. SOURCE CHARACTERISTICS OF SOLAR EUV AND UV

Wavelength (Å)	Ion Source	Source Region[a]	$\text{Log}_{10}T$ peak[b]
1 - 8	Soft X-rays	HC	>6.5
168 - 190		M4	
169 - 173	Fe IX	T	5.8
178 - 183	Fe XI	T+CC	6.1
190 - 206		M2	
200 - 204	Fe XIII	CC	6.2
206 - 255		M3	
255 - 300		M1	
284	Fe XV	HC	6.3
304	He II	Ch+BT	4.8
335	Fe XVI	HC	6.4
510 - 580	(554 O IV)	M6	
584	He I	Ch+BT	4.5
590 - 660	(610 Mg X) (630 O V)	M5	
1026	H Ly-β	Ch+BT	4.3
1216	H Ly-α	Ch+BT	4.3
2050	Al I continuum	Ph	<4.0
10830	He I	Ch+BT	
$F_{10.7}$	10.7 cm	Ch+T+CC+HC	
R_z	Zurich sunspot #	Ph	
P	Plage Index	Ch	

[a] Source Region code: HC = hot corona, strong contribution from above 2×10^6 K; CC = cool corona, 1 to 2×10^6 K; T = chromosphere-corona transition region; BT = base of the transition region; Ch = chromosphere; Ph = upper photosphere; M1 = mixture of HC & Ch+BT; M2 = mixture of T & CC; M3 = mixture of Ch+BT, T, CC & HC; M4 = mixture of T & CC; M5 = mixture of Ch, T & CC; M6 = mixture of Ch & T. From Donnelly [1987a].
[b] $T = 10^{\text{peak}}$ in K.

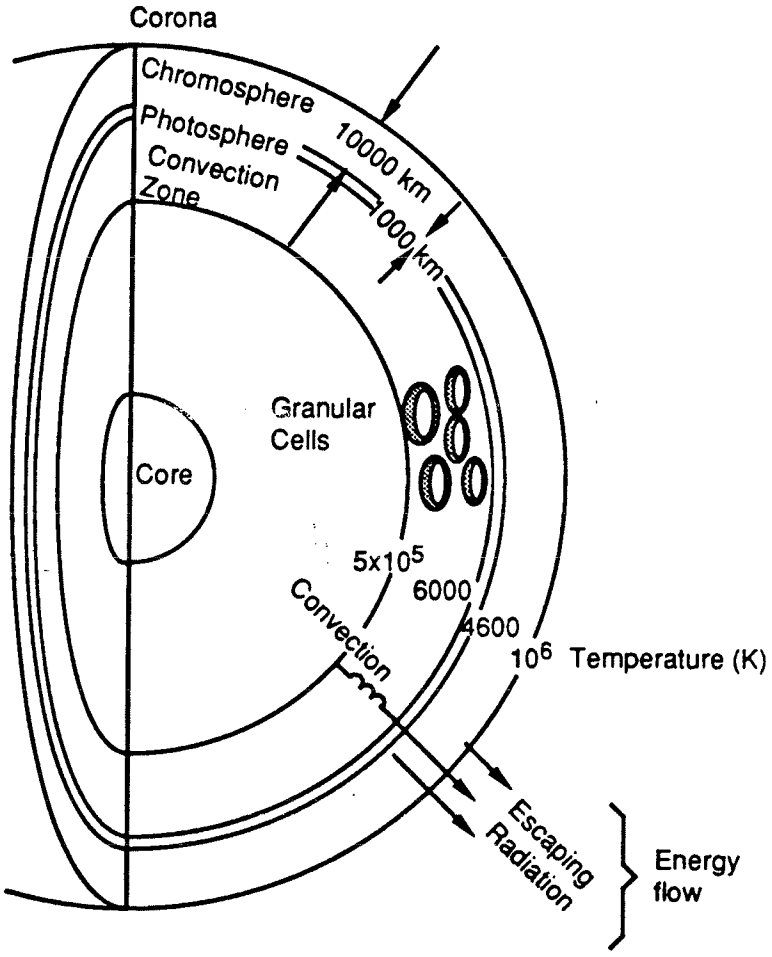

Figure 2.6 **Schematic diagram of the solar atmosphere.** The solar atmospheric regions are shown where the chromosphere and corona are particularly important for this study. This figure is reproduced from Brasseur and Solomon [1984].

10,000 km thick. At the upper levels, the temperature reaches $10^4 - 10^5$ K and is the source for emission lines in the FUV and EUV resulting from ionization of several elements. Visible light emissions are weak in this region, although bright UV plages are observed in the chromosphere as are prominences of large and relatively stable gas clouds within the upper levels. Solar flares are eruptive disturbances which occur in chromospheric active regions and can eject large numbers of energetic particles. Chromospheric fluxes penetrate to the thermosphere of the Earth and are absorbed at those altitudes. Above the chromosphere is the corona which extends to several solar diameters. Particles in the corona have a temperature on the order of 10^6 K. It, too, is disturbed by prominences and flares originating in the chromosphere and is a region where free electrons exist. Some coronal fluxes penetrate to the lower thermosphere and mesosphere and, along with some chromospheric emissions, are partially responsible for the Earth's ionosphere. Between the chromosphere and corona is a mixed layer referred to as the transition region. In this study, only the chromospheric and coronal fluxes will be used, since these are principal thermospheric energy sources.

Specifically for the AE-E time period, Table 2.5 outlines some characteristics of selected X-ray, EUV, and FUV lines from the solar corona and chromosphere. Within each wavelength group is listed the low solar activity flux and the date within the AE-E time frame for that value, the high solar activity flux and the AE-E date, and the ratio between high and low activity conditions for part of solar cycle 21. The chromospheric or coronal emissions are separated and keyed to (1) or (2), respectively. The reader is reminded that the wavelengths between 18 and 100 Å were not measured directly by AE-E, but by the August 1979 AFGL rocket described earlier. In this light, they represent the best available typical emission level. In this table, He II, 850-900

TABLE 2.5. X-RAY, EUV, AND FUV FLUX AND WAVELENGTH RATIOS

Wavelength[a] (Å)	Low activity Flux[b]	Low Date	High activity Flux[b]	High Date	High:Low
1-8 (2)	1.67E+03	77093	8.22E+05	80310	491.8
18-30 (2)	9.29E+06	77224	1.21E+08	79314	13.0
30-50 (1)	1.23E+07	77218	2.99E+07	79314	2.4
30-50 (2)	1.92E+07	77224	2.16E+08	79314	11.2
50-100 (1)	2.49E+08	77218	6.04E+08	79314	2.4
50-100 (2)	2.19E+08	77224	1.09E+09	79314	5.0
150-200 (1)	2.71E+08	77218	5.78E+08	79314	2.1
150-200 (2)	1.79E+09	77224	7.87E+09	79314	4.3
200-250 (1)	4.11E+08	77218	8.76E+08	79314	2.1
200-250 (2)	7.35E+08	77224	5.80E+09	79314	7.8
250-300 (1)	3.64E+08	77218	6.99E+08	79314	1.9
250-300 (2)	1.25E+09	77224	1.37E+10	79314	10.9
304 (1)	6.84E+09	77218	1.18E+10	79314	1.7
300-350 (2)	1.46E+09	77224	1.40E+10	79314	9.6
584 (1)	2.17E+09	77218	5.70E+09	79314	2.6
630 (1)	1.76E+09	77218	3.37E+09	79314	1.9
850-900 (1)	6.11E+09	77218	1.61E+10	79314	2.6
900-950 (1)	5.70E+09	77218	1.45E+10	79314	2.5
1026 (1)	6.03E+09	77218	1.59E+10	79314	2.6
1216 (1)	3.66E+11	77275	9.84E+11	79348	2.6

[a] 1: chromospheric (Lyman-α similarity); 2: coronal (1-8 Å similarity).
[b] in units of photons cm^{-2} sec^{-1}.

Å, and Lyman-β dominate the photon flux totals for low activity while 850-900 Å, Lyman-β, and 900-950 Å dominate high activity. The time series emissions are calculated from equation (1.2) and have common chromospheric or coronal indicators in either Lyman-β or Fe XVI. Thus, the calculated datasets are expected to follow the general variations of these two emissions.

The high-to-low ratio shows an important difference between chromospheric and coronal fluxes. Chromospheric fluxes vary from low to high solar activity by no more than a factor of 2.6 while coronal emissions show much higher variation, ranging from 4.3 for 150-200 Å to 492 for 1-8 Å. As a rule of thumb, coronal emissions show increasingly greater ratios between high-to-low solar activity as the wavelengths get shorter.

Figure 2.7 shows intensities of important soft X-ray line groups from the NSSDC dataset over the AE-E period. These, too, are calculated from equation (1.2). One sees in these data three features in the rise from low-to-high solar activity for each wavelength group. First, there is a solar rotational effect superimposed upon the long-term increase in magnitude for each group. Second, the shorter the wavelength, the greater the magnitude of variation, as noted above. Third, the total emission is largest for the longer, 50-100 Å wavelength group and least for the short wavelength emissions. It is a factor of 10 greater than the other two. The 30-50 Å group has a factor of 2 greater flux than the 18-30 Å group. Figure 2.8 shows a more detailed ratio of high-to-low solar activity soft X-ray fluxes between 18-99 Å. The coronally produced FeXVI, FeXV, and O VIII clearly show greater change from low to high than the other fluxes in this range. The background level of ≈ 2 is representative of the low-to-high solar activity variation in the chromospheric fluxes.

In summary, the NSSDC EUV and soft X-ray data during the AE-E period contain several spectral features. A few chromospheric emissions

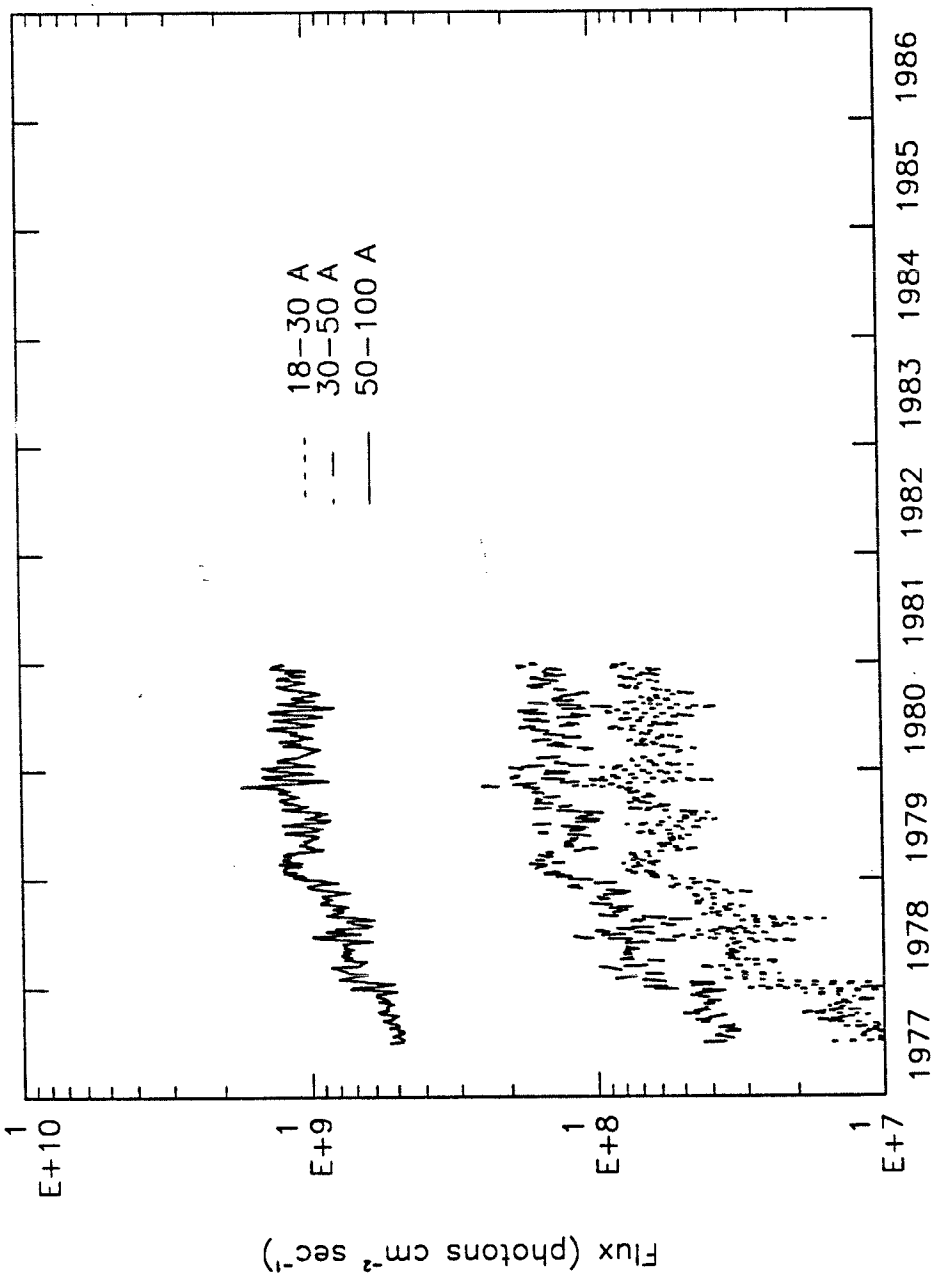

Figure 2.7 NSSDC modeled soft X-ray fluxes. The emission time series are provided on the NSSDC AE-E EUV dataset tape and are described in the text.

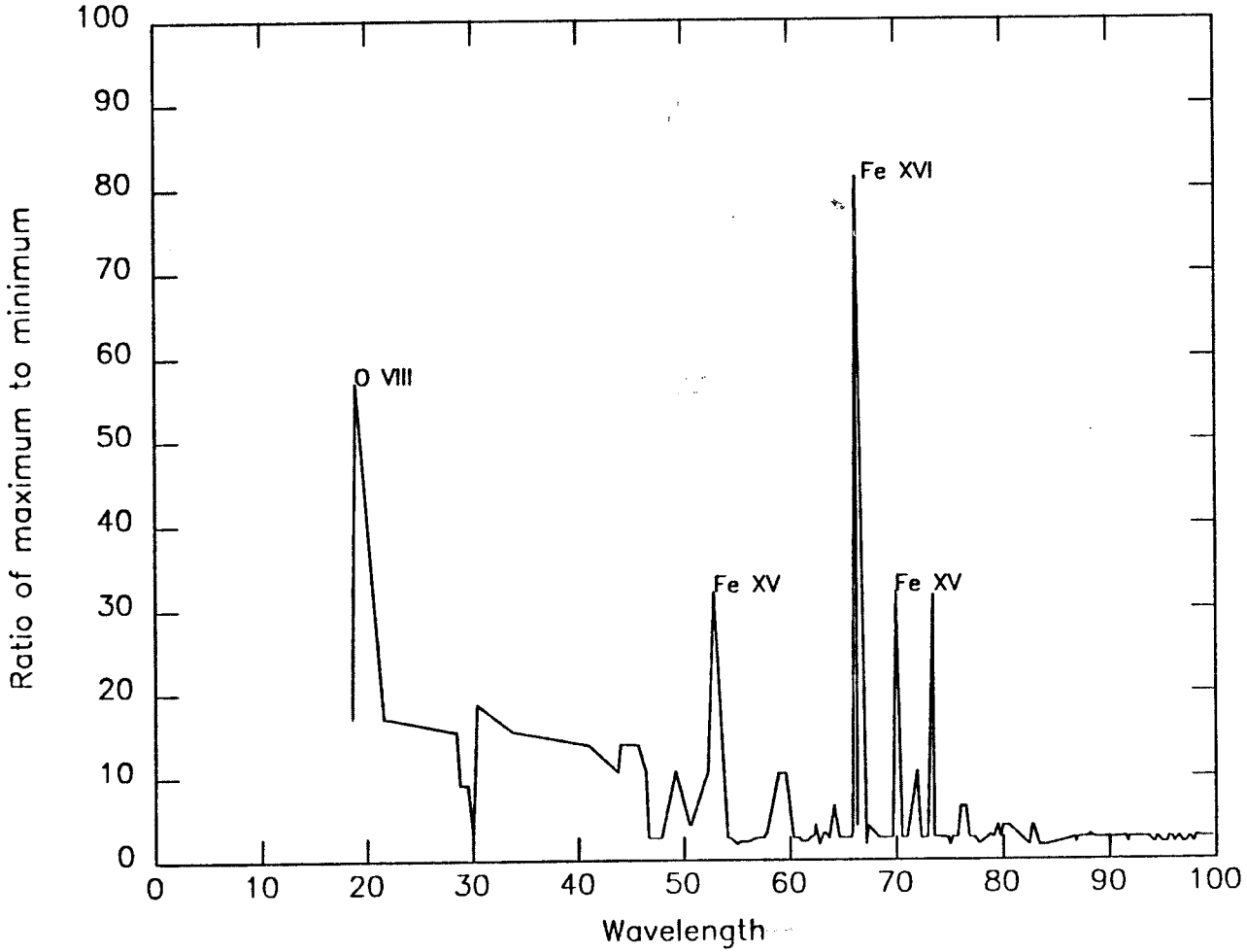

Figure 2.8 **NSSDC soft X-ray flux ratios.** The Fe XV, Fe XVI, and O VIII emissions have much larger ratios of maximum to minimum values than the other wavelengths and are coronally-produced.

dominate the spectrum, including He II (304 Å), H Lyman continuum (700-912 Å), C I continuum (913-1100 Å), and Lyman-β (1026 Å) at all solar activity conditions. C III (977 Å) and the mixed chromospheric and coronal emissions between 150-200 Å additionally contribute significant flux. Chromospheric EUV emissions tend to rise by a factor of 2.5 from low-to-high solar activity while coronal EUV and soft X-ray fluxes rise by a factor of 4 to 80 for the same solar activity variations. Shorter wavelengths, while containing more energy, generally have smaller fluxes, although there are exceptions. H Lyman-α, an FUV chromospheric emission, contains more flux for all solar conditions than any other single line up to 2000 Å.

2.2 Solar Mesosphere Explorer (SME) Data

SME is a NASA Explorer series satellite operated by the Laboratory for Atmospheric and Space Physics (LASP) at the University of Colorado (CU) in Boulder. The primary scientific mission of SME, described by Thomas *et al.* [1980] is to provide a comprehensive study of mesospheric ozone creation and depletion. This includes observations of solar UV flux variations. SME was launched from the Western Test Range into a polar, sun-synchronous, 3 pm ascending node orbit on October 6, 1981. The nearly circular orbit had an initial eccentricity of 0.0032 with an altitude near 540 km. The 97.5 degree inclination allows for orbit precession of approximately 1 degree per day. Science and engineering data are received daily at the Project Operations Control Center located at CU. This site houses the SME mission control, mission planning, and data analysis teams.

The SME satellite has acquired a substantial dataset of solar Lyman-α daily-averaged fluxes between January 1, 1982 and December 31, 1986 and daily-averaged thermospheric nitric oxide densities, $n(\mathrm{NO})$, for a shorter time

period. The satellite orbit definitive ephemeris is also available as a dataset comprised of the orbit ascending node start times since the beginning of the mission.

The Lyman-α data, available from LASP, consist of daily-averaged values of the full-disk flux adjusted to 1 AU. It is regularly observed by a wavelength scanning solar ultraviolet spectrometer with a 7.5 Å bandpass described by Rottman *et al.* [1982]. Figure 2.9 is a plot of the Lyman-α flux absolute intensities with an accuracy of $\pm 5\%$. These data, their relation to other solar fluxes, and their effect upon the terrestrial atmosphere, are interpreted in Chapter III.

A brief description of the emission mechanism is appropriate here. The solar hydrogen atom Lyman-α emission is a result of the electronic transition from the second energy level to the first (ground) state. This is the lowest electron energy level transition in the hydrogen atom. Lyman-β is the transition from the third level to the first, giving a slightly higher potential energy difference and, therefore, a shorter wavelength. H Lyman-α and H Lyman-β emissions both originate in the solar chromosphere and are a result of temperatures in that region.

In Figure 2.9, the SME observed daily-averaged Lyman-α extends from January 1, 1982 through December 31, 1986. The data in this study has been filtered in frequency space with a sinc function. The filter was chosen to remove features with periodicities of less than 10 days. White [1972] describes this filtering technique. The resulting time series has three distinct characteristics which are immediately apparent. First, the overall decline from high to low solar activity reduces Lyman-α by about a factor of 2, i.e., from 4×10^{11} to about 2.3×10^{11} photons cm^{-2} sec^{-1}. This is in line with the decreasing trend observed by Rottman [1987]. It is not clear whether Lyman-α reached higher

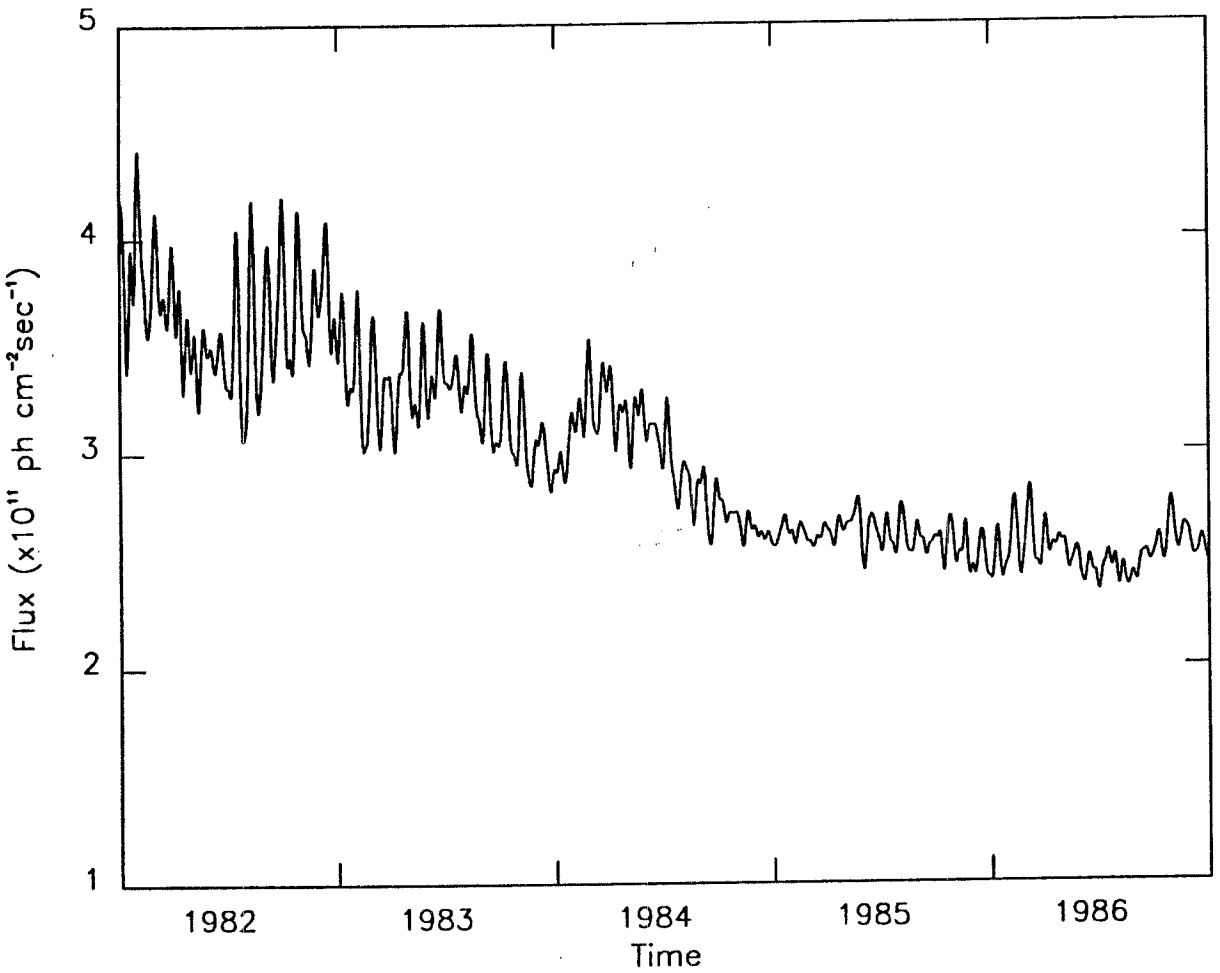

Figure 2.9 **SME observed daily-averaged Lyman-α.** This time series is filtered at 10 days and extends from January 1, 1982 through December 31, 1986. The long-term solar cycle 21 decline and the 27-day solar rotations are evident. The ratio of AE-E solar minimum Lyman-α data to SME solar minimum data is 1.3.

levels in 1981 prior to SME. Second, Rottman [1983] showed a power spectrum analysis with a strong 27-day periodicity from solar rotational effects as well as absolute fluxes in the range of 3 ($\pm$1) $\times 10^{11}$ photons cm^{-2} sec $^{-1}$. Third, there are long-term periods in the data, both from visual inspection and power spectrum analysis, on the order of several solar rotations. A minimum in the data appears to exist in August 1986, potentially indicating a quiet sun background value near 2.3×10^{11} photons cm^{-2} sec $^{-1}$.

The $n(NO)$ data have been collected by a separate ultraviolet spectrometer on the SME satellite described by Rusch *et al.* [1984]. It has been the primary instrument studying mesospheric ozone. It has also observed the nitric oxide γ–band (1,0) emission feature at a fixed grating position which corresponds to 2149 Å. This lower thermospheric nitric oxide dataset is described by Barth *et al.* [1988] and its use is discussed in Chapter IV.

The density of NO is regulated by chemical production and loss mechanisms outlined in Chapter III. These are partially dependent upon energy available from solar fluxes. It is sufficient to state here that NO is indirectly affected by coronally-produced soft X-ray solar fluxes and their long-term variations, as noted by Barth *et al.* [1988].

The $n(NO)$ dataset consists of daily-averaged, 5° latitude bin values. Within each latitude bin, there are 3.33 km altitude bins between 100 and 140 km. For most days from January 6, 1982 through August 25, 1986, there were 1 to 4 orbits in which NO was observed. Using a limb-scanning technique which gives altitude information, the flourescent scattering of the NO molecule was recorded. A peak in the NO emission near 110 km regularly occurred and the daily-averaged time series of NO densities at this peak is plotted in Figure 2.10. The data inversion from radiances to density is described by Siskind [1988]. Figure 2.10 shows the daily-averaged NO measurements between $\pm$30°

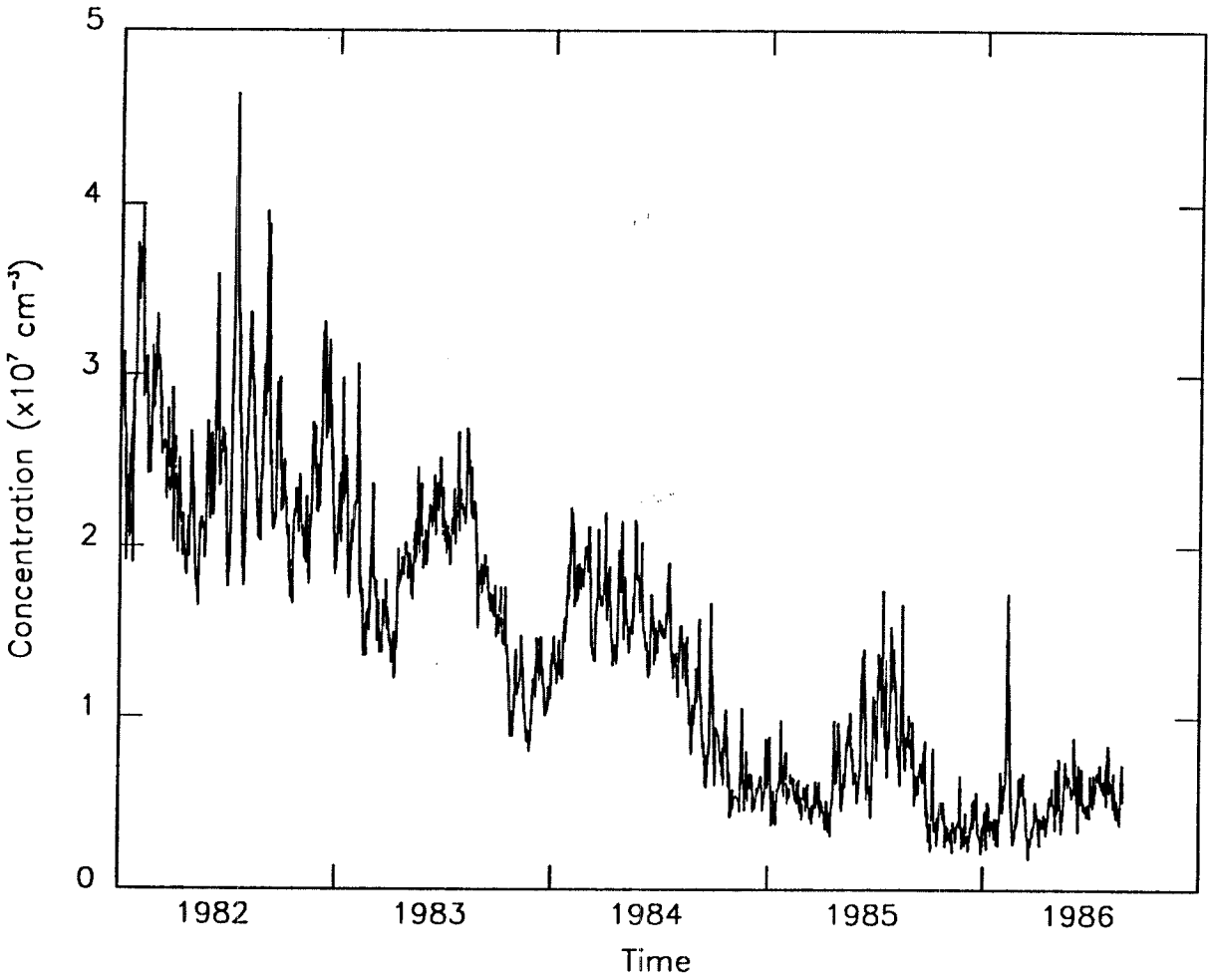

Figure 2.10 **SME observed daily-averaged nitric oxide.** This time series of daily equatorial region NO densities extends from January 6, 1982 through August 30, 1986.

latitude at 110 km with three distinct features. First, the overall decline in NO density from higher to lower solar activity ranges over an order of magnitude between 3×10^7 and 3×10^6 molecules cm^{-3}. Second, Barth *et al.* note a strong 27-day solar rotational periodicity in the data. Third, there are longer timescale periodicities which exist in the data over several solar rotations.

The third set of data from SME, the orbit period rate change, is obtained by differencing the orbit ascending node times which are found in the satellite definitive ephemeris. The ephemeris is generated by the Goddard Space Flight Center (GSFC) ground tracking and data systems group. Accuracy in the dataset is in the millisecond range. One data point per orbit exists, with a total of 15 to 16 orbits per day. The original orbit period rate change data is processed in the following manner. There are 28,987 orbits or datapoints covering a period of five years. Outlying points are defined as those beyond the 3σ level. Empirically it is found that values greater than $|\pm 2 \times 10^{-5}|$ should be zeroed. The resulting dataset is then interpolated over all zero points and smoothed with a moving average of ± 97 points which is equivalent to a 13-day smooth. The result is the elimination of the J_2 and all m-daily geopotential terms, with only the long-term secular change in the period rate change remaining. The processed 15-16 orbit per day data are then daily-averaged. These data are plotted in Figure 2.11 from January 1, 1982 through December 31, 1986.

The dimensionless quantity, dP/dt, or $\dot{P}$, is a good indicator of the long-term atmospheric drag effects upon the spacecraft. It is the daily-averaged rate at which the satellite orbit period changes. Two overall features can be discerned in the data. First, the long-term $\dot{P}$ declines by nearly an order of magnitude from high to low solar activity. This shows considerable orbit period rate change during high solar activity produced by substantial

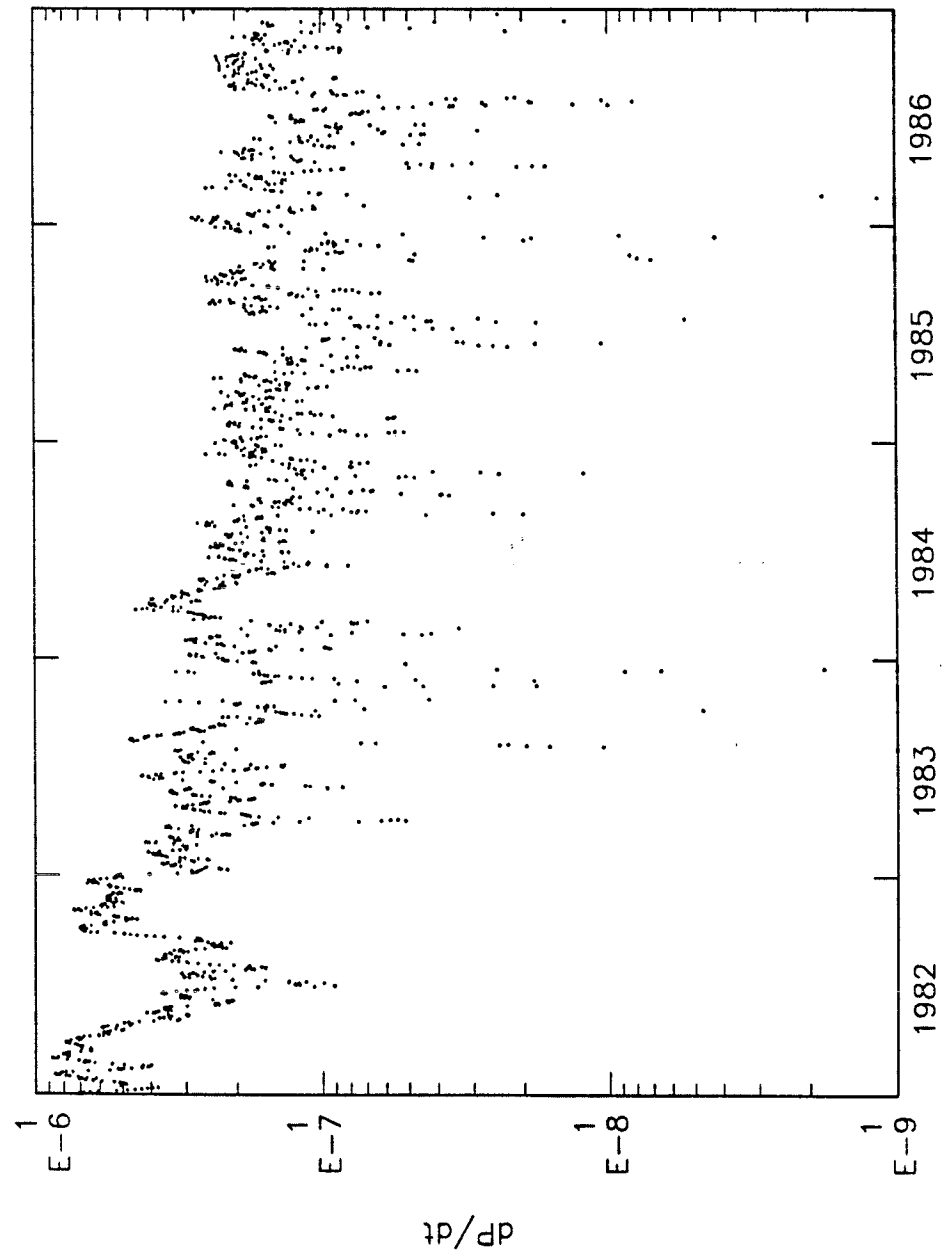

Figure 2.11 SME daily orbit period rate change. This time series of daily smoothed orbit period rate change data extends from January 1, 1982 through December 31, 1986. Units are dimensionless.

atmospheric density causing drag. At lower solar activity, there is a lower $\dot{P}$ corresponding to lower atmospheric density and lower atmospheric drag forces. Secondly, there are also features with long-period timescales similar to the solar data shown above. Chapters III, IV, and V explain the use and interpretation of these data.

2.3 World Data Center (WDC) Data

$F_{10.7}$, which was previously called the Covington index F, is a mixed emission produced in the chromosphere, chromosphere-corona transition region, cool corona, and hot corona. This is shown in Table 2.4. Because of the coronal input, it's temporal variation reflects different solar processes than solely the chromospheric and transition region emissions. A number of mechanisms are suspected for the creation of this low-energy emission. Among them include gyroresonance absorption and emission in small bright emission cores as proposed by Alissandrakis *et al.* [1980] and thermal bremsstrahlung emission in large active regions as interpreted by Felli *et al.* [1981]. However, the ratio of production by one mechanism to another is still uncertain. Since this radio wavelength flux has such a low energy, it does not interact with the gases in the terrestrial atmosphere and, thus, contributes nothing to thermospheric heating. However, as noted in Chapter I, $F_{10.7}$ is used extensively as an indicator of EUV solar activity in empirical and numerical density models.

Solar 10.7 cm radio flux, $F_{10.7}$, has been recorded daily since February 14, 1947 and is released on a regular basis adjusted to 1 AU. It is observed at radio wavelengths (2800 MHz) at the Earth's surface and collected by a receiver at the Ottawa, Canada observatory. The WDC in Boulder now makes available a complete record of $F_{10.7}$ daily flux variations which covers 40 years (1947-1986) between the decline of cycle 18 through cycle 21. The measured

flux, which is interpolated over missing data and smoothed with a 27-day running mean in units of $\times 10^{-22}$ W m^{-2} Hz^{-1}, is shown in Figure 2.12. These 10.7 cm flux values are based on measurements at 1700 UT. There are four items in this dataset which deserve recognition. First, there is an approximate 11-year period for each cycle between minimums. This corresponds to the same periodicity and phase as in the sunspot record. Second, each of the odd-numbered cycles tends to be larger in magnitude than the even-numbered cycles. This has been pointed out by Sargent [1984] in sunspot cycles dating back to cycle 10. Third, each of the cycles has a relatively sharp rise to maximum over a 2-3 year time span and a shallower decline to minimum over 4-5 years. Fourth, in cycles 19, 20, and 21, there was a relatively flat solar minimum period with rotational features superimposed upon an apparent threshold level near 70×10^{-22} W m^{-2} Hz^{-1}. This threshold level becomes significant when interpreting EUV fluxes and their effect upon the terrestrial atmosphere discussed in Chapter III.

Figure 2.13 shows the daily $F_{10.7}$ values for cycle 21 and the minimum of cycle 20 which are comparable to the sunspot values mentioned in Chapter I. This figure also shows more detail in cycle 21, with the points from day 200, 1976 and day 50, 1979 marked by boxes. These dates correspond to the NSSDC files of the full EUV spectrum.

A geomagnetic index of auroral region activity is the A_p index. Figure 2.14 shows this 7-day smoothed index from January 1, 1975 through December 31, 1986. A_p is the planetary equivalent amplitude index introduced by Bartels [1951] to aid in standardizing the daily magnetic field characterization. It indicates the magnitude of disturbance of the terrestrial magnetic field. It's relation to the derived K_p geomagnetic index is described by Mayaud [1980]. In brief, the range of variation of the most unsettled horizontal magnetic

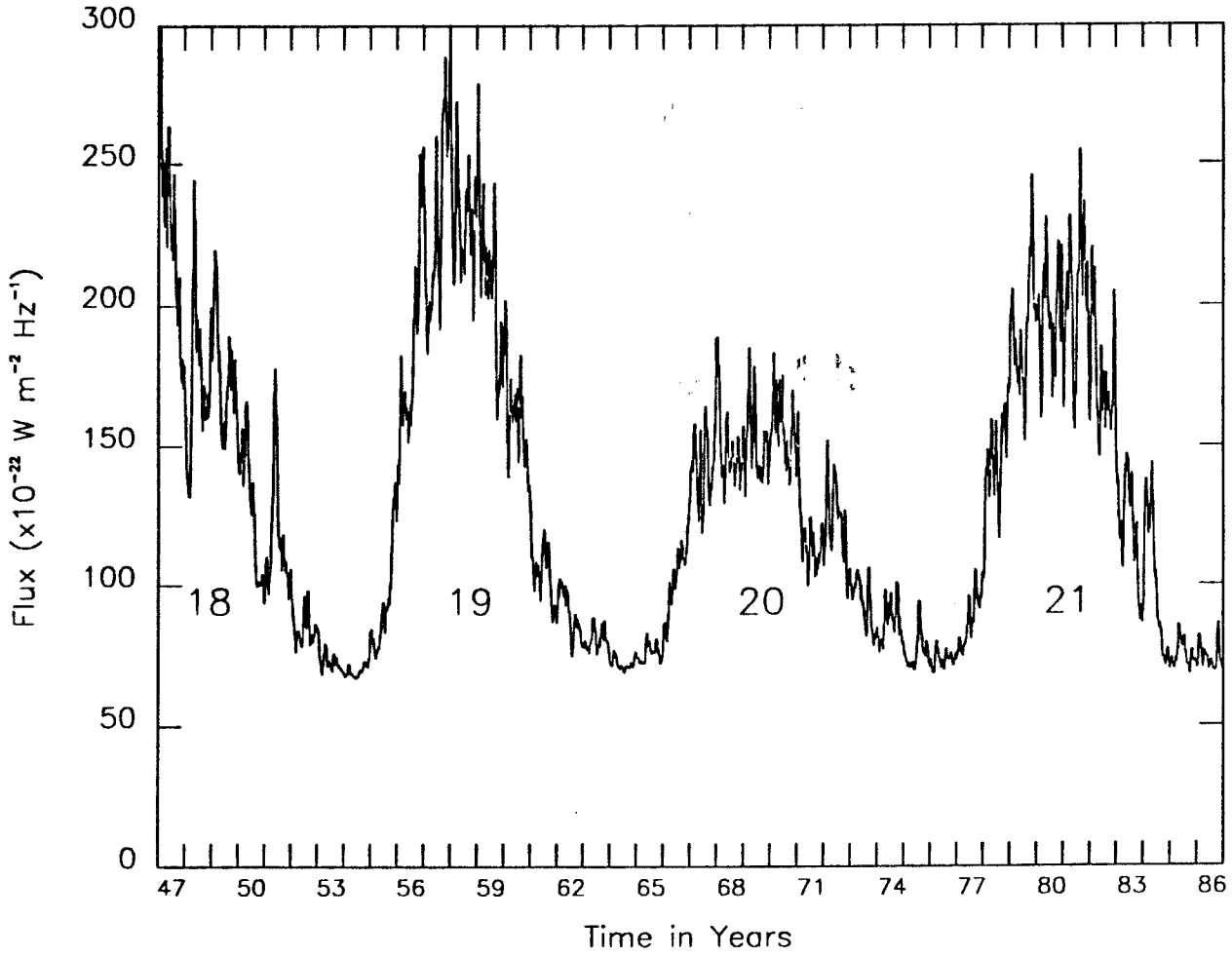

Figure 2.12 **Ottawa 10.7 cm flux for 1947-1986.** The dataset covers the period February 14, 1947 through December 31, 1986.

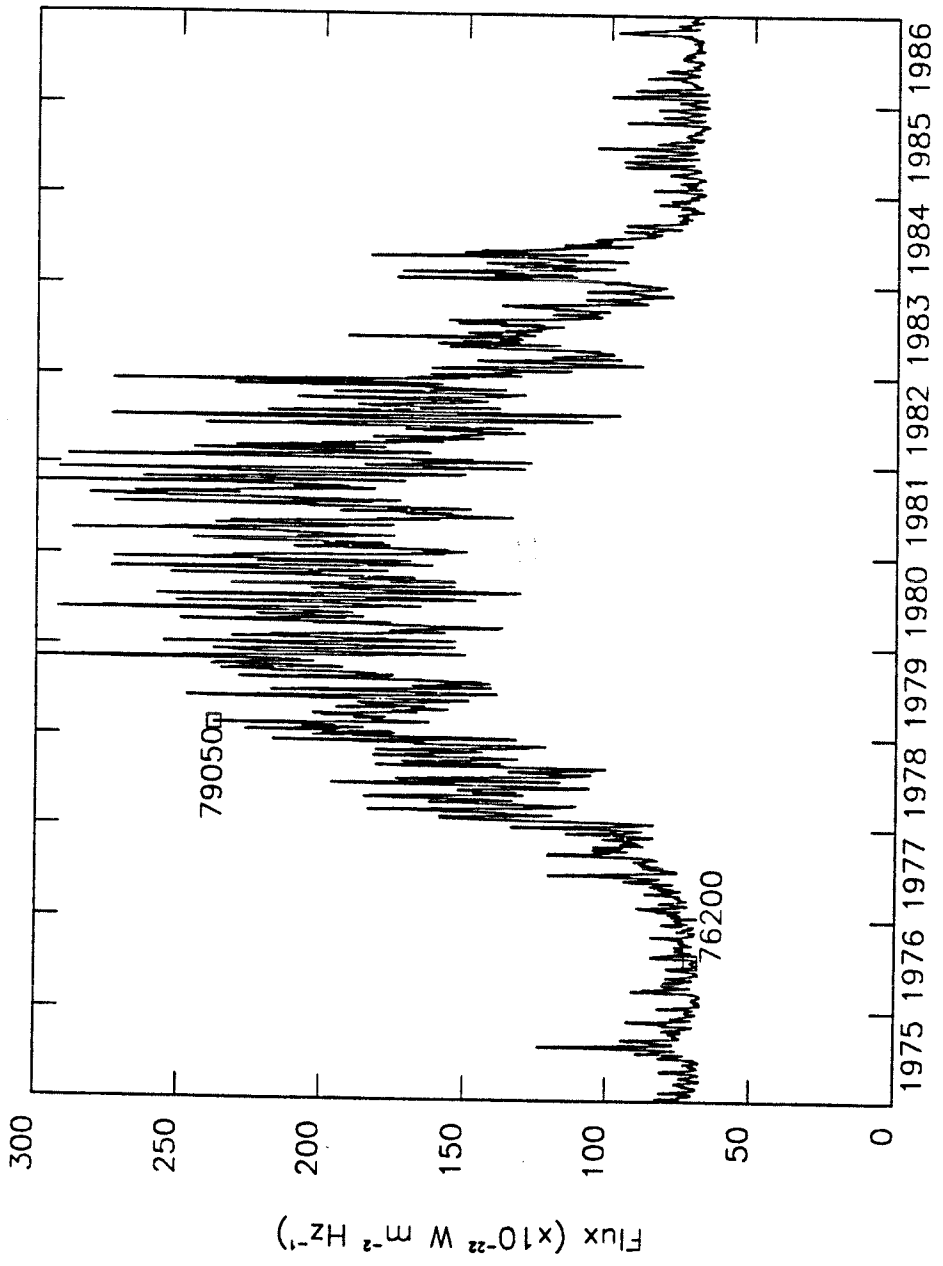

Figure 2.13 Ottawa 10.7 cm flux for 1975-1986. The dataset extends from January 1, 1975 through December 31, 1986. Boxes mark day 200 of 1976 (low solar activity) and day 50 of 1979 (high solar activity).

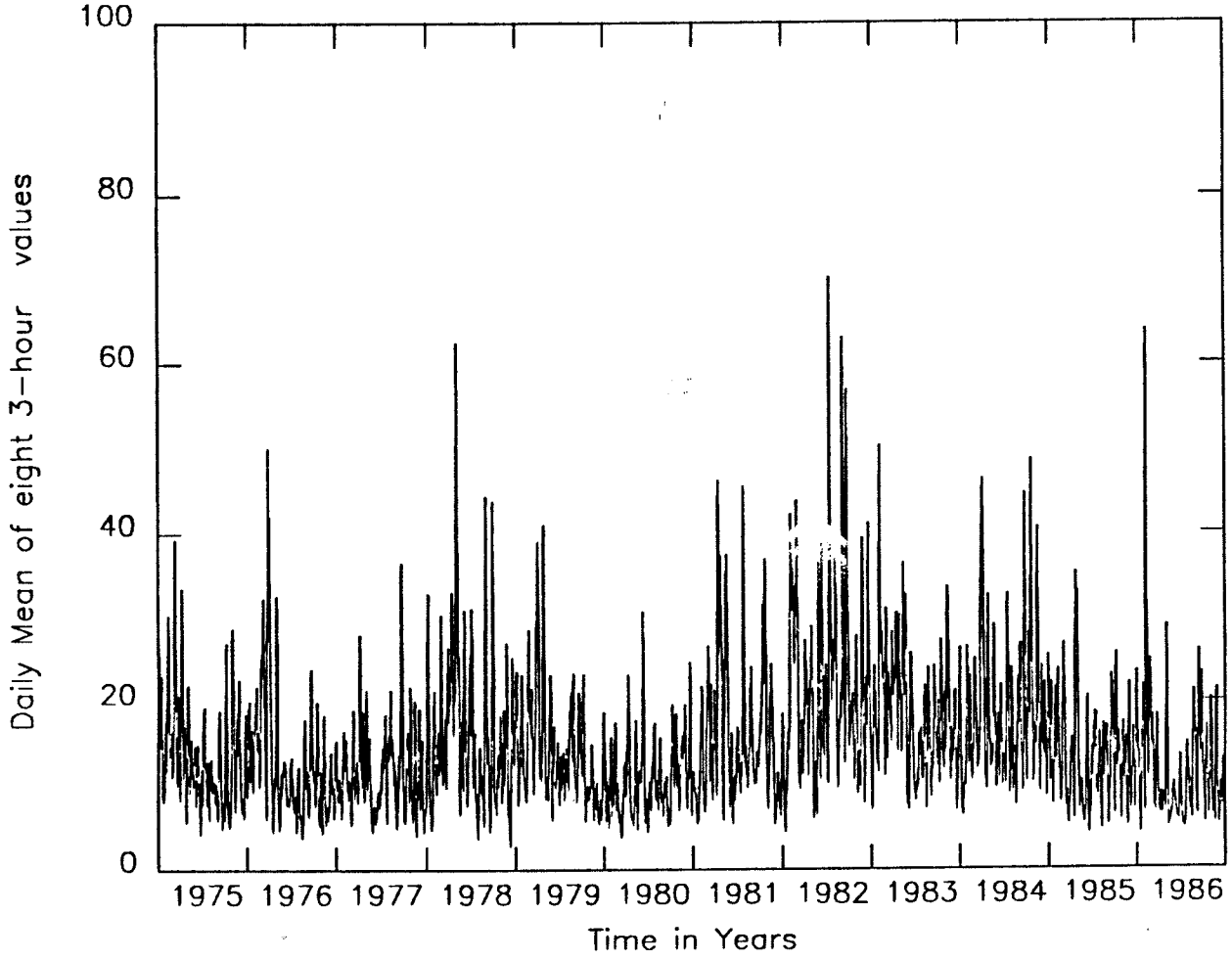

Figure 2.14 **Geomagnetic index A_p for 1975-1986.** The dataset extends from January 1, 1975 through December 31, 1986. These are the daily means of eight 3-hour values.

field component over a 3-hour period is measured by a network of subauroral stations. K numbers, between 0 - 9, are determined, which are a code for the range of classes of the disturbed magnetic field. Since these code numbers have a quasi-logarithmic scale, they are converted into a standardized K_p value which takes into account several factors, including the station geomagnetic latitude. The $3K_p$ value from 0 - 27 is then related to a linear a_p 3-hour value, which is scaled between 0 and 400. The daily A_p value is obtained as the average of the eight 3-hour a_p values. Both are available on a regular basis from the *Solar-Geophysical Data* reports produced by NOAA. The dataset shown in Figure 2.14 is the A_p value and is dimensionless. The notable feature in the A_p index is that there is little significant long-term variation over a solar cycle whereas the day-to-day variations are large. Hence, there is no apparent solar cycle control of A_p. This allows A_p to be used as an index for geomagnetic effects upon the atmosphere where charged particles, which follow the terrestrial magnetic field lines, interact with neutral gas particles and cause atmospheric heating.

2.4 Geostationary Operational Environmental Satellites Data

X-ray flux is created in the hot coronal regions of the solar atmosphere where the heavier elements, including Fe, Mg, and Si, are highly ionized. Very hot electrons interact with these ions to produce X-rays through either the bremsstrahlung process or through recombination to form lower level ionized constituents.

The NASA Solar Meteorological Satellite (SMS) and the NOAA GOES series satellites have observed solar X-ray fluxes and flare events since the mid-1970s. Fluxes in the range of 1-8 Å have been observed every 3 seconds by the GOES satellites which are in a geosynchronous orbit. These data are deposited

at the NSSDC and are currently available through mid-1983. Early SMS and GOES data is available for the AE-E period. Bouwer [1983] analyzed the X-ray data from the late 1970s and, using an X-ray daily background value, conducted an anharmonic frequency analysis (AFA) of the data which is shown in Figure 2.15. His modeled X-ray flux extends from March 21, 1977 through May 31, 1981. It shows a rise of one and one-half orders of magnitude from low to high solar activity and also shows solar rotational effects, although these do not have a periodicity of 27 days. The GOES data are not corrected to 1 AU.

The January 1, 1980 through December 31, 1986 1-8 Å data shown in Figure 2.16 are given in daily background values. A clearer demonstration of the magnitude of decrease of the flux from high to low solar activity during the decline of cycle 21 can be seen in Figure 2.17. This figure shows a quadratic fit to the monthly means of the background data, indicating a factor of 7 drop from higher to lower solar activity in the 1-8 Å background values. Figure 2.18 shows the daily arithmetic mean values.

To obtain the arithmetic mean data between January 1, 1980 and May 19, 1983, the NSSDC GOES 2 dataset is unpacked from its binary format, summed into the total daily flux, and divided by the total number of counts. The daily background value is obtained by using a method suggested by Bouwer [1983]. The data are read and accumulated in three 8-hour bins. The average is then computed for each 8-hour bin and the lowest value in either the middle bin or the interpolated first and third bins is retained. The objective in this processing is to retain a mid-day background value which ignores solar flare activity. The arithmetic mean value is most useful when one wants the total integrated flux reaching the Earth's atmosphere since it includes flare emissions. However, the Bouwer background method is used in

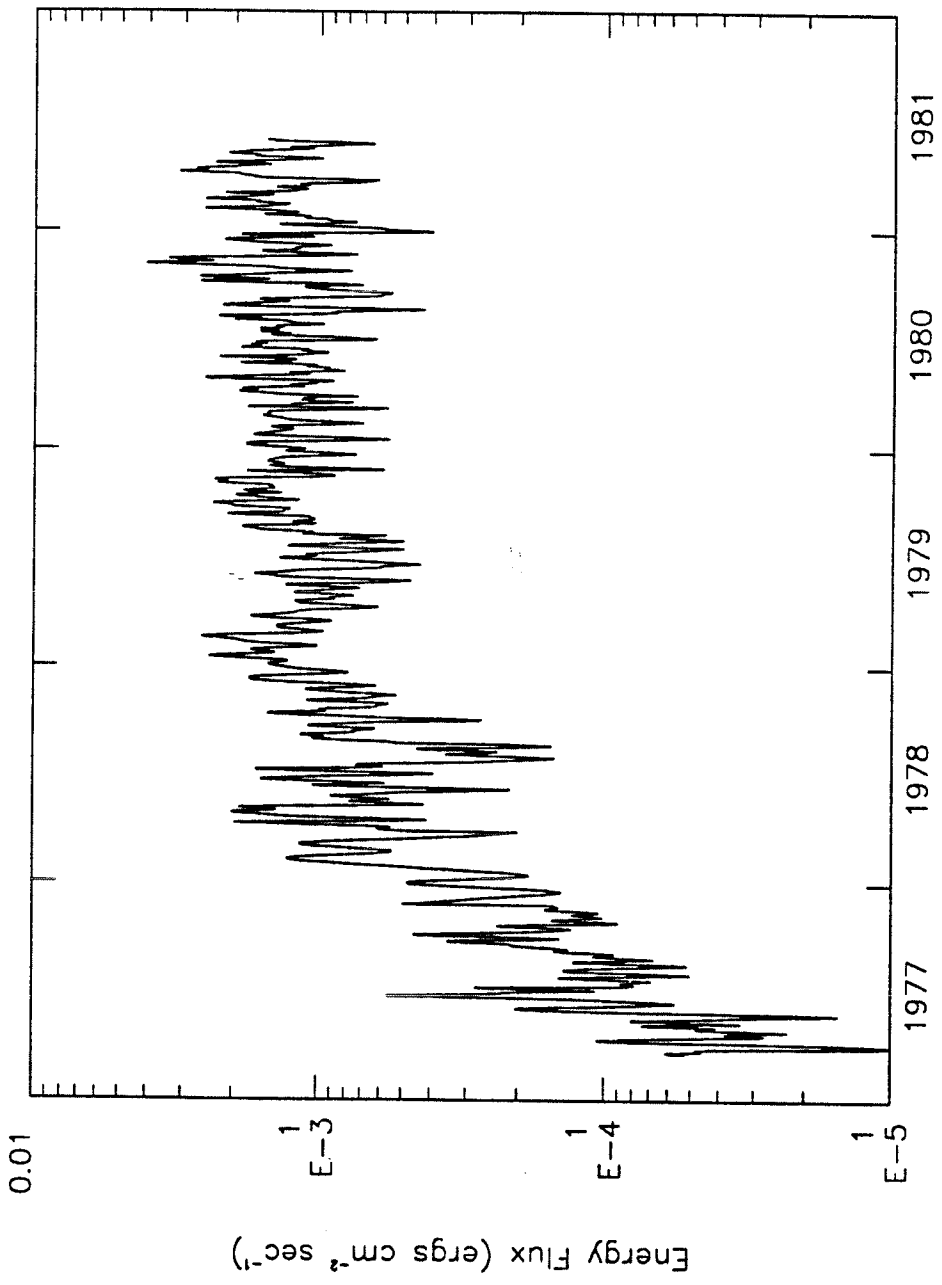

Figure 2.15 Daily background 1-8 Å X-ray flux for 1977-1981. This dataset extends from March 21, 1977 through May 31, 1981 and is from Bouwer [1983].

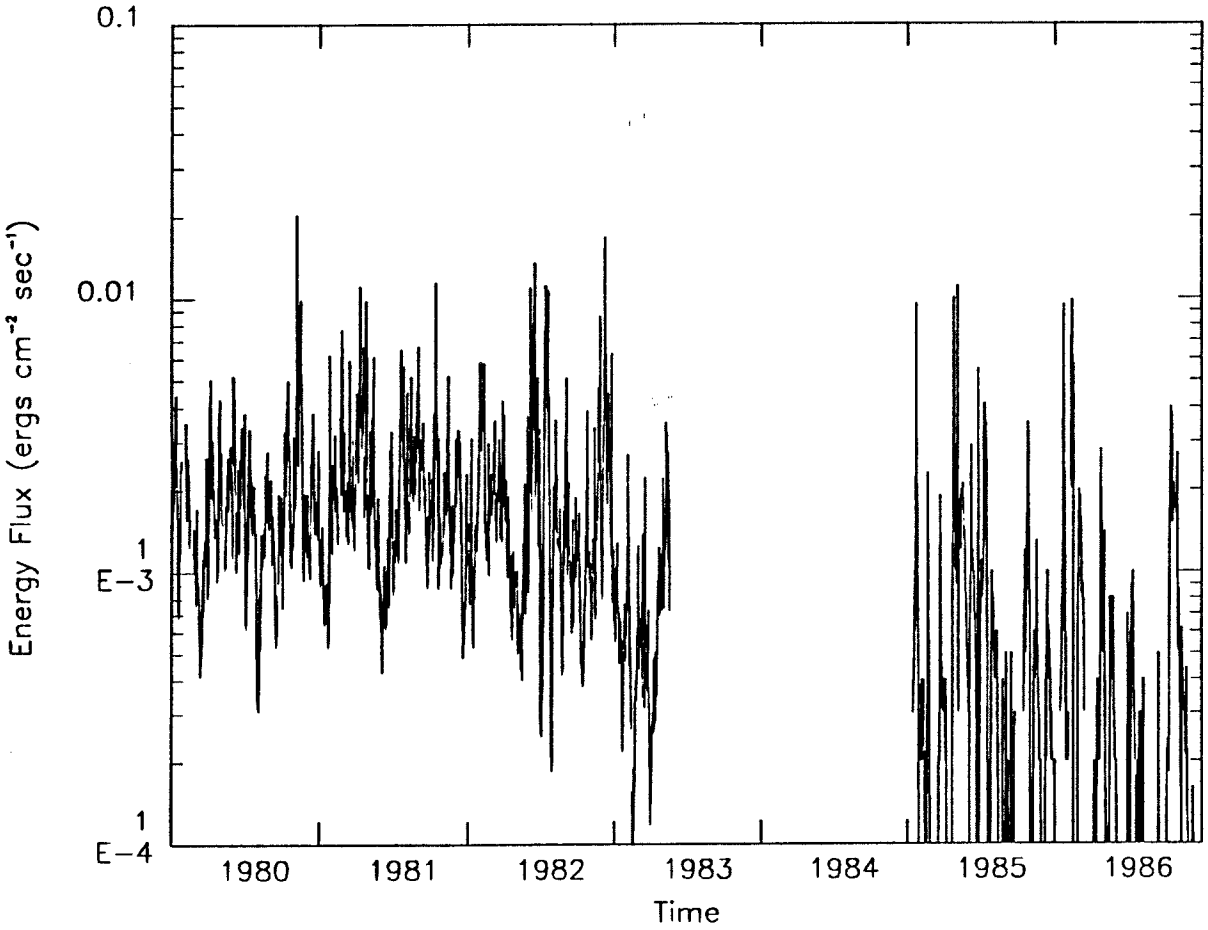

Figure 2.16 **GOES 2 1-8 Å X-ray flux daily background values.** This dataset extends from January 1, 1980 through December 31, 1986 with a gap of missing data between May 20, 1983 and December 31, 1984. The 1980-83 data are found in Appendix B and the 1985-86 data is from the *Solar-Geophysical Data* Reports produced by NOAA. This dataset does not include flare activity.

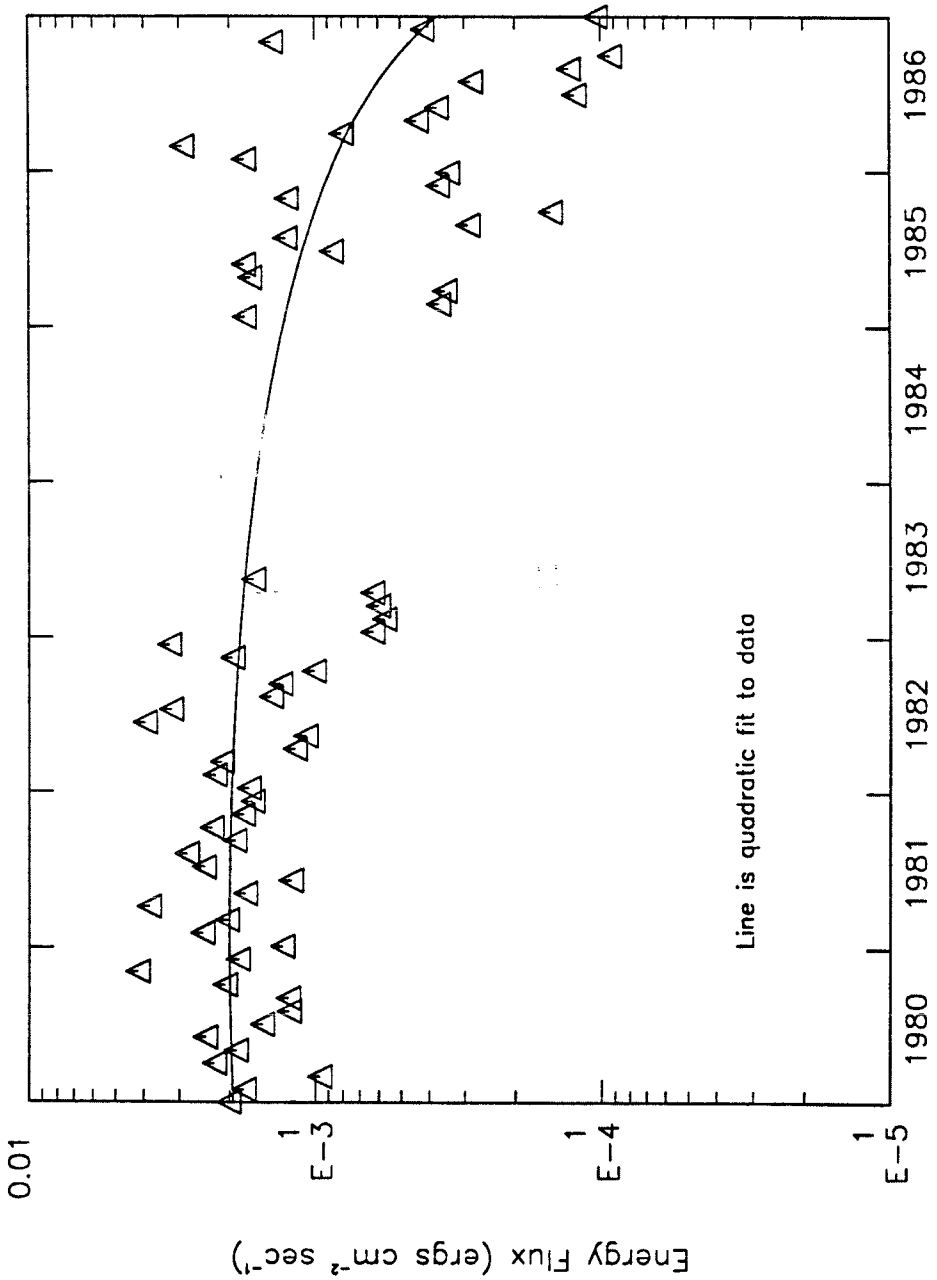

Figure 2.17 GOES 2 1-8 Å X-ray flux monthly mean background values. The dataset extends for the same time periods as in Figure 2.16 with the monthly means and a quadratic line fit to the data plotted to give a general solar cycle decline.

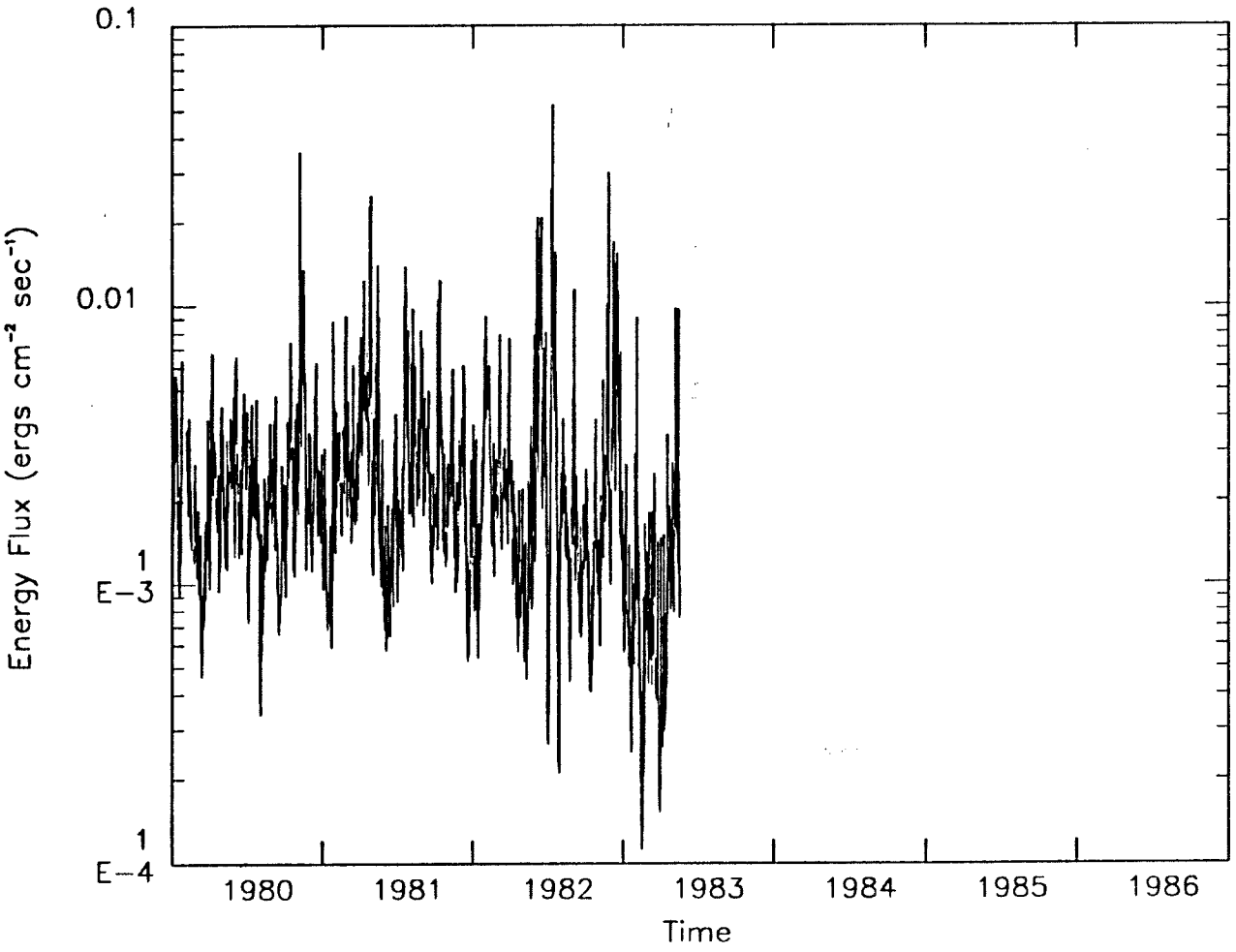

Figure 2.18 **GOES 2 1-8 Å X-ray flux daily mean values.** The dataset extends from January 1, 1980 through May 19, 1983. These data are found in Appendix B and include flare activity.

this study. This is because the only data which were originally available for evaluating the 1-8 Å flux in relation to the AE-E EUV fluxes was given as X-ray background values. For data comparisons to the declining portion of cycle 21, both sets of data are given in Appendix B, where the date, the arithmetic mean, the number of data points, and the background values of the 1-8 Å and the 0.5-4 Å flux are listed. A comparison between the Bouwer data and the new background data in Appendix B is shown in Figure 2.19. While the overall magnitude of the background flux is generally the same, there are differences in the daily values, the periodic amplitudes, and phases. Most notably, during the overlapping data period between January 1980 and May 1981, the dataset generated in this study has a total average value of 47% greater than the Bouwer data. Chapter III discusses the relationship between this flux and the response of the terrestrial atmosphere.

2.5 Summary

The EUV data supplied by the AE-E satellite and the X-ray data supplied by the GOES satellite provide a basis for correlations during rising solar activity which are conducted in the next chapter. The SME Lyman-α, nitric oxide, and orbit period rate change data, as well as GOES X-ray data, provide the basis for modeling EUV flux, modeling the subsequent atmospheric density variations, and allowing comparisons between derived and modeled densities in Chapters III and IV. The $F_{10.7}$ and A_p data allow a comparison between modeling efforts and a means of estimating the charged particle interaction with the polar atmosphere which secondarily affects global thermospheric temperature and density. In summary, these datasets provide the basis for evaluating the solar - terrestrial interaction in the thermosphere over the rise and decline of cycle 21.

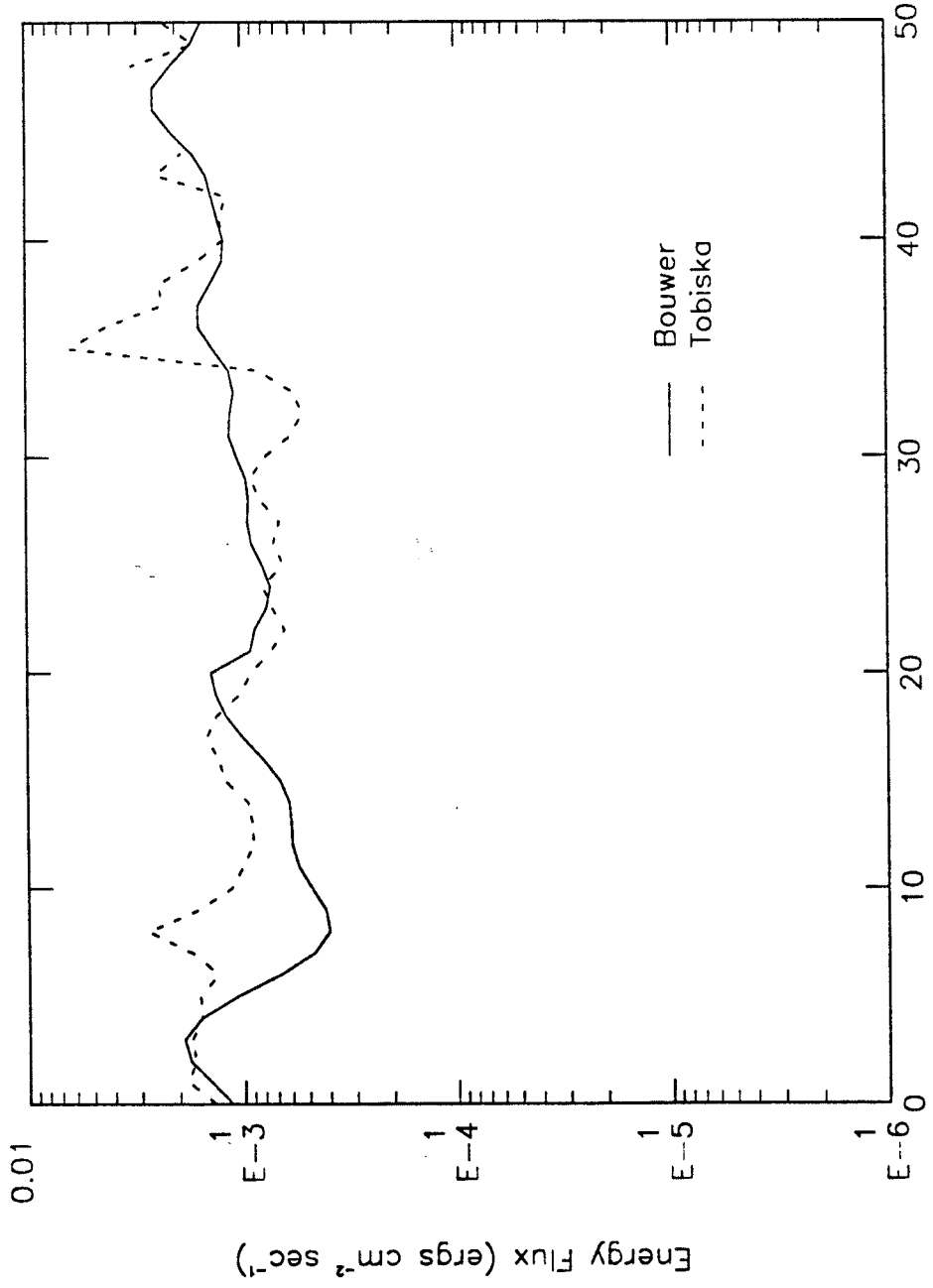

Figure 2.19 Comparison of solar maximum 1-8 Å X-ray background flux. Overlapping Bouwer [1983] and Appendix B datasets in December 1980 are compared. The ratio of the total Bouwer data to the total Appendix B data for overlapping periods is 0.68.

CHAPTER III

SOLAR FLUX - TERRESTRIAL THERMOSPHERE COUPLING

The seven datasets described in Chapter II are analyzed in this chapter and show the link between solar EUV flux and variations in the terrestrial thermosphere. The chapter begins with a summary of the state of EUV flux monitoring, followed by a detailed description of the mechanism of EUV heating of the thermosphere. Correlations of the solar EUV emissions with three flux indices are presented and the dominant EUV emissions, along with the indices which best describe them, are summarized. An example of modeled EUV flux using these indices is given. A secondary thermospheric heat source, auroral heating, is briefly described in the context of solar-terrestrial coupling. Finally, in preparation for the modeling efforts of Chapters IV and V, satellite derived density from orbital decay due to atmospheric drag is outlined as is the variation of nitric oxide (NO) in the lower thermosphere and its variation with solar activity.

3.1 Solar EUV Monitoring

Historically, one of the most important indices of solar EUV activity used in thermospheric density and temperature modeling has been $F_{10.7}$, as noted above. This was due to early high correlations between density variations derived from perturbed satellite orbit elements and the ground based observations of solar emissions at radio wavelengths. While it was later understood that the EUV spectrum heats the upper atmosphere and thereby

causes density variations, the $F_{10.7}$ became a convenient indicator of density variations as a result of 1) the accessibility of the data and 2) the satisfactory empirical modeling of the total atmospheric density using $F_{10.7}$ as an input. The correlation between $F_{10.7}$ and density results from the $F_{10.7}$ origination in the same regions of the solar atmosphere as some of the important EUV fluxes. Chapter II discusses this in more detail.

It has been pointed out by Donnelly [1987b] that, following the AE-E EUV monitoring program, an "EUV hole" has developed. He describes several reasons which have led to the current lack of solar EUV monitoring. Among them include 1) the retirement of EUV investigators, or their transfer into other fields, without the corresponding entrance of new investigators into the community, 2) a focus by the solar physics community on high spatial resolution studies of solar features rather than full-disk fluxes, and 3) the research in areas other than long-term solar EUV variations by those individuals studying solar-terrestrial physics. As a result, there are no recent, no current, and limited future plans to resume solar EUV monitoring leading up to and through the maximum of solar cycle 22.

In the effort to improve the accuracy of density and temperature modeling, not only are more sophisticated physical models needed, but the paucity of EUV data begs for a reliable and consistent solar data source for parameterizing the EUV flux. Between the AE-E solar observations in the 1970s and the 1990s, when regular solar EUV flux measurements may once again begin, the NOAA GOES and NIMBUS series satellites and the NASA SME and Solar Maximum Mission (SMM) satellites are the primary above-atmosphere solar monitors. This leads to the conclusion that either ground-based solar indices, both old and new, or presently available satellite data must be used in a new way to estimate the EUV flux. This chapter will show the rela-

tionship between individual chromospheric and coronal emissions, which are monitored by the above satellites, and the EUV flux. Secondary features of solar-terrestrial coupling are also reviewed, including auroral heating, satellite drag-derived density, and nitric oxide variation. However, as a preliminary discussion, it is important to understand which EUV fluxes contribute to the heating of the terrestrial thermosphere.

3.2 EUV Heating of the Thermosphere

EUV fluxes penetrate to different levels of the thermosphere depending upon the energy of photons at that wavelength, the absorption cross sections of atoms and molecules, and the attenuation of the flux by the thermospheric density. Chapter IV reviews the modeling of these phenomena as used in this study. Figure 1.1 conceptually shows the penetration of EUV emissions in the thermosphere. Stolarski *et al.* [1975] have outlined the most important physical processes leading to neutral gas heating. They indicate that photoionization by EUV flux leads to neutral heating through one of two channels: either ion-neutral reactions or photoelectron energy transfer.

The dominant X-ray, EUV, and FUV energy fluxes which heat the terrestrial thermosphere can be described. Table 3.1 outlines nine EUV emissions, one X-ray flux range, and one FUV emission. The energy flux, in unit of ergs cm^{-2} sec^{-1}, is shown since it describes the solar energy available for heating. Listed are the wavelength range or discrete line, the low solar activity energy flux during the AE-E period and on the date referenced in Table 2.5, the percent of energy flux out of the total energy flux between 18-1050 Å on that date, the high activity energy flux from the corresponding date in Table 2.5, its percent out of the total for that date, and the high-to-low ratios. The wavelength groups combine both chromospheric and coronal emissions, where applicable.

TABLE 3.1. DOMINANT X-RAY, EUV, AND FUV ENERGY FLUXES WHICH HEAT THE TERRESTRIAL THERMOSPHERE

Wavelength (Å)	Low Activity Flux[a]	% Total Flux	High Activity Flux[a]	% Total Flux	High:Low
1-8	0.000008		0.00408		491.8
150-200	0.244500	7.55	0.74559	8.85	3.0
200-250	0.107920	3.33	0.44594	5.29	4.1
250-300	0.128110	3.96	0.76502	9.08	6.0
304	0.459720	14.20	0.69487	8.25	1.5
300-350[b]	0.097395	3.01	0.62516	7.42	6.4
584	0.078331	2.42	0.16429	1.95	2.1
630	0.057702	1.78	0.09395	1.11	1.6
850-900	0.147230	4.55	0.31014	3.68	2.1
900-950	0.129430	4.00	0.26532	3.15	2.0
1216	5.981400		16.08100		2.6
Total %		44.80		48.78	

[a] units of ergs cm^{-2} sec^{-1}.

[b] excluding He II (304 Å).

He II and 150-200 Å are primary energy sources at both low and high solar activity, relative to the total energy flux. 200-250 Å contributes moderate energy flux at both low and high activity compared to the other dominant fluxes. 250-300 Å and 300-350 Å, excluding He II (304 Å), make small total contributions during low activity but large contributions during high solar activity. 850-900 Å and 900-950 Å follow the reverse pattern, i.e., their relative contributions are lower during high activity. In general, it can be summarized that 1) a large increase occurs for the coronally-produced flux in short wavelengths from low to high activity conditions, 2) the longer wavelength EUV ranges show little percentage contribution change due to the lack of coronal emission components, 3) the chromospheric emissions dominate EUV spectral region energy flux during low solar activity, and 4) the coronal emissions dominate

this spectral region energy flux during high solar activity. Nearly one-half of all EUV energy flux comes from these nine emission lines or intervals.

These conclusions support recent work by Roble [1987]. Using a global mean model of the thermosphere, he has outlined the EUV wavelengths responsible for the greatest effect on global mean exospheric temperatures for solar maximum and minimum conditions during the AE-E period in cycle 21. He shows that for solar minimum, the He II, 850-900 Å, 150-200 Å, He I, 900-950 Å, and O V emissions contribute the largest effects, in decreasing order. For solar maximum, the He II, 850-900 Å, 150-200 Å, 300-350 Å, He I, 900-950 Å, 200-250 Å, and 250-300 Å emissions contribute the largest effects, also in decreasing order. Table 3.2 is reproduced from Roble. It shows how much the exospheric temperature is decreased if a particular wavelength is removed from a global mean temperature calculation which includes all 37 wavelengths. To understand EUV heating based on this flux penetration, one must look initially at heat transport processes as well as solar flux conditions.

In general, there are differences in heat transport processes between the upper and lower thermosphere. Heating occurs when an EUV photon is absorbed by a particle. This is called photoabsorption. The route to thermal energy deposition may then proceed through two major paths: 1) photoionization of molecules or atoms, where an electron is stripped from the particle and carries away most of the excess energy as kinetic energy, followed by ion-neutral and photoelectron reactions which convert stored chemical energy into kinetic, or thermal energy, or 2) photodissociation of a molecule, where the chemical bond between atoms is broken, with the initial photon energy being transferred into particle kinetic energy. The upper thermosphere is a heat source and is nearly isothermal. By either of these paths, heat produced at high thermospheric altitudes, i.e., above 200 km, is transported down to cooler,

TABLE 3.2. GLOBAL MEAN TEMPERATURE CHANGE

	Solar Minimum (76200)		Solar Maximum (79050)	
No.	$\lambda(S_{\min})$	$\Delta T(S_{\min})$	$\lambda(S_{\max})$	$\Delta T(S_{\max})$
1	303.78	53.5	303.78	92.0
2	850-900	20.3	850-900	51.7
3	150-200	19.4	150-200	47.6
4	584.33	15.1	300-350	43.9
5	900-950	14.2	584.33	41.7
6	629.73	12.2	900-950	34.5
7	200-250	9.9	200-250	33.6
8	250-300	8.3	250-300	30.0
9	300-350	8.1	303.31	21.6
10	554.37	8.1	629.73	20.2
11	800-850	7.7	284.15	20.1
12	368.07	7.2	800-850	17.0
13	950-1000	6.6	350-400	16.6
14	750-800	5.5	554.37	13.8
15	500-550	5.4	450-500	13.7
16	789.36	4.5	500-550	13.1
17	550-600	4.3	950-1000	13.1
18	400-450	4.2	750-800	11.4
19	609.76	4.1	368.07	10.5
20	703.31	3.6	609.76	9.9
21	450-500	3.5	400-450	7.6
22	256.3	3.3	789.36	7.5
23	303.31	2.8	550-600	7.3
24	350-400	2.6	256.3	5.8
25	650-700	2.4	703.31	5.0
26	465.22	2.4	977.02	3.7
27	770.41	2.1	770.41	3.4
28	600-650	2.1	600-650	3.4
29	765.15	2.0	650-700	3.3
30	977.02	2.0	100-150	3.3
31	700-750	1.9	250-300	3.2
32	100-150	1.8	700-750	3.0
33	284.15	1.7	50-100	2.9
34	1031.91	0.8	765.15	2.8
35	1000-1050	0.6	1031.91	0.5
36	50-100	0.3	1000-1050	0.3
37	1025.72	0.1	1025.72	0.1

From Roble [1987].

lower thermospheric regions by molecular conduction to attain thermal balance. At the bottom of the thermosphere, between 100 and 120 km, there are both sources and sinks of heat and there is a large temperature gradient with respect to altitude. Here, eddy and turbulent conduction play an important role in heat transfer. In this region, significant heat flow occurs from higher, hotter source altitudes to lower, cooler sink altitudes. It is complemented by a secondary heat source from local solar EUV heating. Heat sinks exist in the lower thermosphere and mesosphere. Radiation at 5.3 μm by the vibrational energy level changes in the heteronuclear molecule NO is an important cooling mechanism. At the mesopause near 80-85 km, vibrational energy level changes of O_3, CO_2, and H_2O all contribute to efficient cooling, allowing a thermal balance to be achieved.

In addition to differences in heat transport in various thermospheric regions, there are also differences in the altitude of maximum heating from low to high solar activity. In this study, an analysis is conducted with the calculation of the heat production rate per unit mass, Q, from

$$Q(z) = \sum_i \sum_\lambda \frac{1}{m_i} \sigma_i(\lambda) F(\lambda, z) \varepsilon(z) \quad \text{ergs g}^{-1} \text{ sec}^{-1} \tag{3.1}$$

where λ are the 37 EUV wavelengths outlined by Torr *et al.* [1979] and corrected in Tables 2.2 and 2.3. The Fe XVI line is excluded at this point from the wavelength groups in order to facilitate comparison with other studies. Its total energy flux contribution is also insignificant compared to the primary fluxes discussed above. The wavelength dependent absorption cross section for a constituent, $\sigma_i(\lambda)$, is given by Torr *et al.* and is shown in Figure 3.1. $i = 1,2,3$ for O, O_2, and N_2. The constituent particle mass is m_i, $F(\lambda, z)$ is the wavelength and altitude dependent EUV flux attenuated by the atmosphere at the 37 wavelength intervals represented by the

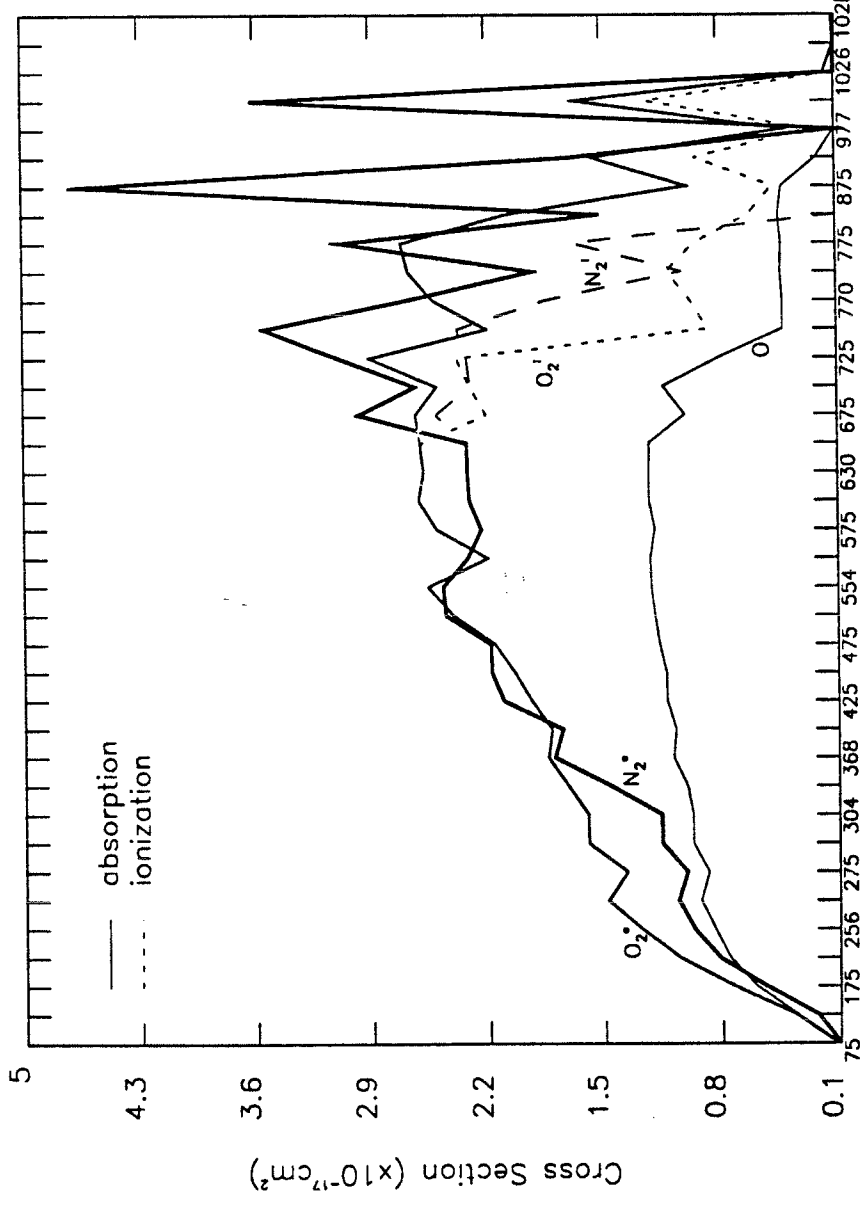

Figure 3.1 Weighted absorption and ionization cross sections. The superscript ^{a} for O_2 and N_2 refers to the absorption cross sections while ^{i} denotes the ionization cross sections. O absorption and ionization cross sections are the same at these wavelengths, as are those for O_2 and N_2 at the lower wavelengths. These cross sections are found in Torr *et al.* [1979]. The numbering of the wavelength intervals are shown in Tables 2.2 and 2.3. For ease of labeling, 75 represents the interval 50-100 Å, for example, while 256 indicates a discrete line.

optical depth τ. These two variables are formulated as

$$F(\lambda, z) = F_\infty(\lambda) e^{-\tau(\lambda, z)} \quad \text{photons cm}^{-2} \text{ sec}^{-1} \tag{3.2}$$

$$\tau(\lambda, z) = \sum_i \int_z^\infty n_i(z) \sigma_i(\lambda) F_\infty(\lambda) dz'. \tag{3.3}$$

$F_\infty(\lambda)$ is the solar EUV flux at the top of the atmosphere, $\varepsilon(z)$ is the parameterized, altitude dependent EUV neutral heating efficiency given by Roble and Emery [1983] which is plotted in Figure 3.2, and $n_i(z)$ is the altitude dependent constituent density.

Figure 3.1, from Torr *et al.* data, shows the O, O_2, and N_2 absorption and ionization cross sections by wavelength group listed in Table 2.2, excluding interval #10 for Fe XVI. The range of 1×10^{-18} to 5×10^{-17} cm^2 peaks at 850-900 Å for the N_2 absorption, at 700-750 Å for the O_2 absorption, and at 600-650 Å for the O absorption. Only O_2 has a significant absorption cross section above Lyman-β and all three constituents have cross sections smaller than $< 1 \times 10^{-18}$ cm^{-2} below 50 Å. The absorption and ionization cross sections for O are the same since only ionization potentials exist for atomic oxygen. The ionization threshold for O_2 is at 1026 Å, just above the solar H Lyman-β line (WLG interval #34) while the ionization threshold for N_2 is 796 Å (WLG interval #29). Both of these are referenced in Figure 1.2.

Figure 3.2 shows the ± 5 km smoothed curve for the parameterized EUV neutral heating efficiency as developed by Roble and Emery. This was based on noon EUV heating with a 60° solar zenith angle for the conditions of April 23, 1974. The peak of heating efficiency, 66%, is at 170 km. The EUV heating efficiency then declines to a constant 15% above 350 km.

By using the fluxes listed in Tables 2.2 and 2.3, excluding Fe XVI, for minimum and maximum solar activity, the heating rates may be calculated from equations (3.1), (3.2), and (3.3). The results are contour plotted in Fig-

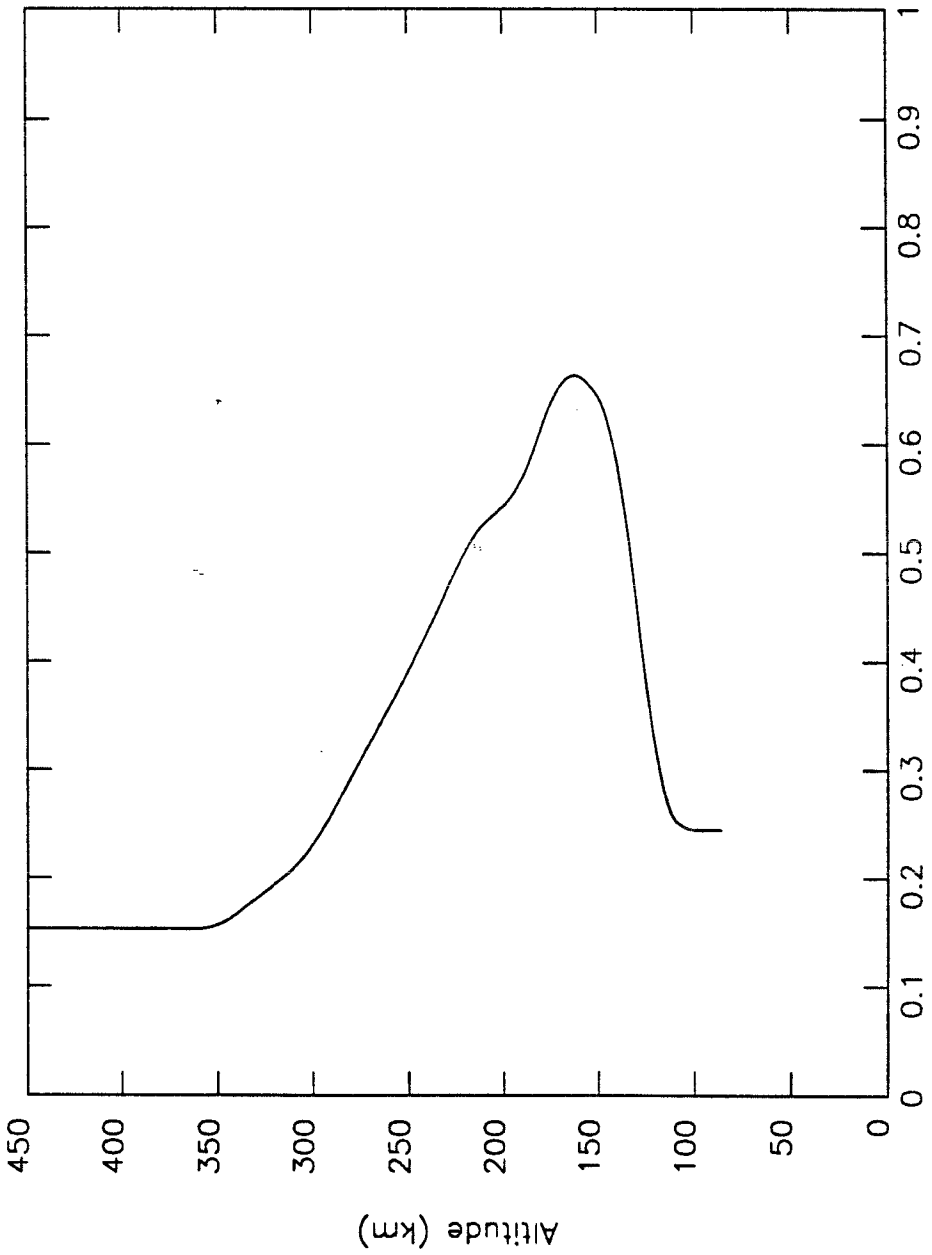

Figure 3.2 Parameterized EUV heating efficiency. This smoothed profile is taken from Roble and Emery [1983].

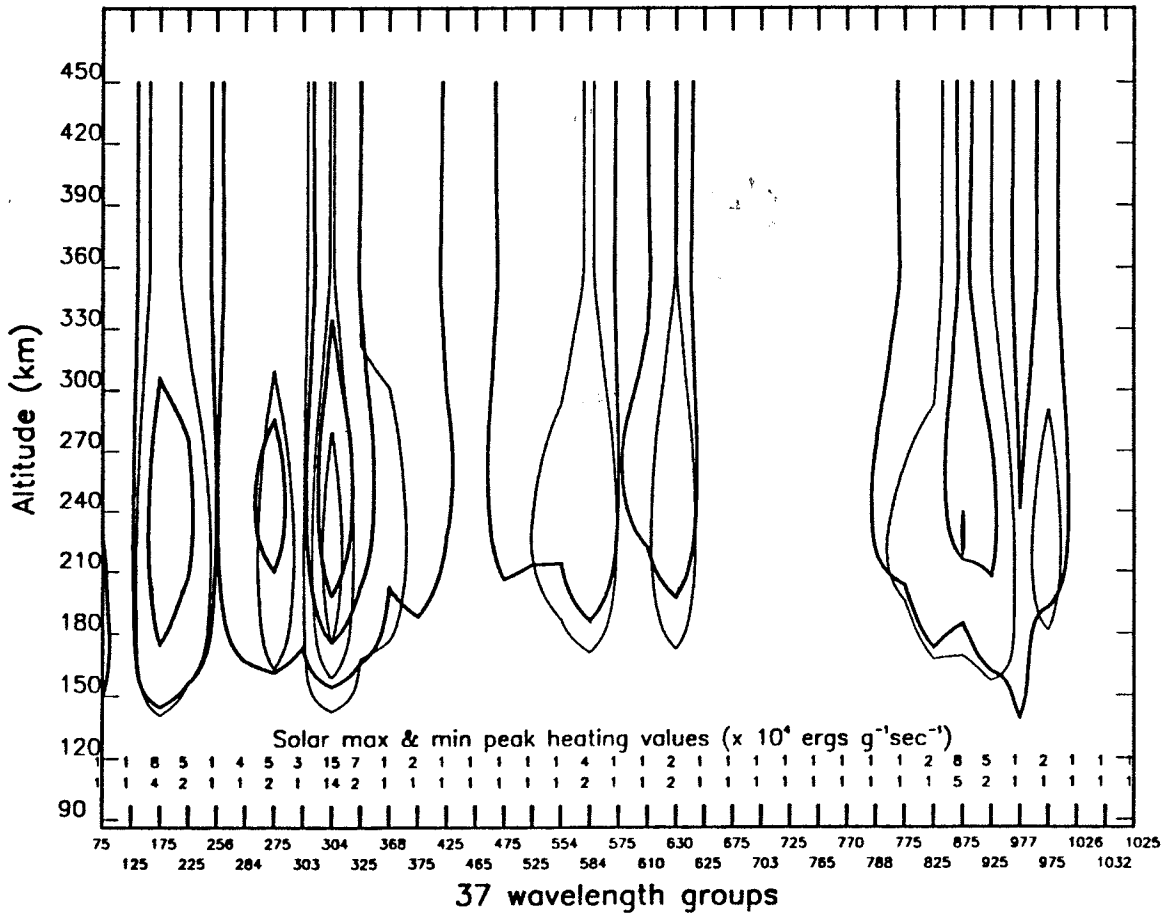

Figure 3.3 **Peak heating rates in 1976 and 1979.** The peak heating per unit mass values are shown for low (light line) and high (heavy line) solar activity. The wavelength group numbering is similar to Figure 3.1. The solar maximum peak heating values are displayed for each wavelength group on the top line in units of $\times 10^4$ ergs g^{-1} sec^{-1} while the solar minimum values are displayed on the bottom line.

ure 3.3 and show the heating in 1976 and 1979 using the SC#21REFW and F79050N files for the 37 wavelength intervals, respectively. The light lines represent the solar minimum conditions and the heavy lines represent solar maximum. In general, the results are similar to those of Roble [1987]. From Figure 3.3, the maximum heating during solar minimum is produced by He II, 850-900 Å, and 150-200 Å, in that order, while for solar maximum the heating is by He II, 850-900 Å, 150-200 Å, and 300-350 Å, also in that order. The maximum and minimum peak heating values, in units of $\times 10^4$ ergs g^{-1} sec^{-1}, are also listed by two significant digits. These same values are also listed under Q_{max} in Tables 3.10 through 3.13 which are discussed in detail in section 3.4.

This contour plot is complemented by Table 3.3 which lists the altitude range, the gas particle being heated, the total heating rate in that altitude range during solar minimum and maximum, the fraction of the total heating for solar minimum and maximum, and the ratio of solar maximum to minimum heating for the altitude range. When comparing by altitude range, N_2 contributes the largest fraction of total heating per unit mass above 210 km and across all wavelengths for both solar minimum and maximum. This is due to the influence of longer wavelength unit optical depth located above 180 km and large absorption cross sections compared to O_2 and O. Below 150 km, O_2 contributes the largest fraction of total heating per unit mass for both maximum and minimum conditions. This is due to the larger absorption cross sections for O_2 compared to O and N_2 at shorter wavelengths which have unit optical depth below 180 km. O_2 is also more sensitive to 977 Å and 1026 Å emissions than N_2 and O. The total heating per unit mass is much smaller in the lower thermosphere than at higher altitudes, however. This is a result of the substantial attenuation of flux above 210 km. For solar maximum to solar minimum, Table 3.3 and Figure 3.3 indicate that, at high thermospheric altitudes, there

TABLE 3.3. SOLAR MINIMUM AND MAXIMUM HEATING RATES, Q

Altitude (km)	GAS	Solar min total Q[a]	fraction of total	Solar max total Q[a]	fraction of total	Max:Min
422-450	O	1.001E+06	0.310	2.954E+06	0.317	2.95
	O_2	1.023E+06	0.317	2.919E+06	0.314	2.85
	N_2	1.199E+06	0.371	3.421E+06	0.368	2.85
392-420	O	1.000E+06	0.310	2.903E+06	0.317	2.90
	O_2	1.022E+06	0.317	2.872E+06	0.314	2.80
	N_2	1.198E+06	0.371	3.367E+06	0.368	2.81
362-390	O	9.984E+05	0.310	2.828E+06	0.317	2.83
	O_2	1.021E+06	0.317	2.802E+06	0.314	2.74
	N_2	1.196E+06	0.371	3.285E+06	0.368	2.74
332-360	O	1.060E+06	0.310	2.894E+06	0.316	2.72
	O_2	1.085E+06	0.317	2.874E+06	0.314	2.64
	N_2	1.271E+06	0.372	3.367E+06	0.368	2.64
302-330	O	1.302E+06	0.310	3.359E+06	0.316	2.57
	O_2	1.333E+06	0.317	3.347E+06	0.315	2.50
	N_2	1.562E+06	0.372	3.906E+06	0.368	2.49
272-300	O	1.735E+06	0.309	4.102E+06	0.316	2.36
	O_2	1.779E+06	0.317	4.103E+06	0.316	2.30
	N_2	2.084E+06	0.372	4.746E+06	0.366	2.27
242-270	O	2.259E+06	0.309	4.670E+06	0.318	2.06
	O_2	2.320E+06	0.318	4.693E+06	0.319	2.02
	N_2	2.710E+06	0.371	5.313E+06	0.362	1.96
212-240	O	2.617E+06	0.310	4.403E+06	0.322	1.68
	O_2	2.694E+06	0.319	4.449E+06	0.326	1.65
	N_2	3.109E+06	0.369	4.793E+06	0.351	1.54
182-210	O	2.336E+06	0.316	2.906E+06	0.332	1.24
	O_2	2.405E+06	0.325	2.973E+06	0.340	1.23
	N_2	2.647E+06	0.358	2.862E+06	0.327	1.08
152-180	O	1.286E+06	0.332	1.106E+06	0.339	0.86
	O_2	1.325E+06	0.342	1.242E+06	0.381	0.93
	N_2	1.252E+06	0.324	9.068E+05	0.278	0.72
122-150	O	1.690E+05	0.327	1.294E+05	0.252	0.76
	O_2	2.223E+05	0.430	2.968E+05	0.579	1.33
	N_2	1.244E+05	0.241	8.620E+04	0.168	0.69
92-120	O	2.248E+03	0.124	3.746E+03	0.098	1.66
	O_2	1.417E+04	0.787	3.182E+04	0.834	2.24
	N_2	1.586E+03	0.088	2.586E+03	0.067	1.63

[a] units of ergs gm^{-1} sec^{-1}

is a factor of 3 difference for total heating per unit mass. Between 150 and 210 km, there is little difference between maximum and minimum heating. In fact, there is less heating during maximum conditions between 150 to 180 km since the atmosphere has expanded above it, leading to a larger optical depth in this region. This prevents the increased flux from penetrating to these levels. Lower than 150 km, the heating rate increases again, reaching a factor of 2 between maximum and minimum as a result of the greatly intensified shorter wavelength emissions penetrating to these altitudes. The optical depth for soft X-rays is near unity in the lower thermosphere for nearly all solar conditions, as demonstrated below in Figure 3.7.

Comparing the heating by wavelength group, the results indicate that below 400 Å O is the dominant species heated as shown in Tables 3.4a and 3.4b. This is due to the large cross section for O below 400 Å compared to N_2 and O_2. This spectral region contains the important He II and 150-200 Å range. In this table, the number 0 represents O, 1 represents O_2, and 2 represents N_2. The magnitude of the total heating is given by symbols representing the range from $> 1 \times 10^4$ to $> 5 \times 10^6$ ergs g^{-1} sec^{-1}. The maximum heating is also indicated by the boldface numbers. Between 400 Å and 770 Å, N_2 dominates the total heating due to its large cross section compared to O_2 and O. Between 787 Å and 1050 Å, N_2 and O_2 alternate in dominant heating per unit mass, depending upon which has the larger cross section.

Therefore, it can be summarized that the EUV fluxes which contribute the largest heating per unit mass in the thermosphere do so above 210 km and are a mixture of chromospheric (He II, 850-900 Å) and transition region - cool coronal (150-200 Å) emissions. While He II has been referenced as a chromospheric line in Table 2.4, the 850-900 Å emissions are also all chromospheric in origin. This is shown in Table 3.5, where the lines are shown as part of

TABLE 3.4a. SPECIES HEATING BY WAVELENGTH GROUP
FOR SOLAR MINIMUM (76200)

Alt	Species Receiving Maximum Heating																																						
450	0	0	0	0	0	0	0	0	0	0	0	0	0	2	2	2	2	2	2	2	2	2	2	2	2	2	2	1	2	1	2	2	1	2	1	1	1	=
420	0	0	0	0	0	0	0	0	0	0	0	0	0	2	2	2	2	2	2	2	2	2	2	2	2	2	2	1	2	1	2	2	1	2	1	1	1	=
390	0	0	0	0	0	0	0	0	0	0	0	0	0	2	2	2	2	2	2	2	2	2	2	2	2	2	2	1	2	1	2	2	1	2	1	1	1	=
360	0	0	0	0	0	0	0	0	0	0	0	0	0	2	2	2	2	2	2	2	2	2	2	2	2	2	2	1	2	1	2	2	1	2	1	1	1	=
330	0	0	0	0	0	0	0	0	0	0	0	0	0	2	2	2	2	2	2	2	2	2	2	2	2	2	2	1	2	1	2	2	1	2	1	1	1	+
300	0	0	0	0	0	0	0	0	0	0	0	0	0	2	2	2	2	2	2	2	2	2	2	2	2	2	2	1	2	1	2	2	1	2	1	1	1	*
270	0	0	0	0	0	0	0	0	0	0	0	0	0	2	2	2	2	2	2	2	2	2	2	2	2	2	2	1	2	1	2	2	1	2	1	1	1	*
240	0	0	0	0	0	0	0	0	0	0	0	0	0	2	2	2	2	2	2	2	2	2	2	2	2	2	2	1	2	1	2	2	1	2	1	1	1	*
210	0	0	0	0	0	0	0	0	0	0	0	0	0	2	2	2	2	2	2	2	2	2	2	2	2	2	2	1	2	1	2	2	1	2	1	1	1	*
180	0	0	0	0	0	0	0	0	0	0	0	0	0	2	2	2	2	2	2	2	2	2	2	2	2	2	2	1	2	1	2	2	1	2	1	1	1	=
150	0	0	0	0	0	0	0	0	0	0	0	0	0	2	2	2	2	2	2	2	2	2	2	2	2	?	2	2	1	2	1	2	2	1	2	1	1	1	.
120	0	0	0	0	0	0	0	0	0	0	0	0	0	2	2	2	2	2	2	2	2	2	2	2	2	2	2	2	1	2	1	2	2	1	2	1	1	1	
	.	.	+	-	.	.	:	.	*	:	:	.	.	.	.	.	:	-	.	.	-	.	.	.	.	.	.	.	.	:	:	+	-	.	:	.				
WLG	1	2	3	4	5	6	7	8	9	10	11	12	13	14	15	16	17	18	19	20	21	22	23	24	25	26	27	28	29	30	31	32	33	34	35	36	37		

Codes used for the above table:

0: O

1: O_2

2: N_2

$> 1 \times 10^4$ ergs g^{-1} sec^{-1}

. $> 1 \times 10^5$ "

: $> 1 \times 10^6$ "

- $> 2 \times 10^6$ "

= $> 3 \times 10^6$ "

+ $> 4 \times 10^6$ "

* $> 5 \times 10^6$ "

TABLE 3.4b. SPECIES HEATING BY WAVELENGTH GROUP FOR SOLAR MAXIMUM (79050)

Alt	Species Receiving Maximum Heating																																				
450	0	0	0	0	0	0	0	0	0	0	0	0	2	2	2	2	2	2	2	2	2	2	2	2	2	2	2	1	2	1	2	2	1	2	1	1	1	*
420	0	0	0	0	0	0	0	0	0	0	0	0	2	2	2	2	2	2	2	2	2	2	2	2	2	2	2	1	2	1	2	2	1	2	1	1	1	*
390	0	0	0	0	0	0	0	0	0	0	0	0	2	2	2	2	2	2	2	2	2	2	2	2	2	2	2	1	2	1	2	2	1	2	1	1	1	*
360	0	0	0	0	0	0	0	0	0	0	0	0	2	2	2	2	2	2	2	2	2	2	2	2	2	2	2	1	2	1	2	2	1	2	1	1	1	*
330	0	0	0	0	0	0	0	0	0	0	0	0	2	2	2	2	2	2	2	2	2	2	2	2	2	2	2	1	2	1	2	2	1	2	1	1	1	*
300	0	0	0	0	0	0	0	0	0	0	0	0	2	2	2	2	2	2	2	2	2	2	2	2	2	2	2	1	2	1	2	2	1	2	1	1	1	*
270	0	0	0	0	0	0	0	0	0	0	0	0	2	2	2	2	2	2	2	2	2	2	2	2	2	2	2	1	2	1	2	2	1	2	1	1	1	*
240	0	0	0	0	0	0	0	0	0	0	0	0	2	2	2	2	2	2	2	2	2	2	2	2	2	2	2	1	2	1	2	2	1	2	1	1	1	*
210	0	0	0	0	0	0	0	0	0	0	0	0	2	2	2	2	2	2	2	2	2	2	2	2	2	2	2	1	2	1	2	2	1	2	1	1	1	*
180	0	0	0	0	0	0	0	0	0	0	0	0	2	2	2	2	2	2	2	2	2	2	2	2	2	2	2	1	2	1	2	2	1	2	1	1	1	=
150	0	0	0	0	0	0	0	0	0	0	0	0	2	2	2	2	2	2	2	2	2	2	2	2	2	2	2	1	2	1	2	2	1	2	1	1	1	.
120	0	0	0	0	0	0	0	0	0	0	0	0	2	2	2	2	2	2	2	2	2	2	2	2	2	2	2	1	2	1	2	2	1	2	1	1	1	
	:	.	*	*	.	+	*	=	*	*	:	-	:	.	:	:	:	+	.	:	-	.	.	.	.	.	.	:	:	-	*	*	:	-	.	.	.	
WLG	1	2	3	4	5	6	7	8	9	10	11	12	13	14	15	16	17	18	19	20	21	22	23	24	25	26	27	28	29	30	31	32	33	34	35	36	37	

Codes used for the above table:
0: O
1: O_2
2: N_2
  $> 1 \times 10^4$ ergs g^{-1} sec^{-1}
. $> 1 \times 10^5$ ”
: $> 1 \times 10^6$ ”
- $> 2 \times 10^6$ ”
= $> 3 \times 10^6$ ”
+ $> 4 \times 10^6$ ”
* $> 5 \times 10^6$ ”

TABLE 3.5. CHROMOSPHERIC FLUX BETWEEN 851.00-900.00 Å FROM SC#21REFW

λ (Å)	F_λ	$\sum F_\lambda$	Source	Key	$C(\lambda)$
851.00	45.0	45.0	H LY(C)	1	1.0000
852.00	46.1	91.1	H LY(C)	1	1.0000
853.00	47.4	138.5	H LY(C)	1	1.0000
854.00	48.5	187.0	H LY(C)	1	1.0000
855.00	49.7	236.7	H LY(C)	1	1.0000
856.00	51.0	287.7	H LY(C)	1	1.0000
857.00	52.4	340.1	H LY(C)	1	1.0000
858.00	53.6	393.7	H LY(C)	1	1.0000
859.00	55.0	448.7	H LY(C)	1	1.0000
860.00	56.4	505.1	H LY(C)	1	1.0000
861.00	57.9	563.0	H LY(C)	1	1.0000
862.00	59.2	622.2	H LY(C)	1	1.0000
863.00	60.7	682.9	H LY(C)	1	1.0000
864.00	62.2	745.1	H LY(C)	1	1.0000
865.00	63.9	809.0	H LY(C)	1	1.0000
866.00	65.5	874.5	H LY(C)	1	1.0000
867.00	67.1	941.6	H LY(C)	1	1.0000
868.00	68.9	1010.5	H LY(C)	1	1.0000
869.00	70.6	1081.1	H LY(C)	1	1.0000
870.00	72.4	1153.5	H LY(C)	1	1.0000
871.00	74.2	1227.7	H LY(C)	1	1.0000
872.00	76.1	1303.8	H LY(C)	1	1.0000
873.00	78.1	1381.9	H LY(C)	1	1.0000
874.00	80.1	1462.0	H LY(C)	1	1.0000
875.00	82.1	1544.1	H LY(C)	1	1.0000

TABLE 3.5. CHROMOSPHERIC FLUX BETWEEN 851.00-900.00 Å FROM SC#21REFW (continued)

λ (Å)	F_λ	$\sum F_\lambda$	Source	Key	$C(\lambda)$
876.00	84.1	1628.2	H LY(C)	1	1.0000
877.00	86.2	1714.4	H LY(C)	1	1.0000
878.00	88.5	1802.9	H LY(C)	1	1.0000
879.00	90.7	1893.6	H LY(C)	1	1.0000
880.00	93.0	1986.6	H LY(C)	1	1.0000
881.00	95.4	2082.0	H LY(C)	1	1.0000
882.00	97.9	2179.9	H LY(C)	1	1.0000
883.00	100.4	2280.3	H LY(C)	1	1.0000
884.00	102.9	2383.2	H LY(C)	1	1.0000
885.00	105.5	2488.7	H LY(C)	1	1.0000
886.00	108.1	2596.8	H LY(C)	1	1.0000
887.00	110.8	2707.6	H LY(C)	1	1.0000
888.00	113.7	2821.3	H LY(C)	1	1.0000
889.00	116.6	2937.9	H LY(C)	1	1.0000
890.00	119.6	3057.5	H LY(C)	1	1.0000
891.00	122.6	3180.1	H LY(C)	1	1.0000
892.00	125.7	3305.8	H LY(C)	1	1.0000
893.00	128.8	3434.6	H LY(C)	1	1.0000
894.00	132.1	3566.7	H LY(C)	1	1.0000
895.00	135.4	3702.1	H LY(C)	1	1.0000
896.00	138.9	3841.0	H LY(C)	1	1.0000
897.00	142.4	3983.4	H LY(C)	1	1.0000
898.00	145.9	4129.3	H LY(C)	1	1.0000
899.00	149.7	4279.0	H LY(C)	1	1.0000
900.00	153.5	4432.5	H LY(C)	1	1.0000

50 lines with a total flux of 4432.5×10^6 photons cm^{-2} sec^{-1} are included. The wavelength range is dominated by 900.00 Å H Lyman continuum with a flux of 153.50×10^6 photons cm^{-2} sec^{-1}, a key = 1, and a $C(\lambda) = 1.0000$.

the H Lyman continuum. In this table, the wavelength, the flux at that wavelength, the cumulative sum of fluxes through the range, the flux source, and the Hinteregger *et al.* [1981] key and wavelength dependent scaling parameter are listed. The 150-200 Å range is composed of 34 coronal lines and particularly dominated by the Fe IX transition region, cool coronal line at 171.08 Å as shown in Table 3.6a. Table 3.6b lists the 12 chromospheric region lines in the 150-200 Å range. The information in Tables 3.5, 3.6a, and 3.6b is reprinted from SC#21REFW.

As examples, Figures 3.4, 3.5, and 3.6 show the calculated EUV flux for the chromospheric He II and 850-900 Å and the coronal plus chromospheric components for the 150-200 Å emissions. All show a rise over three and one half years from low-to-high solar activity. He II and 850-900 Å have the same magnitude of flux while 150-200 Å has one-third as much. These calculated time series are based on the EUV class formulation of Hinteregger *et al.* [1981] in equation (1.2) and reproduced here

$$F_{\text{euv}} = F_{\text{euvref}} + F_{\text{euvref}}(R_k - 1)c(\lambda). \quad \text{photons cm}^{-2}\ \text{sec}^{-1} \tag{3.4}$$

F_{euvref} is the solar minimum reference EUV flux at a specific wavelength found in SC#21REFW, R_k is ratio of the "keyed" flux at a date to solar minimum found in SC#21OBS, $k = 1$ for Lyman-β or $k = 2$ for Fe XVI, and $c(\lambda)$ is the wavelength dependent scaling parameter specified by Hinteregger *et al.* [1981] in SC#21REFW and listed in Tables 3.5, 3.6a, and 3.6b.

Below 210 km, the same emissions as outlined above, especially He II, 850-900 Å, and 150-200 Å, contribute the largest heating rates per unit mass. However, below this level, the optical depth for EUV wavelengths is greater than unity and attenuation significantly decreases the amount of energy flux available for local heating. Figure 3.7 shows unit optical depth for each EUV

TABLE 3.6a. CORONAL FLUX BETWEEN 150.10-198.58 Å FROM SC#21REFW

λ (Å)	F_λ	$\sum F_\lambda$	Source	Key	$C(\lambda)$
152.15	13.1	13.1	NI XII	2	0.07000
154.18	6.9	20.0	NI XII	2	0.07000
157.73	6.2	26.2	NI XIII	2	0.12000
158.37	14.2	40.4	NI X	2	0.01280
159.98	13.0	53.4	NI X	2	0.01280
164.15	3.7	57.1	NI XIV	2	0.20000
171.08	307.5	364.6	FE IX	2	0.01150
174.58	268.8	633.4	FE X	2	0.01590
177.24	162.5	795.9	FE X	2	0.01590
178.05	20.5	816.4	FE XI	2	0.02641
179.27	0.4	816.8	NI XV	2	0.30000
179.75	20.6	837.4	FE XI	2	0.02641
180.41	179.0	1016.4	FE XI	2	0.02641
181.14	21.2	1037.6	FE XI	2	0.02641
182.17	23.1	1060.7	FE XI	2	0.02641
183.45	1.5	1062.2	CA XIV	2	0.15000
184.53	43.8	1106.0	FE X	2	0.01590
184.80	2.3	1108.3	FE XI	2	0.02641
186.60	3.2	1111.5	CA XIV	2	0.15000
186.87	23.1	1134.6	S XI B	2	0.03000
187.95	0.7	1135.3	AR XIV	2	0.40000
188.23	9.7	1145.0	FE XII	2	0.05041
188.31	120.0	1265.0	FE XI	2	0.02641
190.02	42.3	1307.3	FE X	2	0.01590
191.04	10.5	1317.8	FE XII	2	0.05041
191.34	9.0	1326.8	FE XIII	2	0.08811
192.40	40.0	1366.8	FE XII	2	0.05041
192.82	58.8	1425.6	FE XI	2	0.02641
193.52	65.5	1491.1	FE XII	2	0.05041
195.13	107.0	1598.1	FE XII	2	0.05041
196.52	9.7	1607.8	FE XIII	2	0.08811
196.65	2.9	1610.7	FE XII	2	0.05041
197.44	4.0	1614.7	FE XIII	2	0.08811
198.58	7.1	1621.8	FE XII	2	0.05041

34 lines with a total flux of 1621.8×10^6 photons cm^{-2} sec^{-1} are included. The wavelength range is dominated by 171.08 Å Fe IX with a flux of 307.50×10^6 photons cm^{-2} sec^{-1}, a key = 2, and a $C(\lambda) = 0.01150$.

TABLE 3.6b. CHROMOSPHERIC FLUX BETWEEN 150.10-198.58 Å FROM SC#21REFW

λ (Å)	F_λ	$\sum F_\lambda$	Source	Key	$C(\lambda)$
150.10	7.6	7.60	O VI	1	1.04100
160.37	11.0	18.60	UNSPEC'D	1	0.83001
162.00	5.5	24.10	UNSPEC'D	1	0.83001
167.50	19.5	43.60	FE VIII	1	0.41501
168.17	36.0	79.60	FE VIII	1	0.41501
168.55	20.5	100.10	FE VIII	1	0.41501
168.92	12.6	112.70	FE VIII	1	0.41501
169.70	23.4	136.10	UNSPEC'D	1	0.83001
172.17	11.2	147.30	O V	1	0.47301
173.08	21.4	168.70	BLEND	1	0.83001
175.26	33.1	201.80	BLEND	1	0.83001
185.21	18.2	220.00	FE VIII B	1	0.41501

12 lines with a total flux of 220.0×10^6 photons cm^{-2} sec^{-1} are included. The wavelength range is dominated by 168.17 Å Fe VIII with a flux of 36.0×10^6 photons cm^{-2} sec^{-1}, a key = 1, and a $C(\lambda) = 0.41501$.

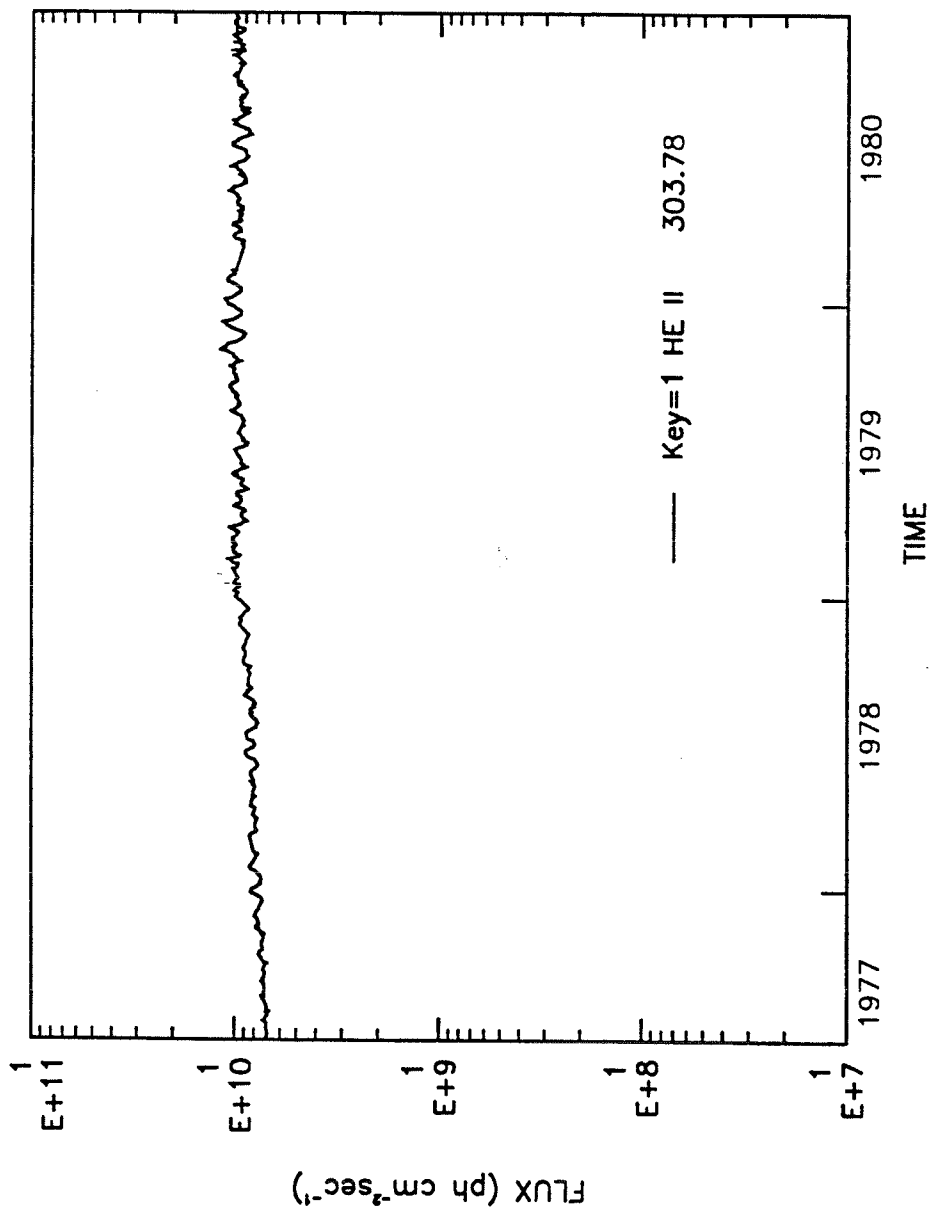

Figure 3.4 He II (304 Å) calculated flux for 1977-1980. Key 1 refers to Hinteregger's EUV chromospheric (Lyman-β) class of emissions. The logarithmic scale is used so that this figure may be compared with Figures 3.5 and 3.6.

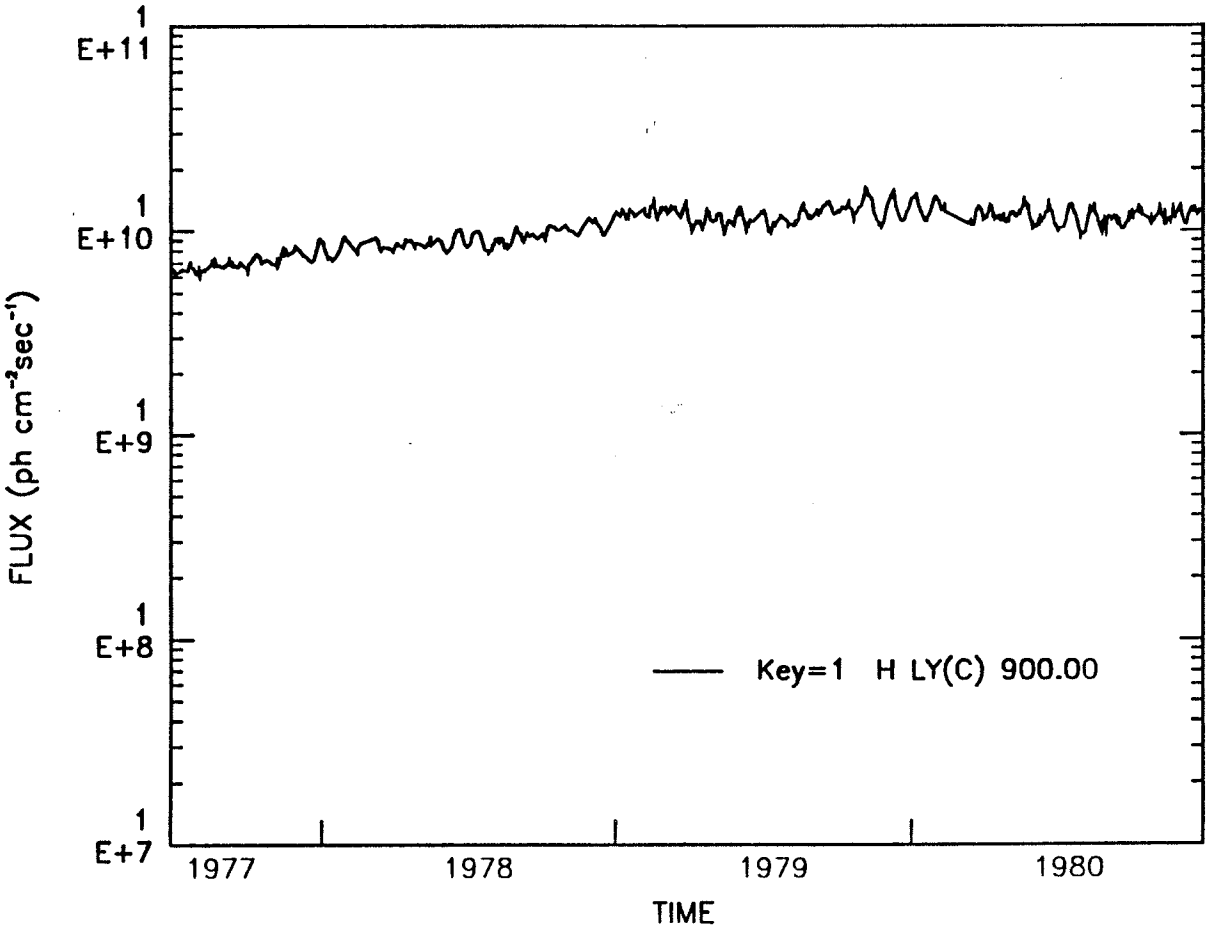

Figure 3.5 **H Lyman continuum (850-900 Å) calculated flux for 1977-1980.** See Figure 3.4 for "key" comment. Ly(c) denotes the Lyman continuum which dominates this spectral range. 900 Å is the dominant line in this interval.

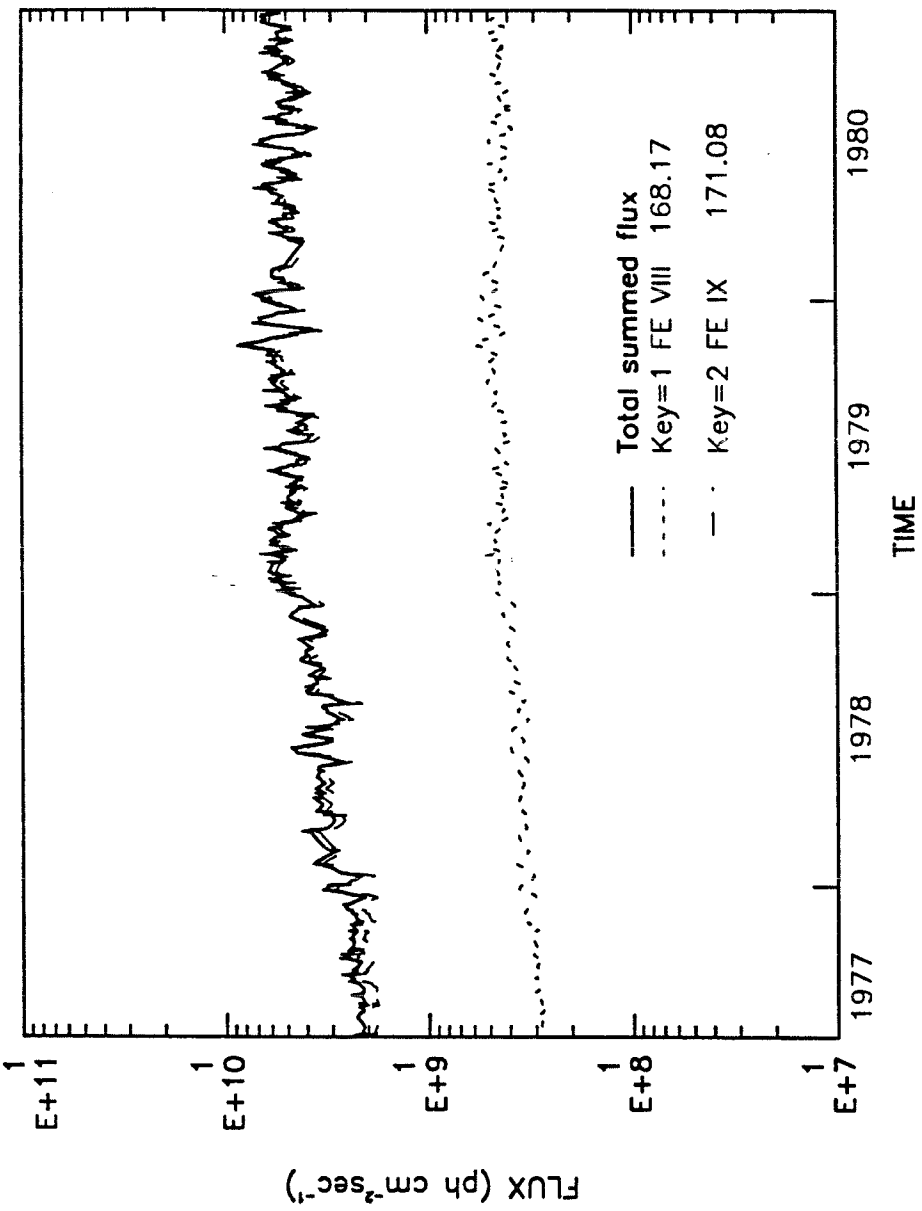

Figure 3.6 150-200 Å calculated flux for 1977-1980. Key = 1 indicates chromospheric emission and key = 2 indicates coronal emission. Fe VIII (168 Å) dominates all the chromospheric emissions in this wavelength interval while Fe IX (171 Å) dominates the coronal emissions in this interval.

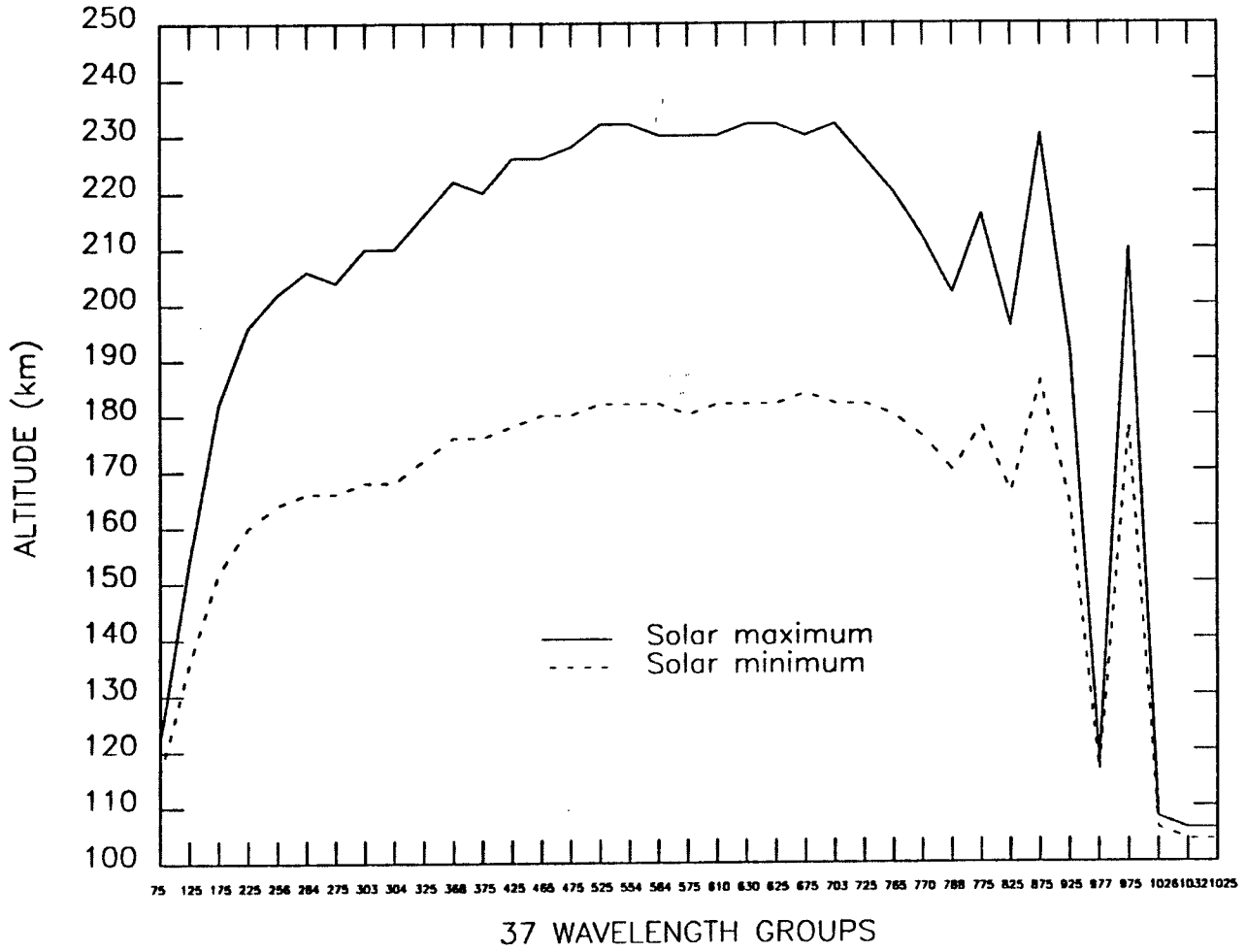

Figure 3.7 **Unit optical depth for solar maximum and minimum.** The wavelength scale is the same as Figures 3.1 and 3.3.

wavelength group or line and the altitude at which it is reached for solar maximum and minimum conditions. The range is from 120 to 230 km, with the important He II, 850-900 Å, and 150-200 Å emissions achieving unit optical depth at 168, 186, and 152 km, respectively, for solar minimum and 210, 230, and 182 km, respectively, for solar maximum. The unit optical depth is higher at solar maximum because the atmosphere has expanded, leading to increased density, and this prevents flux penetration to lower levels.

In summary, EUV heating of the thermosphere depends on the wavelength, heat transport mechanism, solar activity, species cross section, and altitude or density. At all altitudes and for all levels of solar activity, there are nine wavelength intervals which contribute nearly 50% of the EUV heat to the thermosphere. Predominant among these are the chromospheric and cool-corona emissions of He II, 850-900 Å, and 150-200 Å. O is the dominant species heated below 400 Å while N_2 is the dominant species heated above 400 Å. Across all wavelengths, O_2 is the main species heated below 150 km, although the heating rates in this region are much lower than those at higher altitudes. Heat is primarily produced above 210 km and is transported to lower thermospheric and mesospheric regions. There, cooling occurs by infrared radiation of heteronuclear molecules which transfer thermal energy into radiated energy by vibrational energy level transitions. Having now reviewed EUV thermospheric heating and the important wavelengths involved, it is useful to show the relationship between these wavelengths.

3.3 Correlations of Solar EUV with Flux Indices

In reviewing early work on solar EUV radiation, Hinteregger [1969] shows the spectral range between 200 and 1300 Å in Figure 3.8. This was obtained by rocket flights during the minimum of solar cycle 19. It shows

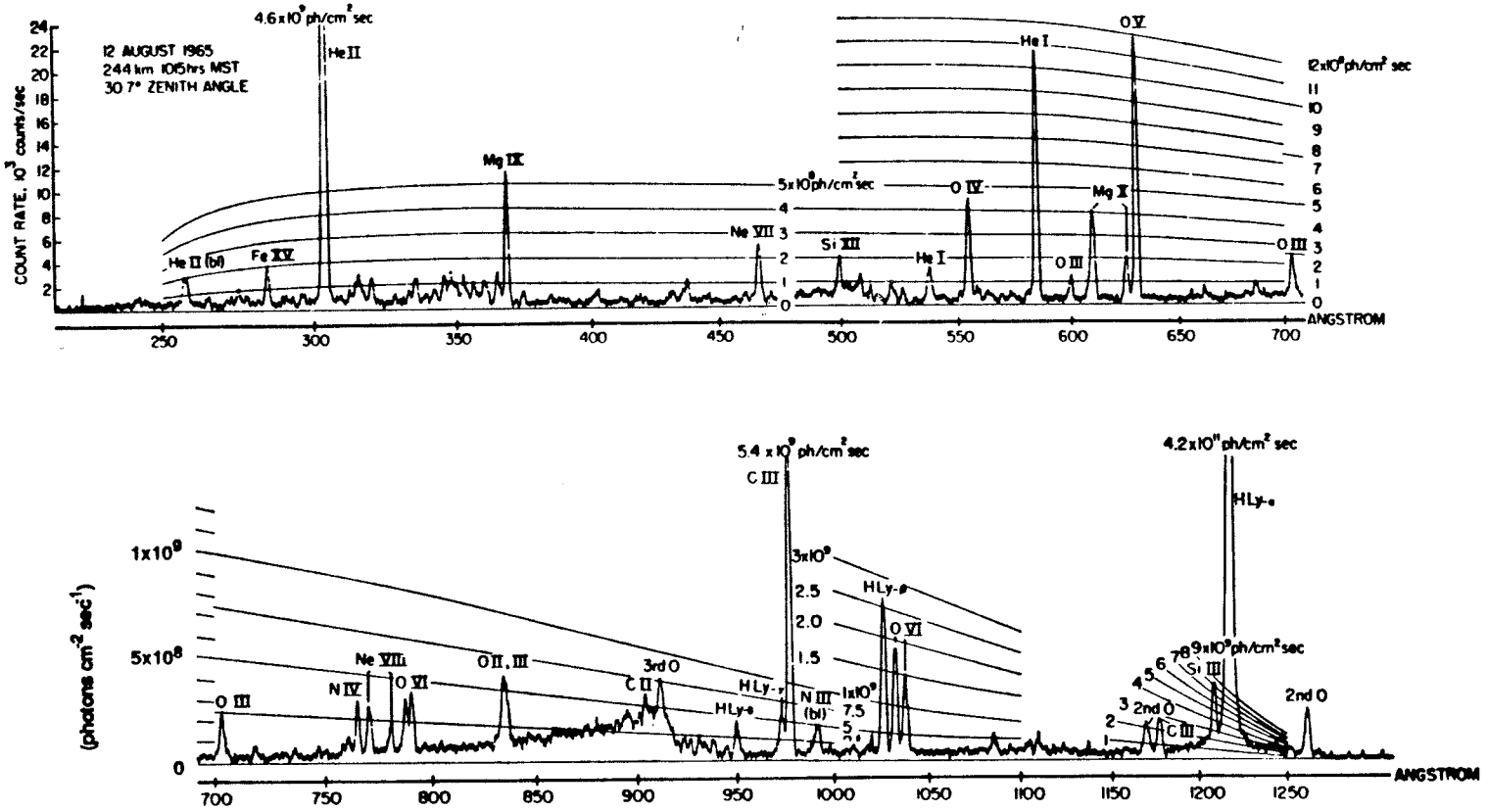

Figure 3.8 **Principal solar radiation between 250-1250 Å.** The solar cycle 19 minimum spectral range is from Hinteregger [1969].

the principal emission and continuum features in the solar EUV spectrum.

Principal emissions occur at Lyman-α, Lyman-β, C III, Lyman continuum, O V, He I, and He II. Many smaller lines are also evident from ionized Fe, Mg, Ne, Si, N, C, and others, showing the complexity of the spectral region.

In comparing Figure 3.8, Table 2.2, Table 2.3, and Table 2.4, it is possible to simplify a representation of EUV fluxes. Schmidtke [1984] reviewed classical EUV indices and suggested other potential EUV indices. In particular, Hinteregger *et al.* [1981] proposed that Lyman-β and Fe XVI are representations of two classes of EUV flux. Based on the review in section 3.2 of the important thermospheric heating emissions, it is now presented that solar EUV flux discrete lines and wavelength ranges may be represented by chromospheric emissions, by coronal emissions, or by a mixture of both. Specifically, it is proposed that solar Lyman-α flux and solar 1-8 Å X-ray flux are good indices for chromospheric and coronal emissions, respectively. Recalling Table 3.1, the intent here is to extend Hinteregger's useful EUV class model to a new model which now uses Lyman-α as a chromospheric emission index instead of Lyman-β and uses 1-8 Å X-rays as a coronal index instead of the Fe XVI line. Figures 2.1, 2.3, and 2.9 in the previous chapter show the daily-averaged Lyman-α for solar cycle 21. Figures 2.1, 2.15, and 2.16 show the 1-8 Å background X-ray flux for cycle 21.

As a chromospheric emission, Lyman-α behaves differently than coronally dominated emissions. Since it is such a strong line, it has been studied for many years. The work prior to 1976 is reviewed by Vidal-Madjar [1977]. Earlier comparisons between purely chromospheric or Lyman-α emissions and the mixed emission $F_{10.7}$ have been conducted since the OSO satellites made measurements in the late 1960s and early 1970s. Timothy and Timothy [1970], Woodgate *et al.* [1973], Chapman and Neupert [1974], Vidal-Madjar [1975],

and Vidal-Madjar and Phissamay [1980] all found generally good correlations for non-solar minimum conditions. An example of the correlation during the declining portion and minimum conditions of solar cycle 21 is shown in Figure 3.9, which compares $F_{10.7}$ and SME Lyman-α. This plot is obtained by conducting a linear fit over the declining period of solar cycle 21 from October 1981 to June 1984. The Lyman-α is then converted to units of 10^{-22} W m^{-2} Hz^{-1} for comparison and is extended through solar minimum. The plotted data starts on October 8, 1981 and continues through December 31, 1987. While both fluxes decline from high to low values with the same slope, and both contain a 27-day periodicity, the relative insensitivity of $F_{10.7}$ to chromospheric changes during solar minimum is apparent. It reaches a threshold near 70×10^{-22} W m^{-2} Hz^{-1}. Whether this $F_{10.7}$ quiet sun background originates mainly in the chromosphere and transition region or whether it contains an important coronal component is not yet clear. However, this graphic demonstration indicates that $F_{10.7}$ is an unreliable indicator of chromospheric EUV emissions during solar minimum conditions. Figure 3.13p below shows the scatter plot of this correlation. This conclusion supports Vidal-Madjar and Phissamay [1980] who also show a low correlation between $F_{10.7}$ and Lyman-α for solar minimum conditions in cycle 20.

The correlations between $F_{10.7}$ and AE-E Lyman-α have also been studied by Bossy and Nicolet [1981], Bossy [1983], Oster [1983], and Donnelly *et al.* [1986a, b]. Donnelly [1987a] has additionally studied the autocorrelations in the temporal trends between various AE-E EUV wavelengths. Their results for the $F_{10.7}$ and Lyman-α comparison have different interpretations. Bossy and Nicolet, Bossy, and Oster have argued that the AE-E Lyman-α results suffer a shift in sensitivity in monochromator #22, after December 21, 1978. Figure 3.10 from Bossy and Nicolet, Figure 3.11 from Bossy, and the

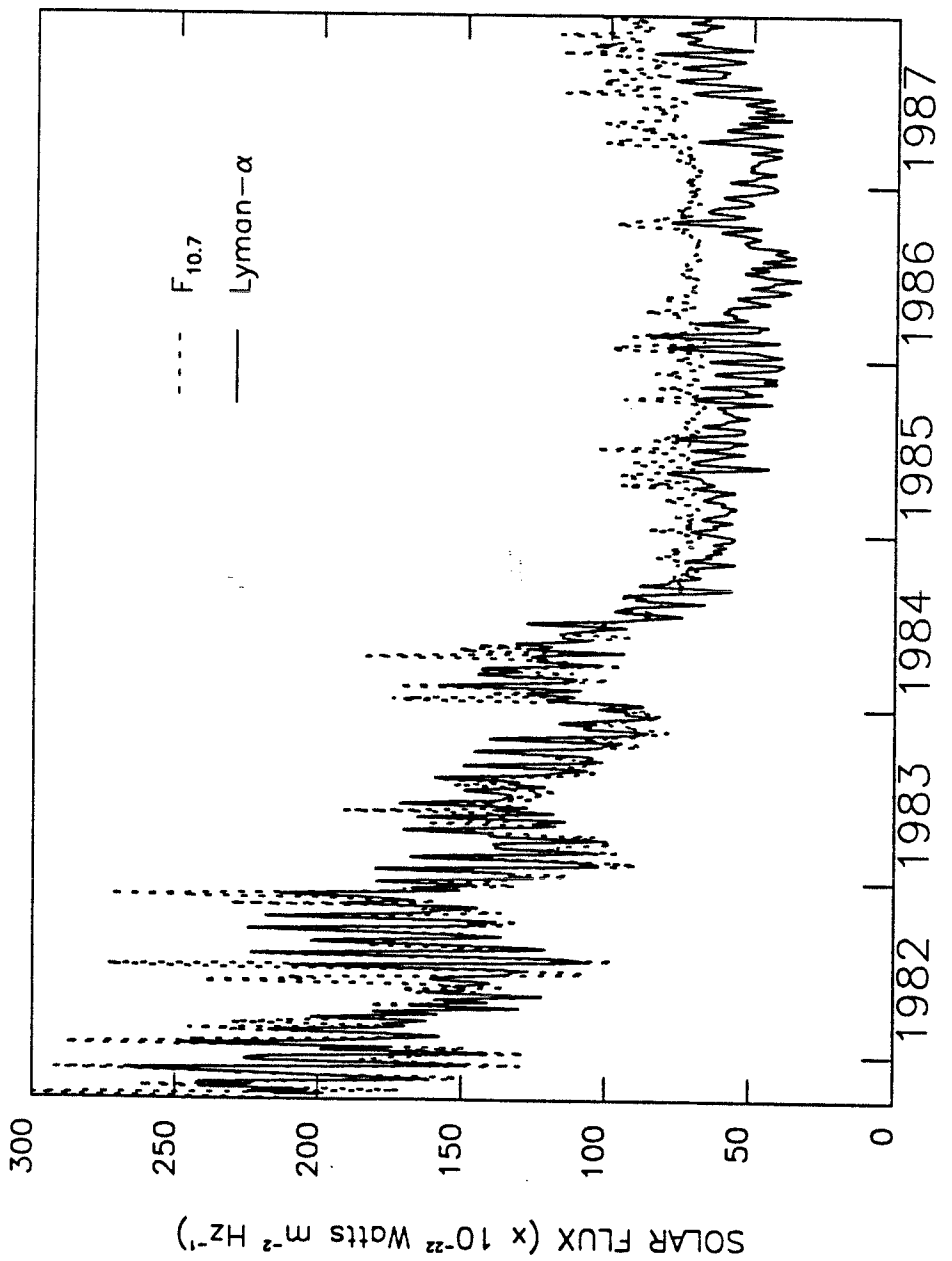

Figure 3.9 $F_{10.7}$ **and Lyman-**α **in solar cycle 21.** The datasets begin October 8, 1981 and continue through December 31, 1987.

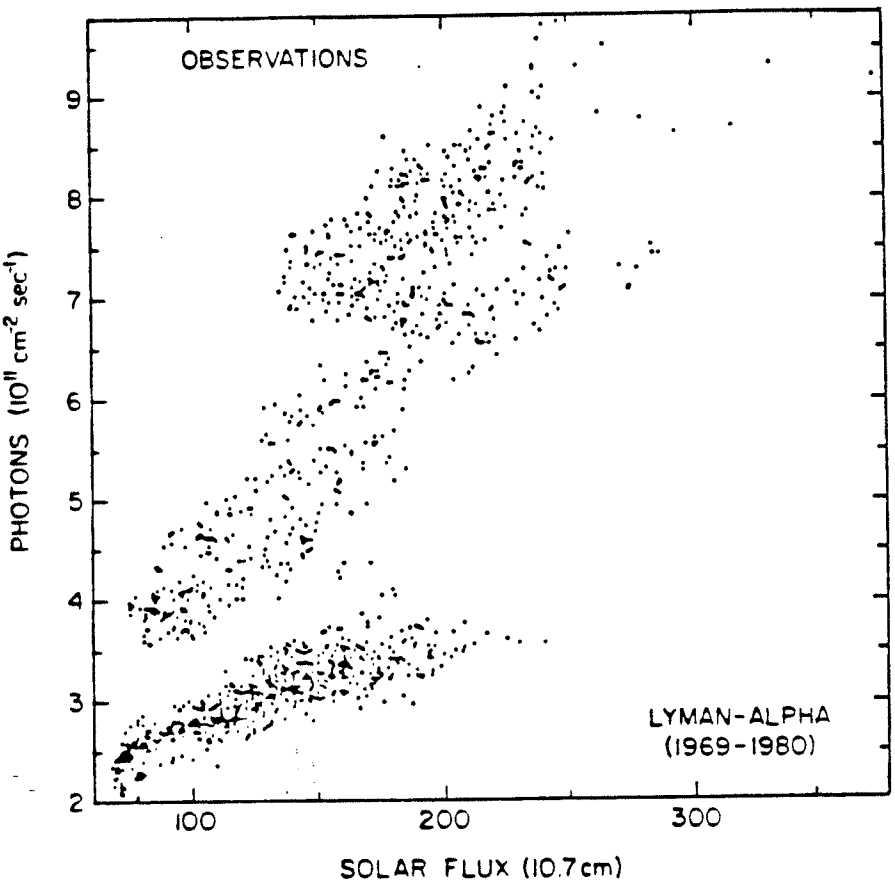

Figure 3.10 **Irradiance of Lyman-α between 1969 and 1980.** This data from the minimum of cycle 19 through the maximum of cycle 21 is from Bossy and Nicolet [1981].

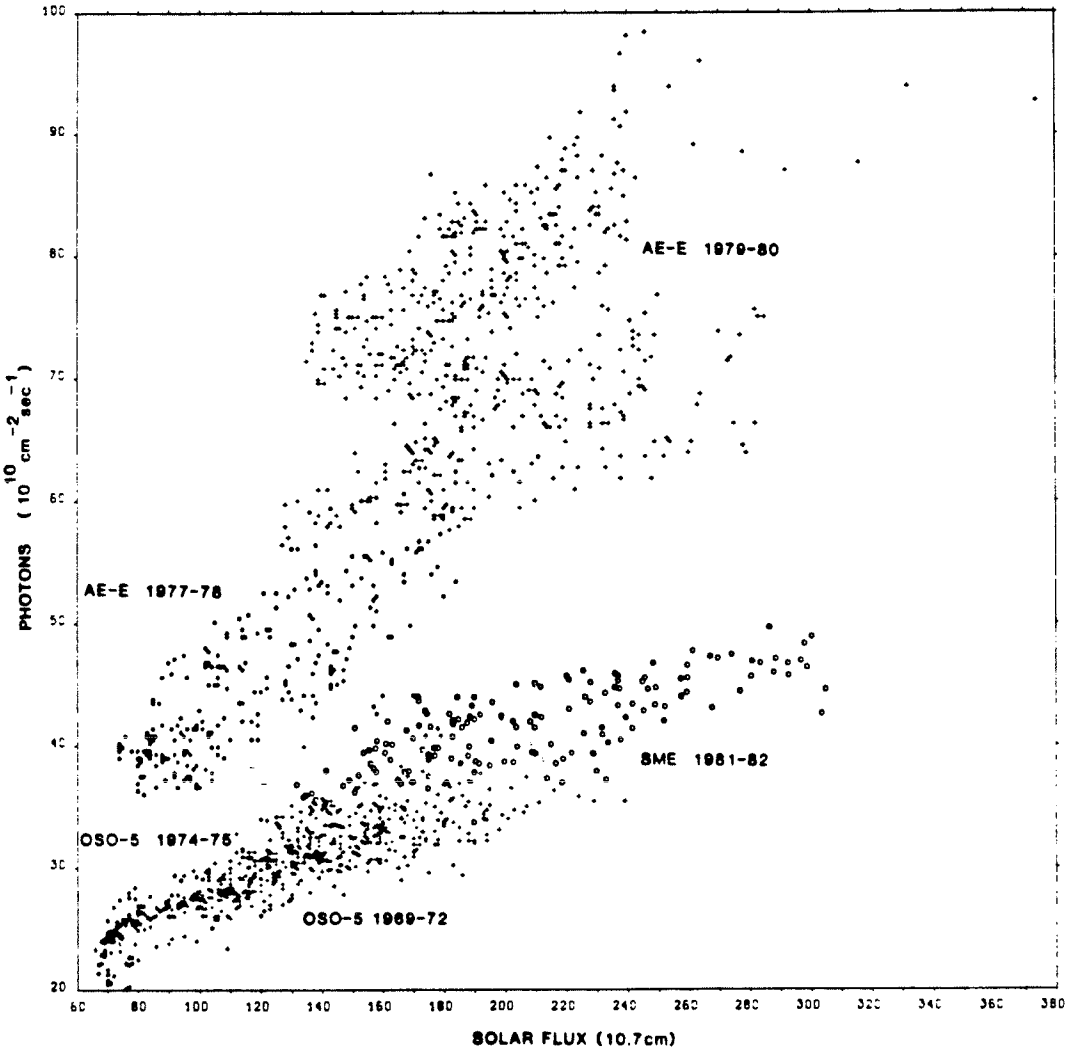

Figure 3.11 **H-Lyman-α 1969-1982.** The five groups in this plot from Bossy [1983] are: OSO-5 (1969-72) and (1974-75), AE-E (1977-78) and (1979-80), and SME (1981-82).

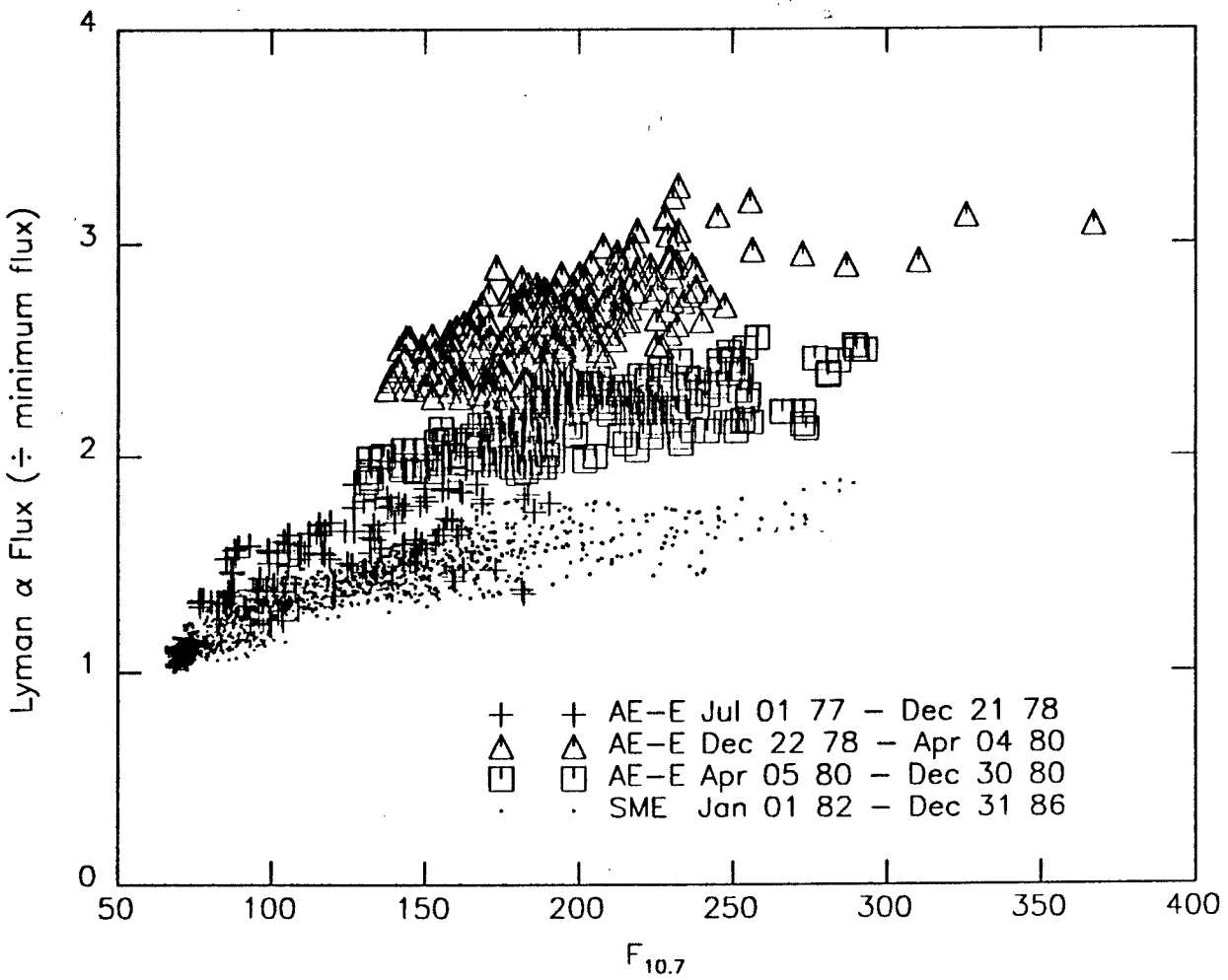

Figure 3.12 **AE-E and SME Lyman-α compared to $F_{10.7}$.** The four sets of data depicted in the legend are from AE-E and SME between July 1977 and December 1986.

Figure 3.12 all show a different correlation between Lyman-α and $F_{10.7}$ after December 21, 1978. In Figure 3.12, the data from AE-E and SME is shown as a ratio to its solar minimum value of 3×10^{11} and 2.3×10^{11} photons cm^{-2} sec^{-1}, respectively. Only the AE-E Lyman-α between December 22, 1978 through April 4, 1980 appears to disagree with the other ratios in the scatter plot with $F_{10.7}$. The AE-E data beginning July 1, 1977 through December 21, 1978 and April 5, 1980 through December 30, 1980 appears to agree with the SME correlation to $F_{10.7}$. Donnelly *et al.* [1986a, b] disagree with the finding of Bossy and Nicolet, Bossy, and Oster, with respect to their revisions of wavelengths other than Lyman-α, demonstrating that some EUV and UV fluxes measured by separate AE-E monochromators and the NIMBUS-7 satellite show similar and concurrent differences with respect to $F_{10.7}$. Fukui [1988] suggests that the unique increase in the AE-E Lyman-α may be a result of a secondary production mechanism for the flux which is triggered in high solar activity. While this question is still being investigated, the correlations in this study take the periods from July 1, 1977 through December 21, 1978, December 22, 1978 through April 4, 1980, and April 5, 1980 through December 30, 1980 separately when comparing the AE-E Lyman-α flux to other EUV fluxes. This study performed linear regression fits of the data, giving the correlations shown in the scatter plots, Figures 3.13a through 3.13n. The scatter plot between $F_{10.7}$ and rising activity AE-E Lyman-α is shown in Figure 3.13o. The scatter plot between $F_{10.7}$ and SME Lyman-α is shown in Figure 3.13p. These linear fits were conducted over the AE-E data for the rising portion of solar cycle 21 only, between July 1, 1977 and December 21, 1978.

In Table 3.7 and the Figures 3.13a - 3.13n, the wavelength group, the solar minimum reference value of July 13-18, 1976, the intercept, slope, and linear coefficient of correlation, r, are shown. The latter correlation indicator

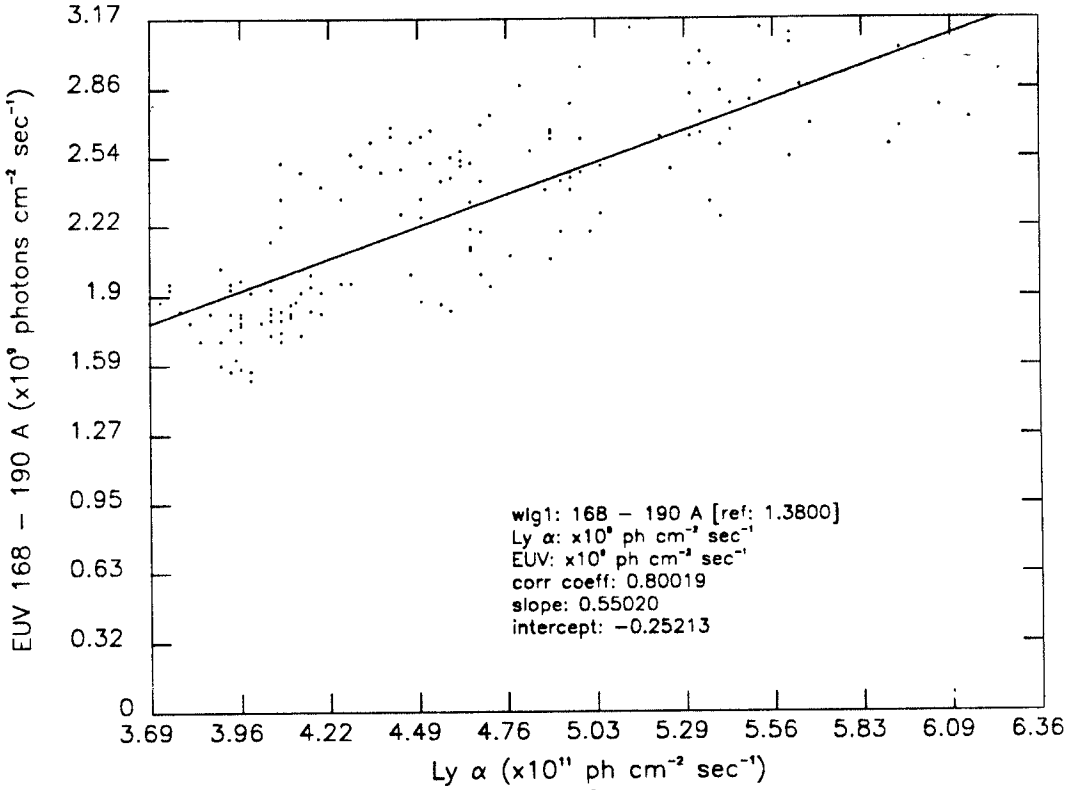

Figure 3.13 (a) **Lyman-α and 168-190 Å correlation.**

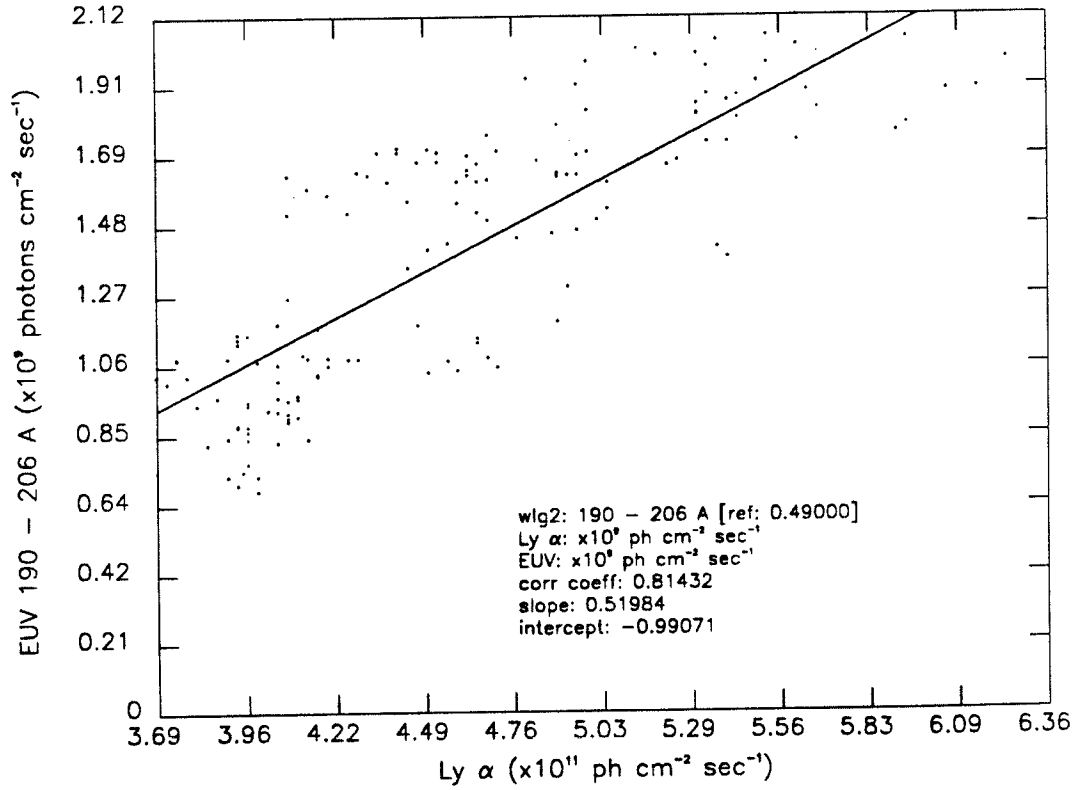

Figure 3.13 (b) **Lyman-α and 190-206 Å correlation.**

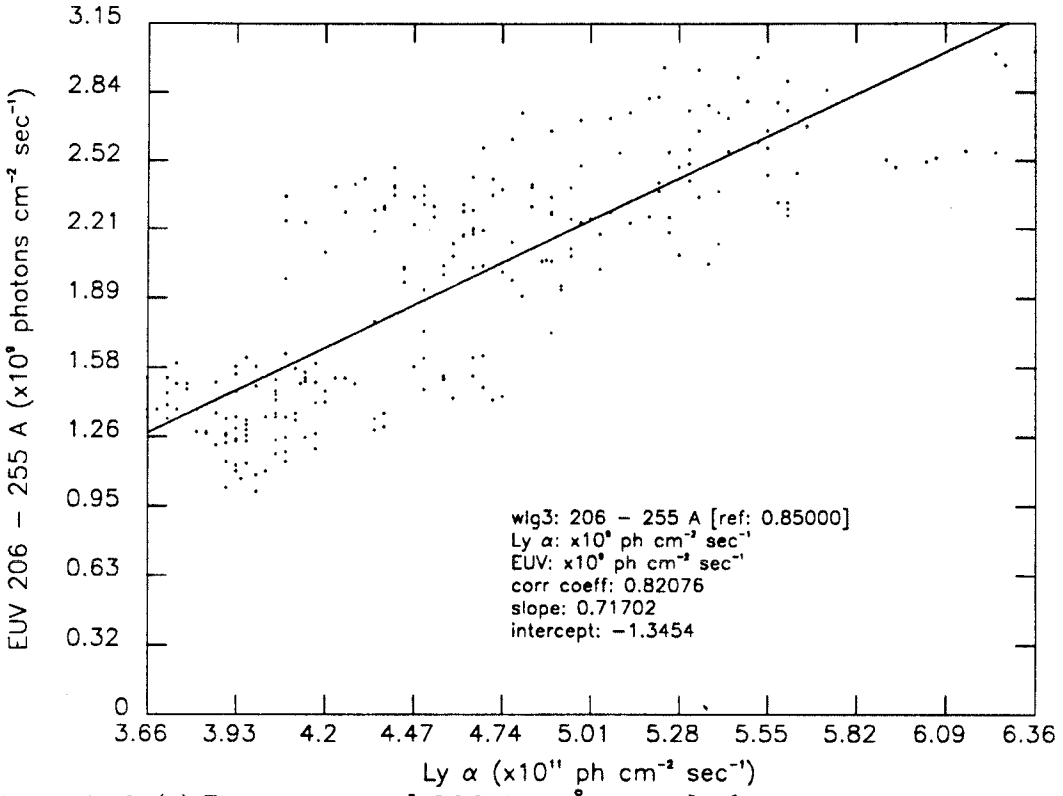

Figure 3.13 (c) **Lyman-α and 206-255 Å correlation.**

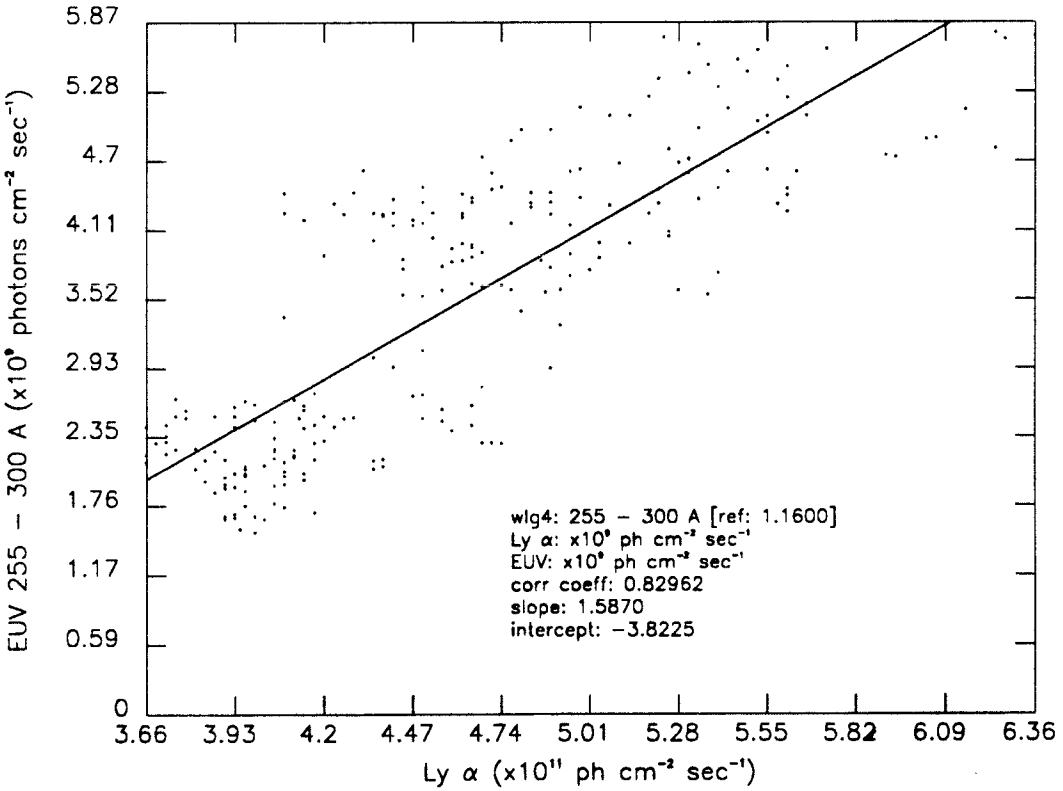

Figure 3.13 (d) **Lyman-α and 255-300 Å correlation.**

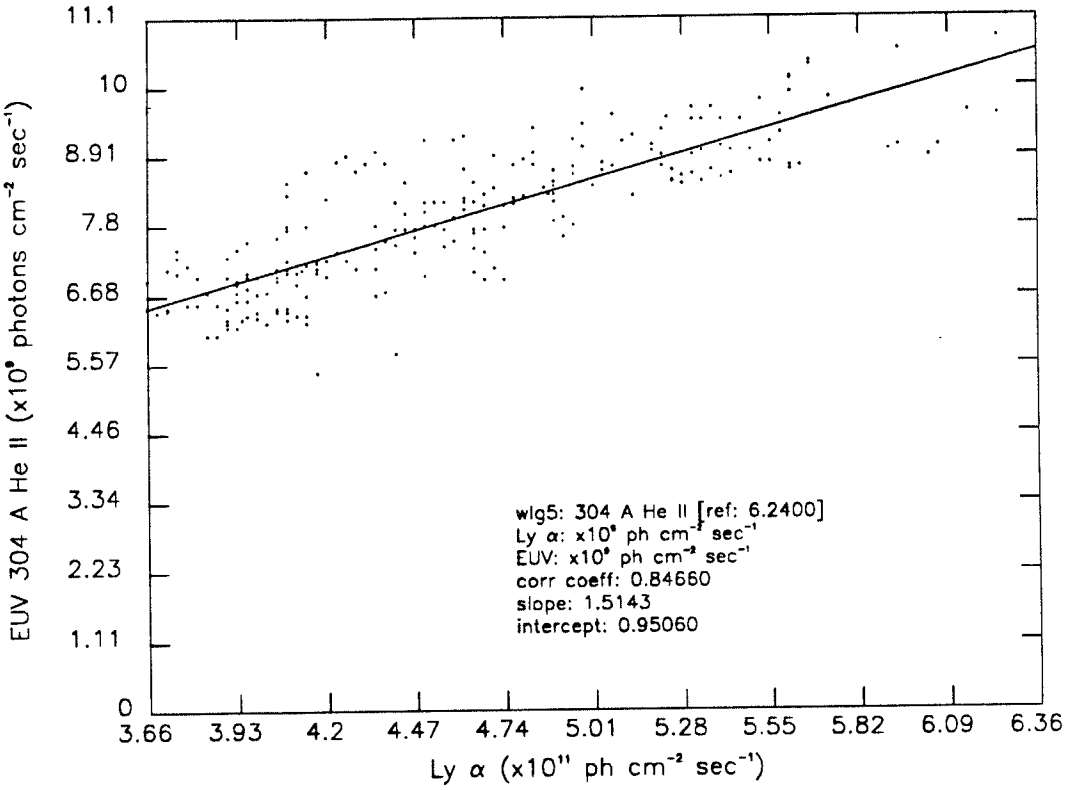

Figure 3.13 (e) **Lyman-α and 304 Å (He II) correlation.**

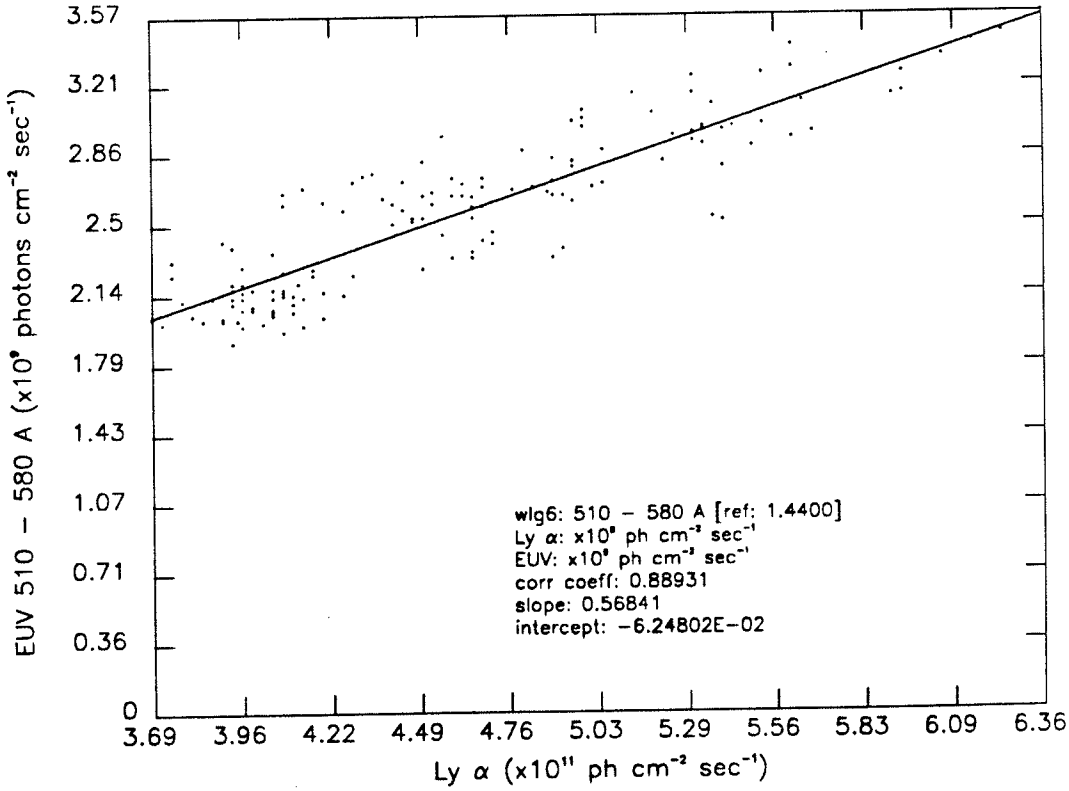

Figure 3.13 (f) **Lyman-α and 510-580 Å correlation.**

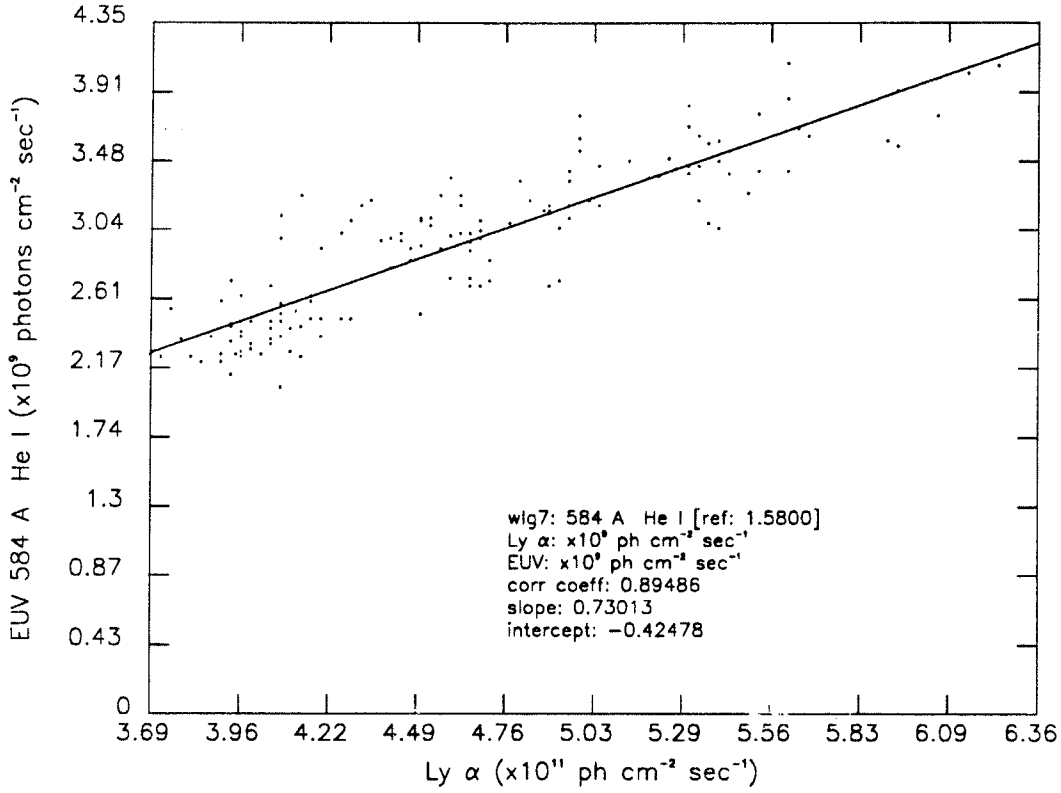

Figure 3.13 (g) **Lyman-α and 584 Å (He I) correlation.**

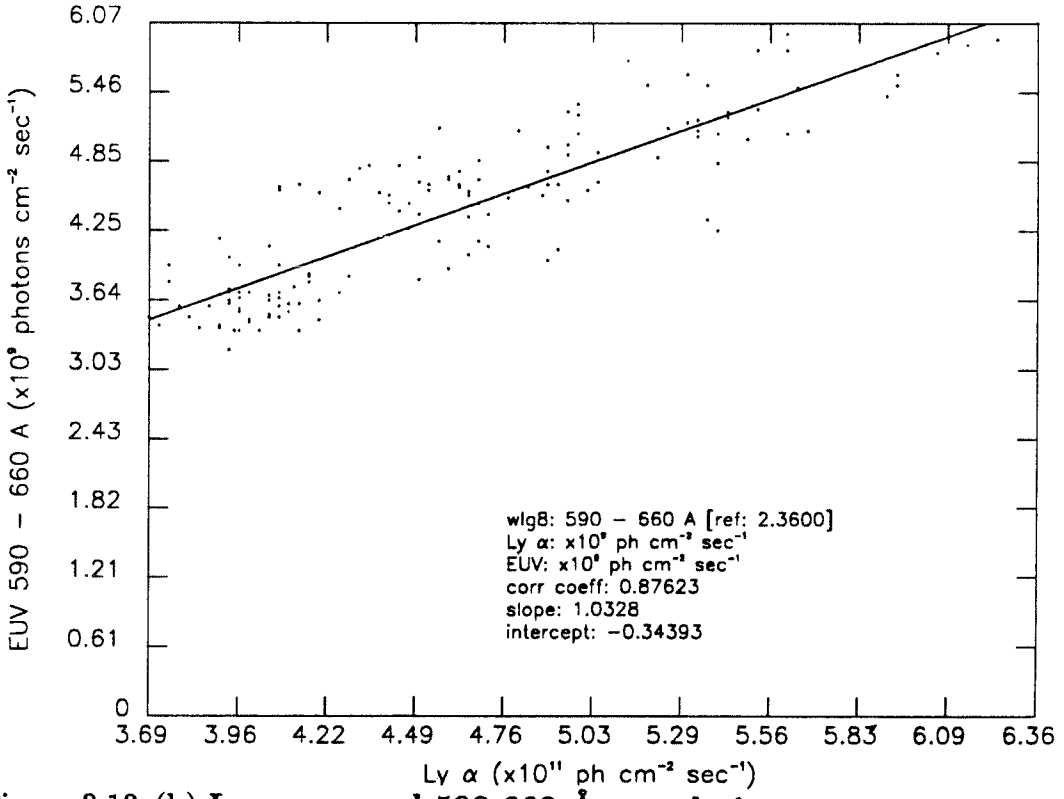

Figure 3.13 (h) **Lyman-α and 590-660 Å correlation.**

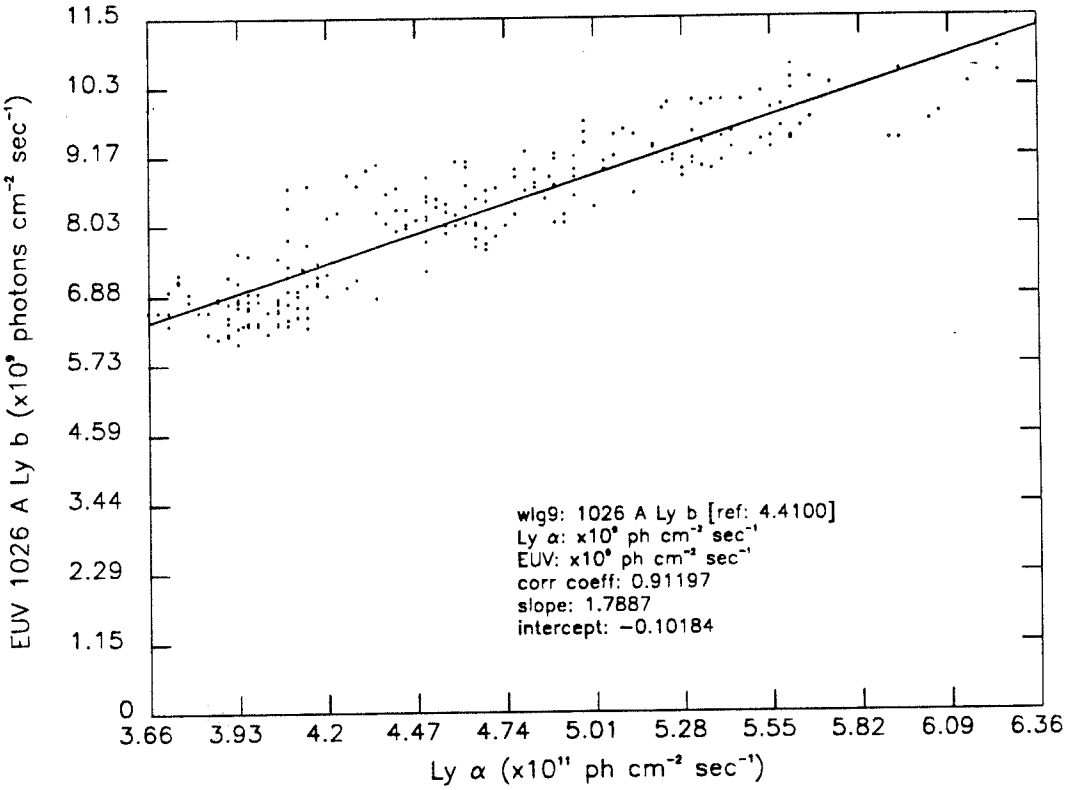

Figure 3.13 (i) **Lyman-α and 1026 Å (Lyman-β) correlation.**

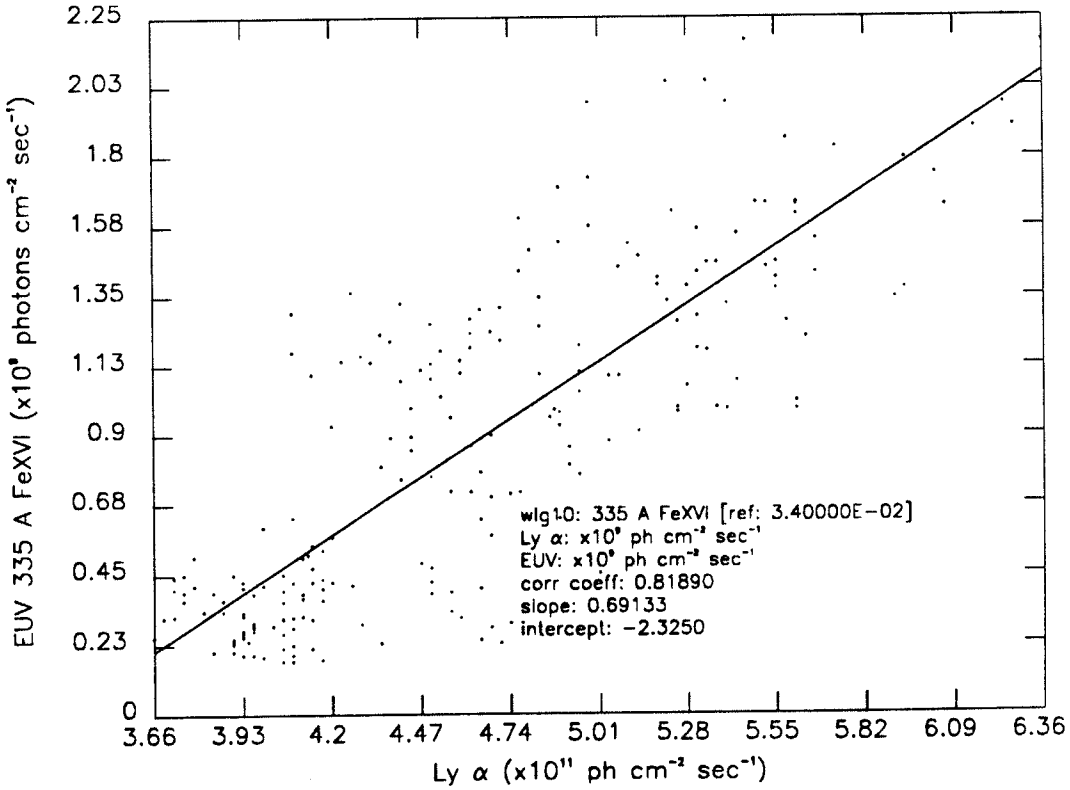

Figure 3.13 (j) **Lyman-α and 335 Å (Fe XVI) correlation.**

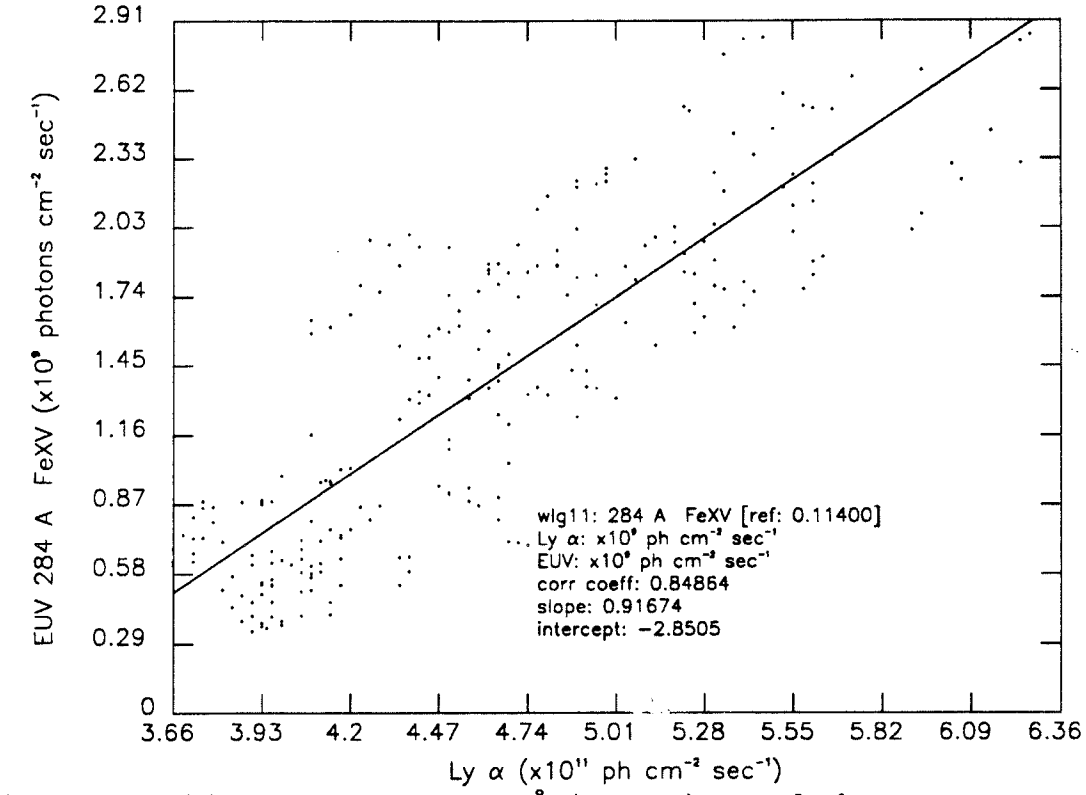

Figure 3.13 (k) **Lyman-α and 284 Å (Fe XV) correlation.**

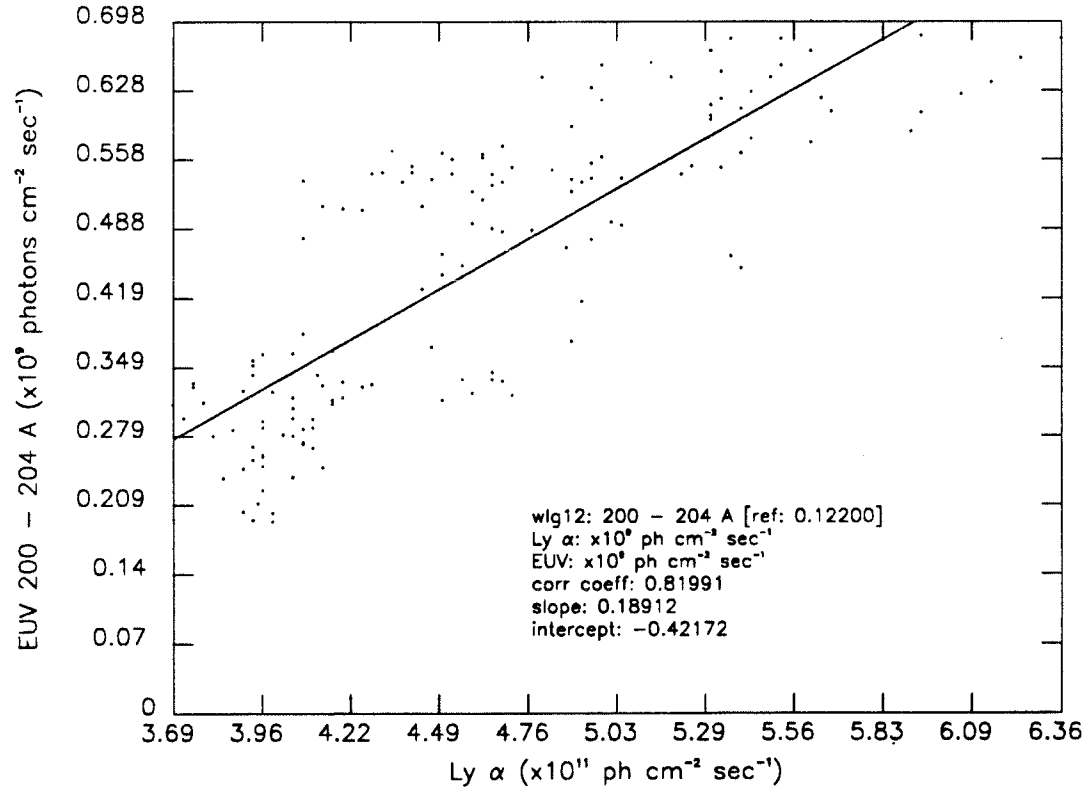

Figure 3.13 (l) **Lyman-α and 200-204 Å correlation.**

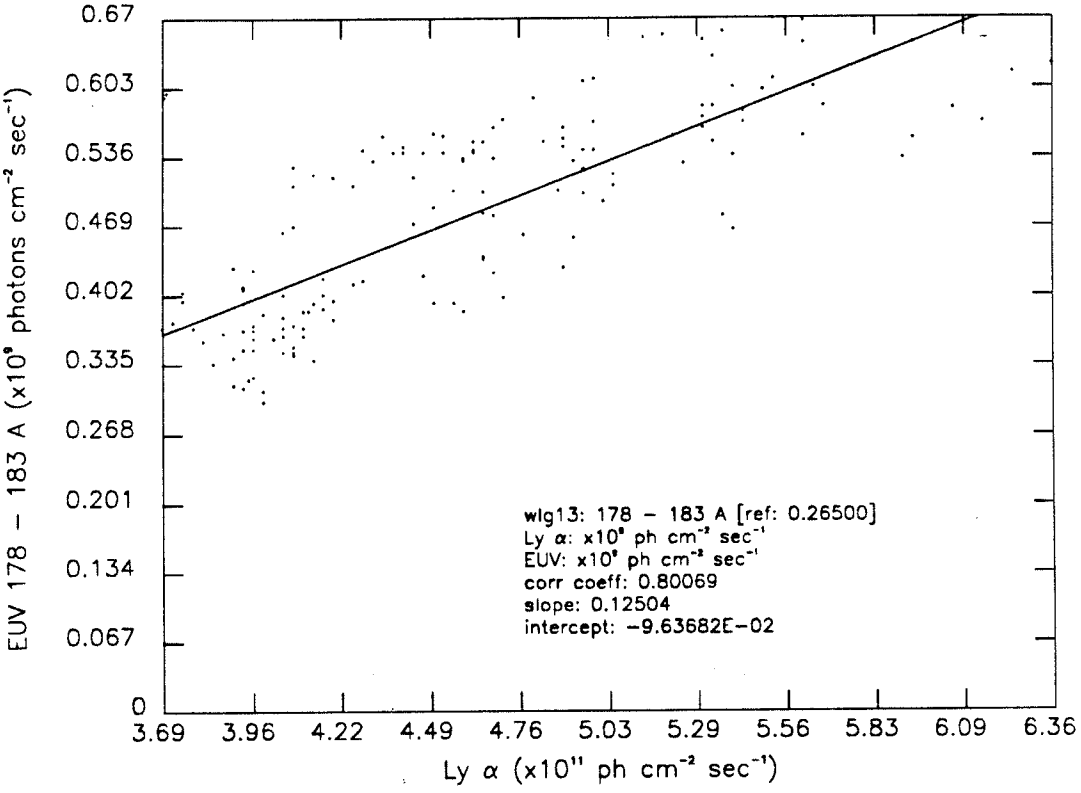

Figure 3.13 (m) **Lyman-α and 178-183 Å correlation.**

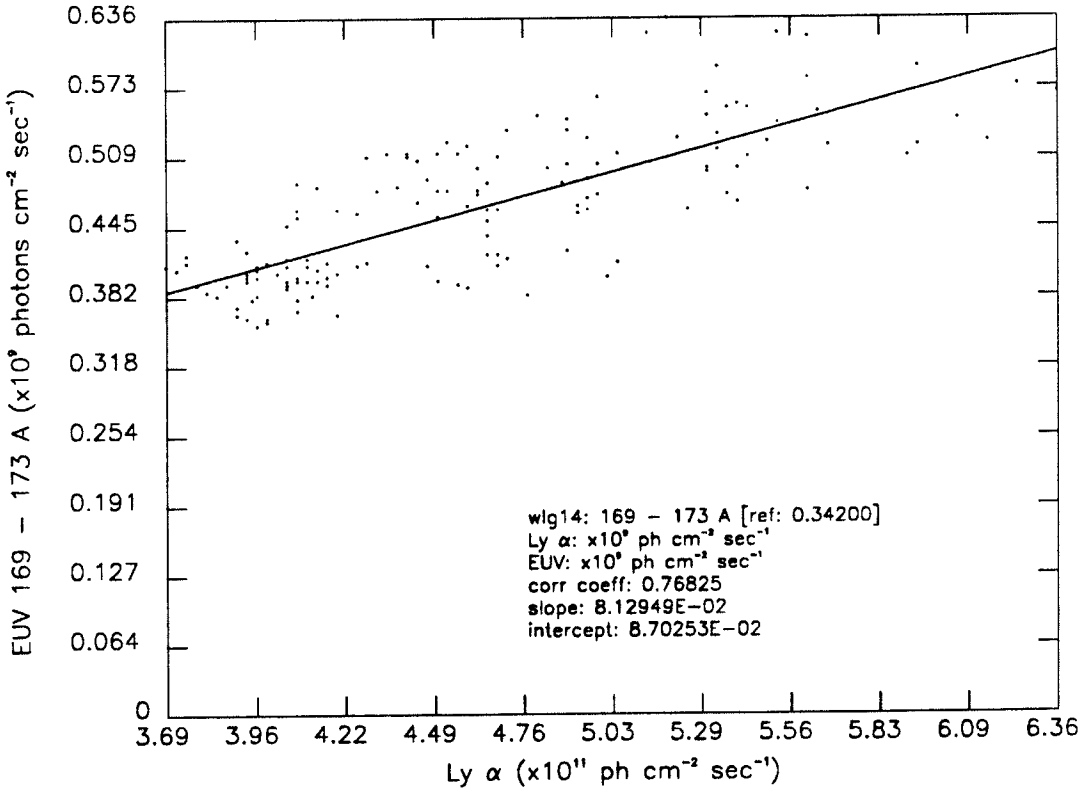

Figure 3.13 (n) **Lyman-α and 169-173 Å correlation.**

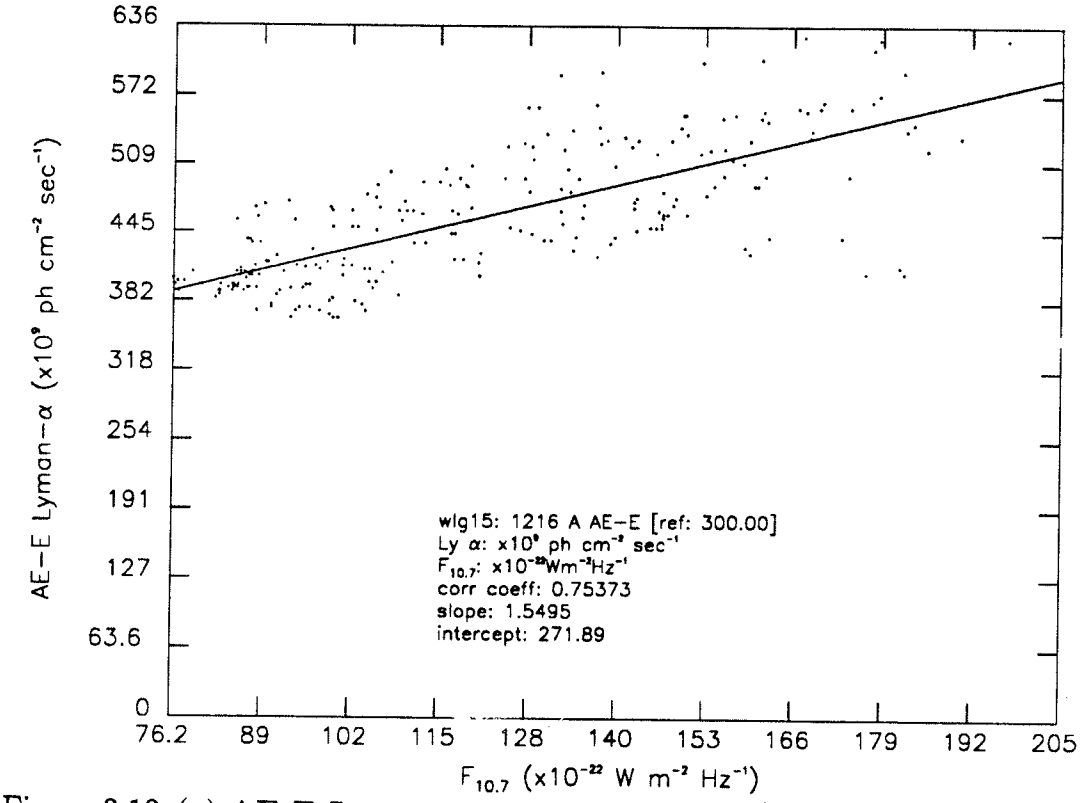

Figure 3.13 (o) **AE-E Lyman-α and $F_{10.7}$ correlation.**

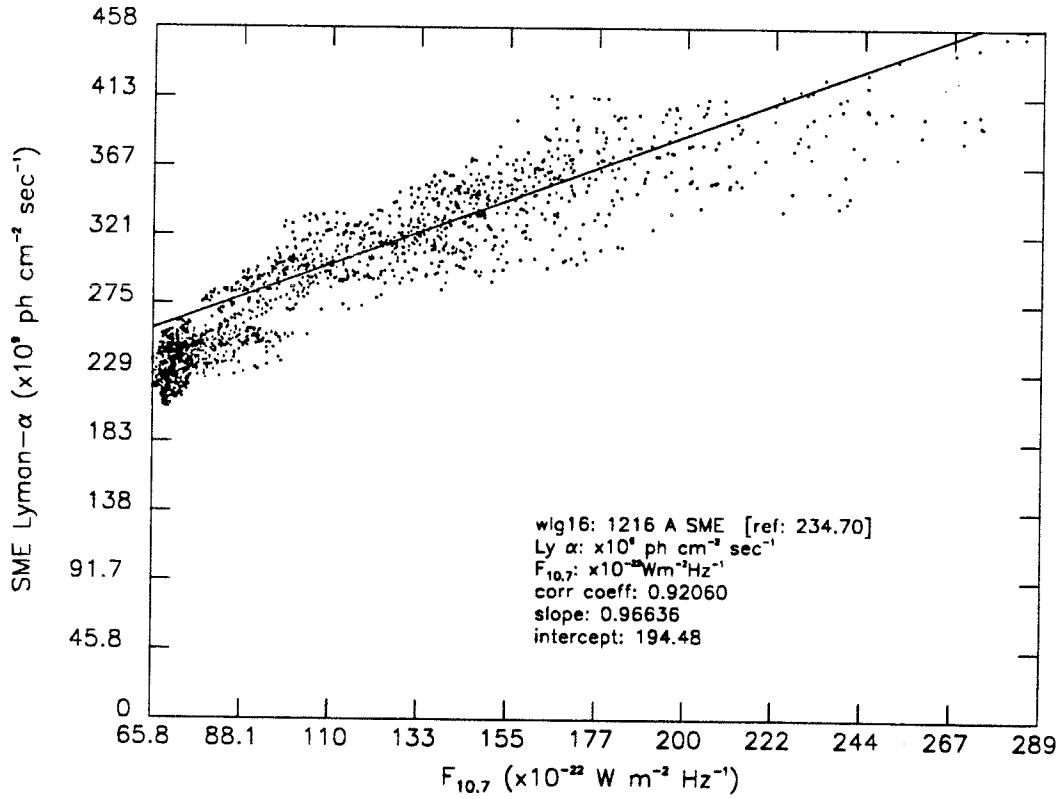

Figure 3.13 (p) **SME Lyman-α and $F_{10.7}$ correlation.**

is strongly influenced by the long-term trends in the datasets. The short-term correlations are much worse. Figures 3.14a - 3.14n show similar correlations between the AE-E EUV fluxes and $F_{10.7}$. Table 3.8 lists the $F_{10.7}$ and EUV flux correlations and may be compared with Table 3.7. From the evidence in these 30 figures and two tables, the following conclusions can be reached. Except for a 27-day periodicity in the all the datasets resulting from the solar rotation, there seems to be no good indicator of short-term EUV fluxes in either the Lyman-α or the $F_{10.7}$. Over the rising portion of the solar cycle 21, $F_{10.7}$ correlates with the long-term variation in the solar flux from the 169-173 Å, 178-183 Å, 168-190 Å, 190-206 Å, 200-204 Å, 206-255 Å, 284 Å, 255-300 Å, and 335 Å emissions. These correlations are 0.86, 0.87, 0.89, 0.88, 0.88, 0.91, 0.92, 0.91, and 0.95, respectively. Lyman-α correlates with the long-term flux from the 510-580 Å, 584 Å, and 590-660 Å emissions. These correlations are

TABLE 3.7. EUV[a] AND LYMAN-α[a] CORRELATIONS

	EUV Wavelength (Å)	Solar minimum[a]	Intercept[a]	Slope	Correlation coefficient
1	168-190	1.380	-0.252	0.550	0.800
2	190-206	0.490	-0.990	0.519	0.814
3	206-255	0.850	-1.345	0.717	0.821
4	255-300	1.160	-3.822	1.587	0.830
5	304	6.240	0.950	1.514	0.847
6	510-580	1.440	-0.062	0.568	0.889
7	584	1.580	-0.424	0.730	0.895
8	590-660	2.360	-0.343	1.032	0.876
9	1026	4.410	-0.101	1.788	0.912
10	335	0.034	-2.325	0.691	0.819
11	284	0.114	-2.850	0.916	0.849
12	200-204	0.122	-0.421	0.189	0.820
13	178-183	0.265	-0.096	0.125	0.801
14	169-173	0.342	0.087	0.081	0.768
15	AE-E Lyman-α-$F_{10.7}$	300.0	271.89	1.5495	0.754
16	SME Lyman-α-$F_{10.7}$	234.7	194.48	0.9663	0.921

[a] $\times 10^9$ photons cm^{-2} sec^{-1}.

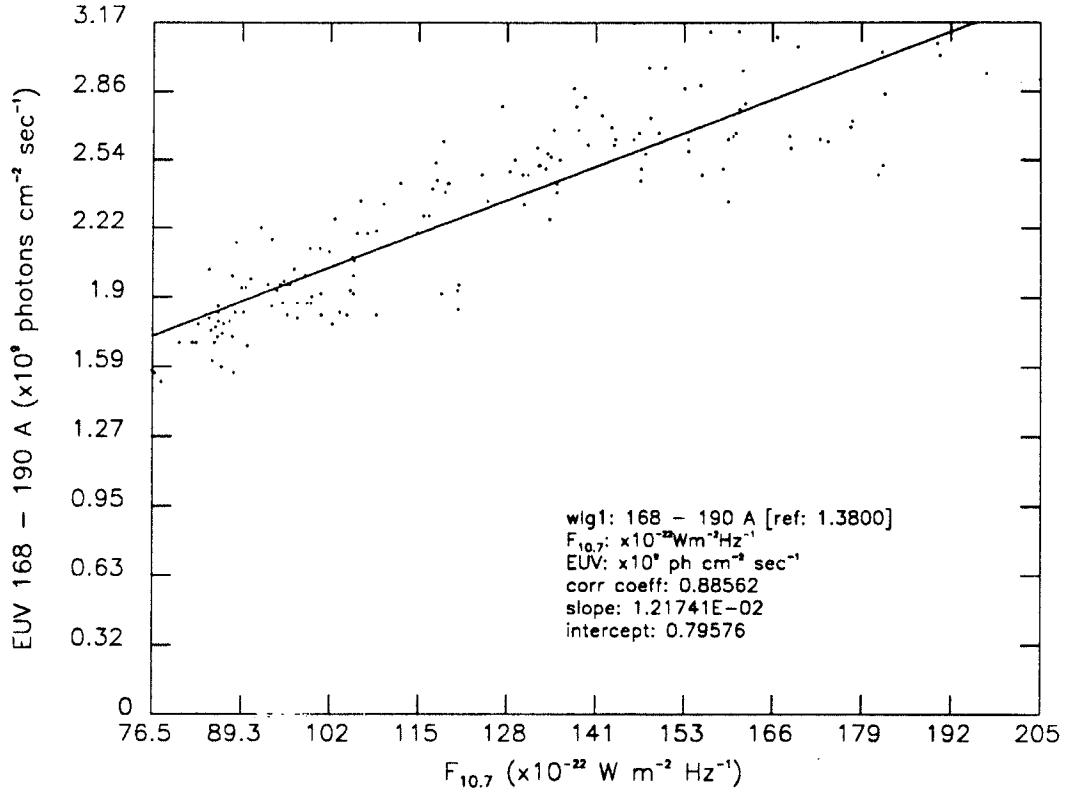

Figure 3.14 (a) $F_{10.7}$ and 168-190 Å correlation.

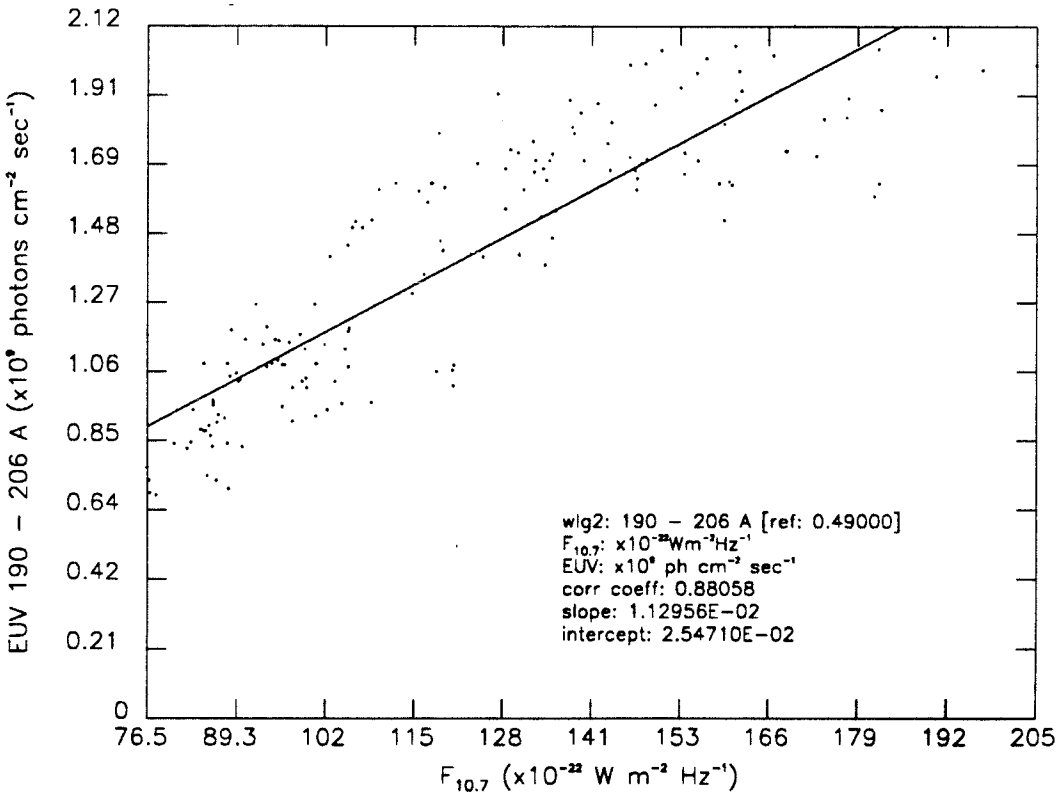

Figure 3.14 (b) $F_{10.7}$ and 190-206 Å correlation.

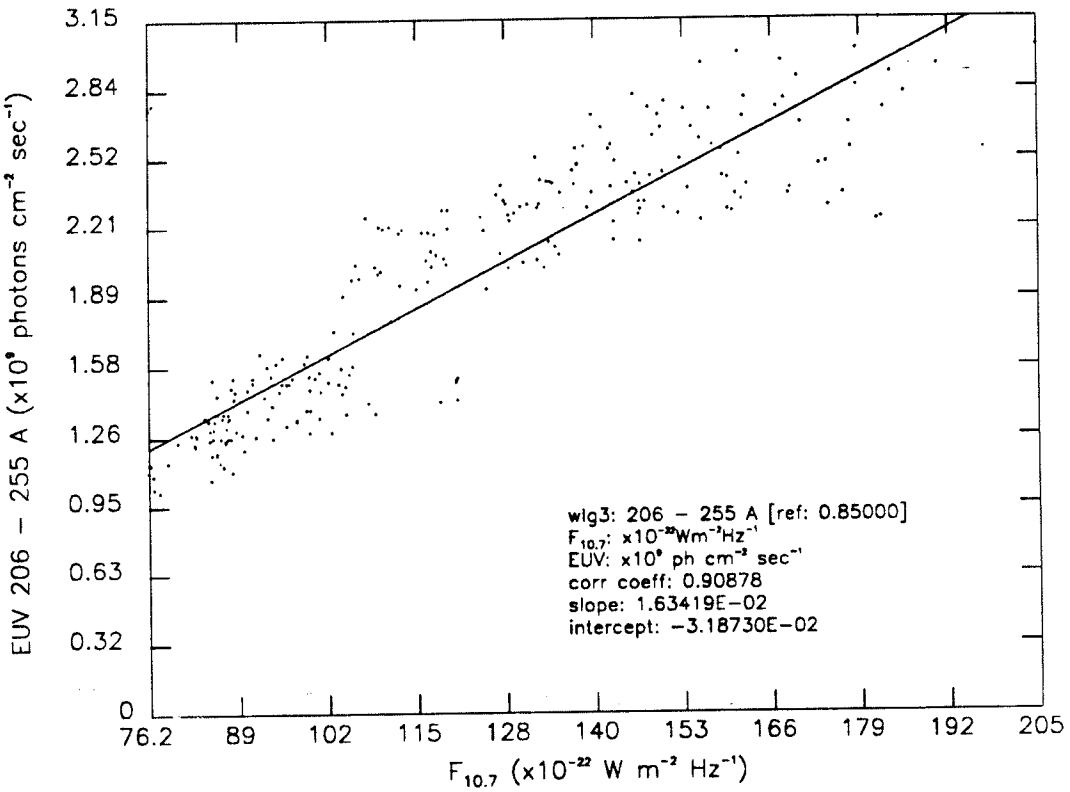

Figure 3.14 (c) $F_{10.7}$ **and 206-255 Å correlation.**

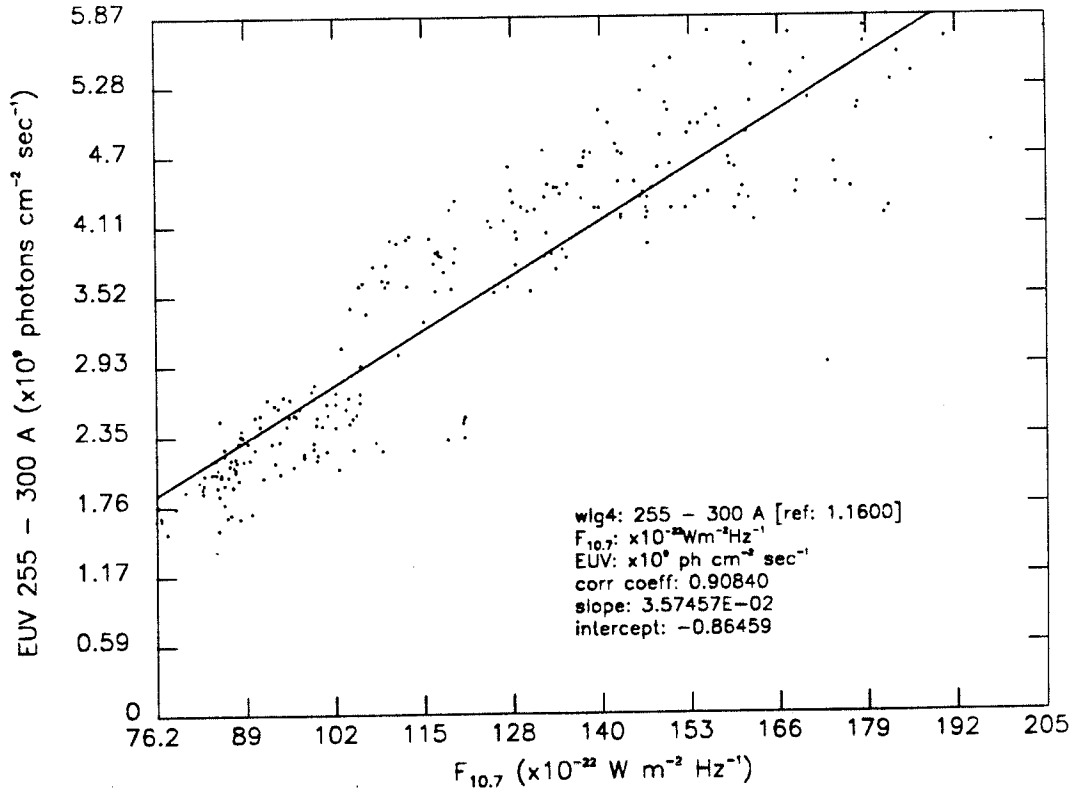

Figure 3.14 (d) $F_{10.7}$ **and 255-300 Å correlation.**

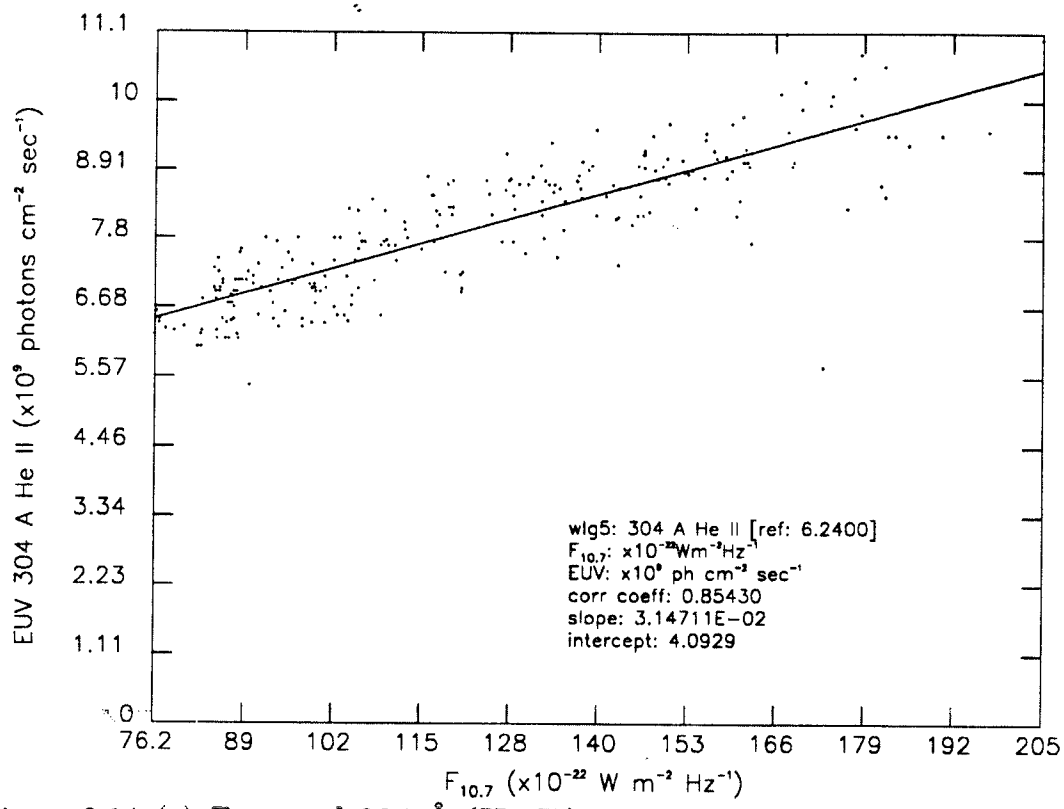

Figure 3.14 (e) $F_{10.7}$ **and 304 Å (He II) correlation.**

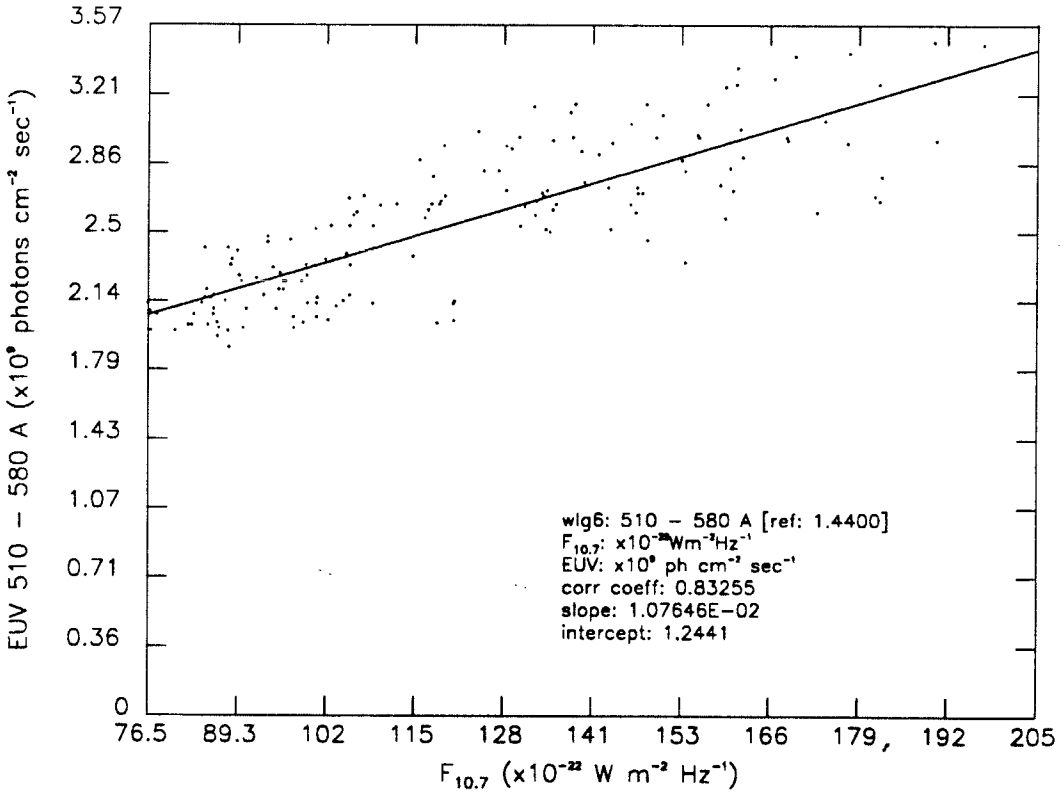

Figure 3.14 (f) $F_{10.7}$ **and 510-580 Å correlation.**

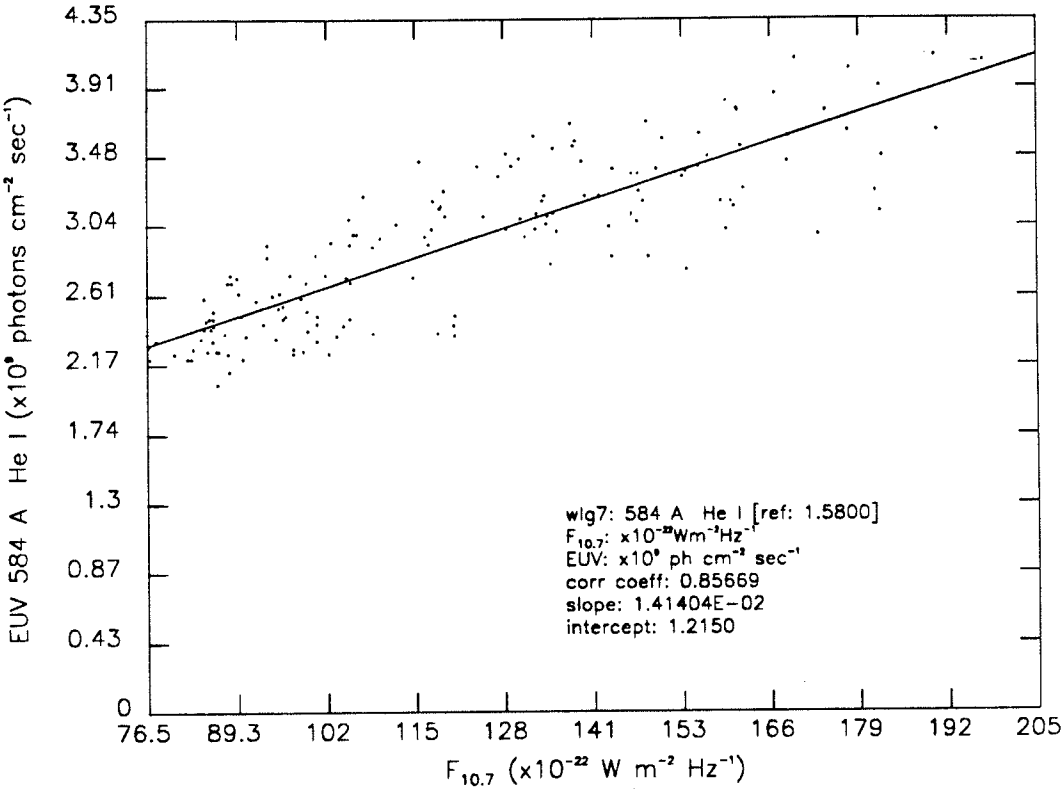

Figure 3.14 (g) $F_{10.7}$ **and 584 Å (He I) correlation.**

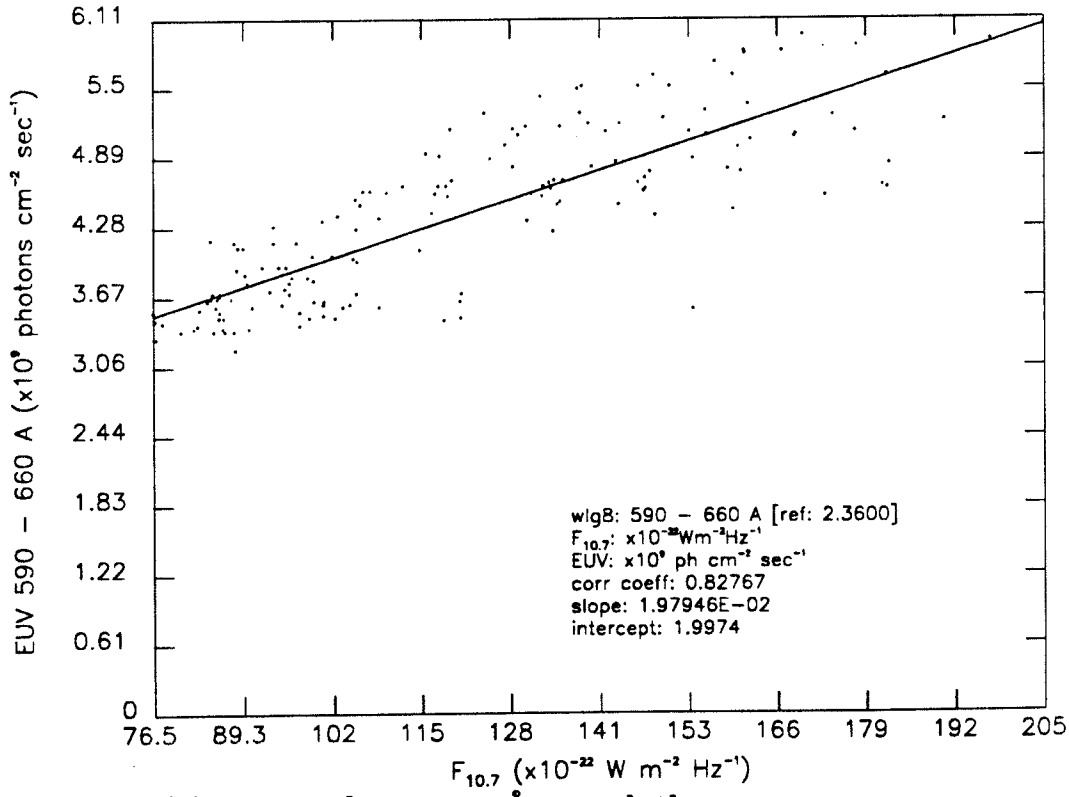

Figure 3.14 (h) $F_{10.7}$ **and 590-660 Å correlation.**

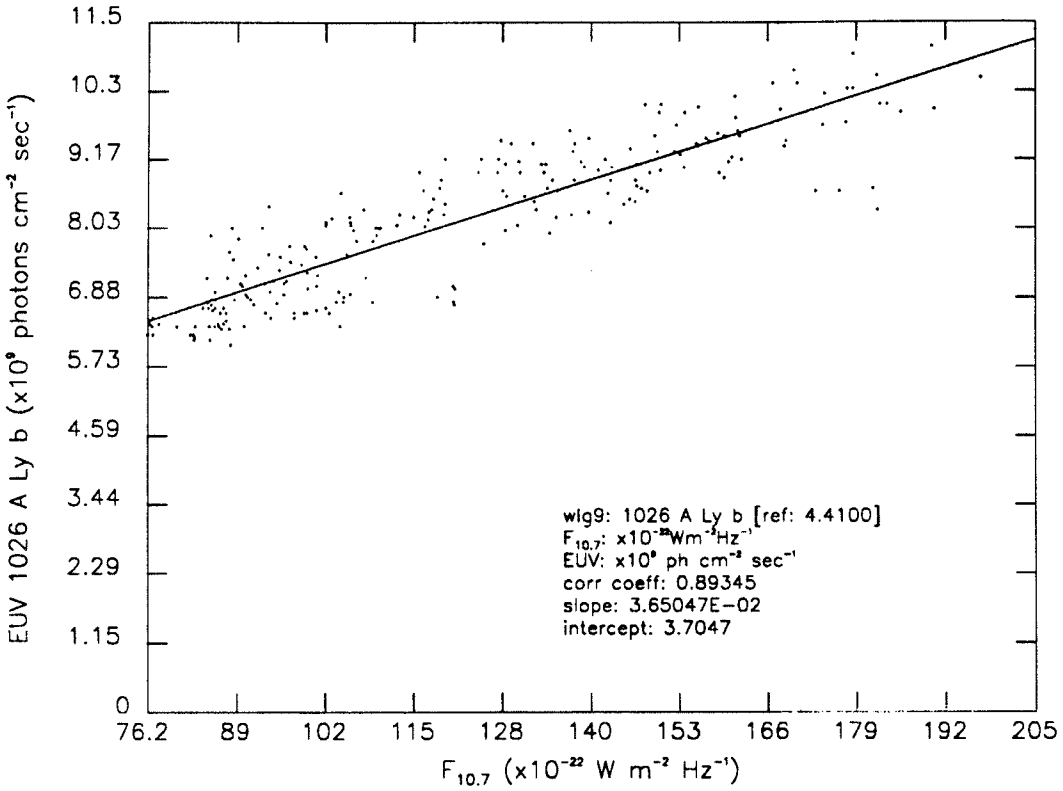

Figure 3.14 (i) $F_{10.7}$ **and 1026 Å (Lyman-β) correlation.**

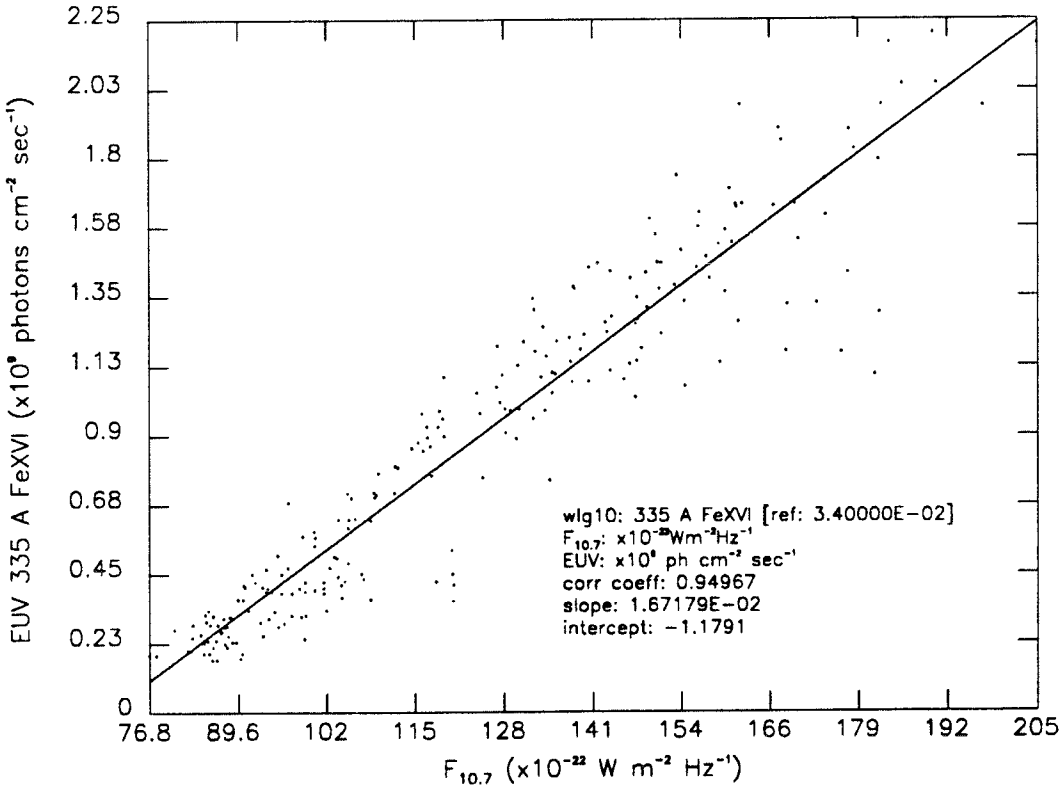

Figure 3.14 (j) $F_{10.7}$ **and 335 Å (Fe XVI) correlation.**

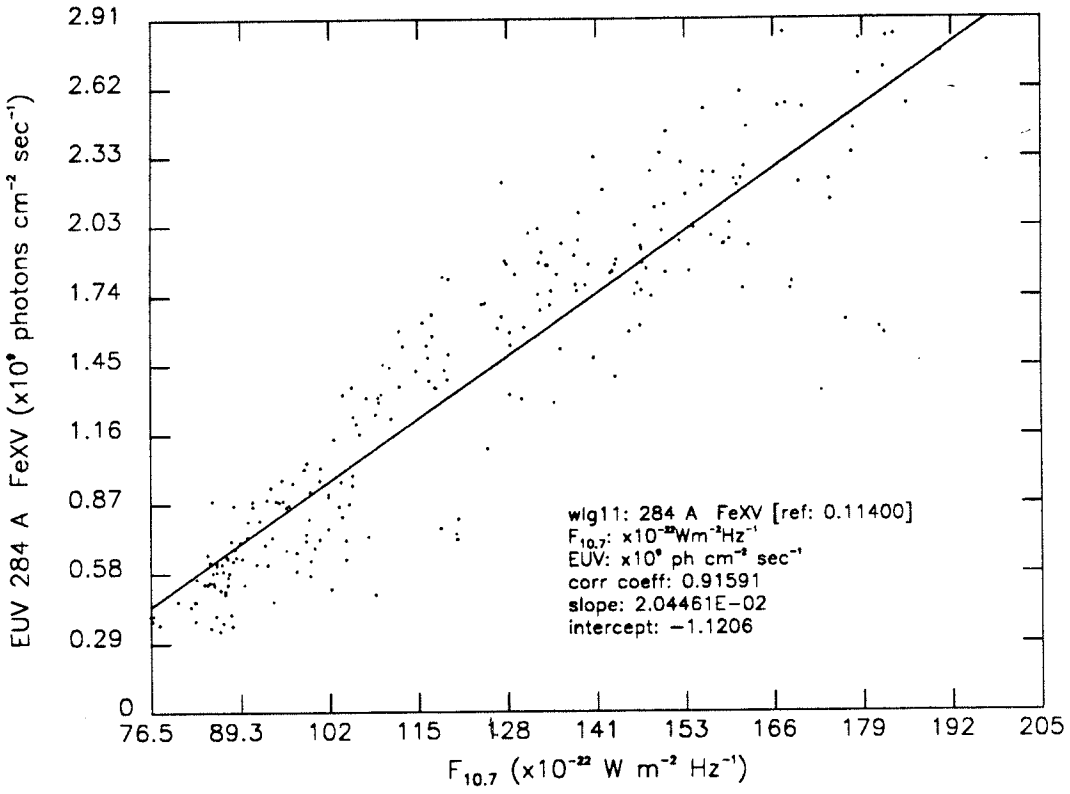

Figure 3.14 (k) $F_{10.7}$ and 284 Å (Fe XV) correlation.

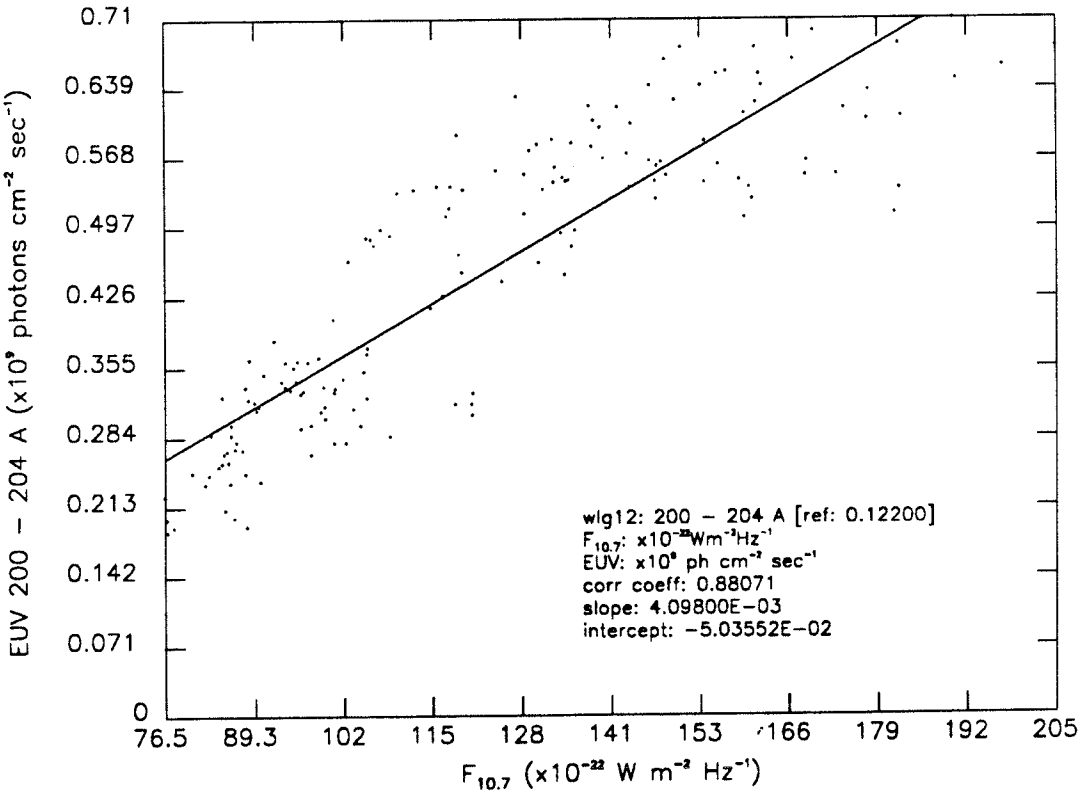

Figure 3.14 (l) $F_{10.7}$ and 200-204 Å correlation.

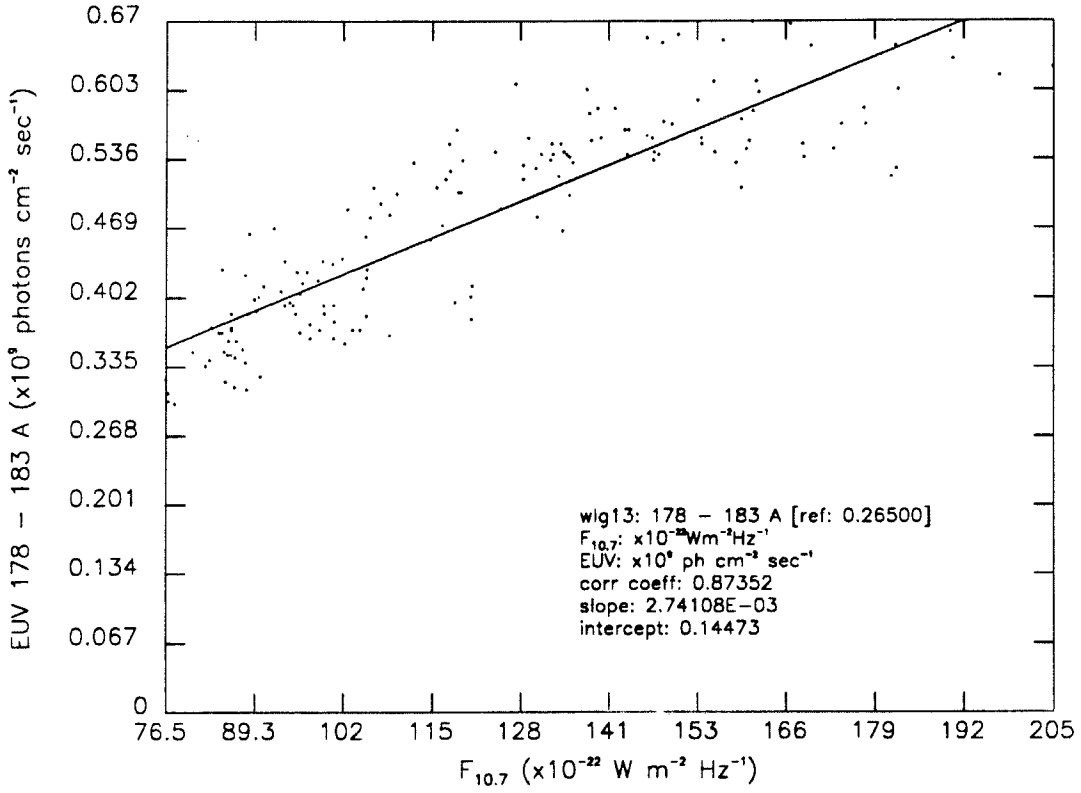

Figure 3.14 (m) $F_{10.7}$ **and 178-183 Å correlation.**

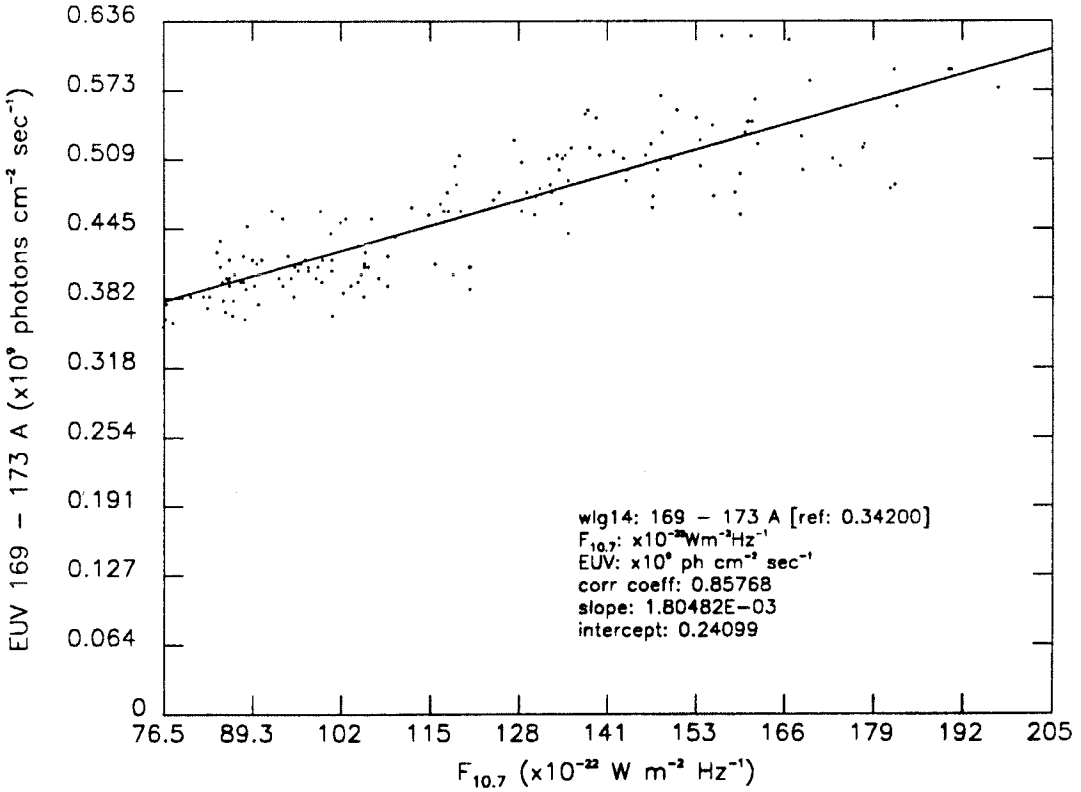

Figure 3.14 (n) $F_{10.7}$ **and 169-173 Å correlation.**

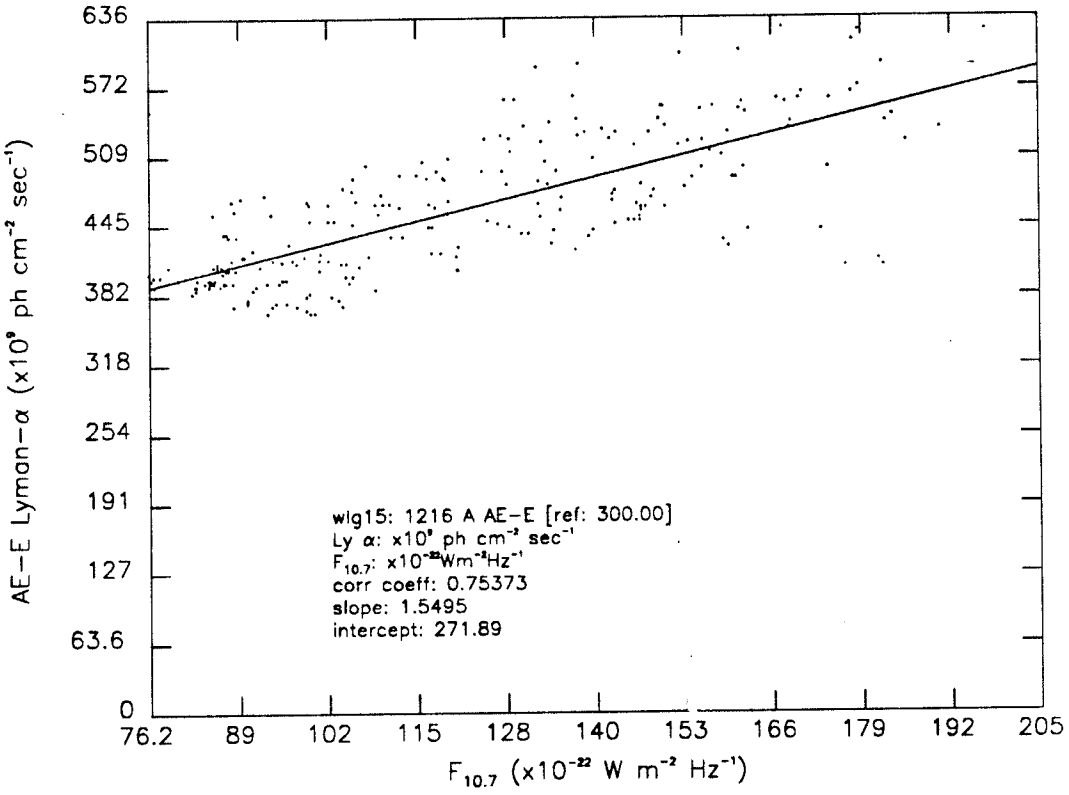

Figure 3.14 (o) **AE-E Lyman-α and $F_{10.7}$ correlation.**

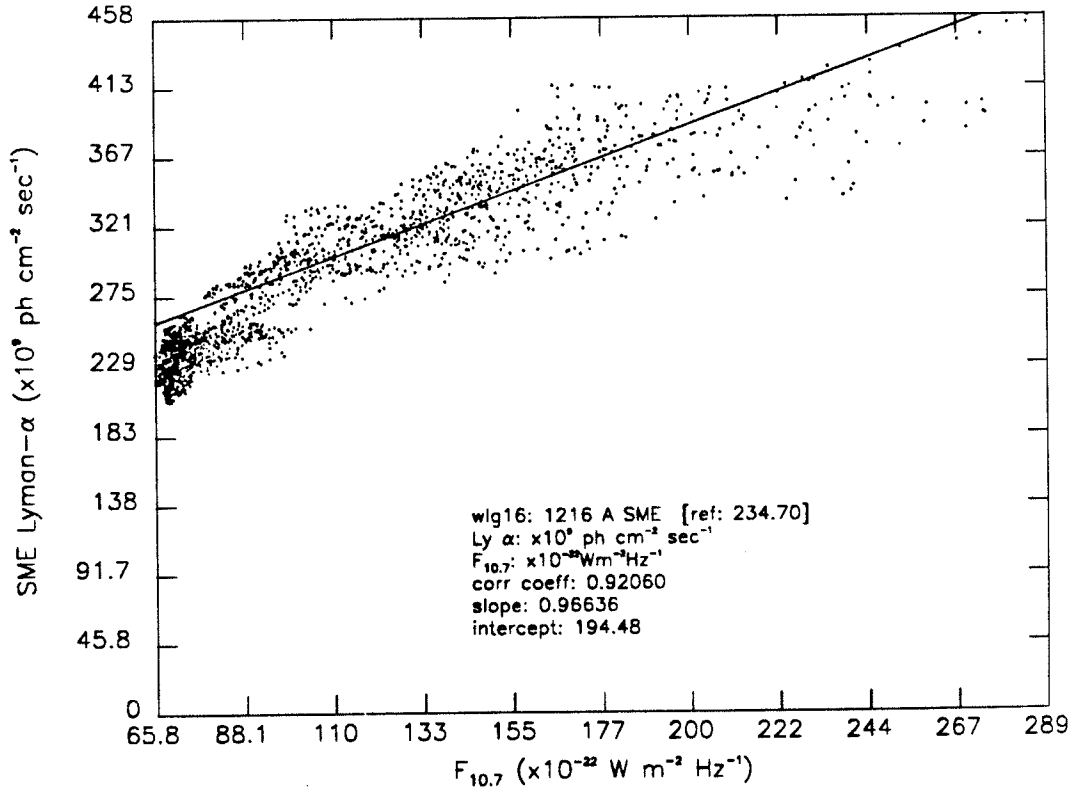

Figure 3.14 (p) **SME Lyman-α and $F_{10.7}$ correlation.**

0.89, 0.89, and 0.88, respectively. Both Lyman-α and $F_{10.7}$ correlate strongly with He II and H Lyman-β emissions, although Lyman-α has a slightly greater long-term correlation coefficient than the $F_{10.7}$. The Lyman-α coefficient of correlation with He II and Lyman-β is 0.85 and 0.91, respectively, while the $F_{10.7}$ correlation coefficient is 0.85 and 0.89, respectively. The lowest correlation with Lyman-α is 169-173 Å (0.77; transition region) and the lowest correlation with $F_{10.7}$ is 590-660 Å (0.83; chromosphere, transition region, and cool corona).

These results indicate that on time scales of several solar rotations with rising activity the $F_{10.7}$ can be used as an indicator of transition region - cool coronal emissions and the Lyman-α can be used as an indicator of the chromospheric emissions. Whether a comparable representation occurs for waning solar activity and relatively stable (i.e., high or low) activity has not

TABLE 3.8. EUV[a] AND $F_{10.7}$[b] CORRELATIONS

	EUV Wavelength (Å)	Solar minimum[a]	Intercept[a]	Slope	Correlation coefficient
1	168-190	1.380	0.795	0.012	0.886
2	190-206	0.490	0.025	0.011	0.881
3	206-255	0.850	-0.031	0.016	0.909
4	255-300	1.160	-0.864	0.035	0.908
5	304	6.240	4.092	0.031	0.854
6	510-580	1.440	1.244	0.010	0.833
7	584	1.580	1.215	0.014	0.857
8	590-660	2.360	1.997	0.019	0.828
9	1026	4.410	3.704	0.036	0.893
10	335	0.034	-1.179	0.016	0.950
11	284	0.114	-1.120	0.020	0.916
12	200-204	0.122	-0.050	0.004	0.881
13	178-183	0.265	0.144	0.002	0.874
14	169-173	0.342	0.241	0.001	0.858
15	AE-E Lyman-α-$F_{10.7}$	300.0	271.89	1.5495	0.754
16	SME Lyman-α-$F_{10.7}$	234.7	194.48	0.9663	0.921

[a] $\times 10^{9}$ photons cm^{-2} sec^{-1}.
[b] $\times 10^{-22}$ W m^{-2} Hz^{-1}.

yet been definitely determined. An important question may be posed: do the full-disk coronal fluxes reach a long-term "quiet sun" threshold during solar minimum conditions, as suggested by $F_{10.7}$, or do they continue decreasing to a short-term minimum as suggested by Lyman-α? This question may be resolved by the study of purely coronal emissions such as the 1-8 Å X-ray flux when compared to $F_{10.7}$.

The 1-8 Å X-ray daily background flux, which is described in Chapter II, is correlated with the AE-E EUV data in Figures 3.15a - 3.15n. Table 3.9 compares with Tables 3.7 and 3.8, listing the 1-8 Å X-ray background flux correlated with the wavelengths and wavelength groups available in SC#21OBS. The natural logarithm of the 1-8 Å background flux for the period of July 1, 1977 through December 21, 1978 shows the highest long-term linear correla-

TABLE 3.9. EUV[a] AND 1-8 Å X-RAY[b] CORRELATIONS

	EUV Wavelength (Å)	Solar minimum[a]	Intercept[a]	Slope	Correlation coefficient
1	168-190	1.380	2.382	0.404	0.837
2	190-206	0.490	1.498	0.378	0.839
3	206-255	0.850	2.097	0.520	0.850
4	255-300	1.160	3.793	1.138	0.850
5	304	6.240	8.191	0.990	0.790
6	510-580	1.440	2.648	0.362	0.796
7	584	1.580	3.057	0.469	0.808
8	590-660	2.360	4.579	0.666	0.792
9	1026	4.410	8.473	1.206	0.842
10	335	0.034	1.004	0.542	0.880
11	284	0.114	1.549	0.652	0.864
12	200-204	0.122	0.484	0.137	0.839
13	178-183	0.265	0.502	0.091	0.833
14	169-173	0.342	0.476	0.059	0.801
15	Lyman-α	300.0	473.47	47.493	0.680
16	$F_{10.7}$	68[c]	129.62	31.319	0.887

[a] $\times 10^9$ photons cm^{-2} sec^{-1}.

[b] $ln(\text{X} - \text{rays} \times 10^{-5}$ photons cm^{-2} sec$^{-1})$.

[c] $\times 10^{-22}$ W m^{-2} Hz^{-1}.

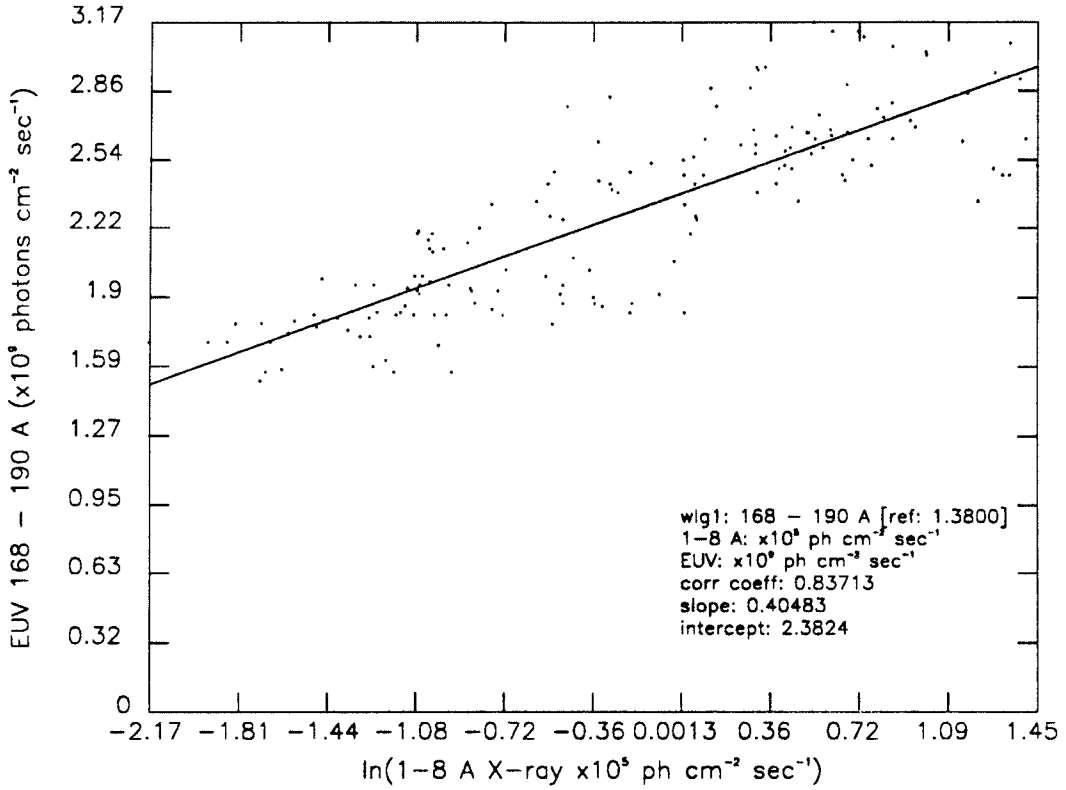

Figure 3.15 (a) **1-8 Å X-ray and 168-190 Å correlation.**

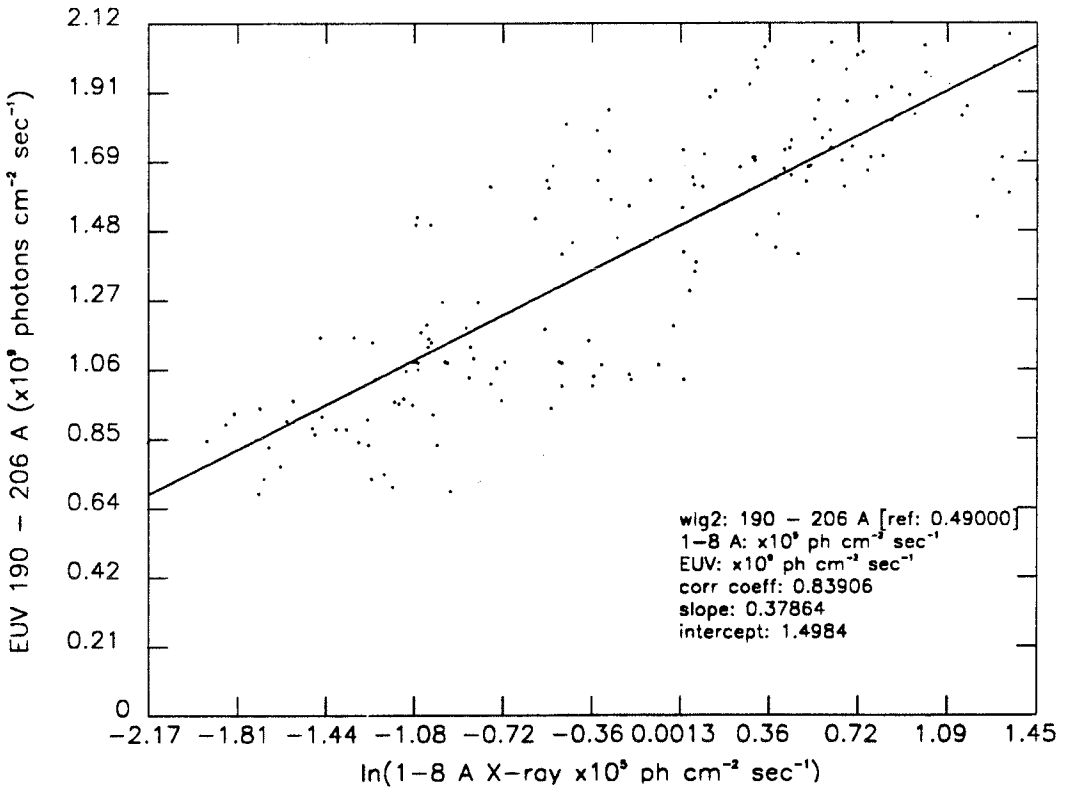

Figure 3.15 (b) **1-8 Å X-ray and 190-206 Å correlation.**

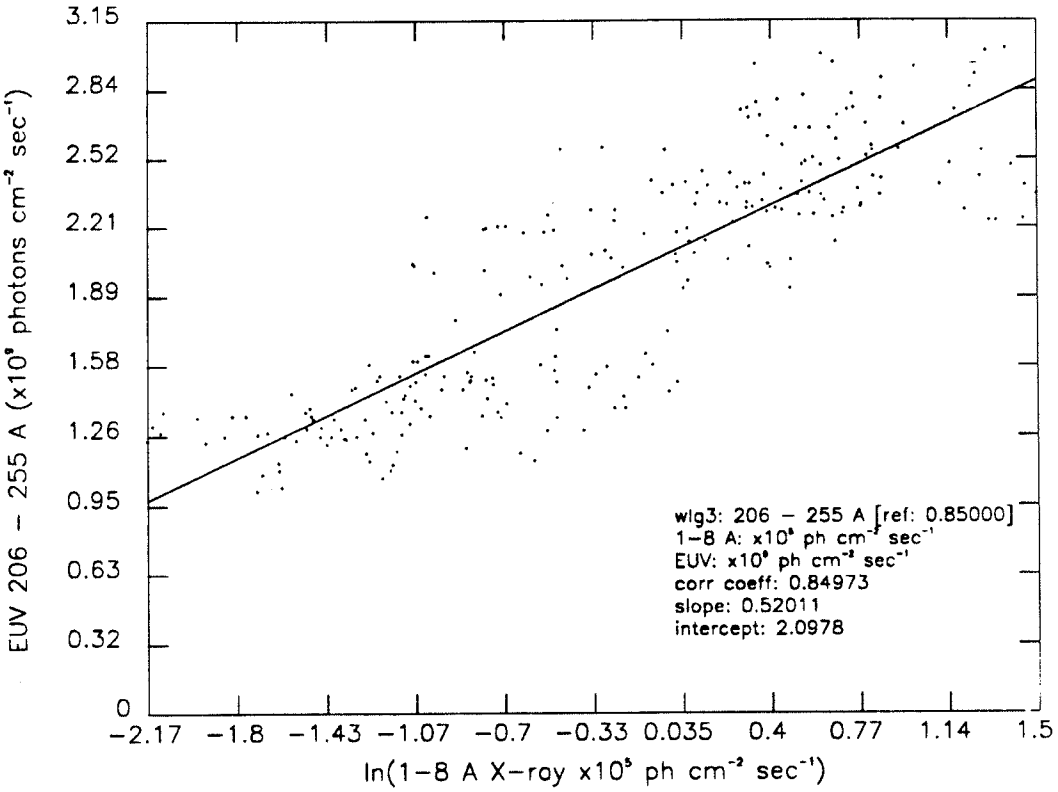

Figure 3.15 (c) **1-8 Å X-ray and 206-255 Å correlation.**

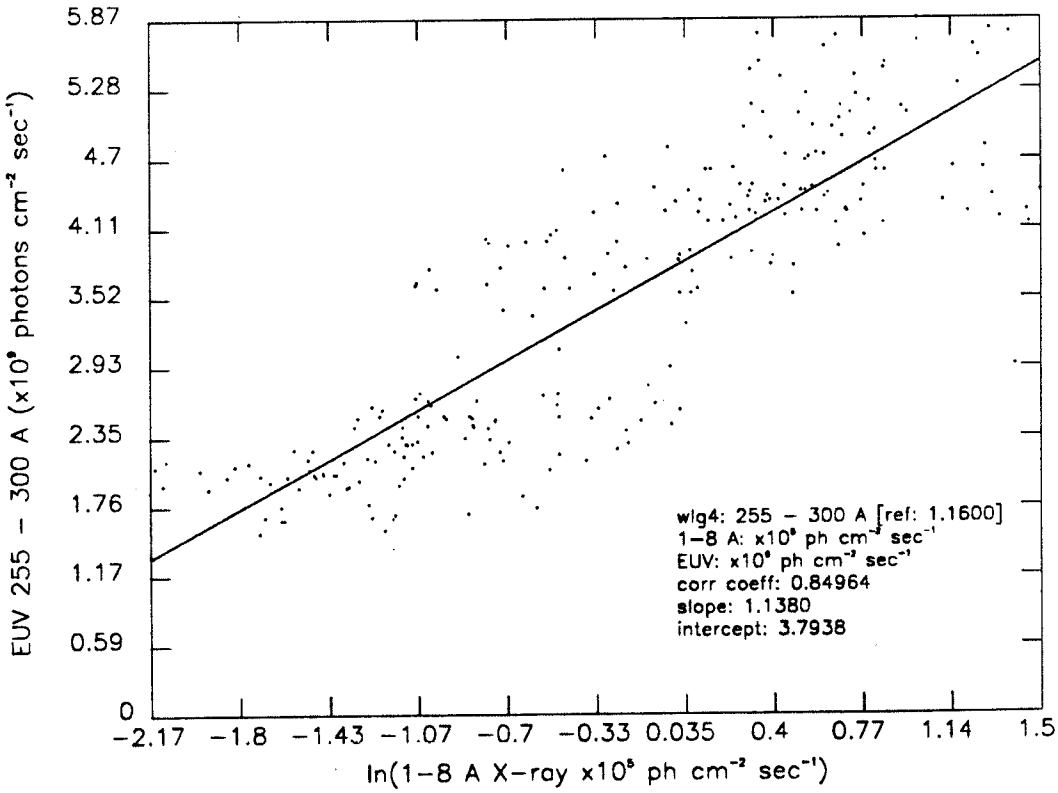

Figure 3.15 (d) **1-8 Å X-ray and 255-300 Å correlation.**

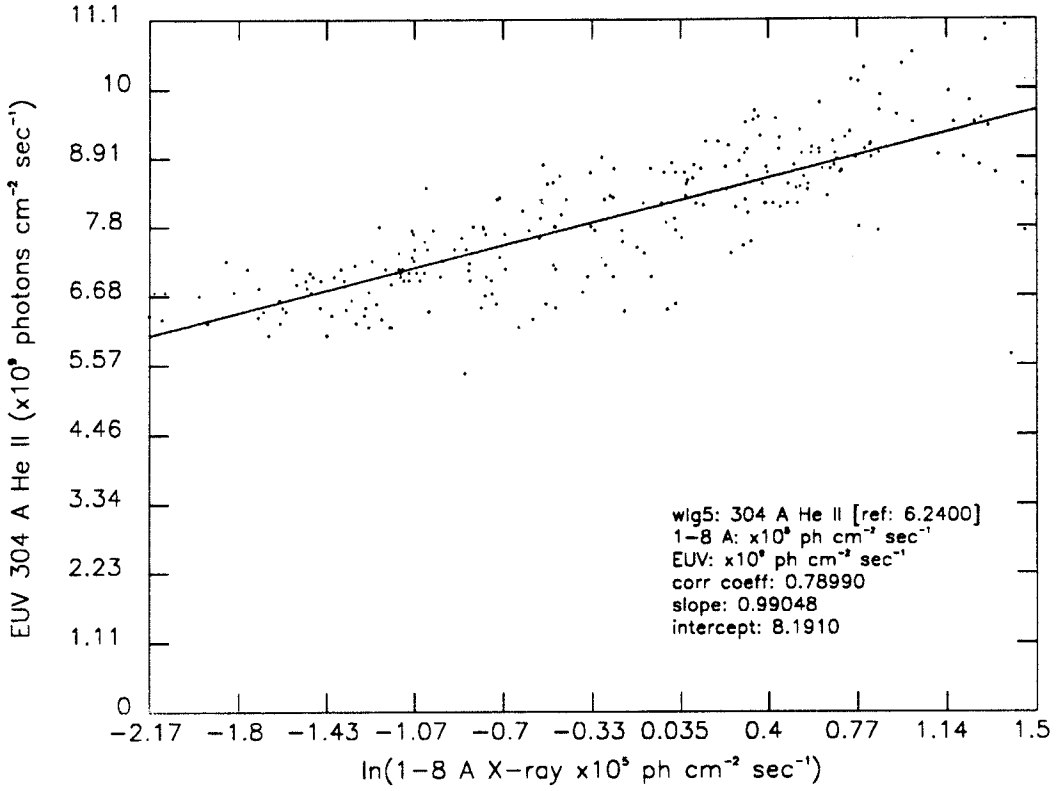

Figure 3.15 (e) **1-8 Å X-ray and 304 Å (He II) correlation.**

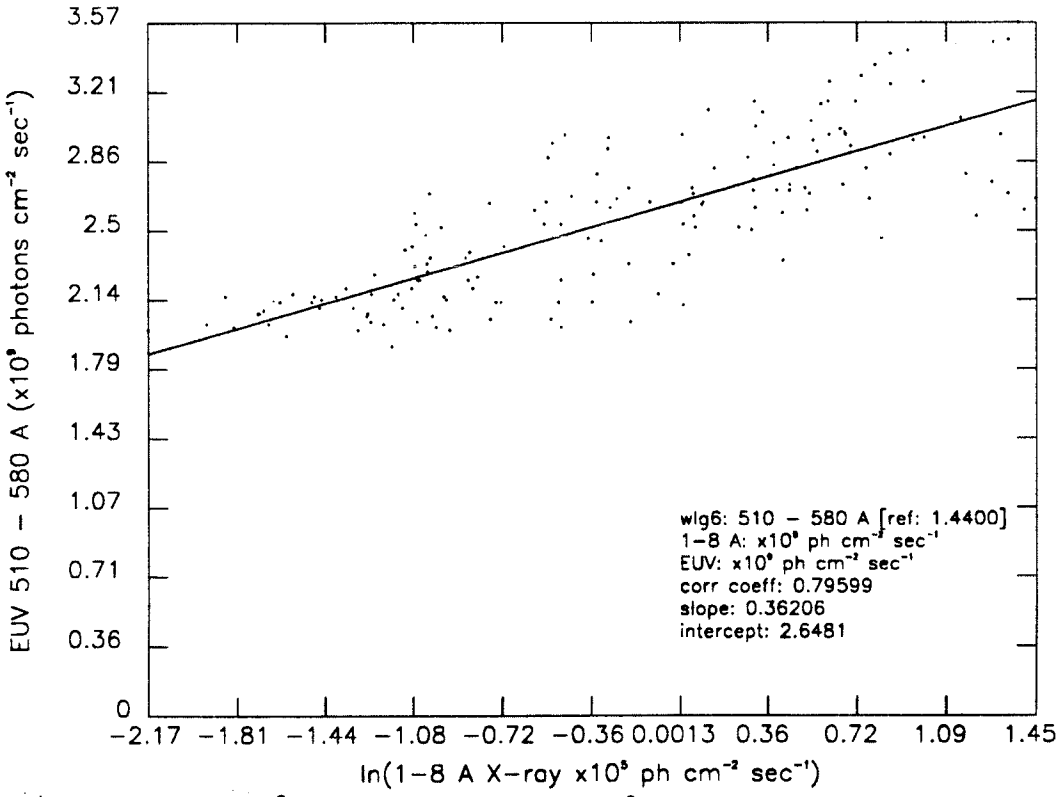

Figure 3.15 (f) **1-8 Å X-ray and 510-580 Å correlation.**

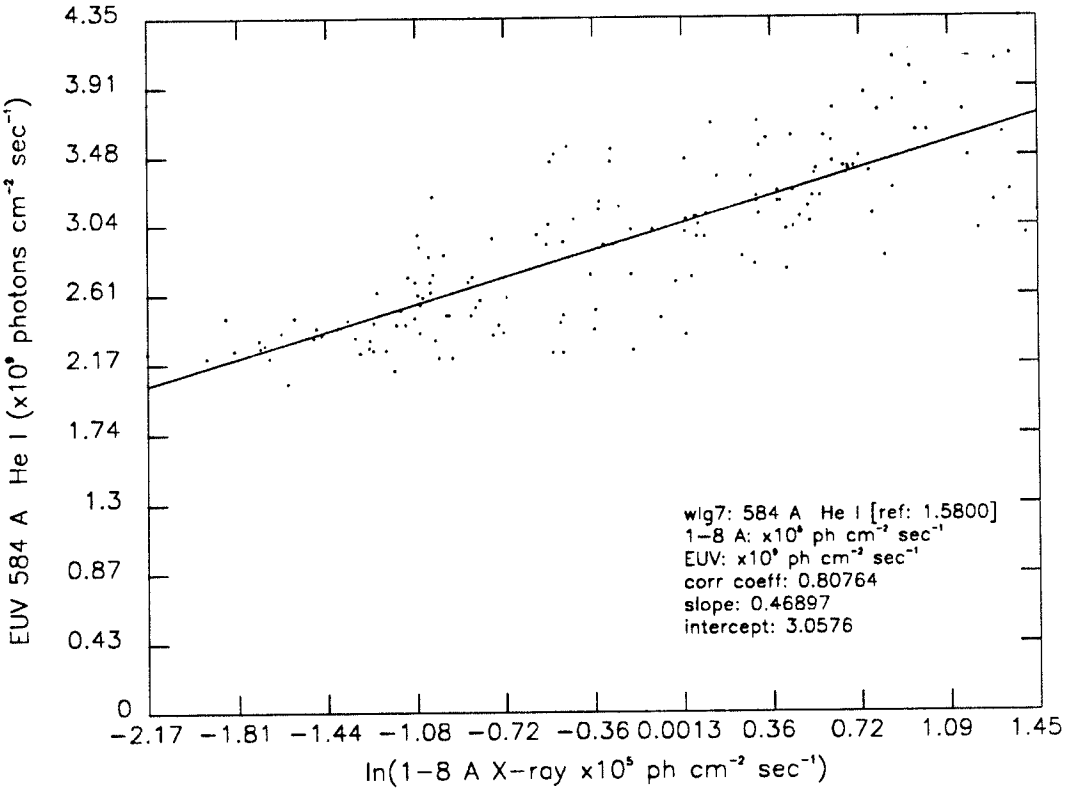

Figure 3.15 (g) 1-8 Å X-ray and 584 Å (He I) correlation.

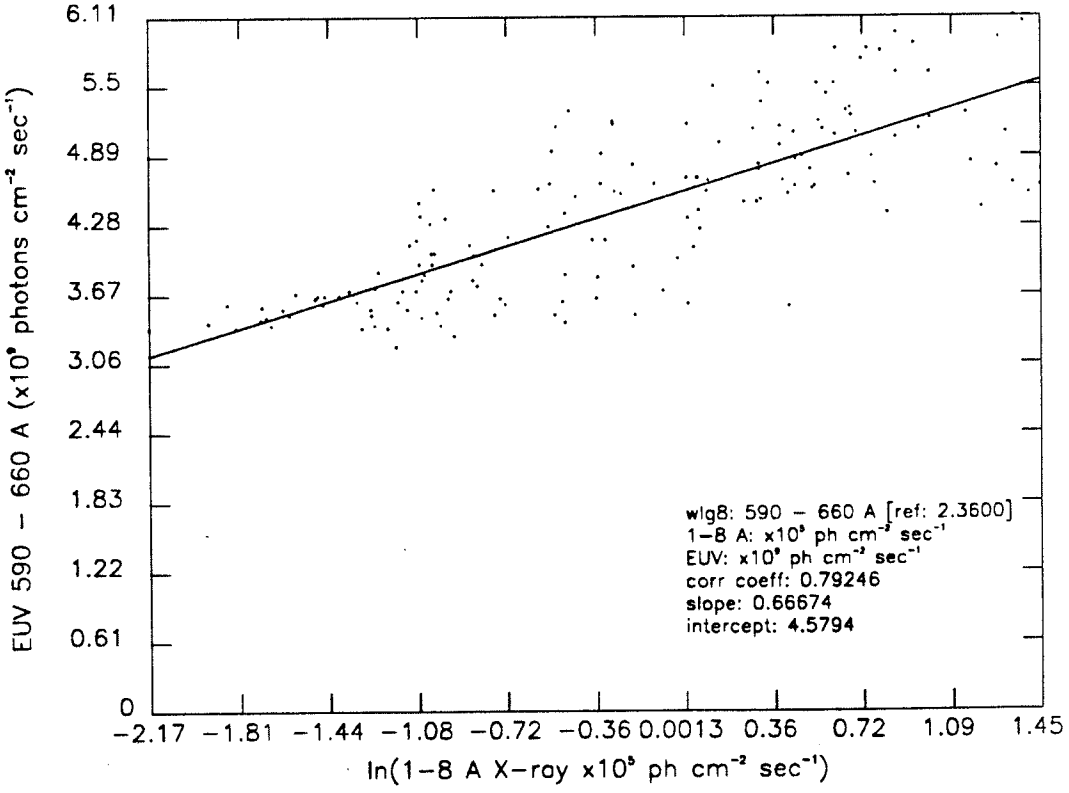

Figure 3.15 (h) 1-8 Å X-ray and 590-660 Å correlation.

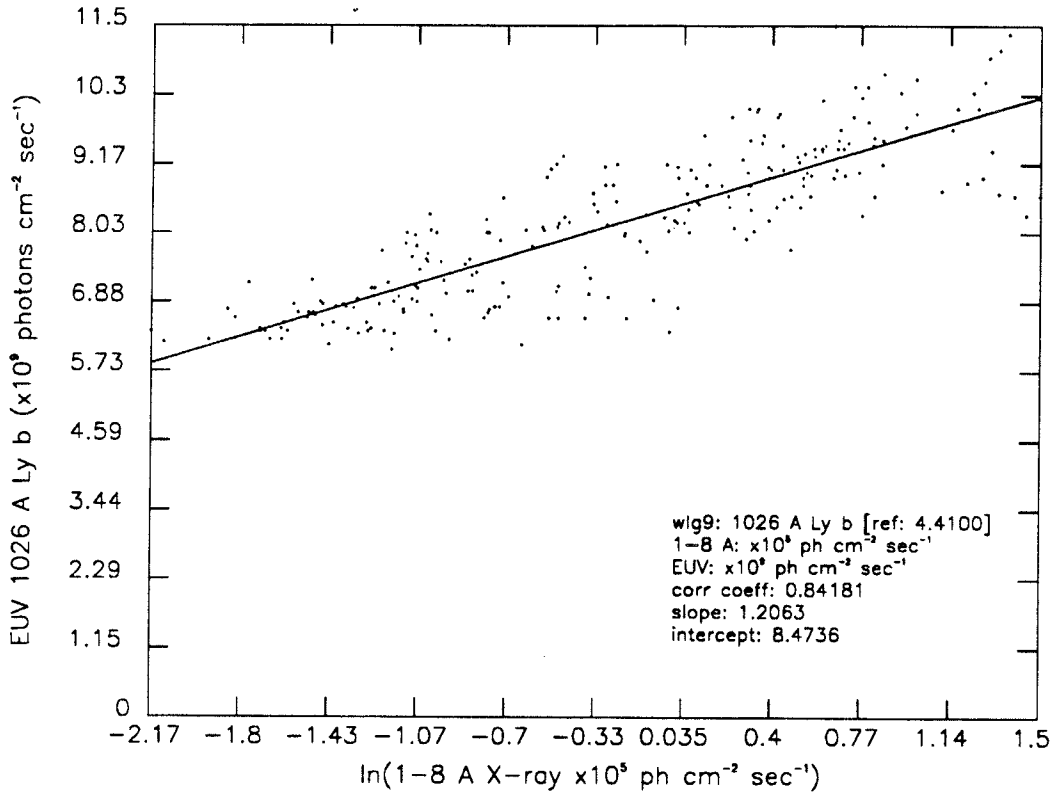

Figure 3.15 (i) **1-8 Å X-ray and 1026 Å (Lyman-β) correlation.**

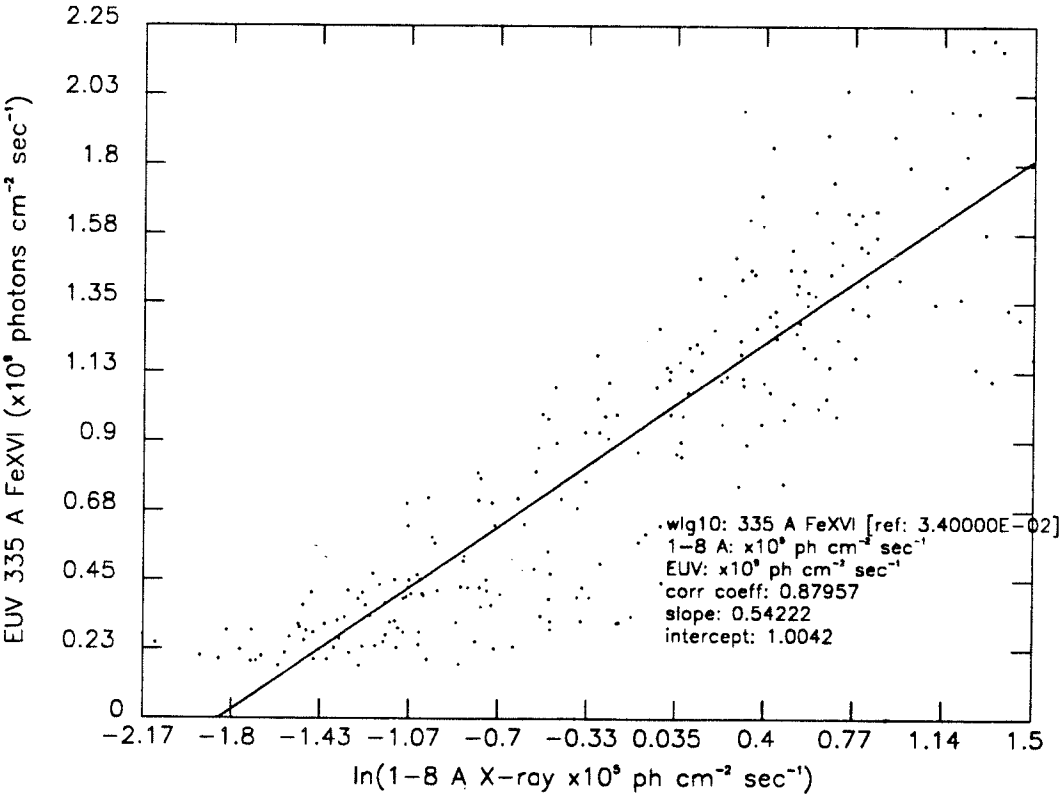

Figure 3.15 (j) **1-8 Å X-ray and 335 Å (Fe XVI) correlation.**

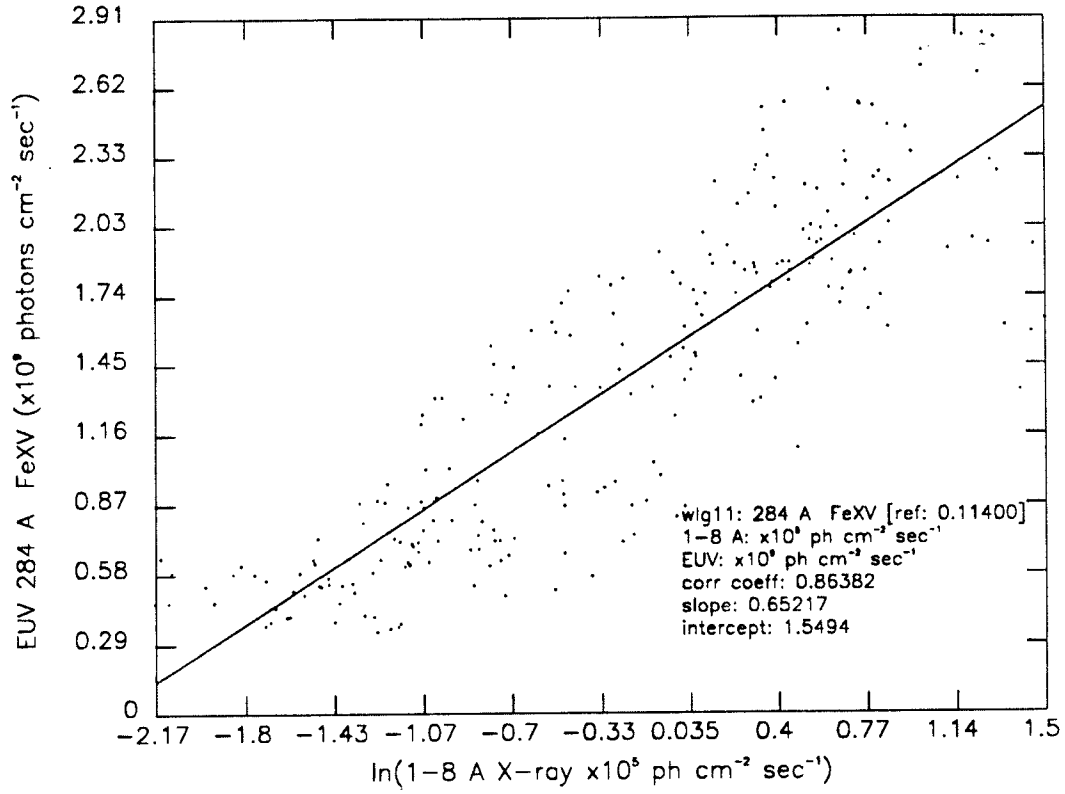

Figure 3.15 (k) **1-8 Å X-ray and 284 Å (Fe XV) correlation.**

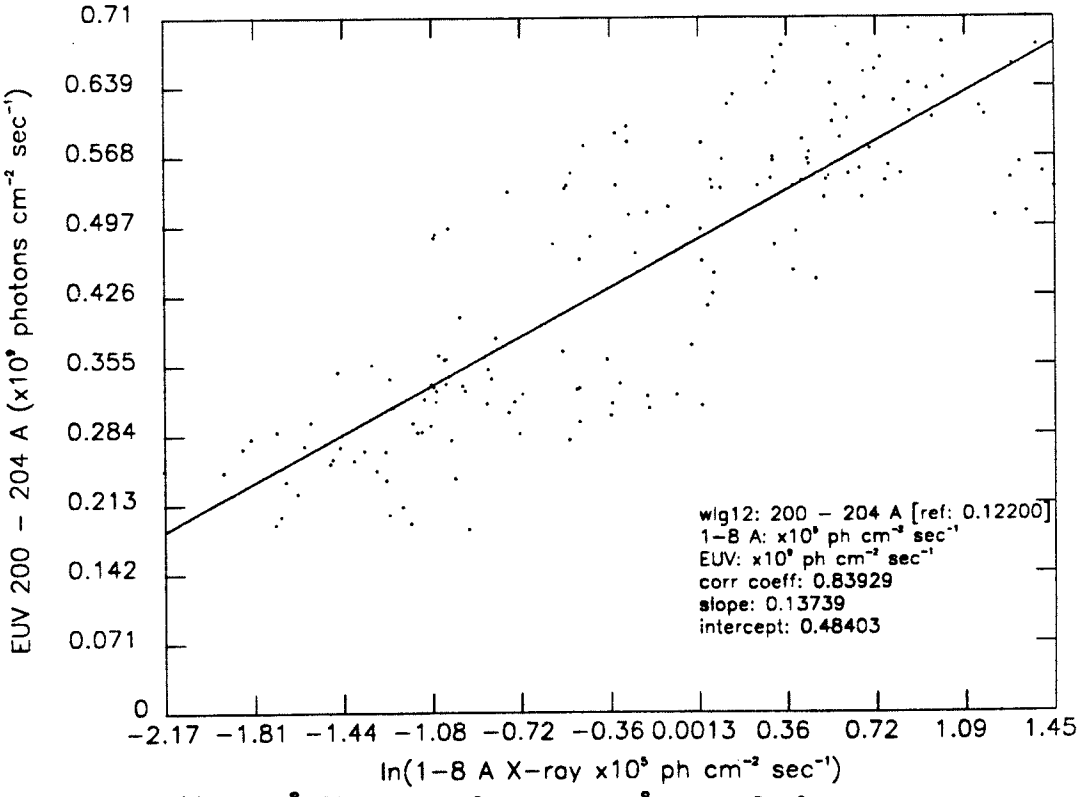

Figure 3.15 (l) **1-8 Å X-ray and 200-204 Å correlation.**

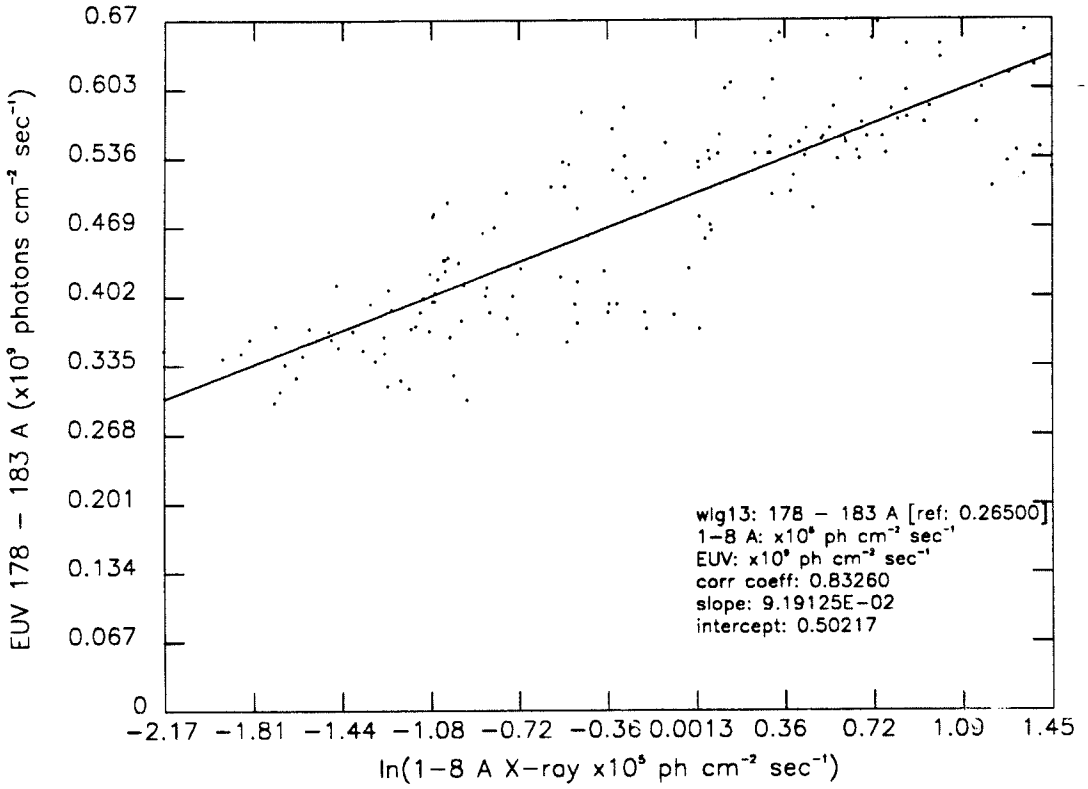

Figure 3.15 (m) **1-8 Å X-ray and 178-183 Å correlation.**

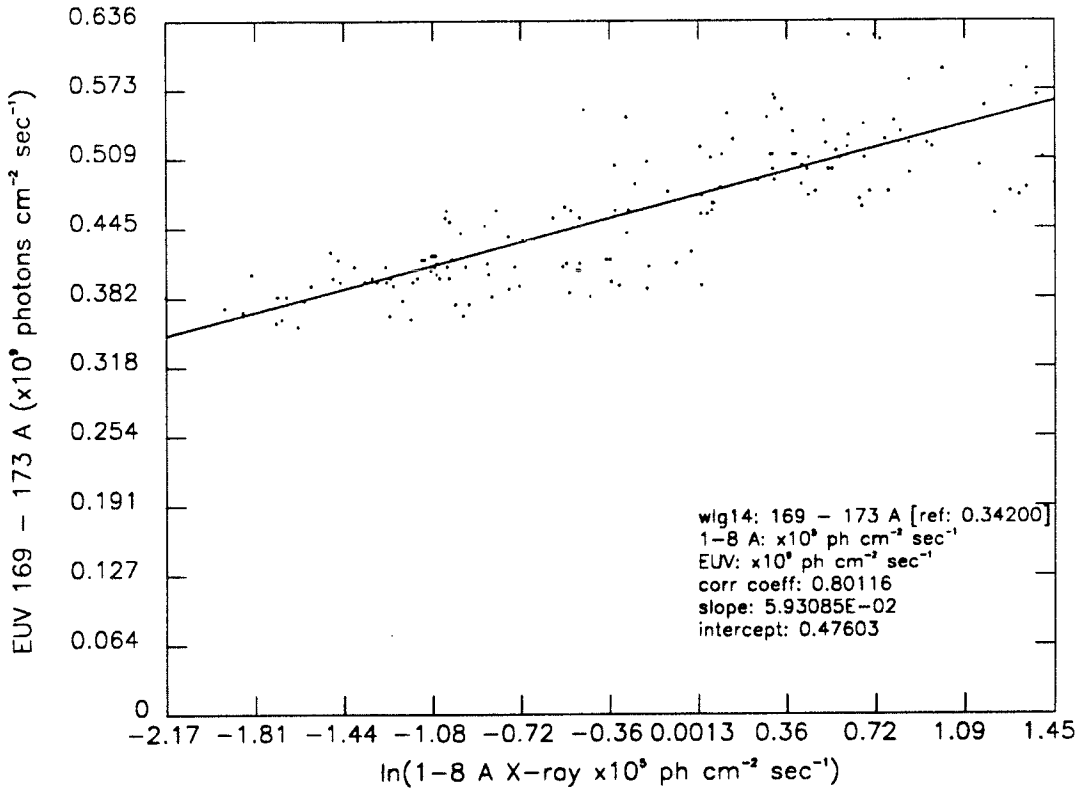

Figure 3.15 (n) **1-8 Å X-ray and 169-173 Å correlation.**

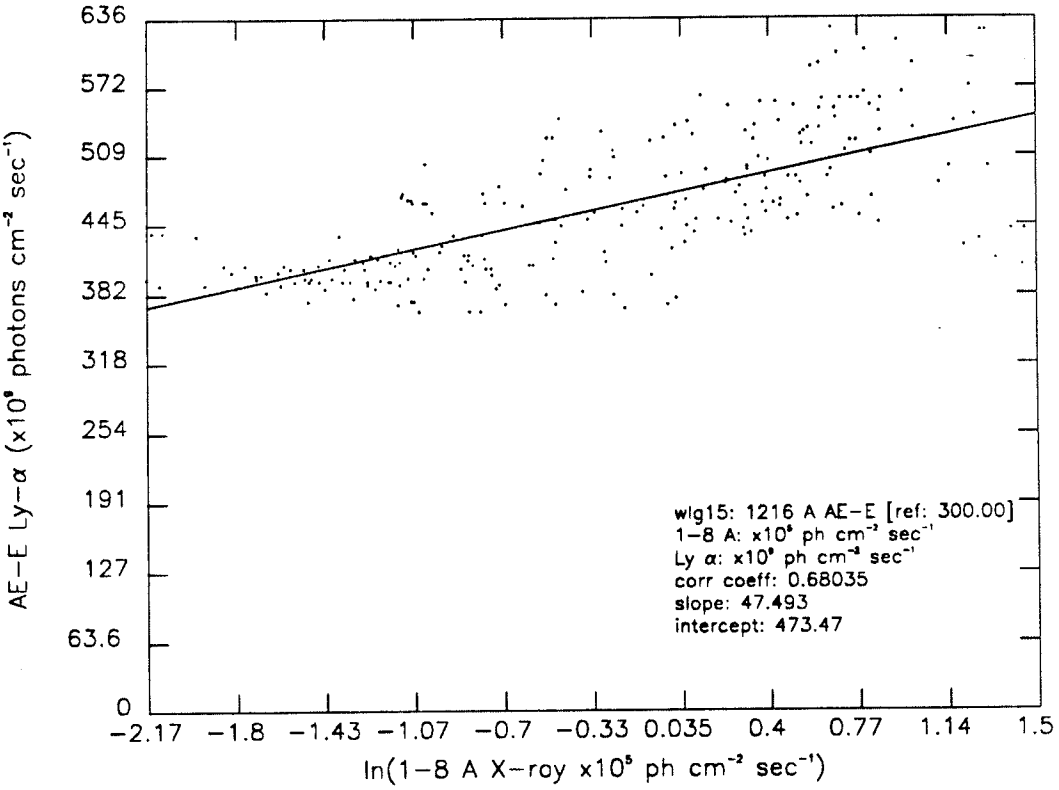

Figure 3.15 (o) **AE-E Lyman-α and 1-8 Å X-ray correlation.**

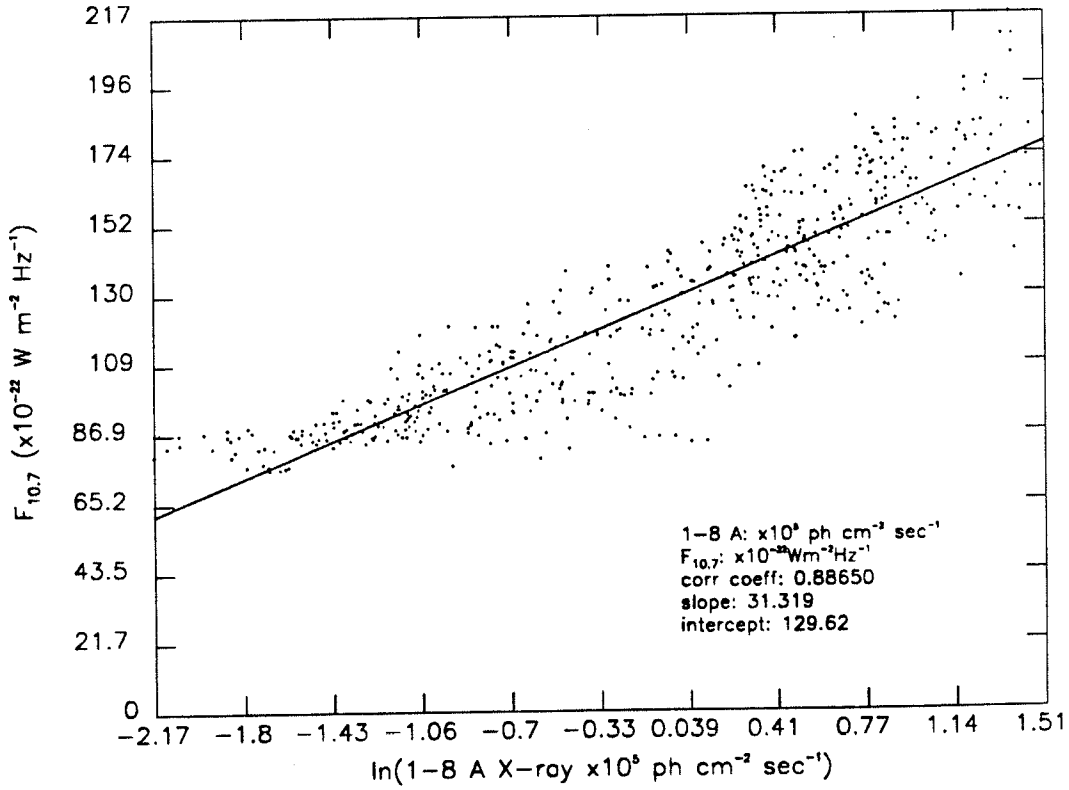

Figure 3.15 (p) **$F_{10.7}$ and 1-8 Å X-ray correlation.**

tion with 335 Å, where r = 0.88. The lowest correlation is with He II, where r = 0.79. These results go in the direction one might expect if 1-8 Å is considered a coronal emission index. The coronally-produced emissions which were correlated with $F_{10.7}$, and listed above, show correlation coefficients ranging from r = 0.80 to 0.86. The chromospheric emissions, correlated with Lyman-α above, show lower correlations near 0.80. An unexpected, and as yet unexplained result, is the relatively high correlation with Lyman-β for this dataset, where r = 0.84, while the correlation with Lyman-α is 0.68. The conclusion from these linear correlations is that during rising solar activity, 1-8 Å X-rays model coronal EUV emissions, while $F_{10.7}$ models the transition region - cool corona EUV emissions, and Lyman-α models chromospherically-produced EUV emissions.

In addition to the long-term linear correlations described above, Donnelly [1987a] describes other temporal variations. He particularly details the temporal correlation measure called the persistence of solar-rotational variations. This is a measure of the repeatability of solar rotation related episodes which is derived from the autocorrelation function. His results indicate that the solar-rotational episodes have high persistence for the chromospheric UV and EUV fluxes, low persistence for the $F_{10.7}$ and hot coronal fluxes of Fe XV and Fe XVI, and very low persistence for the hot coronal 1-8 Å X-rays and transition region fluxes like Fe IX. Donnelly also indicates that the half-max durations of the solar rotational variations during high cycle 21 activity are much longer in the X-ray background flux, for $T > 3 \times 10^6$K, than in the coronal emissions represented by $F_{10.7}$. Both the 1-8 Å and $F_{10.7}$ episode durations and decay characteristics differ from the rather short duration chromospheric emission solar rotational episodes. Hence, the temporal variations of coronally-produced emissions behave differently than the chromospherically-

produced emissions, thus emphasizing the temporal distinctions between 1-8 Å, $F_{10.7}$, and Lyman-α.

3.4 Dominant EUV Fluxes and Their Indices

It is possible to summarize 1) which are the dominant EUV emissions in relation to terrestrial thermospheric heating and 2) which are good indices to use for chromospheric and coronal EUV flux. The selection of these dominant fluxes and indices are based on the physics of EUV heating presented in section 3.2 and on the correlations discussed in section 3.3. The result of this work is a model of EUV energy flux using Lyman-α and 1-8 Å X-rays to calculate an EUV emission time series.

In reviewing the dominant EUV emissions, there are both chromospheric and coronal fluxes which heat the thermosphere. The most important are He II, 850-900 Å, 150-200 Å, 300-350 Å, He I, O V, 900-950 Å, and 200-250 Å for solar minimum and maximum conditions, generally in that order. Tables 3.10, 3.11, 3.12, and 3.13 list these wavelengths for minimum and maximum conditions for both chromospheric and coronal fluxes. They give the total energy flux at the wavelength or wavelength range, the maximum heating per unit mass among all species at that wavelength, the species receiving the maximum heating, the altitude of maximum heating, the intercept, and the slope during rising solar activity for a linear regression fit from Lyman-α or the natural logarithm of 1-8 Å X-rays to the EUV flux from equation (3.4).

From these tables and Figure 3.3, one notes that He II has the highest energy flux and largest maximum heating of all wavelengths for all solar conditions. O is the species with the largest maximum heating per unit mass for He II as well as for all wavelengths less than 400 Å. N_2 dominates the heating from 400-770 Å, while both N_2 and O_2 contribute the maximum heating for

TABLE 3.10. SOLAR MINIMUM CHROMOSPHERIC ENERGY FLUX

λ (Å)	F_λ^a	Q_{max}^b	Species[c]	Altitude[d]	Intercept[e]	Slope[f]
18.62- 29.52						
30.02- 49.22	6.41				8.64	0.96
50.52- 99.99	68.03	0.44	O	168	91.69	10.18
100.54-148.40	16.11	0.26	O	180	24.46	2.36
150.10-198.58	31.81	4.42	O	210	98.36	3.80
200.02-249.18	37.38	2.26	O	216	115.32	4.47
256.32-256.32	21.14	0.66	O	218	115.85	1.65
284.15-284.15						
251.10-299.50	26.91	2.01	O	218	117.58	2.62
303.31-303.31						
303.78-303.78	455.61	14.45	O	220	2495.80	35.65
303.31-349.85						
368.07-368.07						
356.01-399.82	0.99	0.48	O	222	4.32	0.09
401.14-436.70	10.27	0.86	N_2	224	44.75	1.00
465.22-465.22						
453.00-499.37	12.21	0.63	N_2	226	18.87	1.78
500.00-550.00	23.29	1.01	N_2	226	71.81	2.78
554.37-554.37	34.37	1.55	N_2	226	156.79	3.23
584.33-584.33	76.82	2.73	N_2	226	15.09	13.03
554.37-599.60	131.54	0.87	N_2	226	241.71	18.57
609.76-609.76						
629.73-629.73	57.06	2.53	N_2	226	253.03	5.49
609.76-644.10	60.25	0.29	N_2	226	264.90	5.84
650.30-700.00	5.97	0.36	N_2	226	20.19	0.68
703.36-703.36	13.05	0.59	N_2	226	65.43	1.12
701.00-750.00	18.76	0.26	N_2	226	74.22	1.96
765.15-765.15	6.49	0.27	N_2	224	22.21	0.73
770.41-770.41						
787.71-787.71	8.40	0.86	O_2	218	38.31	0.79
750.01-800.00	55.64	1.22	N_2	224	184.15	6.44
801.00-850.00	62.62	1.75	O_2	216	99.89	9.10
851.00-900.00	144.38	5.14	N_2	228	16.33	24.69
901.00-950.00	127.05	2.94	N_2	216	79.84	20.60
977.02-977.02	153.20	0.67	O_2	166	486.87	18.08
951.00-1000.0	201.47	1.64	N_2	222	587.21	24.70
1025.7-1025.7	121.63	0.16	O_2	162	13.76	20.80
1031.9-1031.9	89.08	0.07	O_2	162	-14.76	15.67
1001.0-1050.0	304.64	0.09	O_2	162	181.14	49.57

[a] Energy flux in units of $\times 10^{-3}$ ergs cm^{-2} sec^{-1} with a total sum of 2.38 ergs cm^{-2} sec^{-1}.

[b] Maximum heating: all species and all flux in units of $\times 10^4$ ergs g^{-1} sec^{-1}.

[c] Atomic or molecular species with largest heating per unit mass for this λ.

[d] Altitude of maximum heating in km.

[e] Intercept a_1 in units of $\times 10^{-4}$ ergs cm^{-2} sec^{-1} in the equation $E_\lambda = a_1 + b_1 \mathrm{Ly}_\alpha$.

[f] Slope b_1 in units of $\times 10^{-3}$ ergs in the equation $E_\lambda = a_1 + b_1 \mathrm{Ly}_\alpha$. Lyman-$\alpha$ is in units of $\times 10^{11}$ photons cm^{-2} sec^{-1}.

TABLE 3.11. SOLAR MINIMUM CORONAL ENERGY FLUX

λ (Å)	F_λ^a	Q_{max}^b	Species[c]	Altitude[d]	Intercept[e]	Slope[f]
18.62- 29.52	8.36				0.1693	19.11
30.02- 49.22	10.37				0.1820	20.38
50.52- 99.99	59.59	0.44	O	168	0.4631	47.91
100.54-148.40	10.47	0.26	O	180	0.0547	5.25
150.10-198.58	209.74	4.42	O	210	1.4138	142.99
200.02-249.18	68.39	2.26	O	216	0.8487	92.67
256.32-256.32						
284.15-284.15	21.57	0.24	O	218	0.7258	83.63
251.10-299.50	97.63	2.00	O	218	1.6649	186.12
303.31-303.31	24.83	0.56	O	220	0.4808	54.15
303.78-303.78						
303.31-349.85	94.62	2.12	O	222	1.4296	158.53
368.07-368.07	43.48	1.75	O	224	0.1492	12.65
356.01-399.82	58.09	0.48	O	222	0.4875	51.00
401.14-436.70	11.47	0.86	N_2	224	0.0766	7.73
465.22-465.22	8.37	0.37	N_2	224	0.0318	2.79
453.00-499.37	13.70	0.63	N_2	226	0.1568	16.99
500.00-550.00	2.38	1.01	N_2	226	0.0522	5.92
554.37-554.37						
584.33-584.33						
554.37-599.60						
609.76-609.76	16.76	0.78	N_2	226	0.1181	12.03
629.73-629.73						
609.76-644.10	20.00	0.29	N_2	226	0.1444	14.77
650.30-700.00	1.95	0.36	N_2	226	0.0056	0.45
703.36-703.36						
701.00-750.00						
765.15-765.15						
770.41-770.41	6.95	0.30	N_2	222	0.0409	4.03
787.71-787.71						
750.01-800.00	10.64	1.22	N_2	224	0.0625	6.16
801.00-850.00						
851.00-900.00						
901.00-950.00						
977.02-977.02						
951.00-1000.0						
1025.7-1025.7						
1031.9-1031.9						
1001.0-1050.0						

[a] Energy flux in units of $\times 10^{-3}$ ergs cm^{-2} sec^{-1} with a total sum of 0.80 ergs cm^{-2} sec^{-1}.

[b] Maximum heating: all species and all flux in units of $\times 10^4$ ergs g^{-1} sec^{-1}.

[c] Atomic or molecular species with largest heating per unit mass for this λ.

[d] Altitude of maximum heating in km.

[e] Intercept a_2 in units of ergs cm^{-2} sec^{-1} in the equation $E_\lambda = a_2 + b_2 ln(\text{Xray}_{1-8})$.

[f] Slope b_2 in units of $\times 10^{-3}$ ergs cm^{-2} sec^{-1} in the equation $E_\lambda = a_2 + b_2 ln(\text{Xray}_{1-8})$. 1-8 Å X-rays are in units of ergs cm^{-2} sec^{-1}.

TABLE 3.12. SOLAR MAXIMUM CHROMOSPHERIC ENERGY FLUX

λ (Å)	F_λ^a	Q_{max}^b	Species[c]	Altitude[d]	Intercept[e]	Slope[f]
18.62- 29.52						
30.02- 49.22	13.88				8.64	0.96
50.52- 99.99	147.21	1.18	O	172	91.69	10.18
100.54-148.40	34.50	0.51	O	216	24.46	2.36
150.10-198.58	61.37	8.03	O	226	98.36	3.80
200.02-249.18	72.17	5.76	O	234	115.32	4.47
256.32-256.32	34.01	0.88	O	240	115.85	1.65
284.15-284.15						
251.10-299.50	47.29	5.91	O	242	117.58	2.62
303.31-303.31						
303.78-303.78	732.76	15.70	O	248	2495.80	35.65
303.31-349.85						
368.07-368.07						
356.01-399.82	1.74	2.75	O	256	4.32	0.09
401.14-436.70	18.07	1.15	N_2	260	44.75	1.00
465.22-465.22						
453.00-499.37	26.10	1.80	N_2	262	18.87	1.78
500.00-550.00	44.96	1.59	N_2	264	71.81	2.78
554.37-554.37	59.52	1.58	N_2	264	156.79	3.23
584.33-584.33	178.14	4.34	N_2	264	15.09	13.03
554.37-599.60	275.95	0.95	N_2	262	241.71	18.57
609.76-609.76						
629.73-629.73	99.79	2.62	N_2	264	253.03	5.49
609.76-644.10	105.67	0.42	N_2	264	264.90	5.84
650.30-700.00	11.29	0.39	N_2	264	20.19	0.68
703.36-703.36	21.81	0.56	N_2	264	65.43	1.12
701.00-750.00	34.02	0.36	N_2	262	74.22	1.96
765.15-765.15	12.24	0.34	N_2	258	22.21	0.73
770.41-770.41						
787.71-787.71	14.54	1.08	O_2	244	38.31	0.79
750.01-800.00	105.71	1.82	N_2	254	184.15	6.44
801.00-850.00	133.43	2.98	O_2	236	99.89	9.10
851.00-900.00	336.38	8.52	N_2	266	16.33	24.69
901.00-950.00	287.21	5.83	N_2	232	79.84	20.60
977.02-977.02	293.79	1.41	O_2	168	486.87	18.08
951.00-1000.0	393.47	2.59	N_2	250	587.21	24.70
1025.7-1025.7	283.39	0.48	O_2	162	13.76	20.80
1031.9-1031.9	210.90	0.21	O_2	162	-14.76	15.67
1001.0-1050.0	690.02	0.22	O_2	162	181.14	49.57

[a] Energy flux in units of $\times 10^{-3}$ ergs cm^{-2} sec^{-1} with a total sum of 4.78 ergs cm^{-2} sec^{-1}.

[b] Maximum heating: all species and all flux in units of $\times 10^{4}$ ergs g^{-1} sec^{-1}.

[c] Atomic or molecular species with largest heating per unit mass for this λ.

[d] Altitude of maximum heating in km.

[e] Intercept a_1 in units of $\times 10^{-4}$ ergs cm^{-2} sec^{-1} in the equation $E_\lambda = a_1 + b_1 \mathrm{Ly}_\alpha$.

[f] Slope b_1 in units of $\times 10^{-3}$ ergs in the equation $E_\lambda = a_1 + b_1 \mathrm{Ly}_\alpha$. Lyman-$\alpha$ is in units of $\times 10^{11}$ photons cm^{-2} sec^{-1}.

TABLE 3.13. SOLAR MAXIMUM CORONAL ENERGY FLUX

λ (Å)	F_λ^a	Q_{max}^b	Species[c]	Altitude[d]	Intercept[e]	Slope[f]
18.62- 29.52	82.34				0.1693	19.11
30.02- 49.22	89.28				0.1820	20.38
50.52- 99.99	245.04	1.18	O	172	0.4631	47.91
100.54-148.40	30.83	0.51	O	216	0.0547	5.25
150.10-198.58	763.10	8.03	O	226	1.4138	142.99
200.02-249.18	427.02	5.76	O	234	0.8487	92.67
256.32-256.32						
284.15-284.15	345.22	4.53	O	244	0.7258	83.63
251.10-299.50	817.92	5.91	O	242	1.6649	186.12
303.31-303.31	234.40	3.48	O	246	0.4808	54.15
303.78-303.78						
303.31-349.85	708.13	7.77	O	252	1.4296	158.53
368.07-368.07	92.15	1.79	O	256	0.1492	12.65
356.01-399.82	255.47	2.75	O	256	0.4875	51.00
401.14-436.70	41.41	1.15	N_2	260	0.0766	7.73
465.22-465.22	19.17	0.39	N_2	260	0.0318	2.79
453.00-499.37	79.46	1.80	N_2	262	0.1568	16.99
500.00-550.00	25.30	1.59	N_2	264	0.0522	5.92
554.37-554.37						
584.33-584.33						
554.37-599.60						
609.76-609.76	63.35	1.31	N_2	264	0.1181	12.03
629.73-629.73						
609.76-644.10	77.18	0.42	N_2	264	0.1444	14.77
650.30-700.00	3.68	0.39	N_2	264	0.0056	0.45
703.36-703.36						
701.00-750.00						
765.15-765.15						
770.41-770.41	22.56	0.51	N_2	252	0.0409	4.03
787.71-787.71						
750.01-800.00	34.51	1.82	N_2	254	0.0625	6.16
801.00-850.00						
851.00-900.00						
901.00-950.00						
977.02-977.02						
951.00-1000.0						
1025.7-1025.7						
1031.9-1031.9						
1001.0-1050.0						

[a] Energy flux in units of $\times 10^{-3}$ ergs cm^{-2} sec^{-1} with a total sum of 4.46 ergs cm^{-2} sec^{-1}.

[b] Maximum heating: all species and all flux in units of $\times 10^4$ ergs g^{-1} sec^{-1}.

[c] Atomic or molecular species with largest heating per unit mass for this λ.

[d] Altitude of maximum heating in km.

[e] Intercept a_2 in units of ergs cm^{-2} sec^{-1} in the equation $E_\lambda = a_2 + b_2 ln(\text{Xray}_{1-8})$.

[f] Slope b_2 in units of $\times 10^{-3}$ ergs cm^{-2} sec^{-1} in the equation $E_\lambda = a_2 + b_2 ln(\text{Xray}_{1-8})$. 1-8 Å X-rays are in units of ergs cm^{-2} sec^{-1}.

wavelengths greater than 770 Å depending upon which constituent cross sectional area is larger at a specific wavelength. The general altitude range for maximum heating is between 162 and 266 km, depending upon solar activity and constituent. The intercept and slope, used in the sum of the Lyman-α photon flux and 1-8 Å energy flux components, results in the modeled EUV energy flux at that wavelength. The modeled emission is given by

$$E_\lambda = a_1 + b_1 \mathrm{Ly}_\alpha + a_2 + b_2 ln(\mathrm{Xray}_{1-8}) \quad \text{ergs cm}^{-2} \text{ sec}^{-1} \qquad (3.5)$$

where a_1 and b_1 are the intercept and slope of the chromospheric component and a_2 and b_2 are the intercept and slope of the coronal component. The chromospheric relation is linear with Lyman-α and is dictated by chromospheric EUV and Lyman-α variations over a factor of 2 to 3. The coronal variation is linear with the natural logarithm of the 1-8 Å X-rays. This relation is driven by the X-ray variations over two to three orders of magnitude compared to the coronal EUV variations over a factor of 3 to 6 in Table 3.1.

The relative order of maximum heating by wavelength, by solar minimum and maximum conditions, and by chromospheric and coronal flux, can be seen in Table 3.14. The top eight wavelengths in order of maximum heating, Q_{max}, are listed. This table duplicates but clarifies some of the information in Tables 3.10 through 3.13. In addition to the He II dominance, 850-900 Å and 150-200 Å emissions contribute the next largest heating rates during both solar maximum and minimum conditions for chromospheric and coronal flux.

Using this information as a guide, indices for use in modeling EUV flux can now be summarized. In the effort to obtain a physical representation of mixed EUV emissions, their individual components are isolated and modeled by solar flux which is physically close in both spectral distribution and terrestrial effect. The resulting modeled flux is then summed to reproduce a

TABLE 3.14. SOLAR ENERGY FLUX IN ORDER OF MAXIMUM HEATING

	λ (Å)	F_λ^a	Q_{max}^b	Species[c]	Altitude[d]	Intercept[e]	Slope[f]
	MINIMUM	CHROMOSPHERIC					
1	303.78-303.78	455.61	14.45	O	220	2495.80	35.65
2	851.00-900.00	144.38	5.14	N_2	228	16.33	24.69
3	150.10-198.58	31.81	4.42	O	210	98.36	3.80
4	901.00-950.00	127.05	2.94	N_2	216	79.84	20.60
5	584.33-584.33	76.82	2.73	N_2	226	15.09	13.03
6	629.73-629.73	57.06	2.53	N_2	226	253.03	5.49
7	200.02-249.18	37.38	2.26	O	216	115.32	4.47
8	251.10-299.50	26.91	2.01	O	218	117.58	2.62
	MINIMUM	CORONAL					
1	150.10-198.58	209.74	4.42	O	210	1.4138	142.99
2	200.02-249.18	68.39	2.26	O	216	0.8487	92.67
3	303.31-349.85	94.62	2.12	O	222	1.4296	158.53
4	251.10-299.50	97.63	2.00	O	218	1.6649	186.12
5	368.07-368.07	43.48	1.75	O	224	0.1492	12.65
6	750.01-800.00	10.64	1.22	N_2	224	0.0625	6.16
7	500.00-550.00	2.38	1.01	N_2	226	0.0522	5.92
8	401.14-436.70	11.47	0.86	N_2	224	0.0766	7.73
	MAXIMUM	CHROMOSPHERIC					
1	303.78-303.78	732.76	15.70	O	248	2495.80	35.65
2	851.00-900.00	336.38	8.52	N_2	266	16.33	24.69
3	150.10-198.58	61.37	8.03	O	226	98.36	3.80
4	251.10-299.50	47.29	5.91	O	242	117.58	2.62
5	901.00-950.00	287.21	5.83	N_2	232	79.84	20.60
6	200.02-249.18	72.17	5.76	O	234	115.32	4.47
7	584.33-584.33	178.14	4.34	N_2	264	15.09	13.03
8	801.00-850.00	133.43	2.98	O_2	236	99.89	9.10
	MAXIMUM	CORONAL					
1	150.10-198.58	763.10	8.03	O	226	1.4138	142.99
2	303.31-349.85	708.13	7.77	O	252	1.4296	158.53
3	251.10-299.50	817.92	5.91	O	242	1.6649	186.12
4	200.02-249.18	427.02	5.76	O	234	0.8487	92.67
5	284.15-284.15	345.22	4.53	O	244	0.7258	83.63
6	303.31-303.31	234.40	3.48	O	246	0.4808	54.15
7	356.01-399.82	255.47	2.75	O	256	0.4875	51.00
8	750.01-800.00	34.51	1.82	N_2	254	0.0625	6.16

[a] Energy flux in units of $\times 10^{-3}$ ergs cm^{-2} sec^{-1}.
[b] Maximum heating per unit mass in units of $\times 10^{4}$ ergs g^{-1} sec^{-1}.
[c] Atomic or molecular species with the largest maximum heating per unit mass for this λ.
[d] Altitude of maximum heating in km.
[e] Intercept a_1 in units of $\times 10^{-4}$ ergs cm^{-2} sec^{-1} in the equation $E_\lambda = a_1 + b_1 \mathrm{Ly}_\alpha$ or intercept a_2 in units of ergs cm^{-2} sec^{-1} in the equation $E_\lambda = a_2 + b_2 ln(\mathrm{Xray}_{1-8})$.
[f] Slope b_1 in units of $\times 10^{-3}$ ergs in the equation $E_\lambda = a_1 + b_1 \mathrm{Ly}_\alpha$ or slope b_2 in units of $\times 10^{-3}$ ergs cm^{-2} sec^{-1} in the equation $E_\lambda = a_2 + b_2 ln(\mathrm{Xray}_{1-8})$. Lyman-$\alpha$ is in units of $\times 10^{11}$ photons cm^{-2} sec^{-1} and 1-8 Å X-rays are in units of ergs cm^{-2} sec^{-1}.

mixed EUV emission. Lyman-α and 1-8 Å X-rays, as purely chromospheric and coronal emissions, are selected as the primary modeling inputs outlined in equation (3.5). The principal justification for selecting these two EUV indices rests with their strong linear correlations. $F_{10.7}$ is neglected in the remaining analysis. As an EUV indicator, it has been discussed extensively in the literature for many years and discussed in this thesis. As a mixed region emission, $F_{10.7}$ follows neither a purely coronal nor chromospheric temporal variation pattern, particularly for solar minimum conditions.

It is important to recall briefly the details of the Lyman-α and 1-8 Å X-ray energy emissions. Figures 3.16 and 3.17 show the energy flux for AE-E Lyman-α and GOES 1-8 Å flux used in this analysis. In Figure 3.16, the AE-E data are plotted in a bold line, the interpolated data are plotted by a dashed line, and the light, solid line is a 13-day smooth through the interpolated data. As noted above, a significant increase in the energy flux occurs at the end of 1978, with the maximum occurring at the end of 1979. Because of the missing data, no better resolution than this is attainable. Figure 3.17 shows the Bouwer 1-8 Å X-ray energy flux where the dashed line is the calculated flux and the heavy, solid line is the 13-day smoothed flux for the AE-E time period. This energy flux increases by over two orders of magnitude from low to high solar activity and also shows solar rotation variability associated with the passage of active regions across the disk. The periodicity in these variations is less than 27 days.

It was concluded in section 3.3 that chromospherically-produced Lyman-α models the chromospheric flux, including He II, 850-900 Å, He I, O V, and 900-950 Å. While there is a high long-term correlation between He II and Lyman-α, where r = 0.85, and He I and Lyman-α, where r = 0.89, there was no direct correlation made between the Lyman-α and the O V, 850-900 Å, and

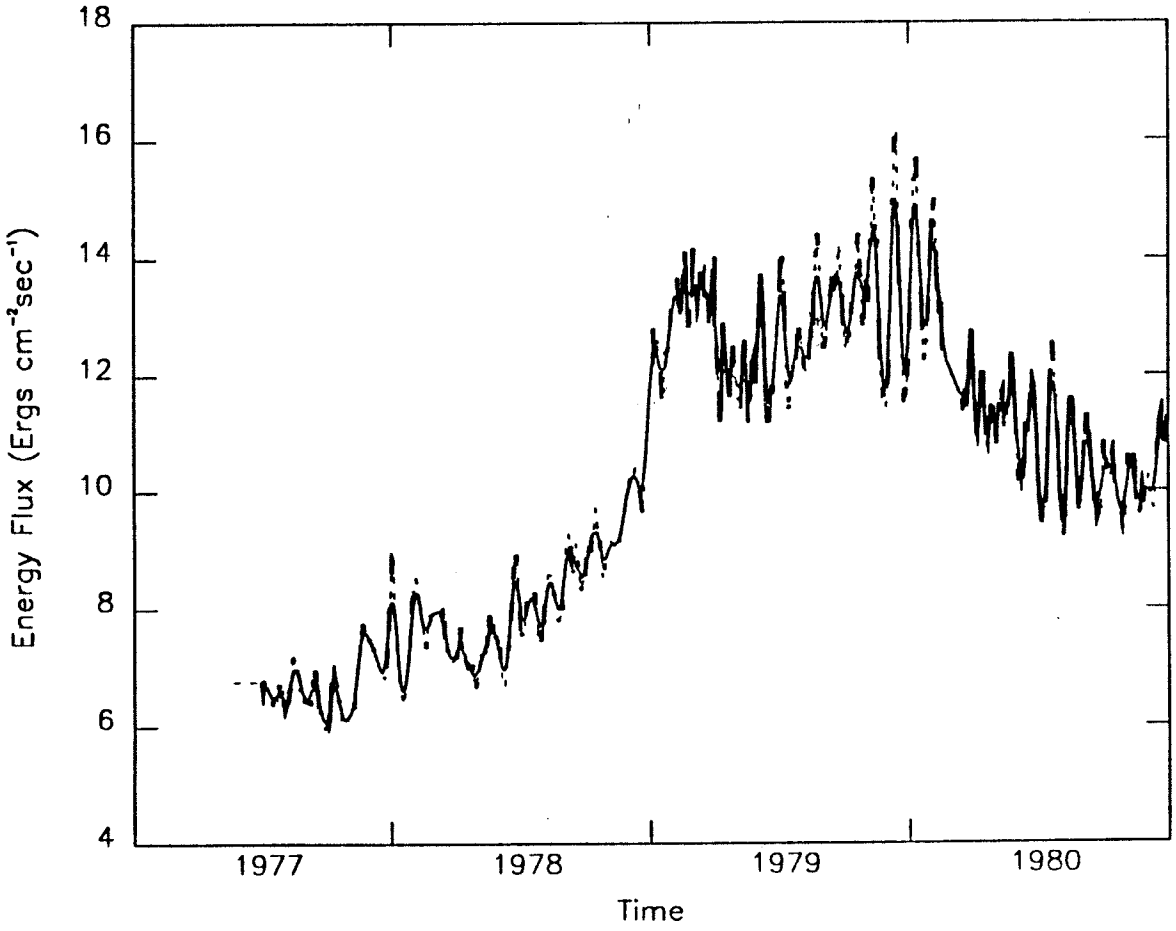

Figure 3.16 **Lyman-α energy flux 1977-1980.** The bold line (with missing data) is the AE-E dataset, the dashed line is the interpolated dataset, and the light solid line is the 13-day smooth through the interpolated data.

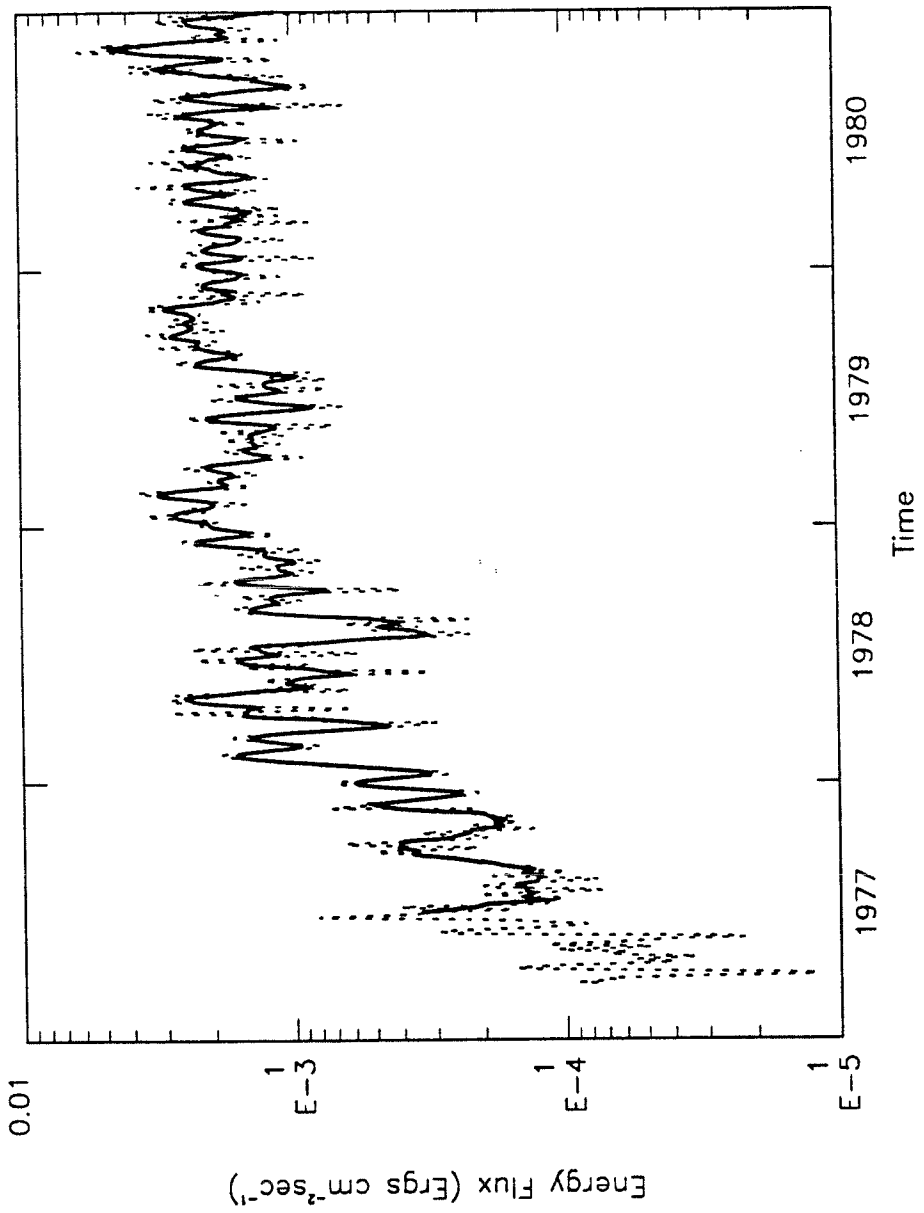

Figure 3.17 1-8 Å X-ray energy flux 1977-1980. The dashed line is the flux given by Bouwer [1983] and the solid line is the 13-day smoothed data during the AE-E time period.

900-950 Å ranges. However, using the EUV class method of determining these energy fluxes based on the Lyman-β energy flux, there is a correlation of r = 0.93 with all three. The high coefficient is similar to the Lyman-β correlation.

It was also concluded that coronal X-rays, in the range of 1-8 Å, model the cool coronal emissions of 150-200 Å, 200-250 Å, 250-300 Å, and 300-350 Å. Correlations between 1-8 Å and 168-206 Å in the AE-E dataset from SC#21OBS give a value of r = 0.84. The energy flux correlation between 1-8 Å and these four emission ranges is r = 0.85. This is comparable to the correlation with Fe XVI. In all the datasets, smoothing the long-term trends tends to raise the correlation.

Additional, heuristic arguments can be made to emphasize the appropriateness of Lyman-α and 1-8 Å X-rays for parameterizing the dominant EUV chromospheric and coronal emissions. First, the emissions described above in connection with thermospheric heating and listed in descending order in Table 3.14 have among the largest magnitudes of photon flux during solar minimum conditions, when there was no sunspot activity, as well as have the largest magnitudes during solar maximum. This is shown in Tables 2.2 and 2.3. These emissions also have the largest energy emissions, shown in Table 3.1 and Figures 3.4, 3.5, and 3.6. Hence, one would expect the largest emissions to be targeted for modeling efforts.

Second, Figures 3.18, 3.19, 3.20, 3.21, 3.22, 3.23, 3.24, 3.25, 3.26, and 3.27 are presented which model the He II, 850-900 Å, 150-200 Å (cool coronal), 150-200 Å (chromospheric), 300-350 Å, He I, 900-950 Å, O V, 200-250 (cool coronal), and 250-300 (cool coronal) fluxes, respectively. These figures give either the chromospheric or coronal components only. The solid line in these plots is the Hinteregger *et al.* [1981] calculated emission from equation (3.4) while the dotted lines are the Lyman-α and 1-8 Å X-rays modeled fluxes, using

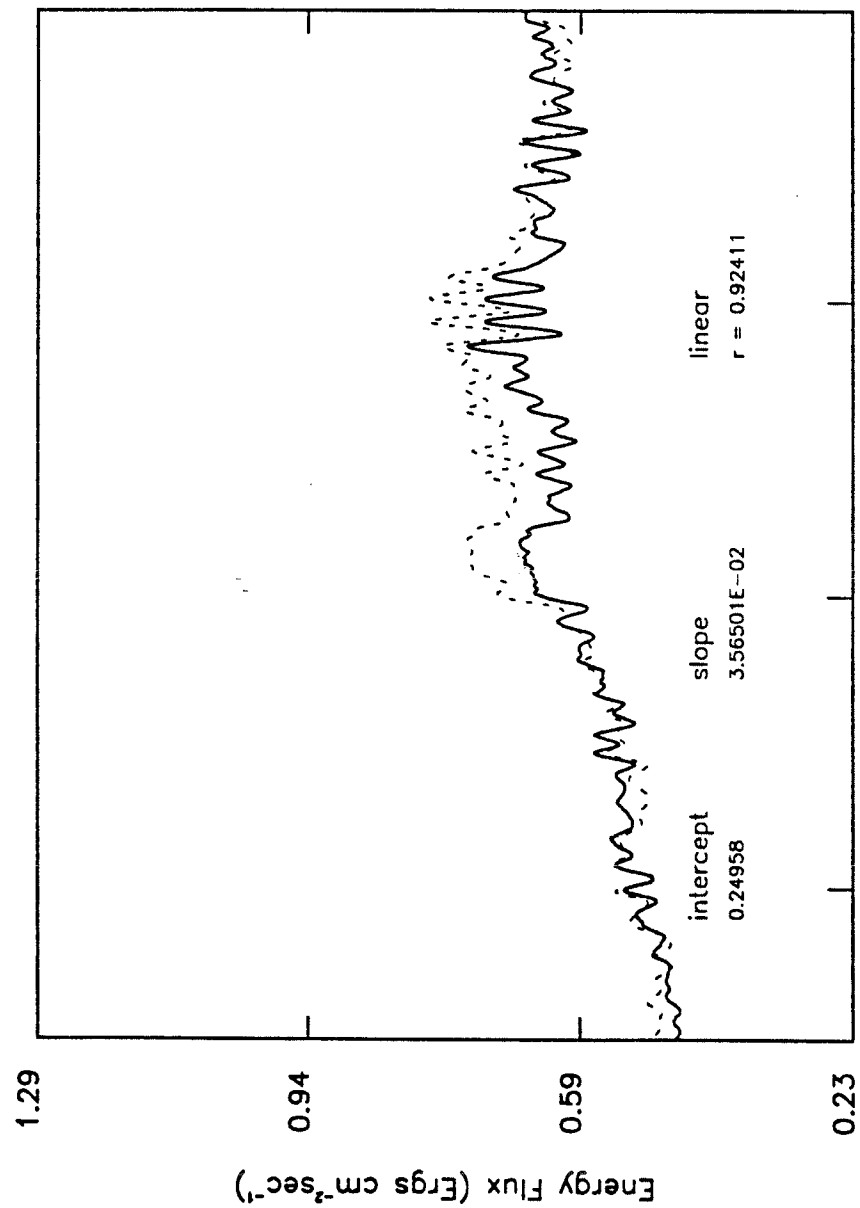

Figure 3.18 Chromospheric flux for 303.78 Å. The solid line is the calculated emission from equation (3.4) of the Hinteregger *et al.* [1981] EUV class formulation and the dashed line is the calculated emission from this model based on equation (3.5) using Lyman-α as the index. The correlation is for the period from July 1, 1977 through December 21, 1978.

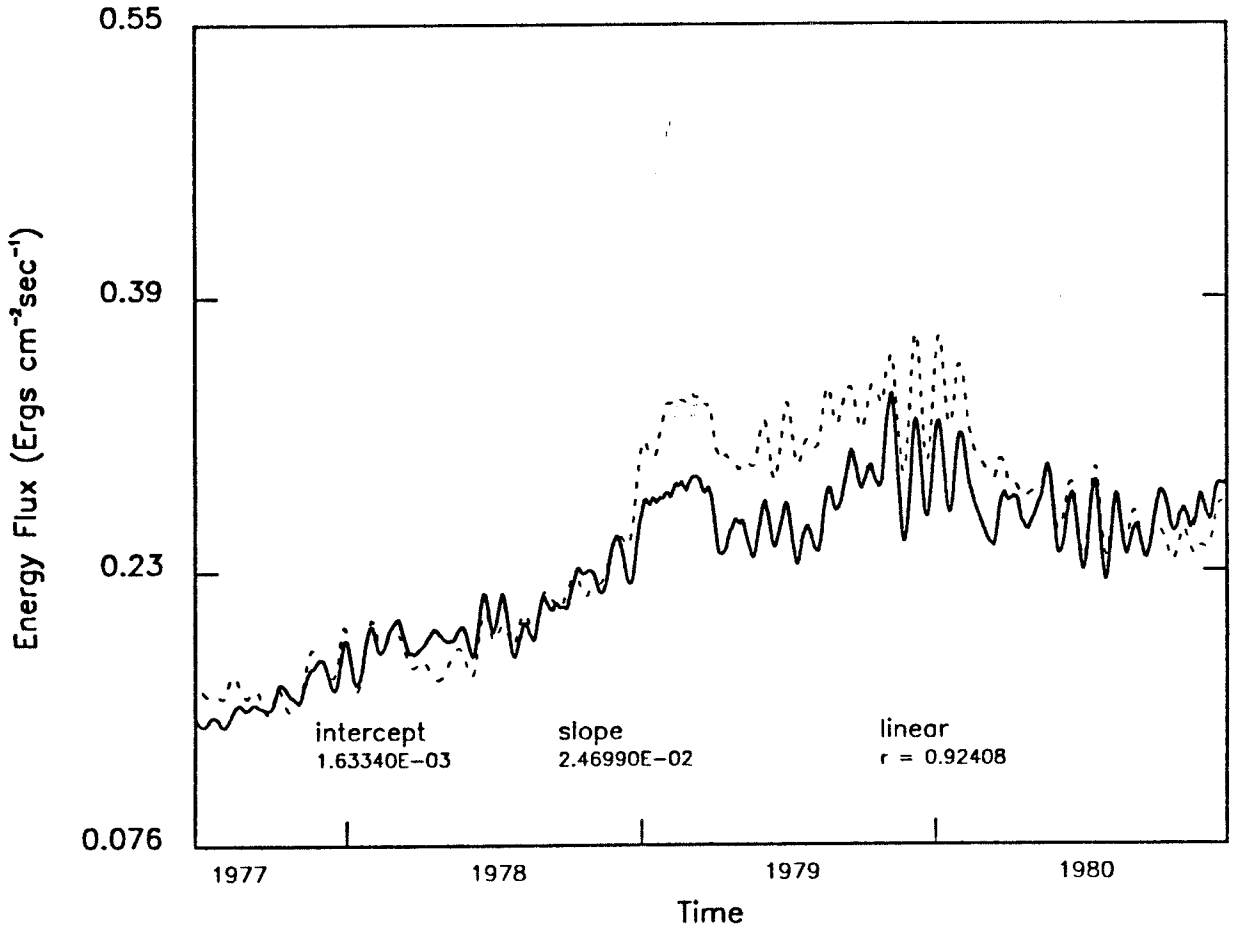

Figure 3.19 **Chromospheric flux for 851-900 Å.** The solid line is the calculated emission from equation (3.4) of the Hinteregger *et al.* [1981] EUV class formulation and the dashed line is the calculated emission from this model based on equation (3.5) using Lyman-α as the index. The correlation is for the period from July 1, 1977 through December 21, 1978.

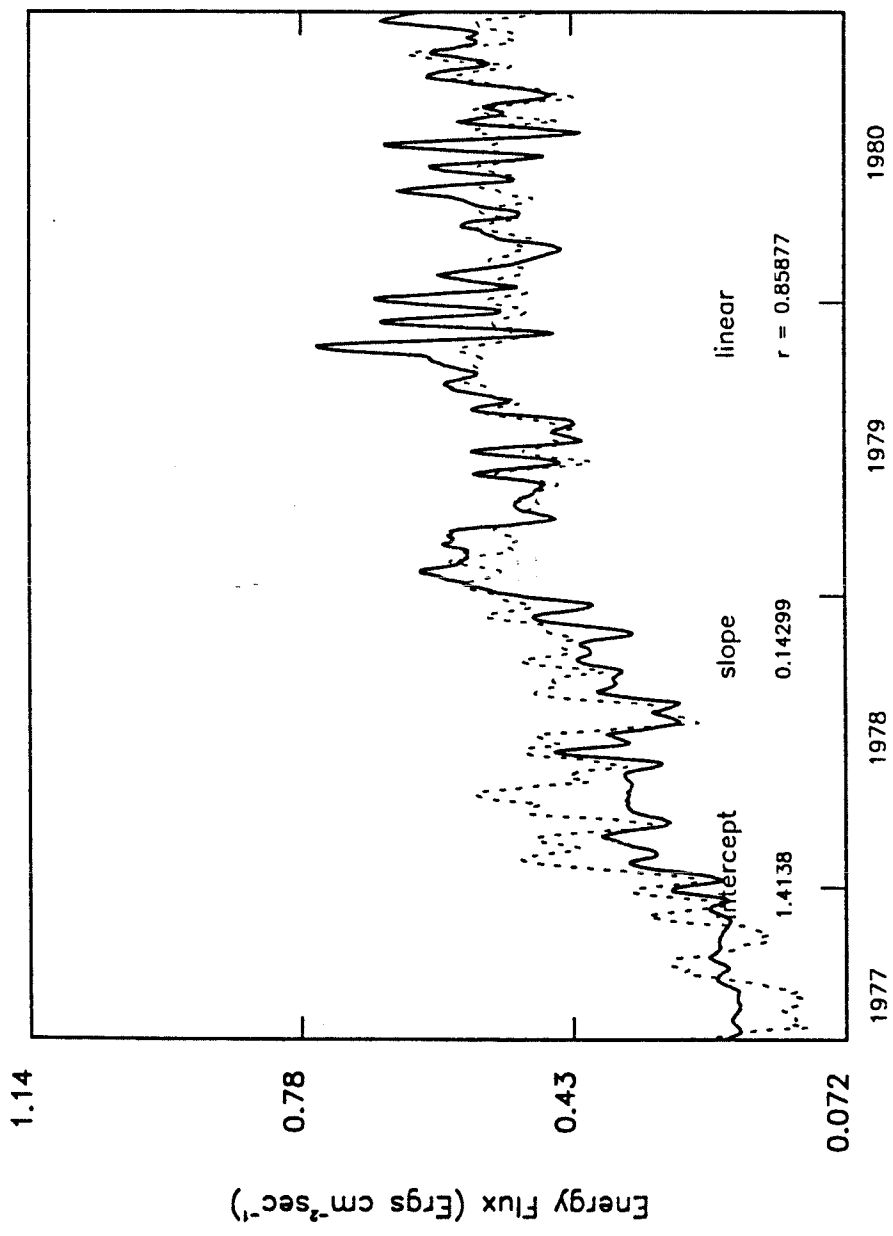

Figure 3.20 Coronal flux for 150-200 Å. The solid line is the calculated emission from equation (3.4) of the Hinteregger *et al.* [1981] EUV class formulation and the dashed line is the calculated emission from this model based on equation (3.5) using the 1-8 Å X-rays as the index. The correlation is for the period from July 1, 1977 through December 21, 1978.

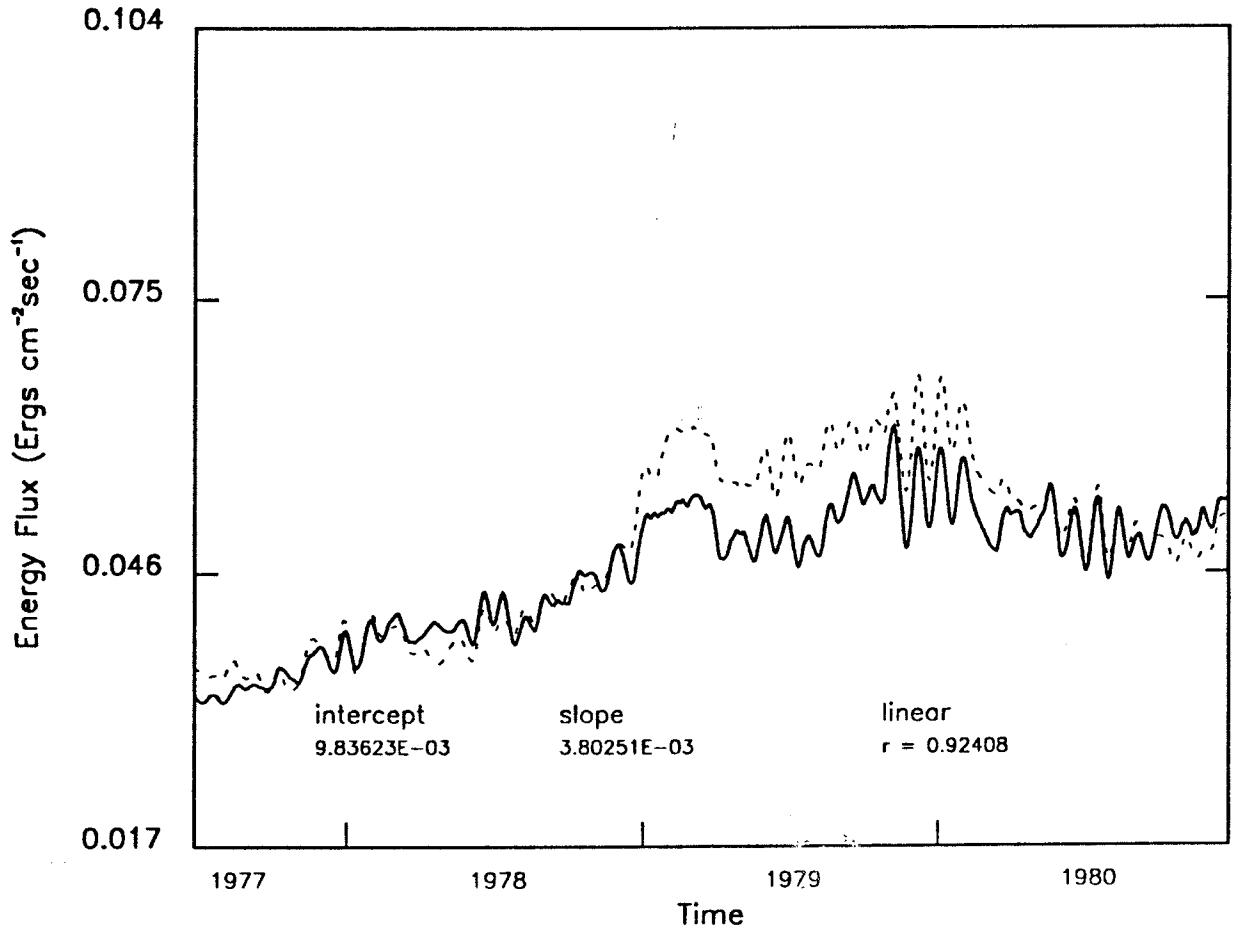

Figure 3.21 **Chromospheric flux for 150-200 Å.** The solid line is the calculated emission from equation (3.4) of the Hinteregger *et al.* [1981] EUV class formulation and the dashed line is the calculated emission from this model based on equation (3.5) using Lyman-α as the index. The correlation is for the period from July 1, 1977 through December 21, 1978.

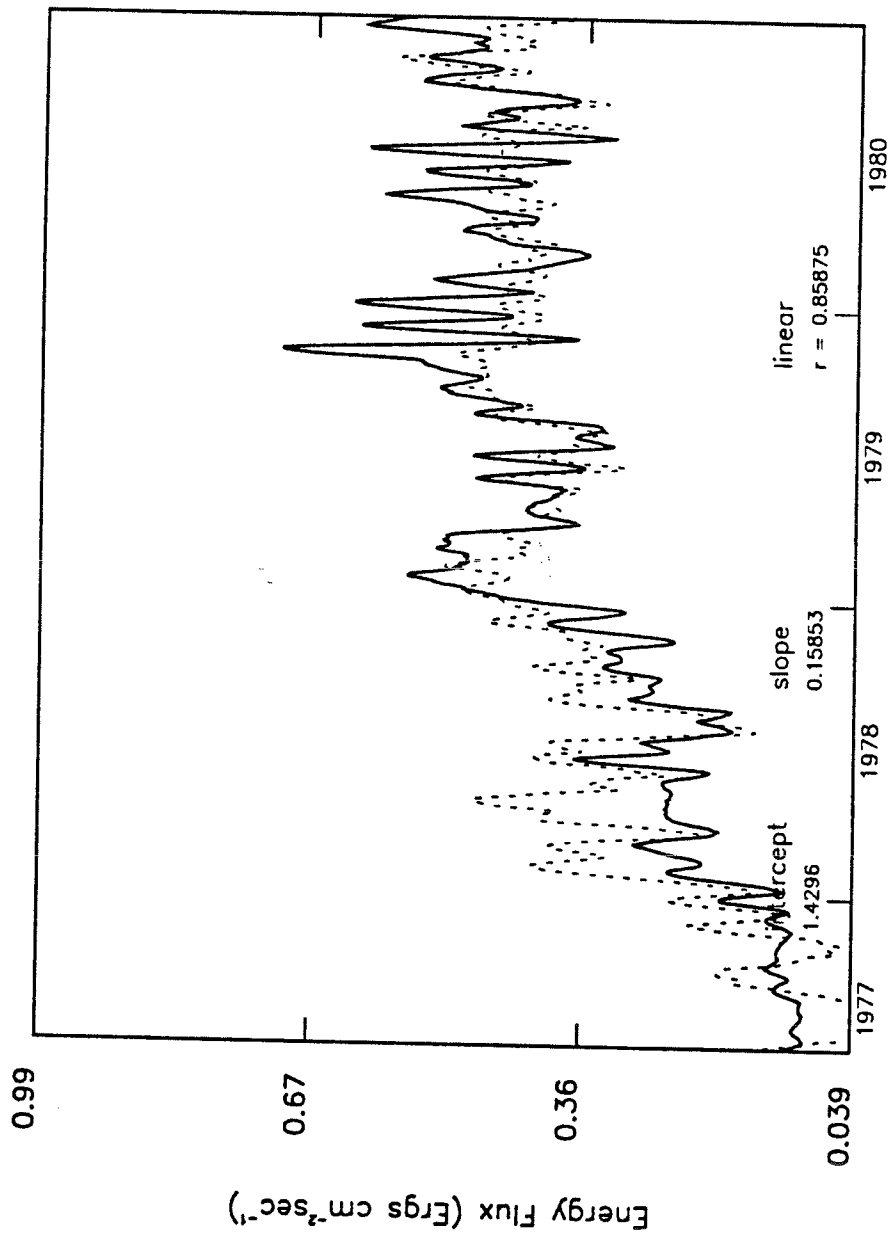

Figure 3.22 Coronal flux for 300-350 Å. The solid line is the calculated emission from equation (3.4) of the Hinteregger *et al.* [1981] EUV class formulation and the dashed line is the calculated emission from this model based on equation (3.5) using the 1-8 Å X-rays as the index. The correlation is for the period from July 1, 1977 through December 21, 1978.

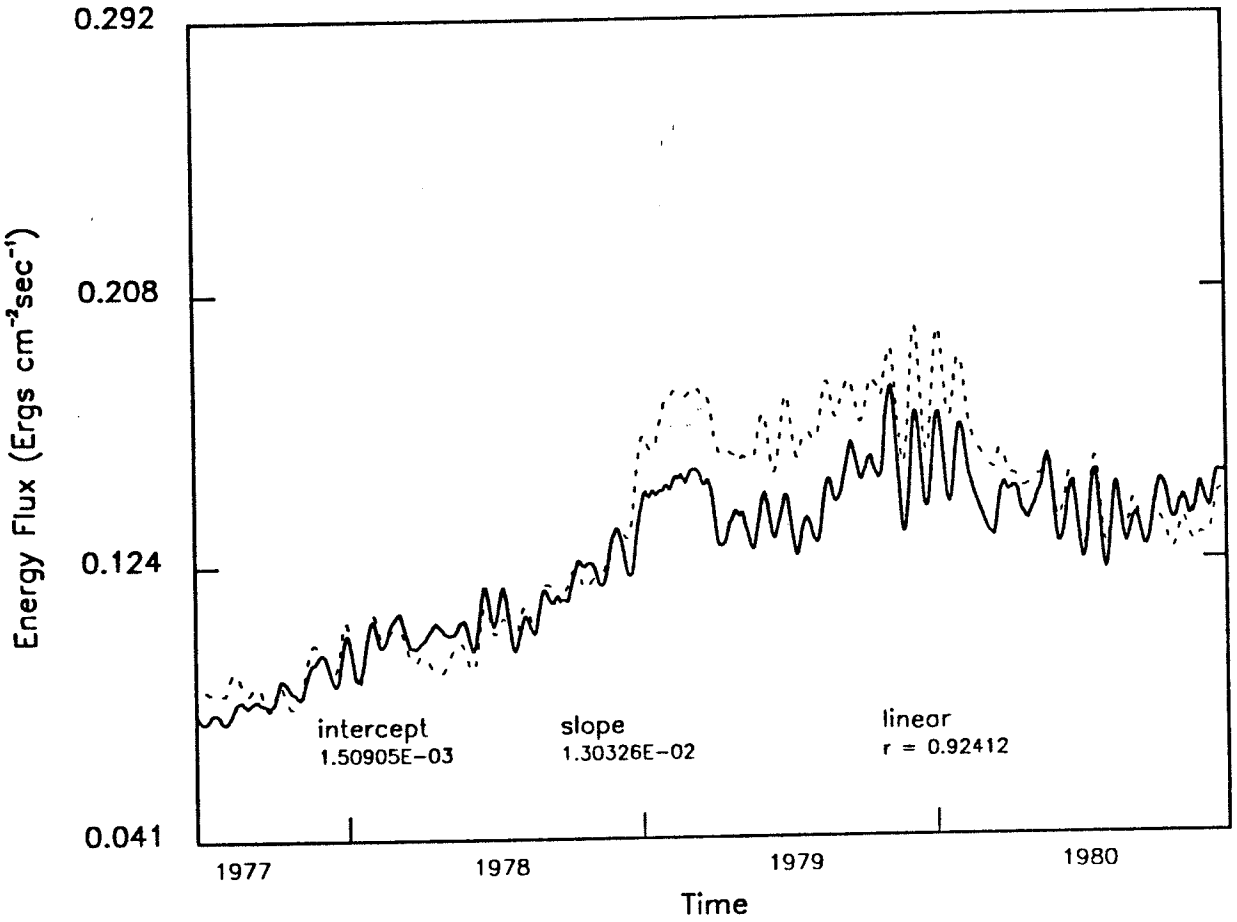

Figure 3.23 **Chromospheric flux for 584.33 Å.** The solid line is the calculated emission from equation (3.4) of the Hinteregger *et al.* [1981] EUV class formulation and the dashed line is the calculated emission from this model based on equation (3.5) using Lyman-α as the index. The correlation is for the period from July 1, 1977 through December 21, 1978.

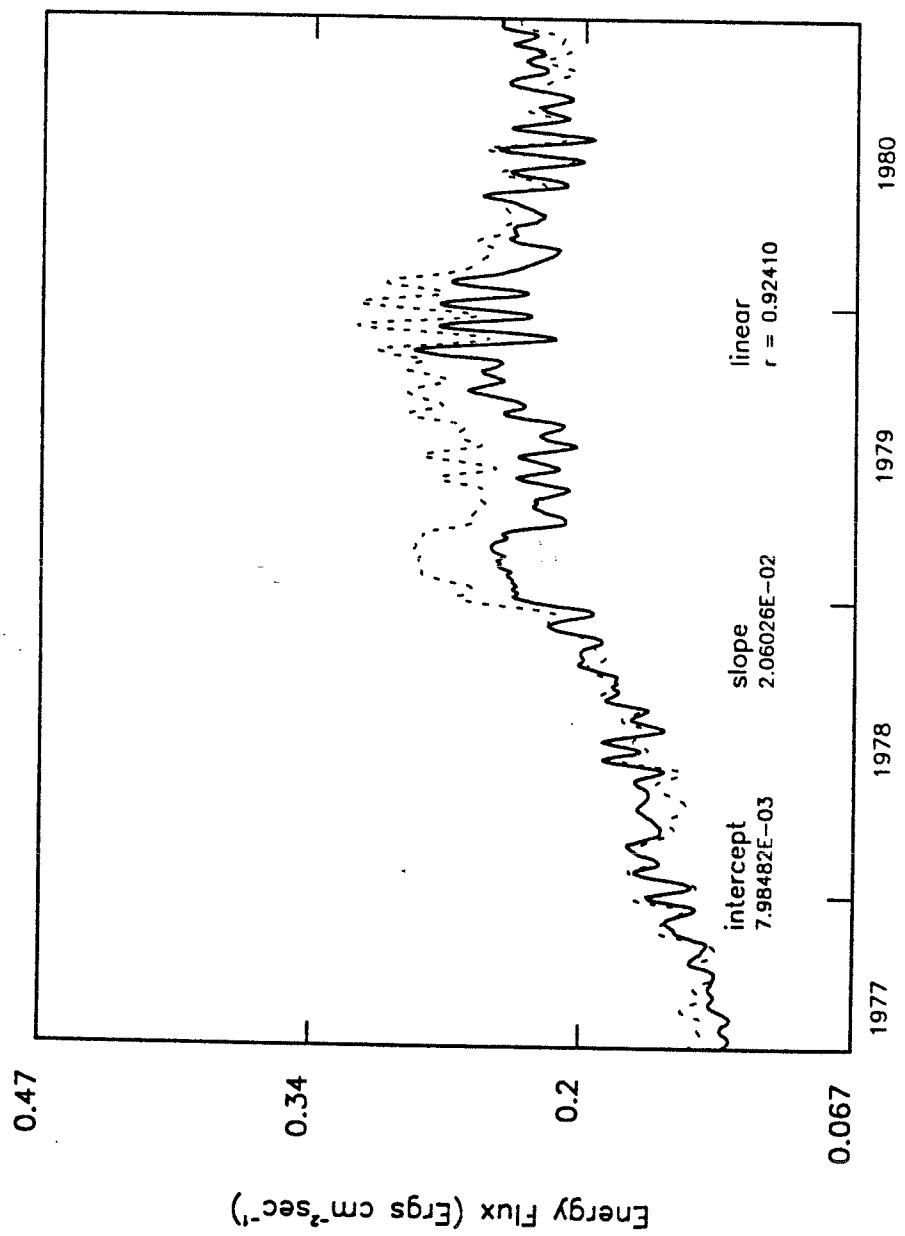

Figure 3.24 Chromospheric flux for 900-950 Å. The solid line is the calculated emission from equation (3.4) of the Hinteregger *et al.* [1981] EUV class formulation and the dashed line is the calculated emission from this model based on equation (3.5) using Lyman-α as the index. The correlation is for the period from July 1, 1977 through December 21, 1978.

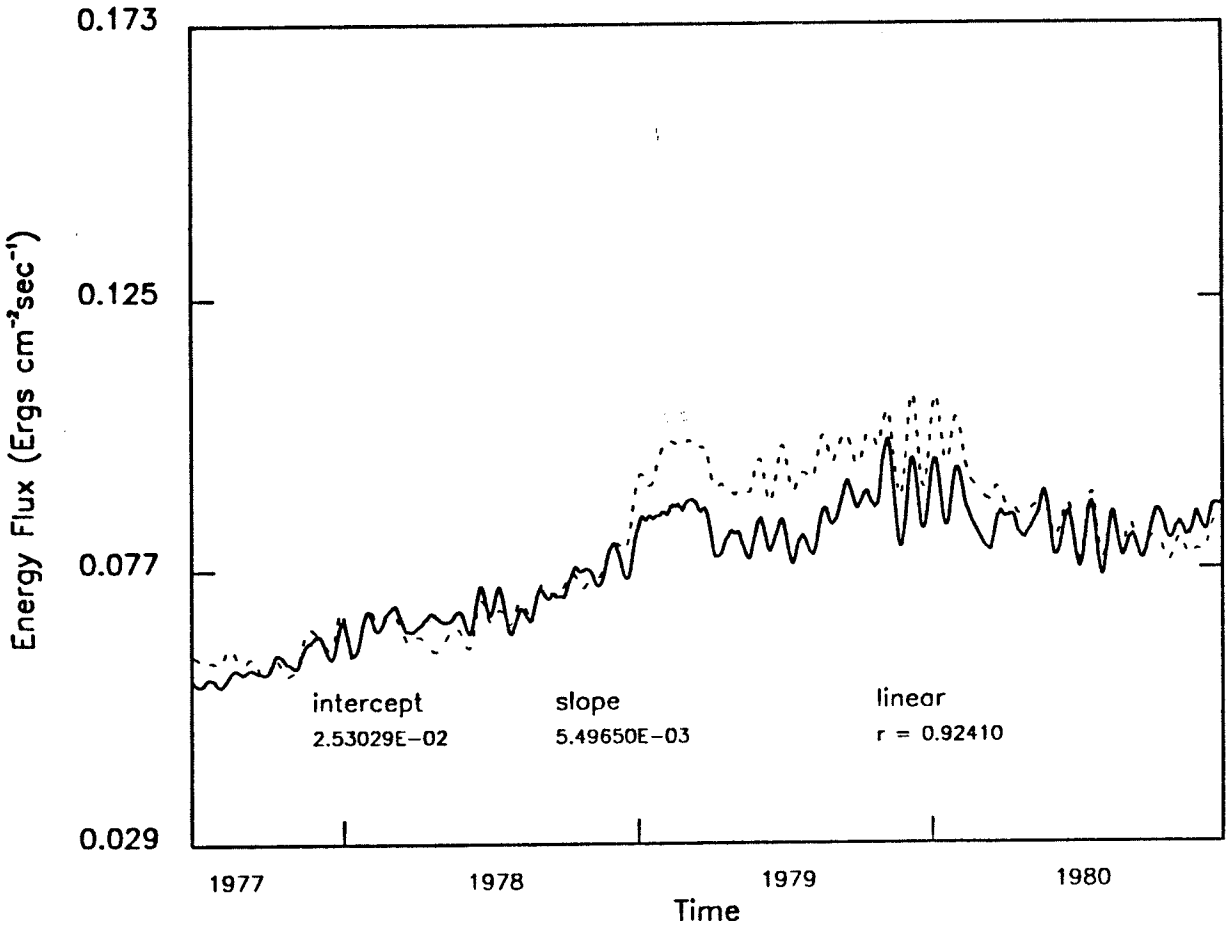

Figure 3.25 **Chromospheric flux for 629.73 Å.** The solid line is the calculated emission from equation (3.4) of the Hinteregger *et al.* [1981] EUV class formulation and the dashed line is the calculated emission from this model based on equation (3.5) using Lyman-α as the index. The correlation is for the period from July 1, 1977 through December 21, 1978.

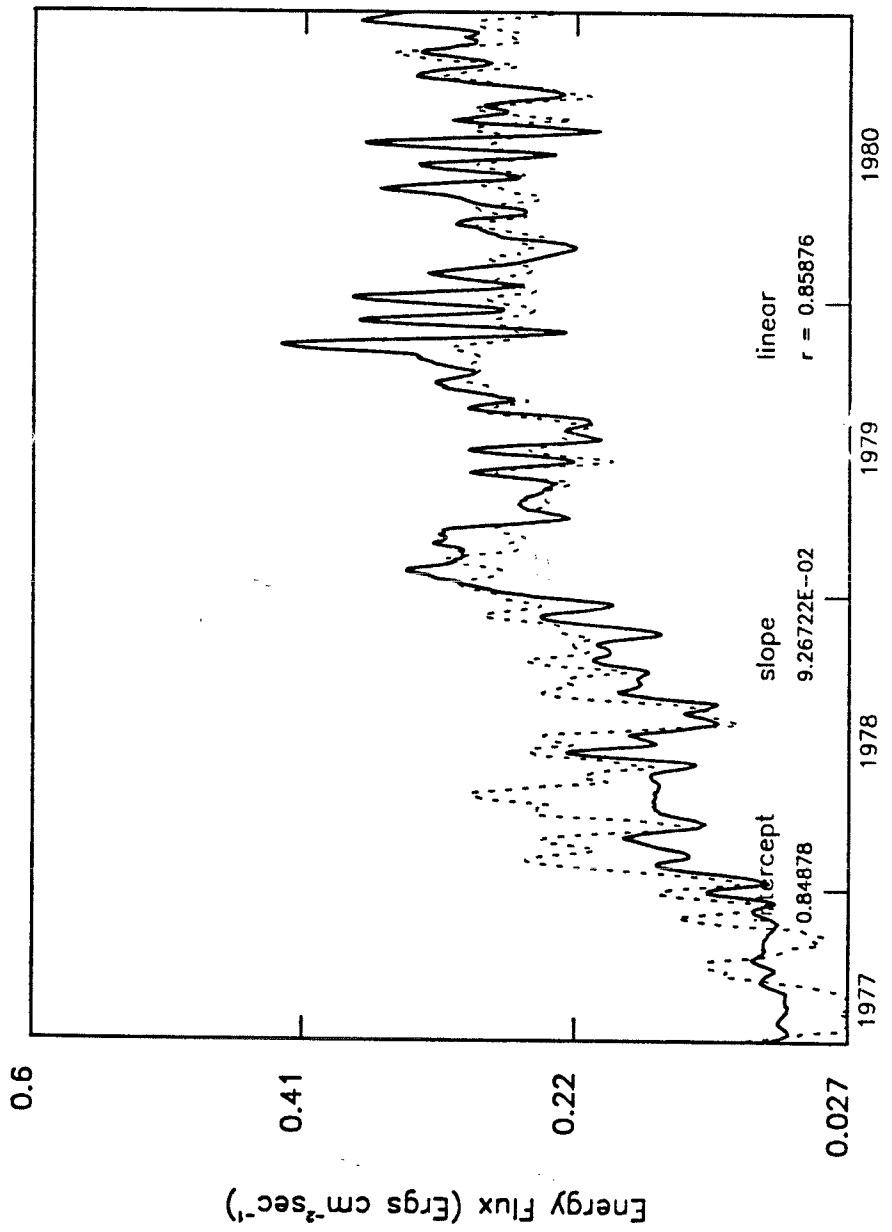

Figure 3.26 Coronal flux for 200-250 Å. The solid line is the calculated emission from equation (3.4) of the Hinteregger *et al.* [1981] EUV class formulation and the dashed line is the calculated emission from this model based on equation (3.5) using the 1-8 Å X-rays as the index. The correlation is for the period from July 1, 1977 through December 21, 1978.

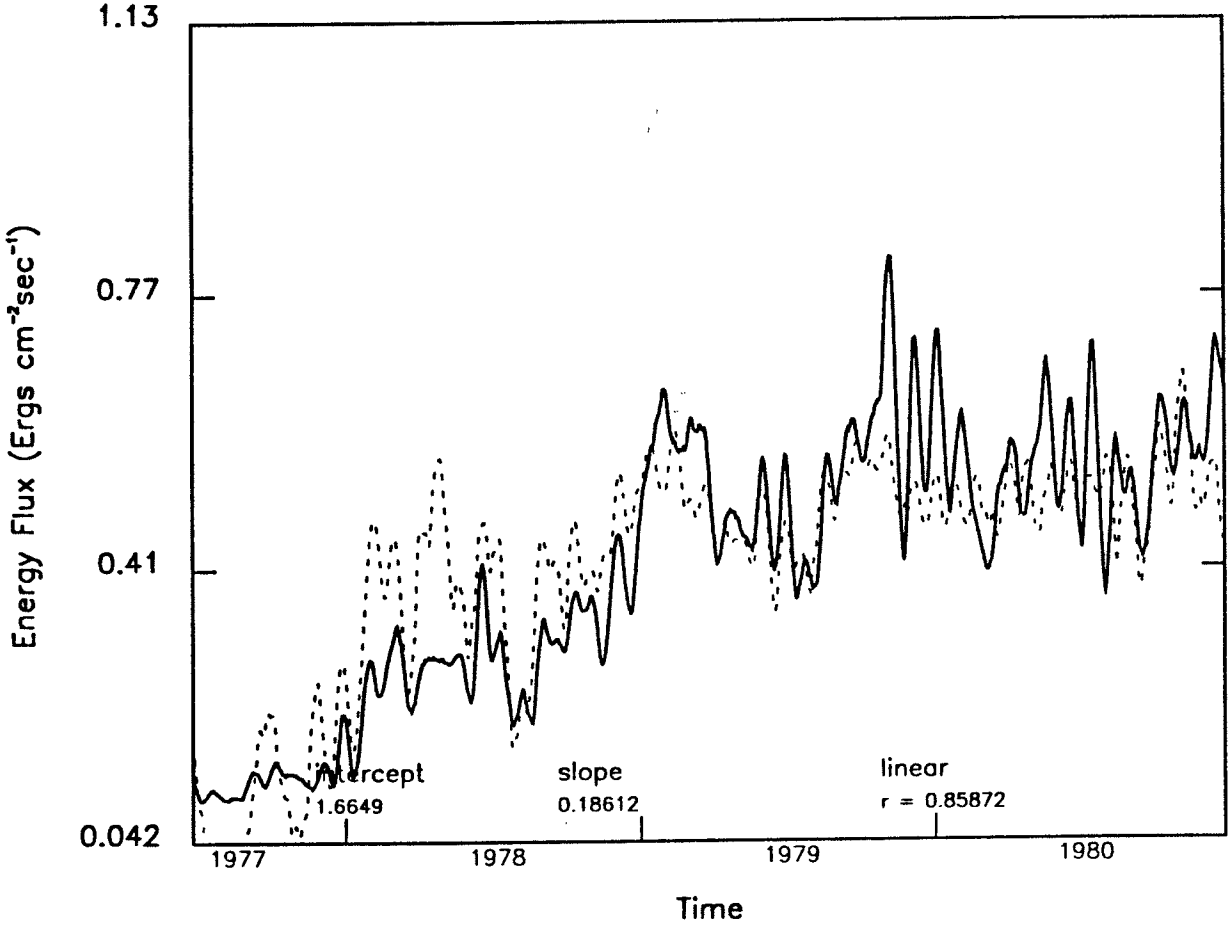

Figure 3.27 **Coronal flux for 250-300 Å.** The solid line is the calculated emission from equation (3.4) of the Hinteregger *et al.* [1981] EUV class formulation and the dashed line is the calculated emission from this model based on equation (3.5) using the 1-8 Å X-rays as the index. The correlation is for the period from July 1, 1977 through December 21, 1978.

either the AE-E Lyman-α from July 1, 1977 through December 21, 1978 or the Bouwer 1-8 Å X-rays for the same time periods. The modeled data are based on equation (3.5).

From these figures, it is apparent that there are very good long-term correlations while the correlations are moderate to poor for shorter time scales. The poor correlation over short time periods results from several error sources, as noted earlier. The AE-E Lyman-α dataset is missing two-thirds of its data, as evident in Figure 3.16, where only the 27-day solar rotational features are distinguishable. Short-term periodicities are therefore considered artifacts and are eliminated by a 27-day smooth prior to correlation. The Bouwer 1-8 Å representation gives periodicities less than 27 days in the X-ray data. However, this dataset is also smoothed over 27 days to eliminate short period terms. Additionally, some of the EUV emissions modeled by 1-8 Å X-rays are mixed emissions and not simply hot coronal fluxes. Despite these error sources, these figures show that the linear fit between the EUV flux and Lyman-α or 1-8 Å X-ray emissions is valid for longer time scales.

The correlations can be extended to periods of time outside the time frame of the correlated datasets, i.e., to 1) declining cycle 21 activity, 2) cycle 21 minimum conditions, 3) rising solar activity in cycle 22, and 4) high solar activity in cycle 22. Extensions 1 and 2 are based on the assumed general calibration agreement between the SME Lyman-α and the AE-E Lyman-α measurements. These, however, have some uncertainty margin which is not yet accounted for. Extensions 3 and 4 are based on the expectation that cycle 22 rising slope and solar maximum relative variation will be similar to cycle 21 although the total flux magnitudes may be offset. Figures 1.3, 1.4, 1.5, and 2.12 of R_z and $F_{10.7}$ EUV indices support this.

As a sample representation of this modeled EUV flux for declining ac-

tivity and minimum conditions in cycle 21, Figure 3.28 plots the three most important energy fluxes of He II, 850-900 Å, and 150-200 Å (cool coronal) for the decline and minimum of cycle 21. He II energy flux is long-term dominant, decreasing from near 0.4 to 0.35 ergs cm^{-2} sec^{-1} between 1982 and 1986. The 850-900 Å energy flux is about a factor of 4 smaller, while the 150-200 Å cool coronal flux totals about 30% smaller. The latter energy flux rises substantially above the He II value for certain time periods which correspond to periods of enhanced coronal activity on the solar disk. The relative magnitude of variation by 150-200 Å emissions is also larger than the He II variation on these moderate time scales. This is explained by the discussion for Figures 2.7 and 2.8, where coronally-produced emissions have substantially greater variation from high-to-low solar activity than chromospheric emissions.

In summary, the dominant solar EUV emissions which heat the thermosphere, such as chromospheric He II and 850-900 Å, as well as cool coronal 150-200 Å, are parameterized by Lyman-α and 1-8 Å X-rays, respectively. This is the fundamental building block in modeling thermospheric heating. There is a secondary factor which adds a refinement, an enrichment of detail in the time series final product. The geomagnetic index, A_p, is this secondary (and empirical) factor used in modeling the auroral region heating. The combination of modeled solar EUV heating and auroral heating leads to a final result which is the modeled thermospheric density at satellite altitudes.

Along with the A_p index, there are two additional solar-terrestrial coupled datasets which will also be briefly introduced in the remaining pages of this chapter. The satellite drag-derived density is the data against which the modeled density will be compared. The lower thermospheric nitric oxide density variation is the dataset which provides the values for the NO cooling mechanism used in the modeled densities of Chapter IV.

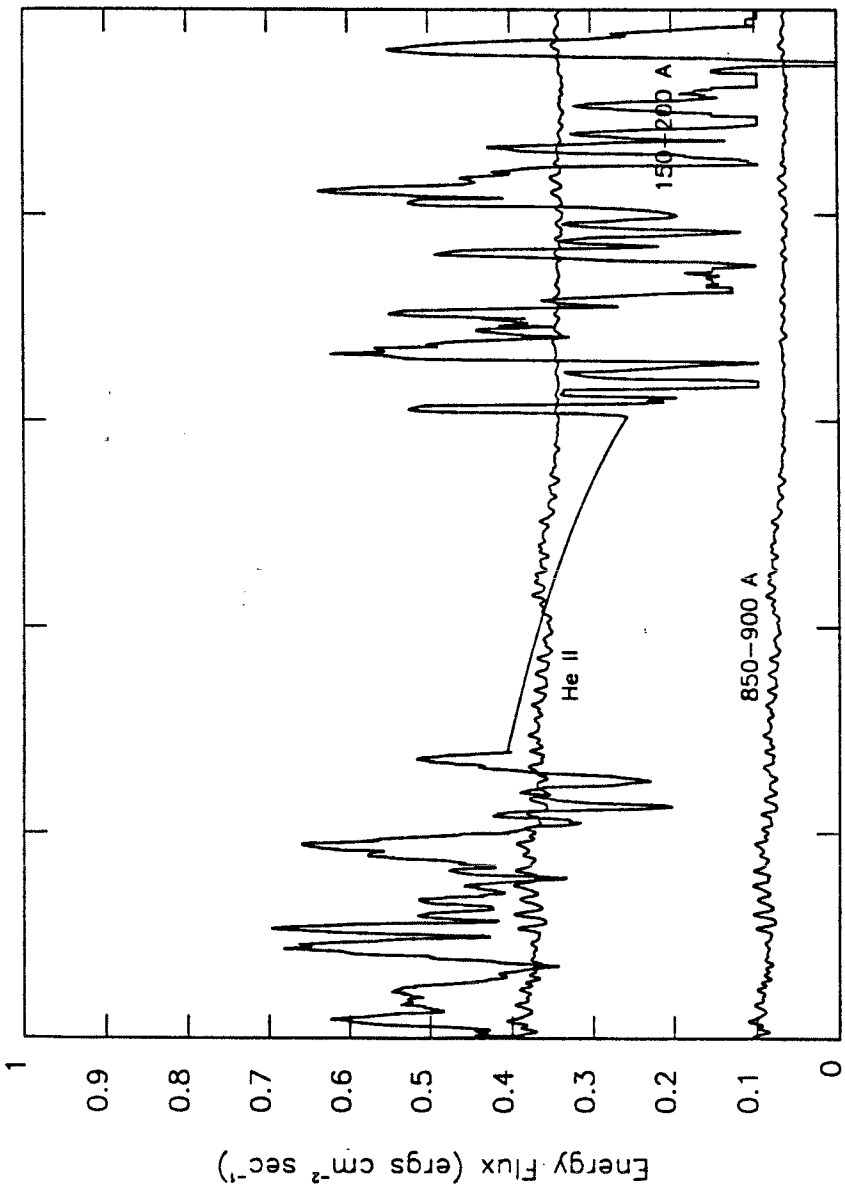

Figure 3.28 **Modeled EUV flux for 1982-1986.** The modeled data extends from January 1, 1982 through December 31, 1986. The He II and the 850-900 Å emissions are based on the Lyman-α index while the 150-200 Å emissions are based on the 1-8 Å X-ray index. The time period between May 1983 and December 1984 in the latter emission is only interpolated data between the earlier NSSDC GOES 2 data and the NOAA published data in 1985 and 1986.

3.5 Auroral Heating

Thermosphereric heating in the auroral regions occurs from particle precipitation and Joule heating for limited periods of time over specific latitudes. During high geomagnetic activity, magnetospheric electrons move along field lines and enter the thermosphere in the auroral regions. These electrons contribute to thermospheric heating by participating in neutral-electron reactions and, secondarily, in neutral-electron collisions. Ions, resulting in part from the enhanced electron density, are driven through the neutral gas by the electric fields. The collisions between these ions and the neutral species produce frictional, or Joule, heating from the ion drag.

While solar EUV flux provides the principal heat input to the thermosphere, it is possible for auroral particle precipitation and Joule heating to provide equal or greater heating in the auroral regions for short periods of time. The auroral regions extend between 60° and 80° north and south latitude. The effect on low Earth polar-orbiting satellites is significant under these heating conditions. Regions of increased heating lead to higher density and more forceful drag. This, in turn, causes substantial along-track error in orbit determination and prediction.

In this study, a limited effort is made to model this energy input through the use of the geomagnetic index, A_p, which characterizes the degree of geomagnetic disturbances. Mayaud [1980] discusses this index in more detail. These disturbances are often concurrent with auroral particle precipitation and Joule heating. Hence, in the atmospheric model of Chapter IV, this index is used to empirically scale the temperature profile in order to approximate the auroral region increased temperature contribution to the total global thermospheric temperature. There are other indices, not described here, which may also model the total energy input during geomagnetically

disturbed conditions. However, the detailed modeling of auroral heating is beyond the scope of this study, which concentrates on the solar EUV contribution to thermospheric heating.

3.6 Satellite Drag-Derived Density

By using an analytic solution of orbit radius as a function of density from King-Hele [1964], as simplified and described by Tobiska [1985] and Tobiska *et al.* [1987], it can be shown that the density of the thermosphere, through which a circular orbiting spacecraft travels, approximates the function

$$\rho = \frac{1}{3\pi r \frac{A}{m} C_d} \dot{P}. \quad \text{kg m}^{-3} \tag{3.6}$$

Here, r is a circular orbit radius, $\frac{A}{m}$ is the spacecraft area to mass ratio, C_d is the spacecraft-specific drag coefficient, and $\dot{P}$ is the dimensionless orbit period rate change obtained by differencing the orbit start times from the definitive ephemeris. For SME, it is shown in Figure 2.11.

The derived mass density, from the atmospheric drag on the SME satellite, is plotted in Figure 3.29. The derived density is processed in a manner similar to the $\dot{P}$ data. The original $\dot{P}$ is used in equation (3.6) to obtain the density. The outlying values beyond $\pm 2\sigma$ are zeroed and the total 28,987 points are then interpolated over the zeroed data and smoothed with a ± 97 point moving average which is equivalent to a 13-day smooth in this dataset. In order to compare this derived density to the other datasets in this study, the results presented in Figure 3.29 are one-day averages of 15 or 16 orbits per day.

There is a long-term decline in the SME derived density by a factor of 10 between high and low solar activity from 1982 through 1986 at SME alti-

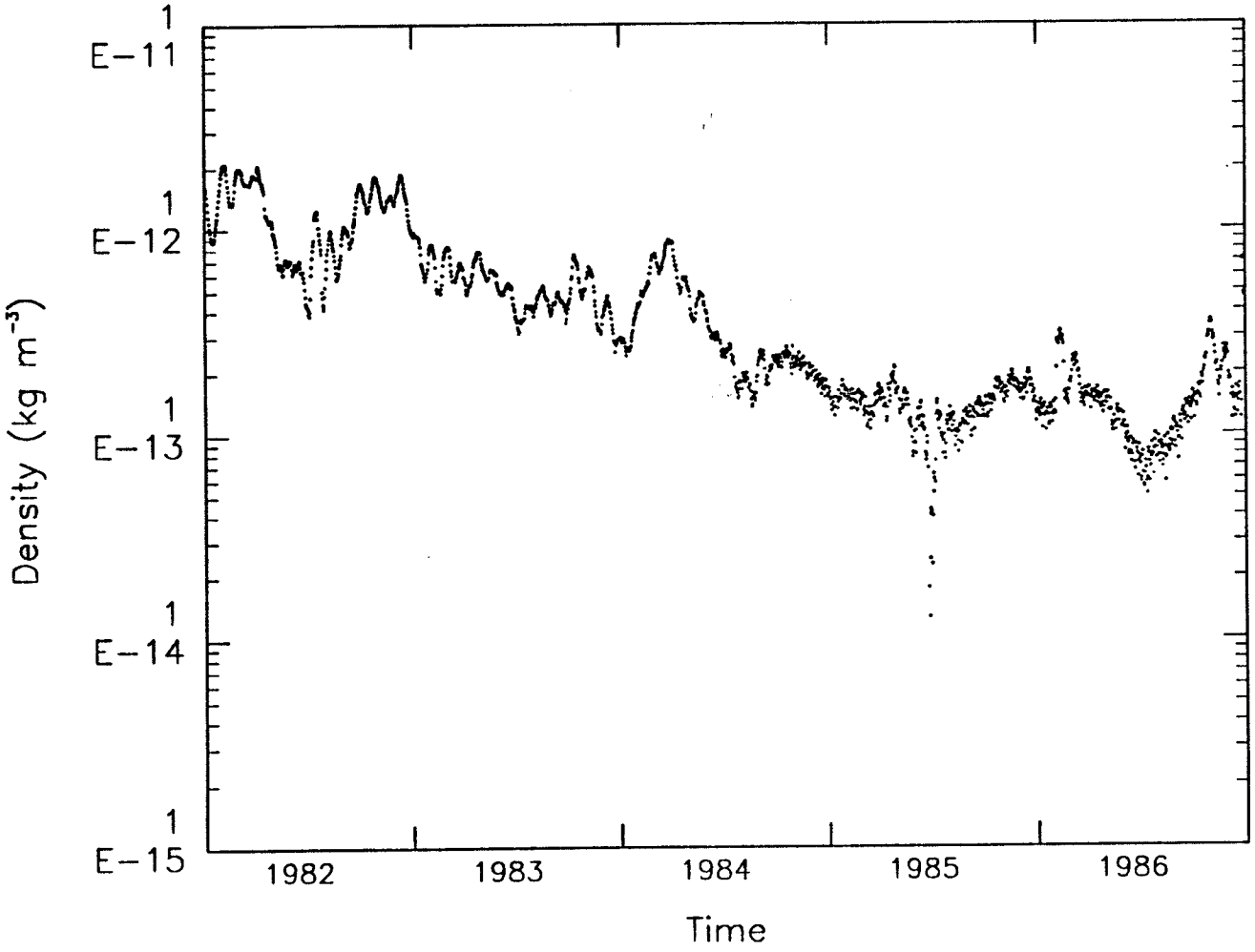

Figure 3.29 **SME derived density for 1982-1986.** This derived density data is from equation (3.6) and is a daily average value based on a 13-day smooth. It extends from January 1, 1982 through December 31, 1986.

tudes (535-510 km). Some features are discernible on shorter time scales, with a power spectrum analysis showing a 27-day period component related to solar rotation effects. The overall profile in Figure 3.29 indicates a continually decreasing derived density at the SME altitudes. The comparison of this derived density to the modeled thermospheric density will be detailed in Chapter IV.

3.7 Lower Thermospheric Nitric Oxide Variation

The variation of lower thermospheric nitric oxide with solar cycle activity has been briefly studied. Golshan and Sechrist [1975] indicated a change in nitric oxide measurements between high and low solar activity and concluded there exists a solar cycle dependence. Barth *et al.* [1988] have used the SME nitric oxide equatorial data at 110 km, presented in Figure 2.10, to demonstrate the long-term solar control of equatorial nitric oxide resulting from the influence of soft X-ray flux in the range of 18-100 Å. This can be explained in more detail. The nitric oxide equatorial data in Figure 2.10 shows similarities to the Lyman-α data in Figure 2.9 in the 27-day periodicity features but not in the magnitude of decline. There are similarities between NO and the 1-8 Å monthly mean background values in Figure 2.17 in which both show nearly an order of magnitude decline from 1982-1986. A mean high value of 3×10^7 molecules cm^{-3} in January 1982 to a mean low value of 4×10^6 molecules cm^{-3} in April 1985 marks nearly an order of magnitude decrease in nitric oxide. The best available soft X-ray coronal emissions, from Table 2.5 and Figure 2.7, change by an order of magnitude from high to low solar activity. Hence, long-term solar control of equatorial nitric oxide is possible.

To understand this solar control, the production and loss of NO in the lower thermosphere must be briefly described. Lower thermospheric NO is

mainly produced from the reaction

$$N(^2D) + O_2 \rightarrow NO + O \tag{3.7}$$

and secondarily by

$$N(^4S) + O_2 \rightarrow NO + O. \tag{3.8}$$

The rate coefficient for reaction (3.8) contains a temperature dependence, where higher temperatures produce more NO. However, the ground state atomic nitrogen, $N(^4S)$, also destroys NO in the loss process

$$NO + N(^4S) \rightarrow N_2 + O. \tag{3.9}$$

Another NO loss mechanism is the charge exchange of NO with ionized molecular oxygen

$$NO + O_2^+ \rightarrow NO^+ + O_2. \tag{3.10}$$

$N(^2D)$ and $N(^4S)$ are produced as a result of the dissociative excitation of molecular nitrogen

$$N_2 + e^* \rightarrow N(^2D) + N(^4S). \tag{3.11}$$

Additionally, $N(^2D)$ is produced by dissociative recombination of ionized nitric oxide

$$NO^+ + e \rightarrow N(^2D) + O \tag{3.12}$$

and as the result of ionization of N_2

$$N_2 + h\nu \rightarrow N_2^+ + e \tag{3.13}$$

and the subsequent reaction with atomic oxygen

$$N_2^+ + O \rightarrow NO^+ + N(^2D). \tag{3.14}$$

This photochemistry is described in more detail by Cleary [1985], Barth *et al.* [1988], and Siskind [1988].

Barth *et al.* suggest that soft X-rays produce substantially more energetic photoelectrons which then leads to an increased concentration of excited atomic nitrogen, $N(^2D)$, through the reaction (3.11). A key element in this suggestion is that the soft X-rays from 20-100 Å, which are coronally produced, vary to a greater extent than the chromospheric fluxes. Specifically, since the soft X-rays have unit optical depth in the lower thermosphere for all solar conditions, and since they ionize major and minor constituents at the 100-120 km level, it is reasonable to conclude that a major source for the photoelectrons in reaction (3.11) is the soft X-ray flux. The specific effect of solar cycle variation in soft X-rays deposited between 100 and 120 km is to produce substantially greater or lesser concentrations of $N(^2D)$ compared to $N(^4S)$ at a relatively fixed altitude level. Not coincidentally, NO concentrations consistently peak between 110 and 120 km for all solar activity. It is easy to see from reaction (3.7) how increased $N(^2D)$ leads directly to increased NO. The relationship of $N(^4S)$ to NO is more complicated, since it both produces and destroys NO by reactions (3.8) and (3.9). In general, however, there is an equilibrium in this creation - destruction process. Thus, the net effect of soft X-ray variation over a solar cycle is to create greater or lesser densities of NO, as pointed out by Barth *et al.*, at a nearly constant altitude level.

This hypothesis is supported in several ways. The unit optical depth plot in Figure 3.7 substantiates the claim for energy deposition at a constant altitude. Figures 2.7 and 2.8 and Tables 3.10 through 3.13 show a factor of 2 to 9 increase, depending upon chromospheric or coronal source region, in the best available soft X-rays and their energy flux from low to high solar activity. 1-8 Å energy flux in Figures 2.16 and 2.17 shows a factor of 7 decrease from

high to low activity. These plots support the Barth *et al.* claim for energy variation available to produce N(^2D).

The variation in the lower thermospheric NO over a solar cycle has important implications for the thermal budget. NO is an efficient radiator at 5.3 μm and greater NO concentrations during high solar activity simply mean that the lower thermosphere has a greater capacity for cooling. Hence, for either high or low solar activity, the lower thermospheric temperatures remain relatively constant, as demonstrated by the MSIS empirical model plots in Figures 1.6b and 1.6d. This greater cooling capacity is partially exhibited in a larger temperature gradient in the lower thermosphere between 120 and 180 km. Chapter IV discusses in more detail the effects of NO cooling for high and low solar activity.

3.8 Summary

In this chapter, it is recognized that the lack of EUV data between the 1970s and the 1990s gives impetus to finding methods for parameterizing EUV flux. Toward this effort, the dominant EUV fluxes which heat the thermosphere are detailed and correlations are made between Lyman-α, $F_{10.7}$, 1-8 Å X-rays, and the EUV fluxes during the period of the rising solar cycle 21 activity. Lyman-α and 1-8 Å X-rays are found to be EUV indices for two reasons: first, they are created in the chromosphere and corona, as are the dominant EUV fluxes which heat the Earth's thermosphere; second, there are high, long-term correlations between these indices and the dominant EUV fluxes during the rise of cycle 21. Additional motivations for using these two emissions as EUV indices comes from their consistent measurement on a daily basis above the atmosphere and the finding that $F_{10.7}$, the historically used EUV index, is found to be insensitive to chromospheric flux changes during

periods of solar minimum conditions.

The dominant EUV energy emissions for the declining period of cycle 21 (1982-1986), based on the SME Lyman-α and GOES 1-8 Å X-ray flux, are calculated from a model of EUV energy flux based on the above linear correlations. A_p is used as an empirical auroral thermospheric heating indicator, satellite drag-derived densities at SME altitudes during the decline of cycle 21 are reviewed, and lower thermospheric equatorial nitric oxide concentration at 110 km is reviewed for its contribution to lower thermospheric cooling and its variations due to coronally-produced soft X-rays.

CHAPTER IV

THERMOSPHERIC MODELING

The collection of observational data in Chapter II and the analysis in Chapter III lay the basis for modeling thermospheric densities and temperatures. Chapter IV describes this modeling and its results. Section 4.1 details the structural and dynamical concepts at the basis of this modeling. It includes a brief description of the basic principles of upper atmospheric physics and a description of the one-dimensional thermosphere model with its initial conditions, boundary conditions, density calculations, and the heating and cooling mechanisms. The model results are discussed in section 4.2 for 1) the two cases of solar maximum and minimum which validate the model in comparison to another model and 2) the modeled time series of densities during the decline of solar cycle 21.

4.1 Thermospheric Structure and Dynamics

4.1.1 Basic Principles

The fundamental parameters for describing both structure and dynamics have been clarified by theorists and experimentalists over the past four decades and are referred to in the previous chapters. The mass of gas atoms and molecules and their distribution, the velocities of these particles, and their thermal characteristics resulting from a variety of photon interactions or chemical reactions are the main physical parameters needed to formulate the structural and dynamical models. The three conservation equations of mass,

momentum, and energy are used as the basic principles in thermospheric modeling.

Banks and Kockarts [1973] have reviewed the thermal structure of the heterosphere in some detail. A brief outline of their discussion follows. In a region of diffusive equilibrium, a simplifying assumption is often made that the low pressure gas is in an ideal state following the Ideal Gas Law. The pressure profile may be written according to the barometric law with a constant scale height, H, where

$$p(z) = p_0 e^{-dz/H} \quad \text{dynes cm}^{-2} \tag{4.1}$$

and where pressure drops off exponentially with altitude, z. p_0 is the reference altitude pressure, $dz = z - z_0$, and is the altitude difference between a gas layer boundary and a reference altitude, and $H = kT/mg$ which is the scale height where k is Boltzmann's constant, T the gas temperature, m is the gas particle mass, and g is the local gravity. Pressures are calculated by numerical integration after the temperature is solved in the energy conservation equation. The reference pressure has the value of the pressure at the next lower altitude level which is -2 km in this study.

A time-dependent model of thermospheric temperature is used where the energy conservation equation is solved and is written as

$$\rho c_v \frac{\partial T}{\partial t} + \nabla \cdot \mathbf{E} = P - L. \quad \text{ergs cm}^{-3} \text{ sec}^{-1} \tag{4.2}$$

The conductive heat flow, $\mathbf{E} = -\lambda \nabla T$, results from a temperature gradient and assumes that there are no diffusion velocities of the gas species. This assumption is based on the condition of diffusive equilibrium and implies that heat conduction occurs on a faster timescale than molecular diffusion. λ is the thermal conductivity coefficient and ∇T is the temperature gradient. The product of the mass density, ρ, the specific heat at constant volume, c_v, and

the rate of change of the temperature, $\partial T/\partial t$ are combined with the heat flow gradient to express the time rate of temperature change equal to the sum of the heating, P, and cooling, L, processes. Equation (4.2) can be rewritten as the one-dimensional, time-dependent energy equation

$$\frac{\partial T}{\partial t} = \frac{\lambda}{\rho c_v}\frac{\partial^2 T}{\partial z^2} + \frac{1}{\rho c_v}(P - L). \quad {}^\circ\mathrm{K\ sec}^{-1} \tag{4.3}$$

The Crank-Nicolson finite difference numerical method of solving this parabolic second order partial differential equation, using the Thomas algorithm, is detailed by von Rosenberg [1969] and is discussed in Appendix A.

4.1.2 One-Dimensional Model

Equation (4.3) is solved for each variable at an nth time step. Starting with an arbitrary temperature and density profile, the new pressure profiles for O, O_2, N_2, CO_2, NO, He, and H are determined. Next, the proper EUV flux for a specific date is obtained, followed by the calculation of the EUV heating rates, the auroral heating rates, the dissociation heating and radiative cooling processes, the thermal conductivity coefficient, and the eddy and turbulent heating rates. Finally, the coefficients for the numerical solution to the partial differential equation are formed. A new temperature profile is then calculated from the matrix solution method of the Thomas algorithm. The new temperature profile is used to recalculate the above heating or cooling rates and coefficients. Convergence is achieved when $|T_{\infty_{n+1}} - T_{\infty_n}| < 0.5^\circ$ K. The following discussion details this model. The processes which are most active below 120 km have limited significance for upper thermospheric conditions and are not discussed in detail.

The model starts with the initial condition of $t_0 = 0$, where the time step described in Appendix A, dt, of 2500 seconds has been empirically determined. It is an optimum time step for both minimizing the iterations re-

quired for convergence and for producing a monotonically decreasing change in exospheric temperature. While von Rosenberg has noted the stability for convergence of the Crank-Nicolson method regardless of most time steps used, this study attempts to maintain a smooth approach to the convergent T_∞ in order to retain relative accuracy within the constraints of the model.

The boundary conditions, as described in Appendix A, are based on the assumption of an isothermal temperature profile at the top of the thermosphere and a steady state temperature condition at the turbopause. This model has an altitude profile on a 2 km grid size between 120 and 450 km. The temperature at 450 km is considered to be the exospheric temperature and the altitude level of 120 km is taken as the turbopause level.

Three major species, O, O_2, and N_2, and four minor neutral species, CO_2, NO, He, and H, are considered in this model. The latter four species do not make a significant compositional contribution to the thermosphere but are important for either their radiative cooling effects (CO_2 and NO) or their contributions to the exospheric density (He and H). Ion temperatures and ion densities are not included. They contribute small temperature and density effects even though they are important in some chemical reactions. The initial major species' arbitrary profiles at t_0 are obtained from the MSIS 83 model for either low or high solar activity conditions. Then, with each temperature iteration, the new pressure profiles are integrated with a 2 km altitude step. The concentration, n, is solved from the pressure solution using the Ideal Gas Law.

NO density profiles 1) are determined from a photochemical model [Cleary, 1985] for either low or high solar activity before the SME time period or 2) are calculated from the SME dataset using the Cravens *et al.* [1985]

formulation

$$n = n_m \left\{ e^{-(z-z_m)/H_t} - 0.5e^{-(z-z_m)/0.5H_t} \right\} \quad \text{molecules cm}^{-3} \qquad (4.4)$$

for $z > z_0$ and $n = 0$ where $z \leq z_0$. This latter method uses the SME NO density, n_m, on a given date at the 110 km level, z_m, and is combined with a fixed topside NO scale height, H_t. This discussion is detailed by Cravens *et al.*

CO_2 is initially given an empirical profile with a mixing ratio at the mesopause of 2.9×10^{-4}. With each new temperature profile, a new column density of CO_2 is solved by integration.

The He and H concentrations vary depending upon the level of solar activity. Both of these constituents are also given an empirical initial profile with a mixing ratio at the mesopause of 5.24×10^{-6} for He and 1.9×10^{-6} for H. This method is used because the CO_2, He, and H profiles are not calculated in the version of MSIS 83 used here. After convergence to T_∞, all densities are extended to 1000 km by integration for astronautical purposes.

The initial solar EUV flux is given by the AE-E observed values at 37 wavelength groups for low or high solar activity. These are described in Chapter II and shown in Tables 2.2 and 2.3 as well as Figures 2.4 and 2.5. The modeled solar EUV flux during the decline of cycle 21 is described in Chapter III in Tables 3.10, 3.11, 3.12, and 3.13. To calculate this EUV flux, the Lyman-α and 1-8 Å X-ray data for a given date is obtained and converted through the linear relations into an energy flux at that wavelength using equation (3.5) which is reproduced here as equation (4.5). At each wavelength, the EUV energy flux, E_λ, is calculated as the sum of the chromospheric and coronal energy flux components, where

$$E_\lambda = a_1 + b_1 \mathrm{Ly}_\alpha + a_2 + b_2 ln(\mathrm{Xray}_{1-8}). \quad \text{ergs cm}^{-2} \text{ sec}^{-1} \qquad (4.5)$$

a_1 and b_1 are the intercept and slope of the chromospheric component and a_2 and b_2 are the intercept and slope of the coronal component.

EUV heating of the thermosphere is described in detail in section 3.2. Equation (3.1) is modified to represent the EUV heating rate per unit volume

$$q_{euv}(z) = \sum_i \sum_\lambda n_i(z)\sigma_i(\lambda)E(\lambda,z)\varepsilon_i(z) \quad \text{ergs cm}^{-3}\ \text{sec}^{-1} \tag{4.6}$$

using the EUV energy flux described above. With a solar zenith angle of 60° and a parameterized neutral constituent heating efficiency described by Roble and Emery [1983] which was discussed earlier, the EUV heating rate is calculated at each wavelength, λ, for each species, i.

Auroral heating processes resulting from the increased electric field strength and conductivity during active geomagnetic periods are parameterized by the A_p index. Here, the A_p value is used to scale the auroral heat flux term empirically by the method described below. It is necessary to include auroral heating to achieve comparable values of T_∞ with MSIS 83 and Roble [1987]. Roble and Kasting [1984] concluded this and supported the results of previous work.

The high latitude heating rate formulation is given by Roble and Kasting and is simplified here, where

$$q_p = AP_p \quad \text{ergs cm}^{-3}\ \text{sec}^{-1} \tag{4.7}$$

$$q_J = BP_J. \quad \text{ergs cm}^{-3}\ \text{sec}^{-1} \tag{4.8}$$

The two components used are 1) the heating due to particle precipitation in the auroral oval and 2) the heating from Joule dissipation of ionospheric currents. The particle and Joule heating rates are parameterized by Chapman functions, which model the vertical distribution only, in the form

$$P_p = \exp(1 + x - \exp x) \tag{4.9}$$

$$P_J = \exp(1 + y - \exp y) \tag{4.10}$$

$$x = (\frac{z_a - z}{D_H}) \tag{4.11}$$

$$y = (\frac{z_b - z}{D_b}). \tag{4.12}$$

In these relations, A and B are the maximum heating rates used in the expressions discussed above and are empirically formulated in this study as

$$A = (-0.0195 + 0.0059A_p)/(\Delta z \sum_z P_p) \quad \text{ergs cm}^{-3}\ \text{sec}^{-1} \tag{4.13}$$

$$B = (-0.26 + 0.06A_p)/(\Delta z \sum_z P_J) \quad \text{ergs cm}^{-3}\ \text{sec}^{-1} \tag{4.14}$$

where $\Delta z = 2 \times 10^5$ cm and $\sum P$ is the total of the Chapman function values at all altitudes which is used to normalize the value at each altitude level. z_a is the height of maximum ionization at 105 km and z_b is the height of maximum Joule heating at 130 km. D_H = 10 km which is the altitude parameter for particle ionization and D_b = 20 km which is the altitude parameter for Joule dissipation discussed by Roble and Kasting. The A_p scaling value is determined from the following empirically determined constraints. Global energy input due to particle precipitation, the numerator of A from equation (4.13), is between 0.01 and 0.14 ergs cm^{-2} sec^{-1} and is used for a 22-day filtered A_p time series in the range of 5 to 27. Global Joule energy input, the numerator of B from equation (4.14), is 0.04 to 1.36 ergs cm^{-2} sec^{-1} over the same filtered A_p range. The 22-day filtered A_p values have periodicities less than 22 days removed. In this study, an A_p value of 17.3 is used for solar maximum conditions which is the average value during a period centering on day 50 of 1979. A_p is set to 5.0 for solar minimum conditions which corresponds to the average value during a period centered on day 200 of 1976. A constant, low level A_p value of 8 is used for the model runs during 1982-1983 and is discussed in detail below.

The heating rates resulting from the photodissociation of O_2 by the Schumann-Runge continuum (SRC) provide another substantial heating component in the lower thermosphere. The ultraviolet flux is first obtained from a SME solar minimum flux level between 1380 and 1730 Å. The UV flux is then scaled up to +20% to give solar maximum flux levels. The scaling factor is based on the variation in Lyman-α. The efficiency of this photodissociation is 33%, is described by Banks and Kockarts [1973], and is the value used here. The integrated column density of O_2 and the cross sections of that species in the SRC provide an appropriate optical depth, τ, given by equation (3.3). The heating rate is

$$P_{\mathrm{SRC}} = J_{\mathrm{O}_2}[\mathrm{O}_2]\varepsilon E \quad \text{ergs cm}^{-3}\ \text{sec}^{-1} \tag{4.15}$$

and depends upon the efficiency, ε, and the wavelength energy, E. The dissociation coefficient, J_{O_2}, is

$$J_{\mathrm{O}_2} = \sum_{\lambda} \sigma(\lambda) F_{\infty}(\lambda) e^{-\tau(\lambda,z)}. \quad \text{sec}^{-1} \tag{4.16}$$

A final heating rate used is a result of energy released by the mechanism of three body recombination of O, where

$$\mathrm{O} + \mathrm{O} + \mathrm{M} \rightarrow \mathrm{O}_2^* + \mathrm{M} \tag{4.17}$$

and where the heat production is given by

$$P_{\mathrm{O}} = k[\mathrm{O}][\mathrm{O}][\mathrm{M}]E. \quad \text{ergs cm}^{-3}\ \text{sec}^{-1} \tag{4.18}$$

It is discussed by Kasting and Roble [1981] who use the rate constant $k = 2.76 \times 10^{-34} \exp(710/T)$ and is recalculated during each temperature iteration. E is the dissociation energy of 5.11 eV which is released when the O atoms

recombine. Both the P_{SRC} and the P_O heating rates are summed to provide a total dissociation heating rate in this model where

$$P = P_{SRC} + P_O. \quad \text{ergs cm}^{-3} \text{ sec}^{-1} \tag{4.19}$$

The quenching of NO from collisions with atomic oxygen is a secondary heating mechanism and is not used here.

Cooling is modeled during each temperature iteration with the NO, CO_2, and O radiation in the 5.3 μm, 15 μm, and 63 μm bands, respectively. NO and CO_2, being heteronuclear molecules, possess a dipole moment and are able to emit in the infrared as their vibrational energy changes from a higher to a lower level. Gordiets *et al.* [1982] show the importance of including the first two cooling mechanisms in the lower thermospheric heat budget. The nitric oxide profile is determined for each EUV flux condition as described above. Gordiets *et al.* describe the collision de-activation rate constant, $k_{10} = 6.5 \times 10^{-11}$ cm^3 sec^{-1} at 300 K, for isotopic exchange with atomic oxygen in NO 5.3 μm cooling. Kockarts [1980] gives the heat loss as

$$L_{NO} = h\nu[\text{NO}]\omega A_{10}(g_1/g_0)e^{-h\nu/kT} \quad \text{ergs cm}^{-3} \text{ sec}^{-1} \tag{4.20}$$

$$\omega = k_{10}[\text{M}]/(k_{10}[\text{M}] + A_{10}). \tag{4.21}$$

$h\nu = 3.726 \times 10^{-13}$ ergs for the 5.3 μm emission, ω is the dilution factor representing the departure of the vibrational levels of NO from a Boltzmann distribution, A_{10} is the Einstein coefficient for spontaneous emission of 13.3 sec^{-1}, g_1 and g_0 are the statistical weights for the $v = 1$ and $v = 0$ vibration levels where $g_1 = g_0$, and k is Boltzmann's constant.

CO_2 cooling from vibrational deactivation in the 15 μm band is written by Gordiets *et al.* as

$$L_{CO_2} = 2.66 \times 10^{-13} e^{-960/T}[CO_2]qF \quad \text{ergs cm}^{-3} \text{ sec}^{-1} \tag{4.22}$$

where

$$q = k_{N_2}[N_2] + k_{O_2}[O_2] + k_O[O], \quad \text{sec}^{-1} \tag{4.23}$$

where the relaxation rate constants are

$$k_{O_2} = 4.4 \times 10^{-15} T \exp(-41/T^{.33}), \quad \text{cm}^{-3}\ \text{sec}^{-1} \tag{4.24}$$

$$k_{N_2} = \frac{1}{3} k_{O_2}, \quad \text{cm}^{-3}\ \text{sec}^{-1} \tag{4.25}$$

$$k_O = 1.5 \times 10^{-11} \exp(-800/T), \quad \text{cm}^{-3}\ \text{sec}^{-1} \tag{4.26}$$

and where

$$F = \frac{1}{2}\lambda \ell(\tau)/(1 - \lambda + \frac{1}{2}\lambda \ell(\tau)). \tag{4.27}$$

$\lambda = A_{10}/(A_{10} + q)$ where A_{10} is the Einstein coefficient for spontaneous emission and the parameter $\ell(\tau)$ is a function of the reduced optical depth, τ, discussed by Kumer and James [1974]. $\ell(\tau)$ is evaluated at each temperature iteration after solving for a new column density of CO_2. Equation (4.22) comes from the more general expression

$$L = \sum_{jk} h\nu [X_j][Y_k] \eta e^{-h\nu/kT} \quad \text{ergs cm}^{-3}\ \text{sec}^{-1} \tag{4.28}$$

where the X_j constituent (CO_2) is de-excited by collisions with the Y_k species. η is a vibrational relaxation parameter while $h\nu$ is the energy of the process.

The cooling by atomic oxygen in the 63 μm band is discussed by Banks and Kockarts [1973]. The heat loss from this radiation is formulated as

$$L_{O_{63\mu m}} = \frac{1.69 \times 10^{-18}[O] e^{-228/T}}{1 + .6\exp(-228/T) + .2\exp(-326/T)}. \quad \text{ergs cm}^{-3}\ \text{sec}^{-1} \tag{4.29}$$

Banks and Kockarts indicate that cooling between 100 and 150 km is always overestimated by equation (4.29). Thus, this expression is multiplied by an efficiency factor of 30% to lower the results for agreement with their values at 120 km.

The total loss of heat due to infrared cooling is the sum of the loss rates and is written

$$L = L_{NO} + L_{CO_2} + L_{O_{63\mu m}}. \quad \text{ergs cm}^{-3} \text{ sec}^{-1} \tag{4.30}$$

The molecular thermal conductivity, λ, is a temperature dependent parameter which varies with the translational energy of a gas particle and the viscosity of a gas mixture. Banks and Kockarts [1973] describe λ as

$$\lambda = AT^{0.69} + BT + C \quad \text{ergs cm}^{-1} \text{ sec}^{-1} \text{ °K}^{-1} \tag{4.31}$$

where $A = 56$, and B and C are complex formulations. The molecular heat conduction is given by

$$q_{mol} = \lambda \frac{\partial^2 T}{\partial z^2} \quad \text{ergs cm}^{-3} \text{ sec}^{-1} \tag{4.32}$$

from equation (4.3).

The eddy heat conductivity and the turbulent heat conductivity, both described by Gordiets *et al.*, are used to calculate gas cooling and heating arising from the dissipation of turbulent kinetic energy due to viscous and bouyancy forces. These processes are only important in the lower thermosphere below 110 km but may play a greater thermal role than CO_2 or NO radiative cooling. The combined expression for eddy and turbulent heat conduction is

$$q_e = q_{ec} + q_{eh} \quad \text{ergs cm}^{-3} \text{ sec}^{-1} \tag{4.33}$$

and is combined with the q_{euv}, q_j, q_p, P, and L heating rate terms to form the Crank-Nicolson coefficients described in Appendix A.

4.2 Model Results

4.2.1 Model Validation: Solar Minimum and Maximum Conditions

The results of this model for both solar minimum and maximum conditions are compared to MSIS 83. These results include the quantitative temperatures and densities as the primary thermospheric parameters obtained from the model validation runs. The heat production by EUV, auroral, SRC, and atomic oxygen three-body reaction and the heat loss by NO and CO_2 infrared cooling and atomic oxygen de-excitation at 63μm are also shown. The molecular conduction results are additionally given.

The temperature profiles shown in Figures 4.1a and 4.1b can be compared to the MSIS 83 temperatures reproduced from Figures 1.6b and 1.6d in Chapter I. Below the turbopause at 120 km, the profiles are identical to MSIS 83 since this model is not calculated below that level. This model has a lower boundary condition with a steady state temperature condition at the turbopause.

This model compares favorably with the MSIS 83 temperatures. For solar minimum, day 200 of 1976, MSIS 83 gives a value of 743 °K for the exospheric temperature while for maximum conditions, day 50 of 1979, the MSIS 83 result is 1357 °K. This model produces 747 °K and 1358 °K for the same solar conditions, respectively. The heavy solid line is the MSIS 83 profile while the light line is the model profile.

Figures 4.2a and 4.2b compare the MSIS 83 concentration profiles with those from this model for solar minimum and maximum conditions. Again, the light lines are from the model while the heavy lines are from MSIS 83. The primary constituents of O, O_2, and N_2 are labeled along with the minor species of CO_2, NO, He, and H. All the constituents are in diffusive equilibrium above the turbopause.

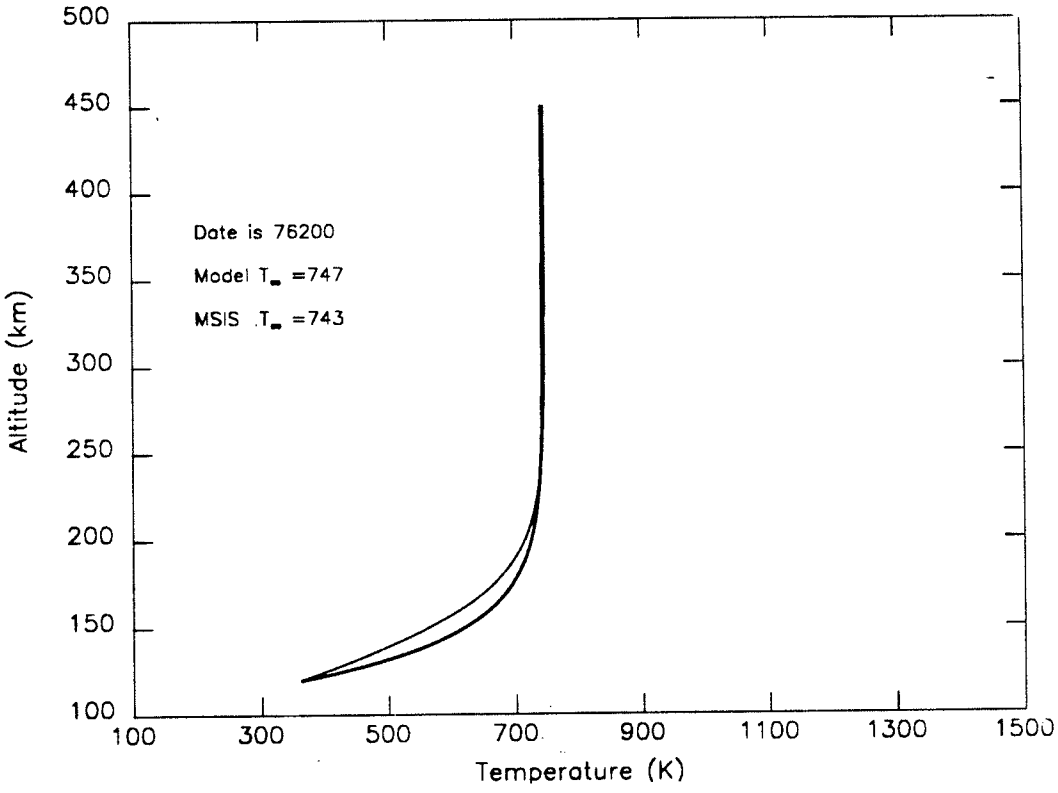

Figure 4.1 (a) **Model and MSIS 83 solar minimum temperatures.**

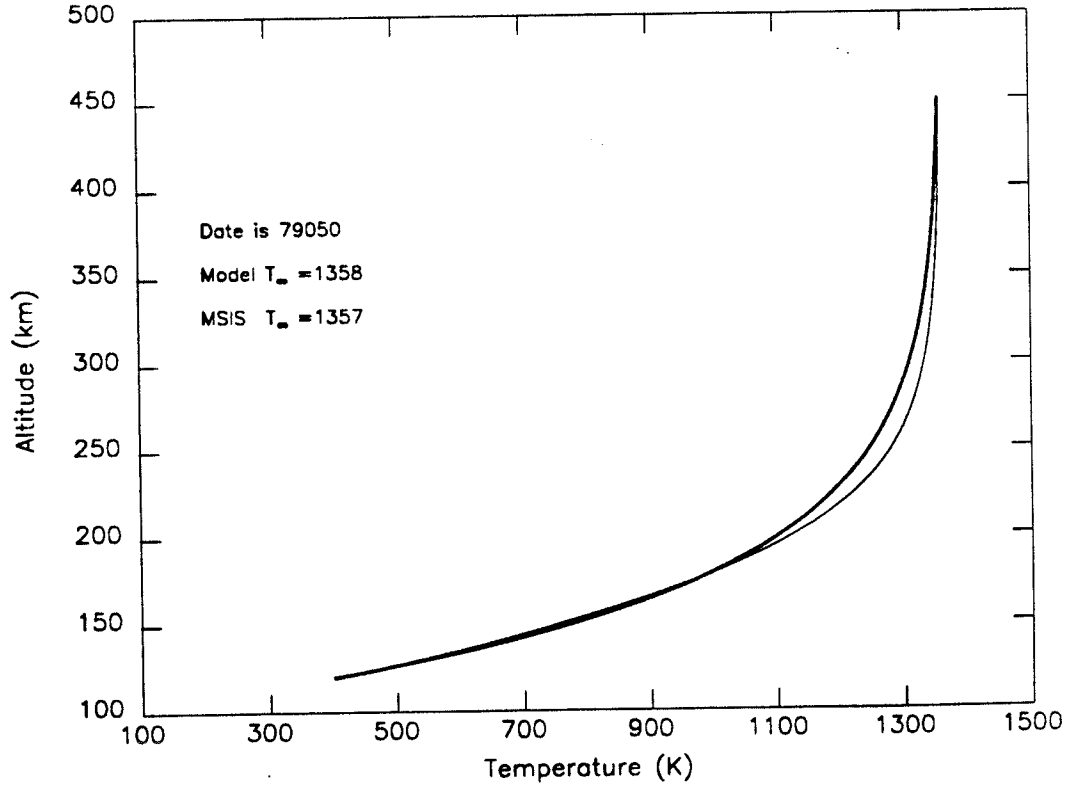

Figure 4.1 (b) **Model and MSIS 83 solar maximum temperatures.**

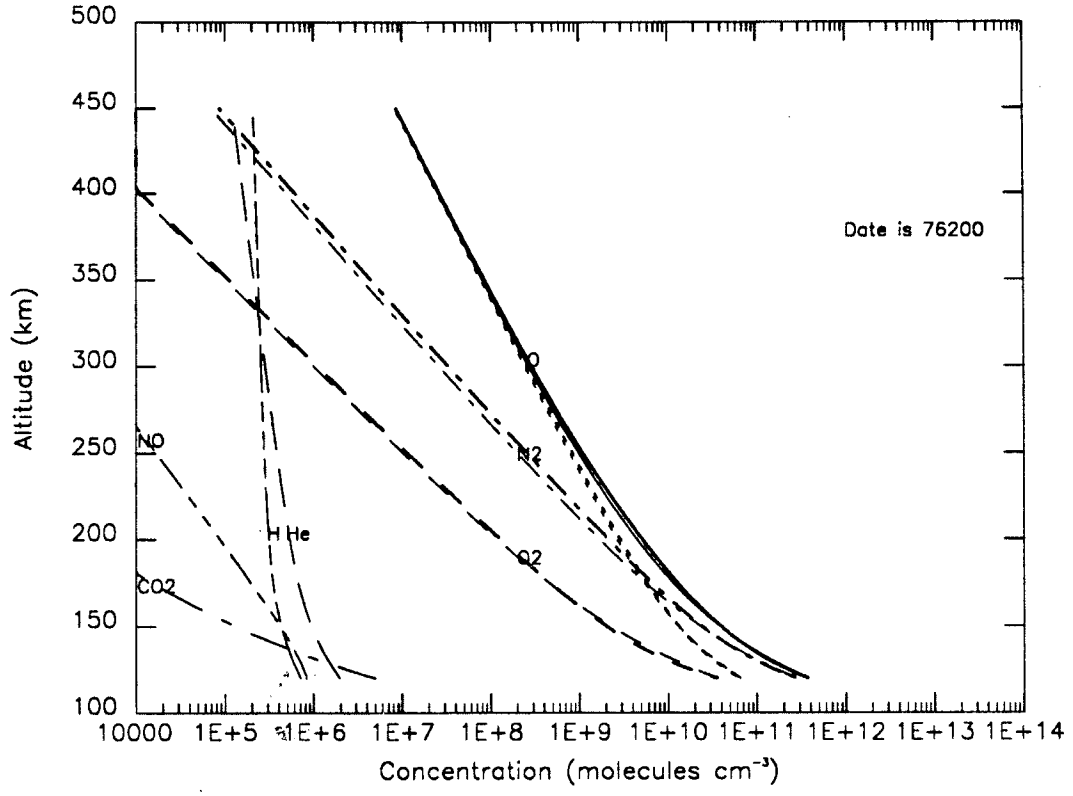

Figure 4.2 (a) **Model and MSIS 83 solar minimum concentrations.**

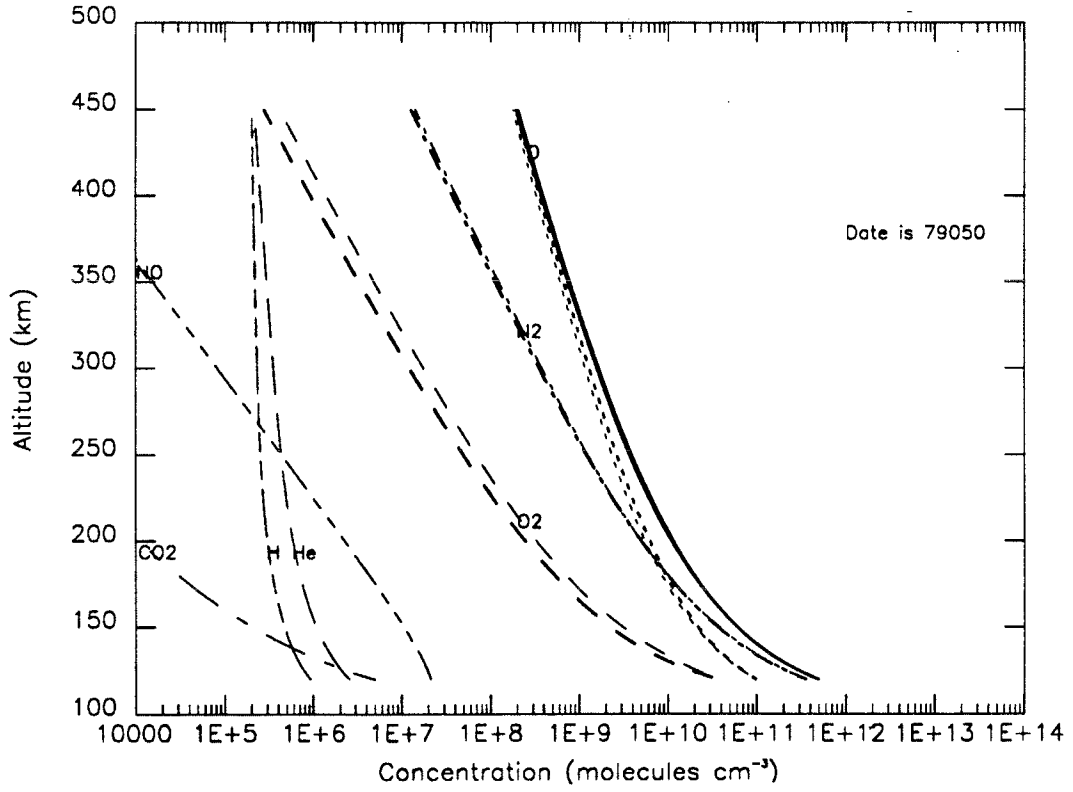

Figure 4.2 (b) **Model and MSIS 83 solar maximum concentrations.**

The heating rate per unit volume from EUV flux, O_2 dissociation from the Schumann-Runge continuum, the auroral particle precipitation and Joule heating, and the energy release from atomic oxygen in three-body reactions is shown in Figures 4.3a and 4.3b for solar minimum and maximum conditions. The EUV heating is the dominant energy input into the thermosphere above 135 km at solar minimum and above 170 km at solar maximum. Joule heating, which peaks at 130 km in this model, is dependent upon magnetospheric and not solar activity. In highly active conditions, it can dominate the heating between 120 and 170 km, as shown in Figure 4.3b. The total global energy input from equations (4.13) and (4.14) for the particle precipitation and Joule heating, respectively, is 0.5×10^{10} W and 2.0×10^{10} W for solar minimum conditions ($A_p = 5$). The values are 4.2×10^{10} W and 3.9×10^{11} W for solar maximum conditions ($A_p = 17.3$). Without active magnetospheric conditions, the O_2 heating from absorption in the SRC dominates the lower thermospheric heating between 120 and 135 km. As noted earlier, this model uses an approximation for the UV flux in the SRC which is obtained from the SME solar minimum (August-September 1986) period and is linearly scaled according to solar activity as determined by the Lyman-α variation. The total heating in Figures 4.3a and 4.3b is shown by the heavy solid line. Figure 4.4 shows the minimum and maximum values of the SRC between 1380 and 1730 Å given by the light and heavy lines, respectively. The spectral ranges are shifted by 20%. The solar minimum and maximum dissociation coefficient, J_{O_2}, is shown in Figure 4.5 and compares favorably with Banks and Kockarts. It has a value of 2.1×10^{-6} sec^{-1} at 120 km, 3.3×10^{-6} sec^{-1} at 140 km, and 3.7×10^{-6} sec^{-1} for solar minimum and 4.0×10^{-6} sec^{-1} for solar maximum at 450 km.

The cooling processes during the low and high solar activity are shown

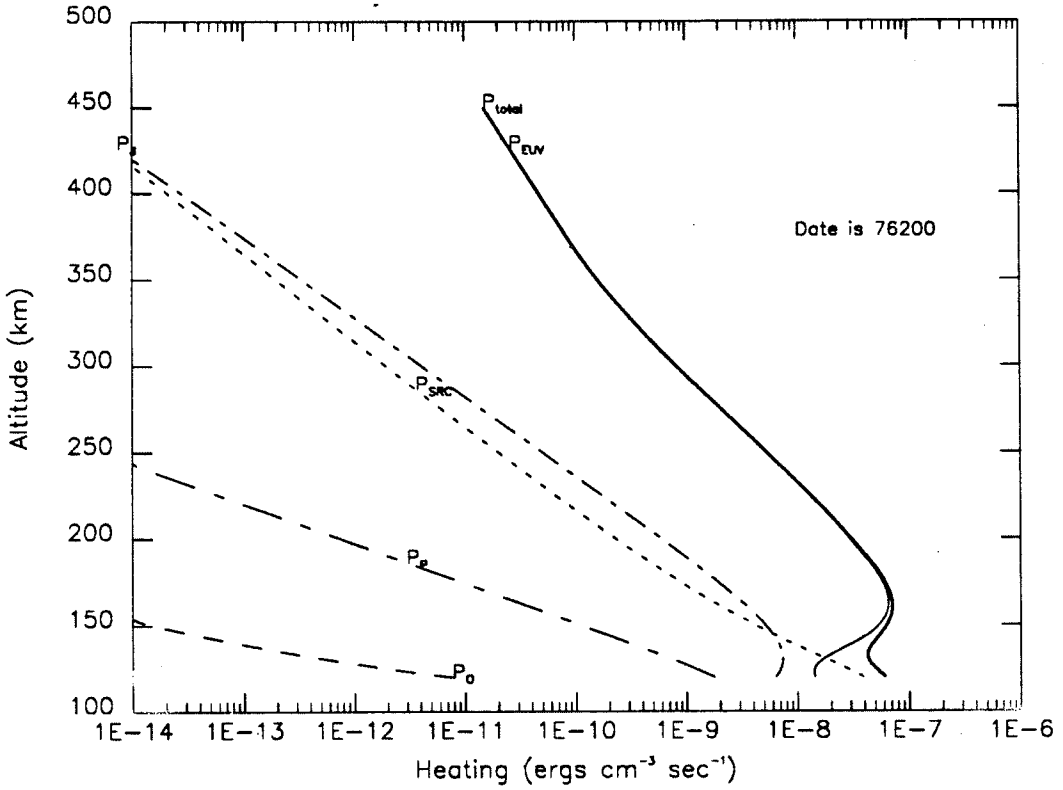

Figure 4.3 (a) **Model solar minimum heating profiles.**

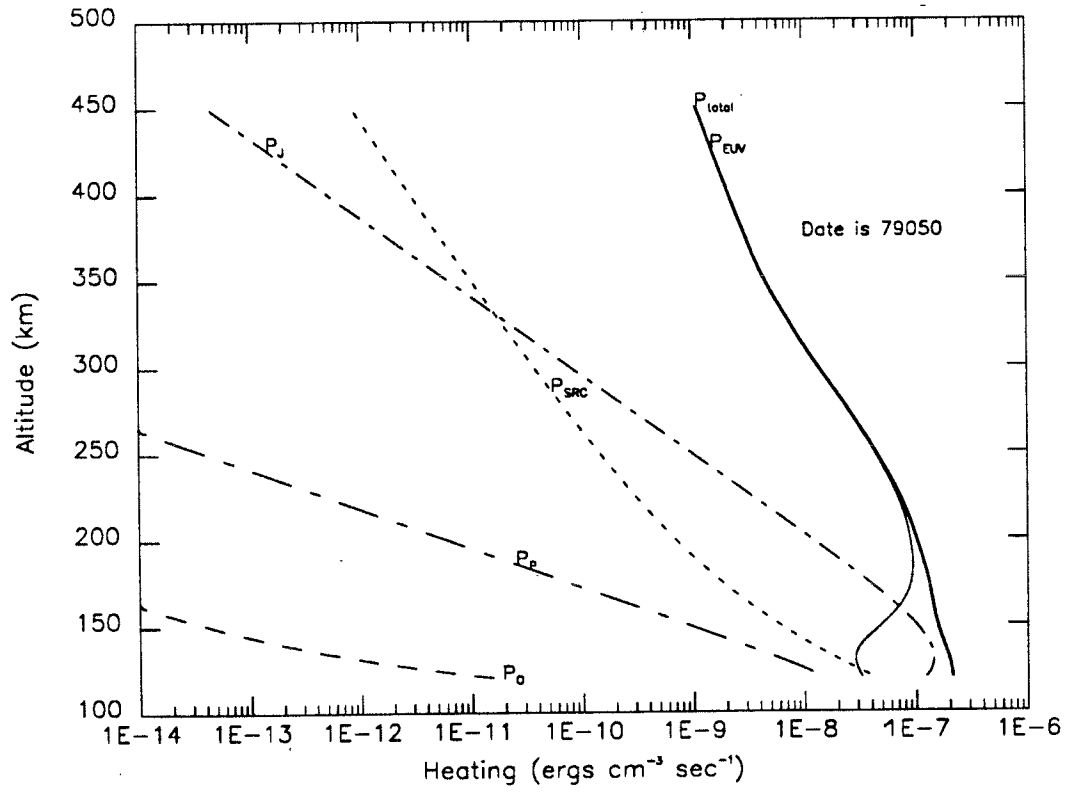

Figure 4.3 (b) **Model solar maximum heating profiles.**

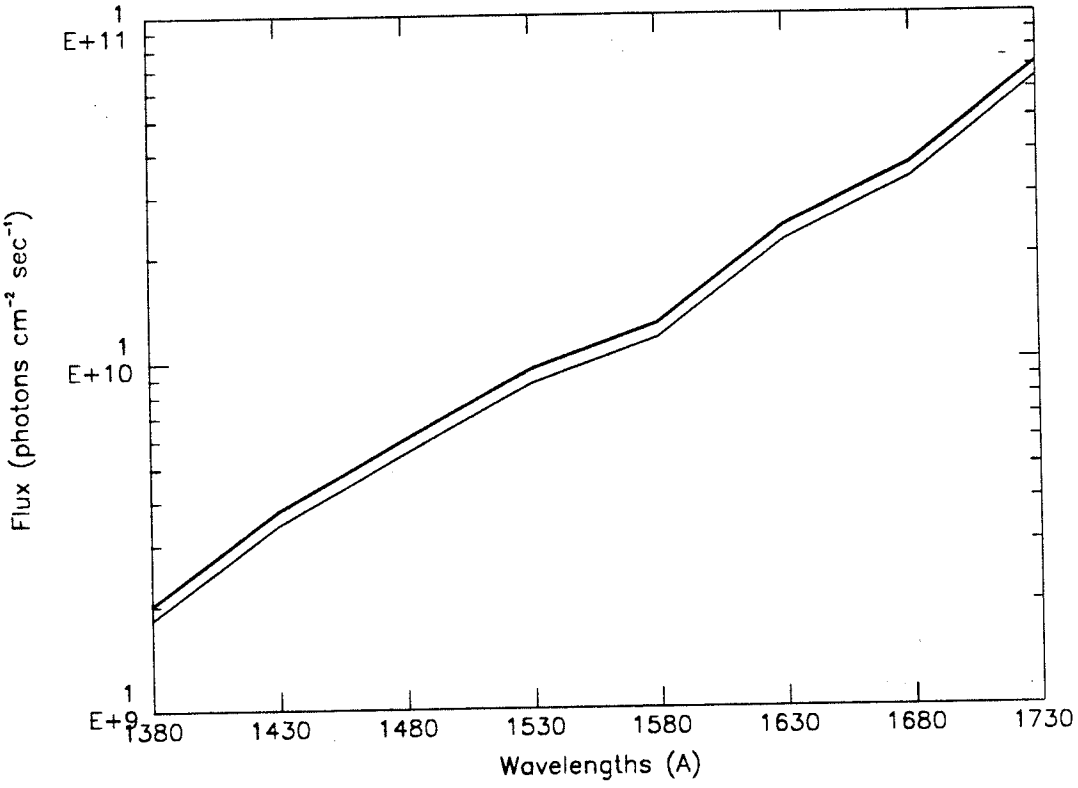

Figure 4.4 **Shumann-Runge continuum: minimum and maximum.**

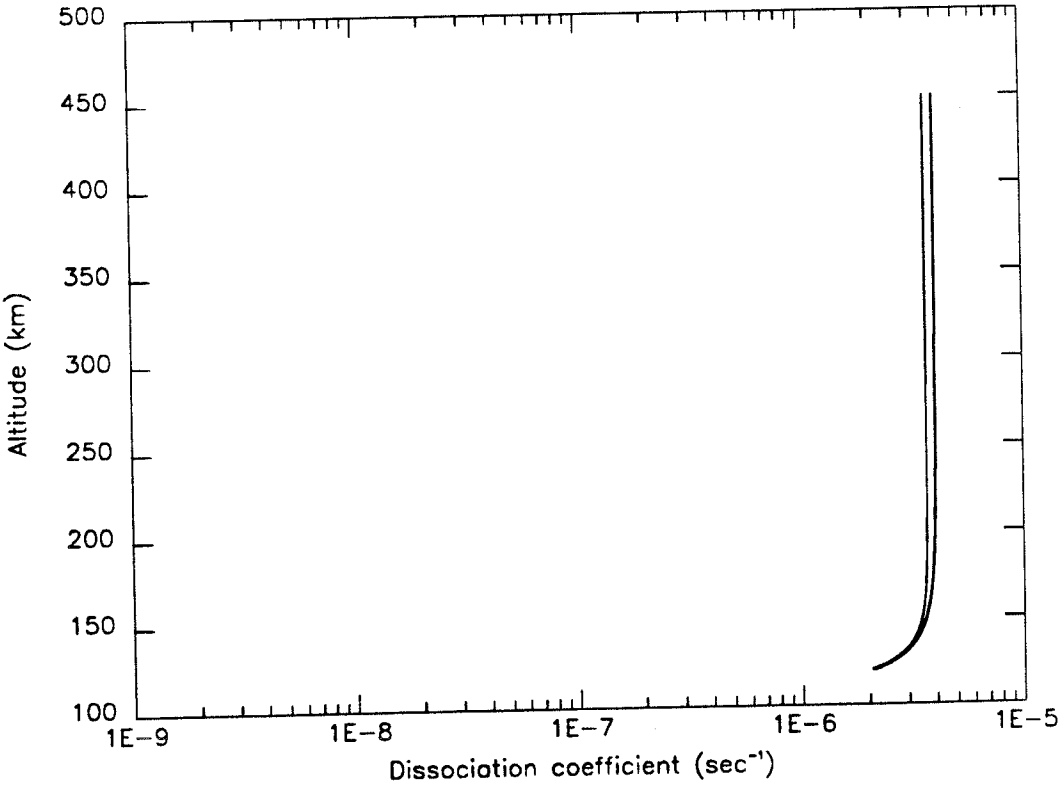

Figure 4.5 **O_2 photodissociation coefficient: minimum and maximum.**

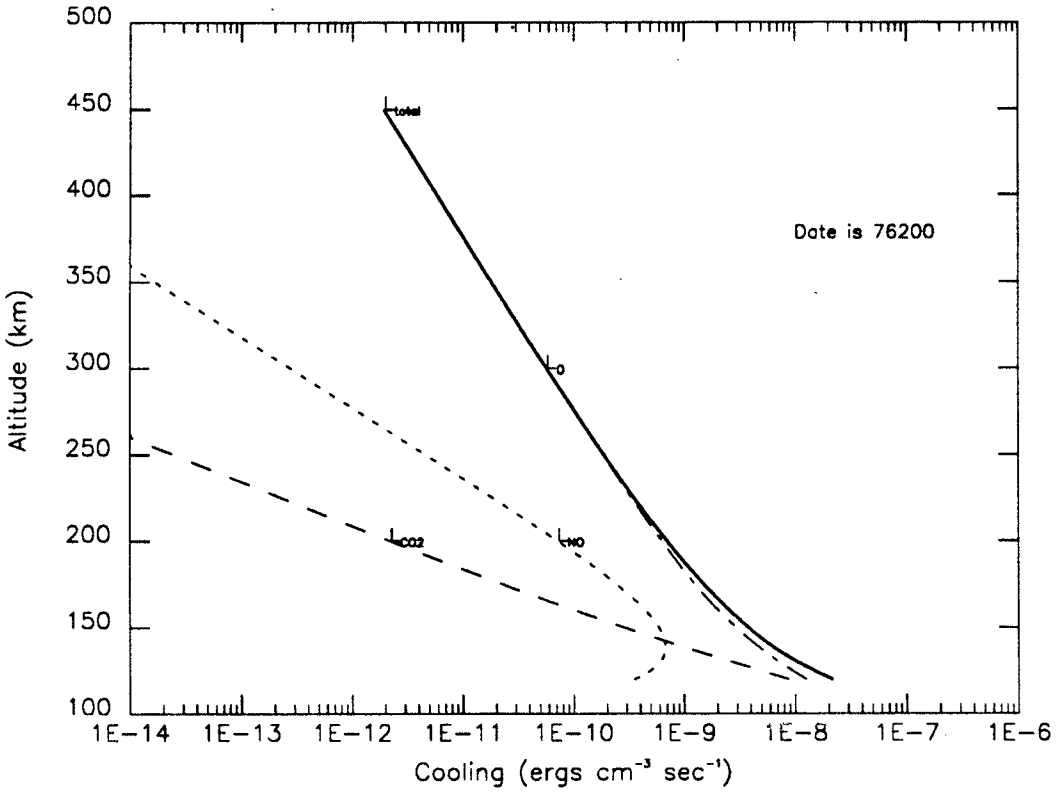

Figure 4.6 (a) **Model solar minimum cooling profiles.**

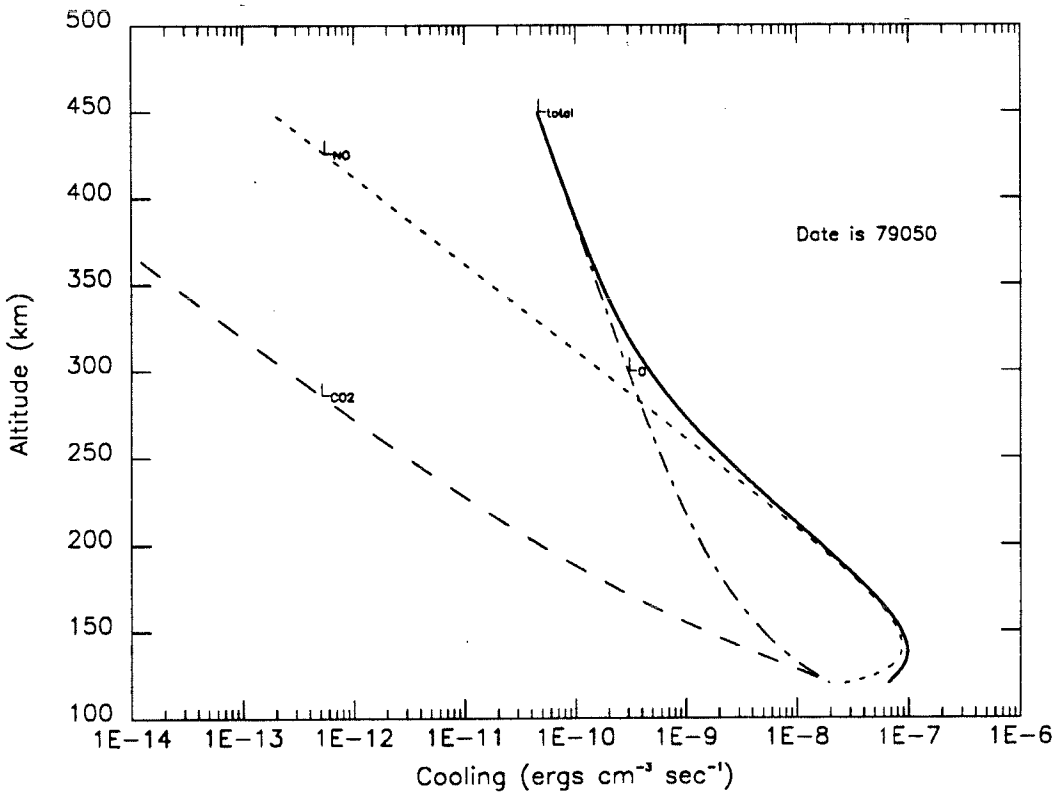

Figure 4.6 (b) **Model solar maximum cooling profiles.**

in Figures 4.6a and 4.6b. While the total cooling is shown by the heavy line, its component parts are dominated by infrared emission at 63μm by atomic oxygen followed by CO_2 and NO cooling above 120 km at solar minimum. However, at solar maximum the NO cooling becomes much more important. While $O_{63\mu m}$ radiation cools the thermosphere above 250 km, NO infrared cooling dominates between 120 and 250 km. Thus, NO density is important in the thermospheric heat budget. The CO_2 15 μm cooling is not a principal heat loss mechanism above 120 km for solar maximum conditions.

Finally, the thermal conductivity coefficient, λ, is shown in Figure 4.7 and also compares favorably with Banks and Kockarts for similar profiles during low and high solar activity. Based on the temperature dependence in equation (4.31), it varies with solar activity and reflects the property of a greater thermally conductive capability in the thermosphere during higher temperature conditions.

The molecular conduction is shown in Figure 4.8 for both low and high solar activity. Its temperature gradient dependence, from equation (4.32), indicates that larger temperature gradients lead to greater cooling capacity.

Figure 4.9 plots the total of all thermal processes described in Figures 4.3, 4.6, and 4.8. This includes all heating, cooling, and conduction for solar minimum and maximum conditions. This plot shows that the model conserves energy between 450 and 120 km.

For astronautical purposes, it is useful to extend the atmosphere to 1000 km. Figures 4.10a and 4.10b show the extended constituent mass densities and total mass density for low and high solar activity. During low activity, He and H both dominate the exosphere above 800 km. However, during high activity, O maintains a substantial profile on the scale of Figure 4.10b. These plots show the range of density change over a solar cycle and indicate that

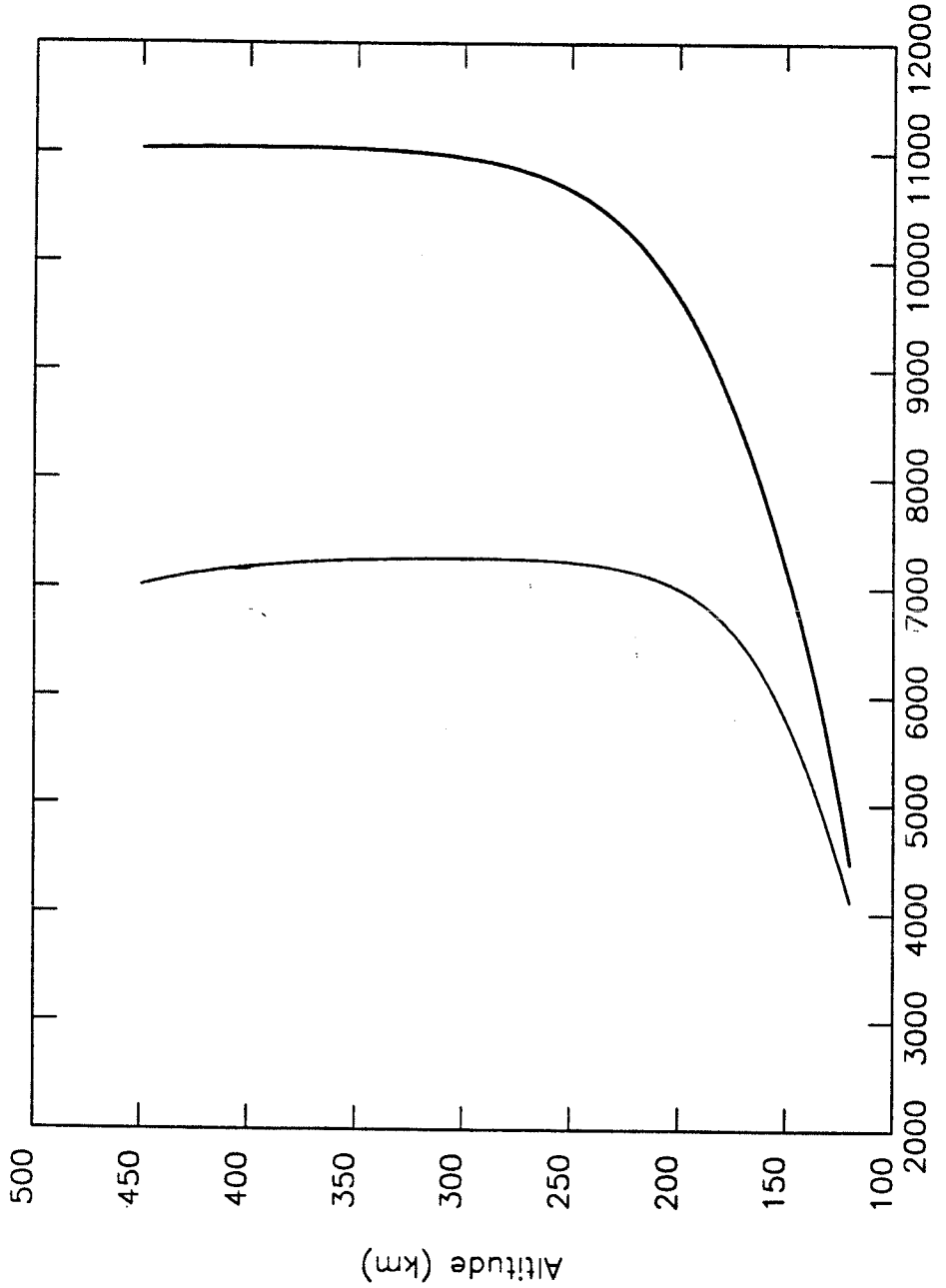

Figure 4.7 Model solar minimum and maximum thermal conductivity coefficient. This plot is based on equation (4.31).

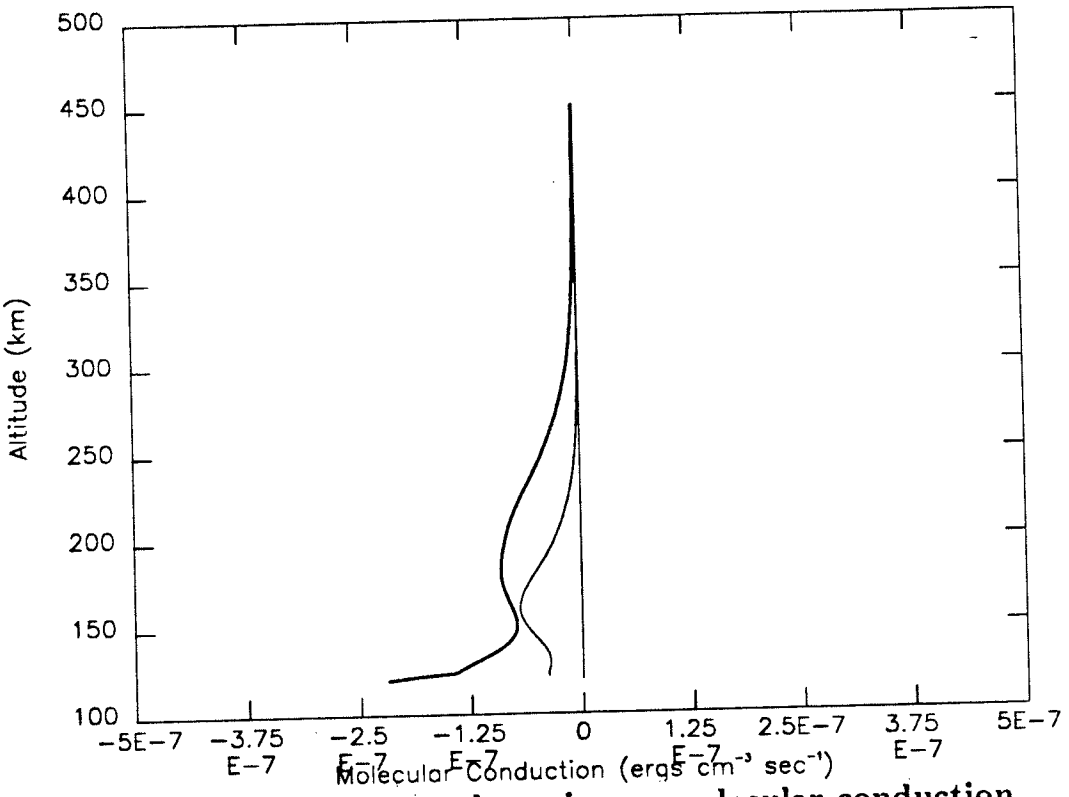

Figure 4.8 Solar minimum and maximum molecular conduction.

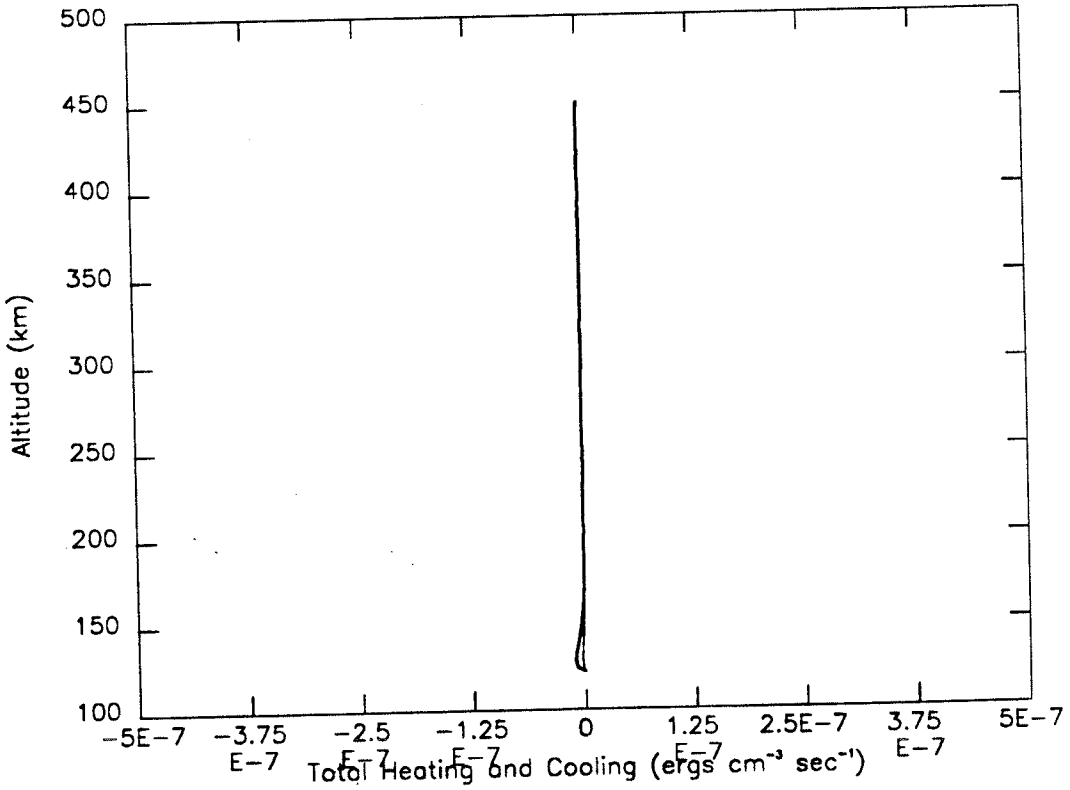

Figure 4.9 Solar minimum and maximum total thermal processes.

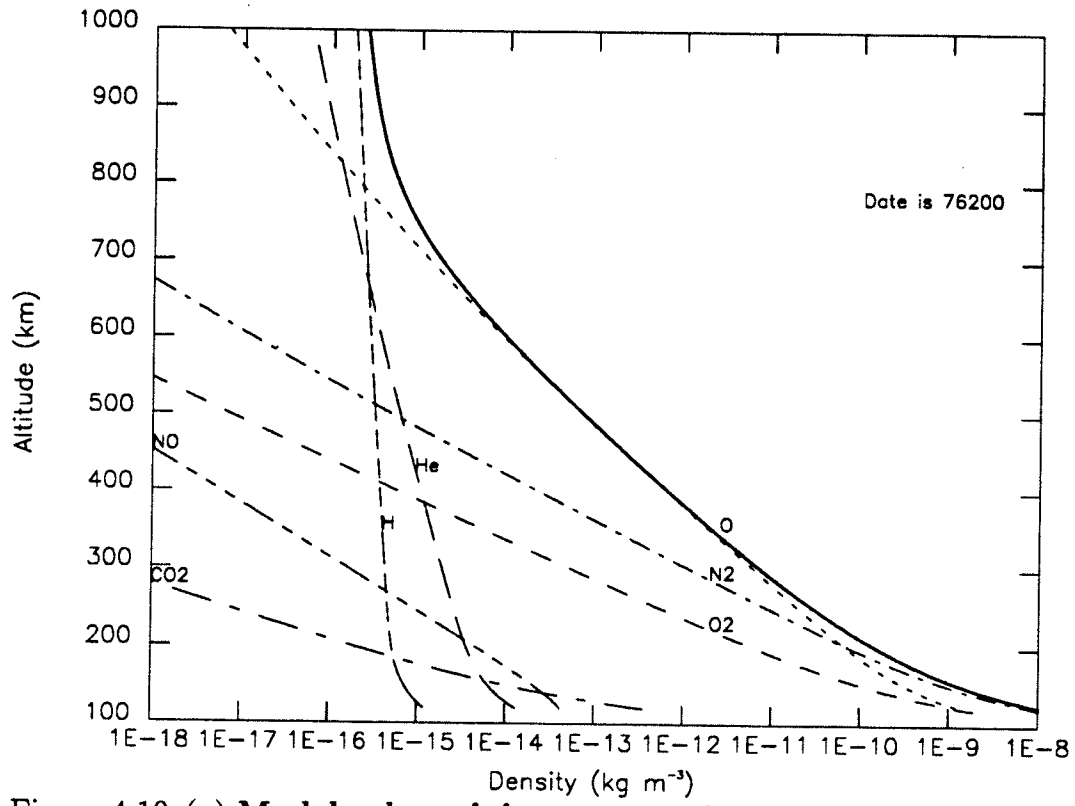

Figure 4.10 (a) **Model solar minimum mass density profiles.**

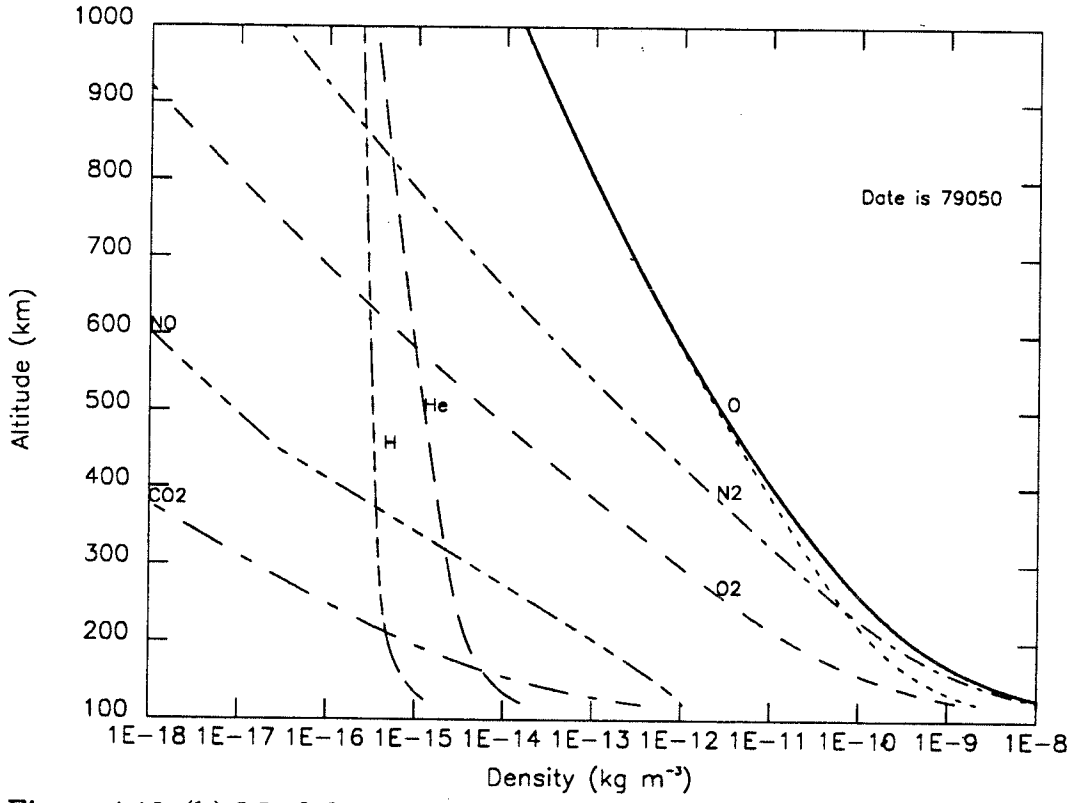

Figure 4.10 (b) **Model solar maximum mass density profiles.**

upper thermospheric mass densities at 500 km vary by more than an order of magnitude, i.e. 35:1, for high to low solar activity. Lower thermospheric densities near the turbopause vary by only 33% from high to low solar activity.

4.2.2 Time Series Calculations: Decline of Cycle 21

This model was run for each day during the period between January 1982 through May 1983. Beyond the latter date, there is currently no GOES 1-8 Å X-ray data publicly available. The energy input indices of Lyman-α, 1-8 Å X-rays, and A_p are filtered datasets. This filtering moderates the daily energy fluctuations and is a method of empirically approximating the longer timescales found in thermospheric density variations compared to the shorter timescale variations in the energy inputs. The SME Lyman-α values are filtered at 10 days, the GOES 1-8 Å X-ray daily background values are filtered at 24 days, and the daily A_p values are filtered at 22 days. Figure 4.11 shows the SME 10-day filtered data, Figure 4.12 shows the 24-day filtered 1-8 Å X-ray data, Figure 4.13 shows the 22-day filtered A_p data, and Figure 4.14 shows the daily $F_{10.7}$ values used in MSIS 83. The dotted line in Figure 4.13 is the daily A_p value used by MSIS 83 and the dotted line in Figure 4.12 is the daily value of the 1-8 Å X-rays from Appendix B.

Figure 4.15a shows these model results using the EUV indices compared to both MSIS 83 and the derived density from the SME satellite orbit decay. This is the period from January 1, 1982 through May 16, 1983 when all the datasets were available. The heavy line represents the SME derived density, the dotted line is MSIS 83, and the light solid line is this model. It is apparent from Figure 4.15a that MSIS 83 generally reproduces the density time series better than this model. Both models follow the solar rotational features in the SME derived density except for June 1982 (days 152-181). Since the

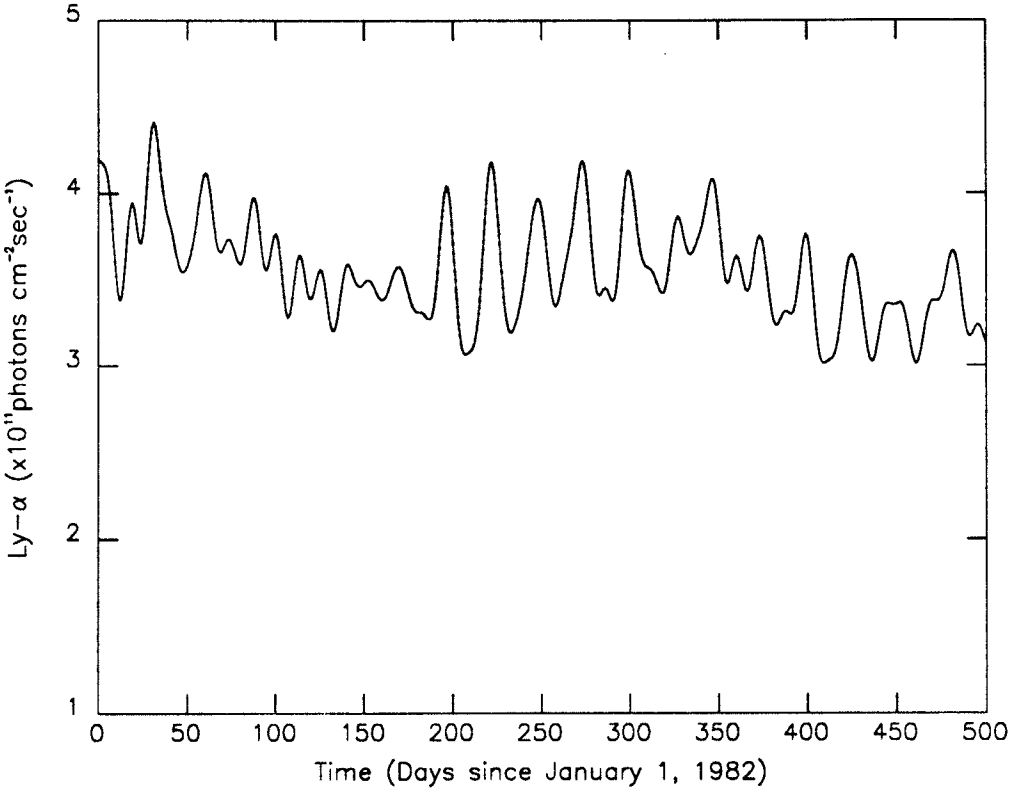

Figure 4.11 **10-day filtered SME Lyman-α.**

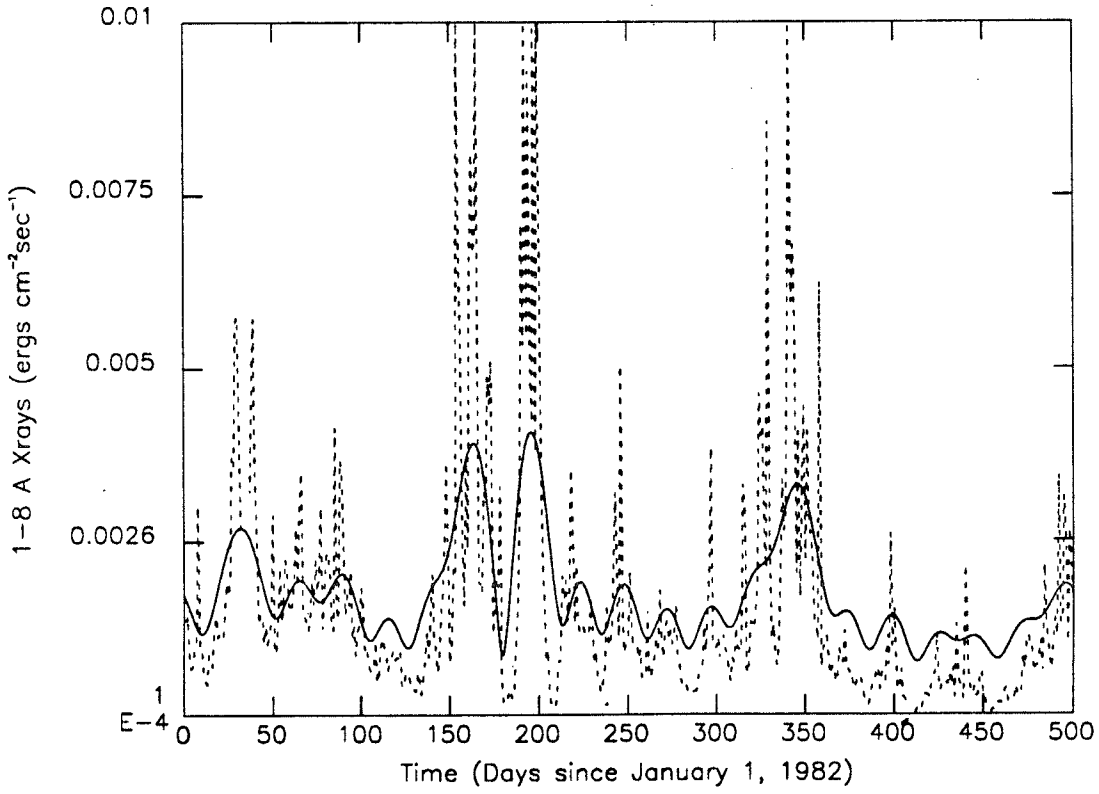

Figure 4.12 **24-day filtered 1-8 Å X-rays.**

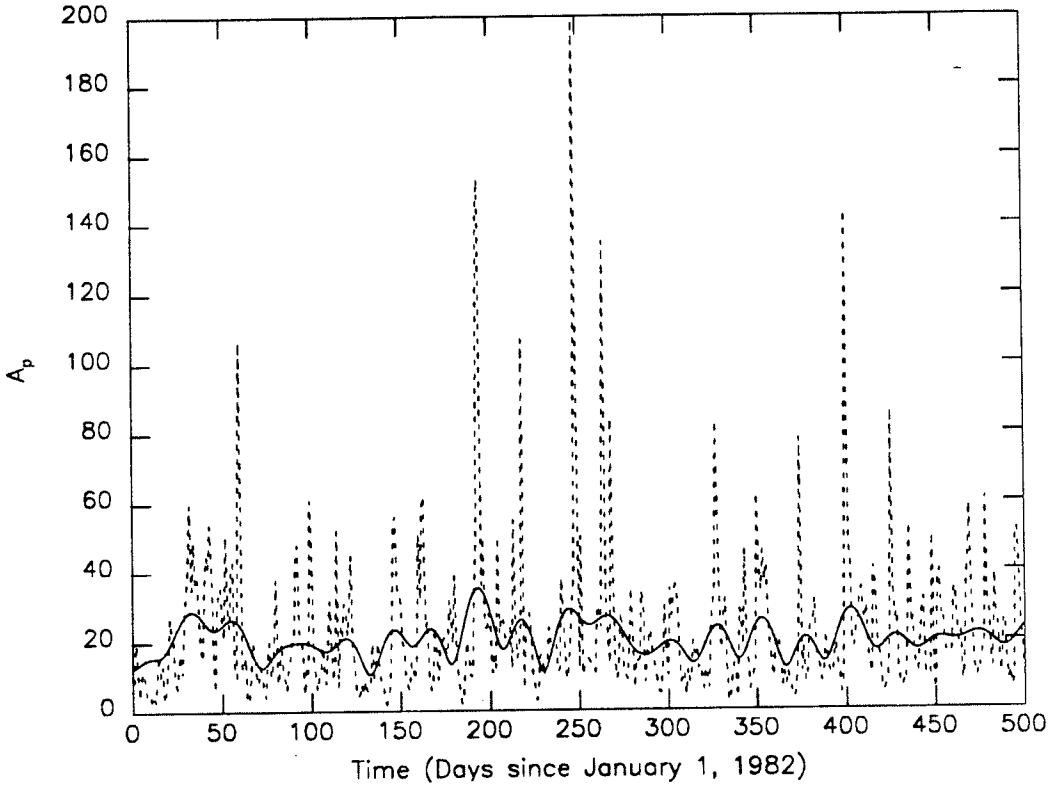

Figure 4.13 **22-day filtered A_p.**

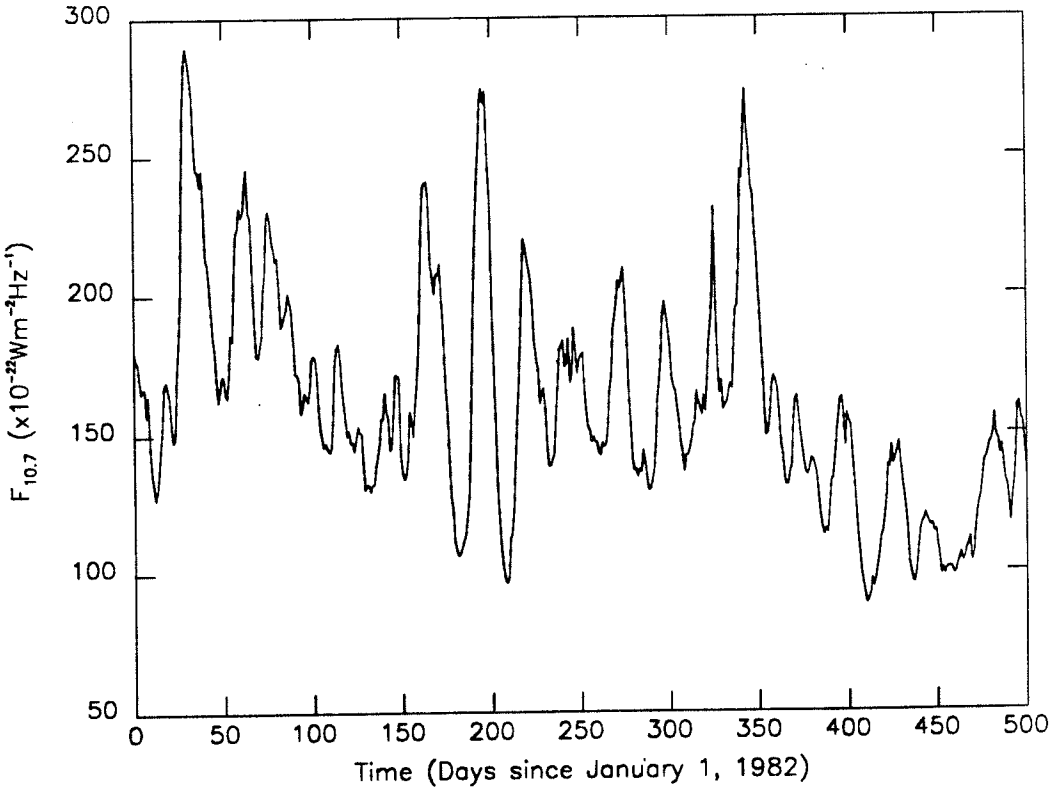

Figure 4.14 **Ottawa $F_{10.7}$.**

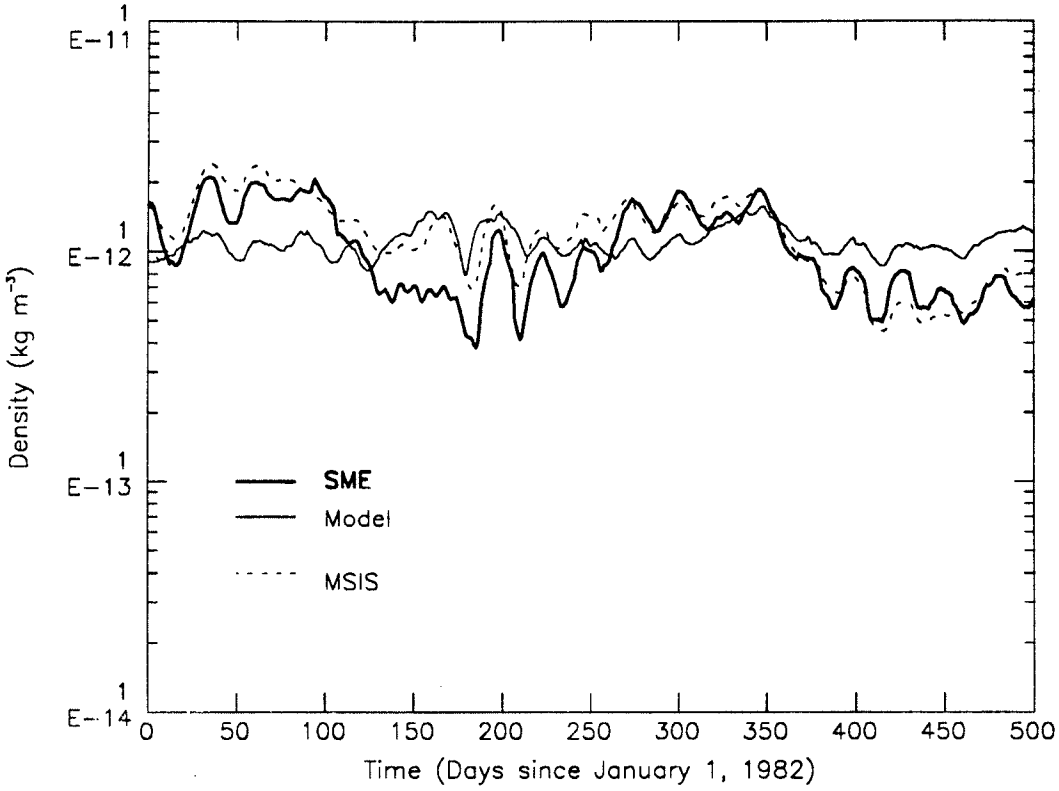

Figure 4.15 (a) **SME derived, model, and MSIS 83 mass densities.**

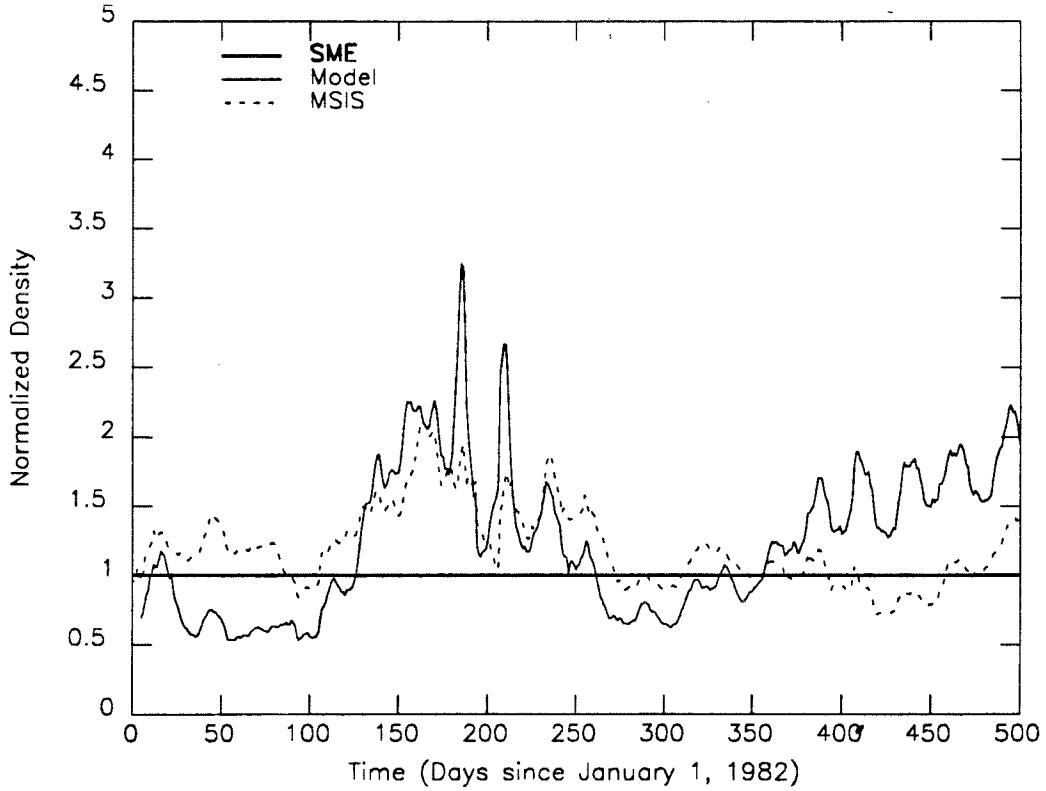

Figure 4.15 (b) **Derived, model, and MSIS 83 normalized densities.**

solar rotational features in this model are a result of the EUV indices energy flux variations and not a result of the variation in the geomagnetic index which has been held constant, this shows that solar EUV activity is the dominant heating component for the SME derived density. Figure 4.15b shows both the MSIS 83 and the model deviations from the normalized SME derived density for this time period. The deviation in both models from the derived density is most noticeable in June of 1982. This is due 1) to the increased variation in the $F_{10.7}$ index for MSIS 83, as shown in Figure 4.14, which indicates increased transition region and cool coronal emissions, and 2) to the increased variation in the purely coronal 1-8 Å X-ray index in this model. SME's derived density does not show this variation, nor does the Lyman-α chromospheric emission in Figure 4.11. Therefore, it is observed that the thermospheric density at low Earth orbiting satellites altitudes during high solar activity follows chromospheric emission variations as compared to coronal or transition region variations.

Figures 4.16a-4.16h show the normalized datasets of densities and indices which are plotted for comparison with one another. Normalization is done by dividing each time series with its linear fit. The correlations with the normalized SME derived density in Figure 4.16a are particularly interesting. MSIS 83 normalized density in Figure 4.16b shows a high correlation, with r = 0.86, during most periods except for two. MSIS 83 densities diverge from SME derived densities in June 1982 and March 1983 where the peaks of the solar rotational features occur at days 164 (June 14, 1982) and 448 (March 25, 1983), respectively. In the first case, June 1982, the chromospheric emissions, exemplified by Lyman-α in Figure 4.11, do not show a rotational feature while the transition region and coronal emissions of $F_{10.7}$ in Figure 4.14 and 1-8 Å X-rays in Figure 4.12 do show a rotational feature. SME derived density follows

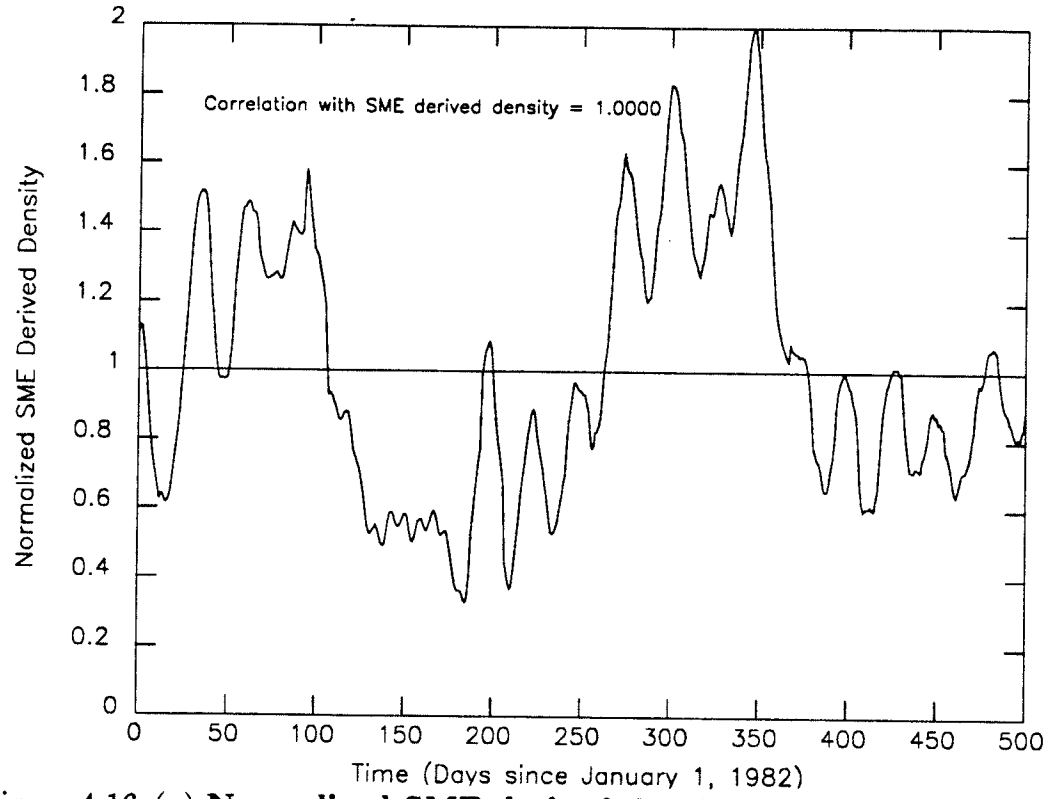

Figure 4.16 (a) **Normalized SME derived density.**

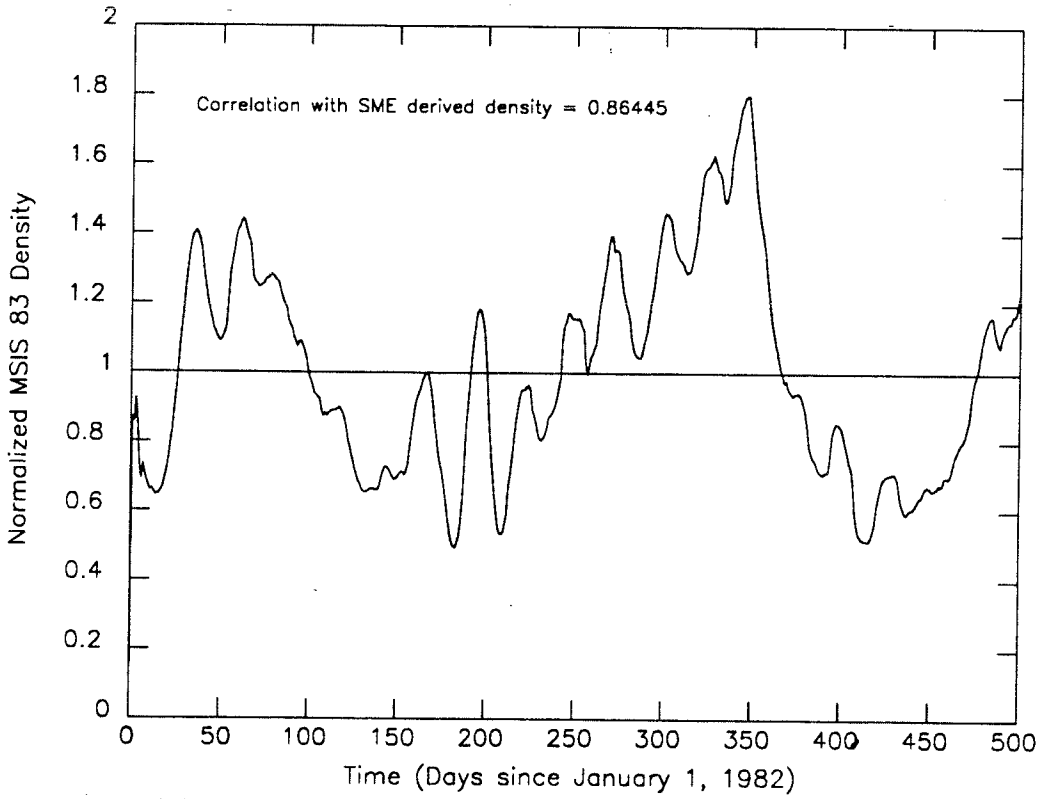

Figure 4.16 (b) **Normalized MSIS 83 density.**

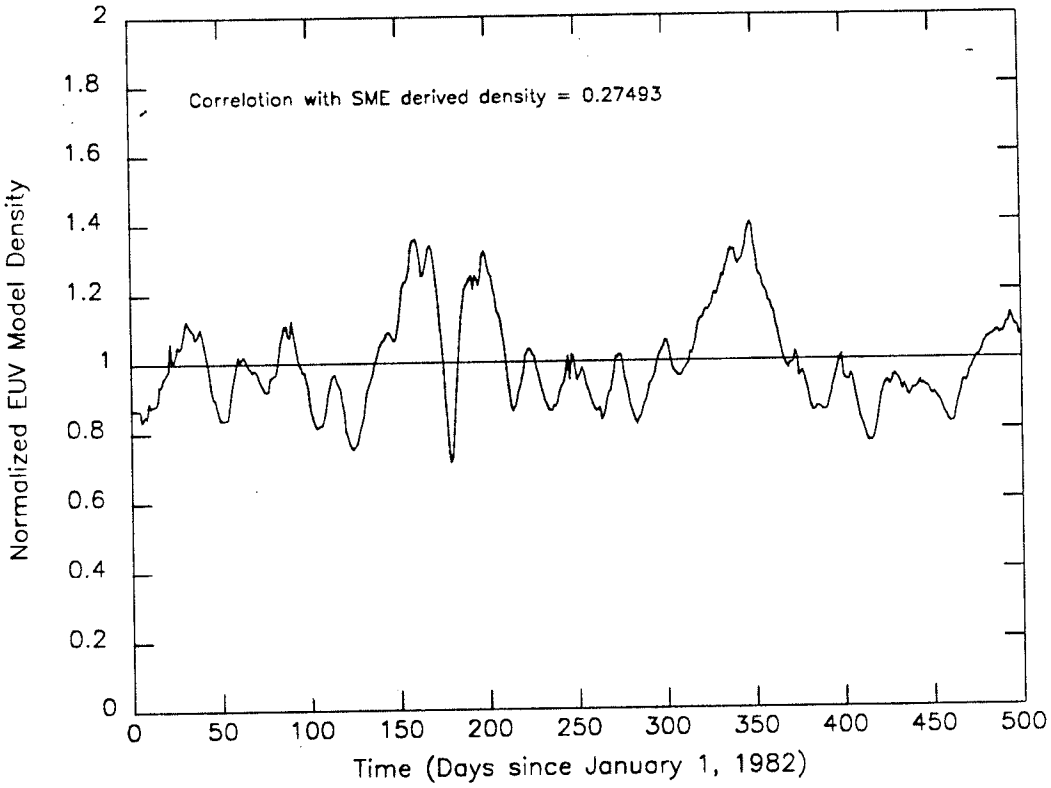

Figure 4.16 (c) **Normalized EUV model density.**

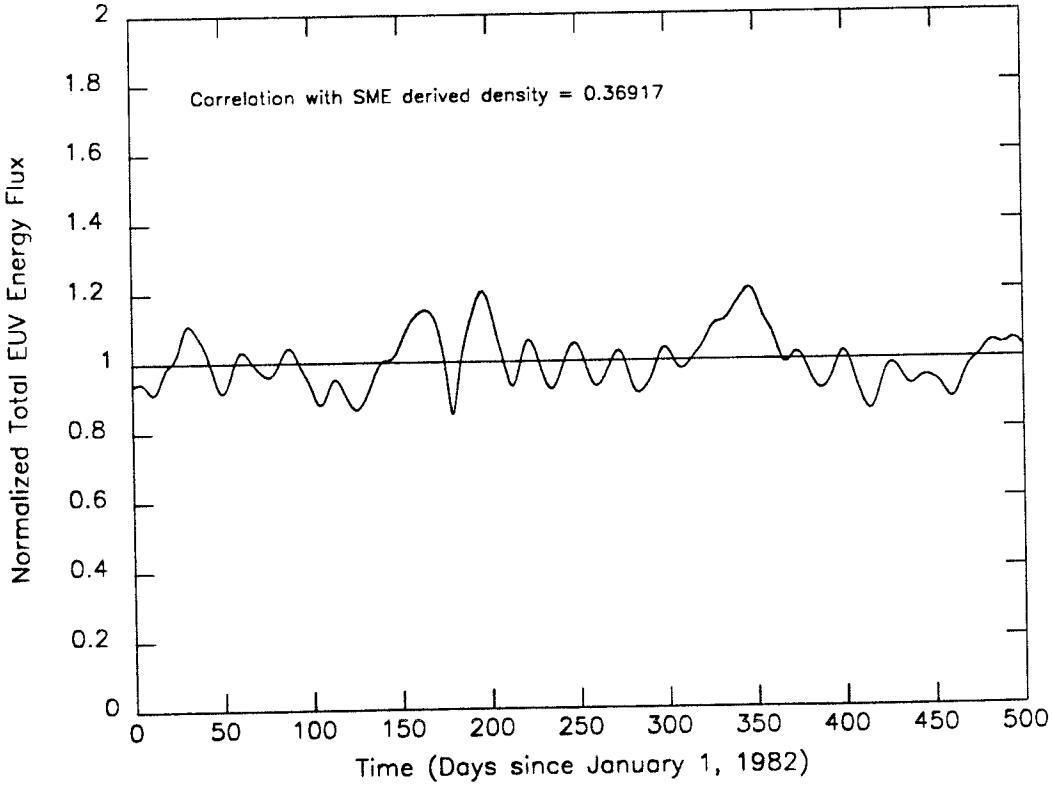

Figure 4.16 (d) **Normalized total EUV energy flux.**

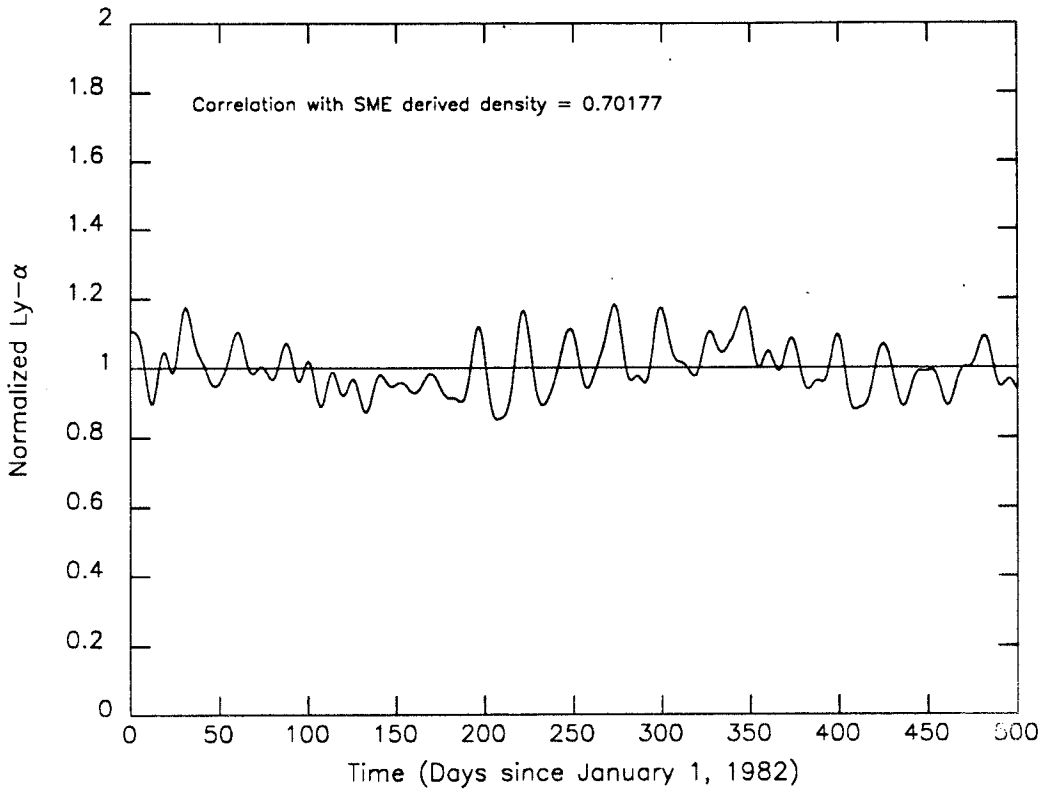

Figure 4.16 (e) **Normalized 10-day filtered SME Lyman-α.**

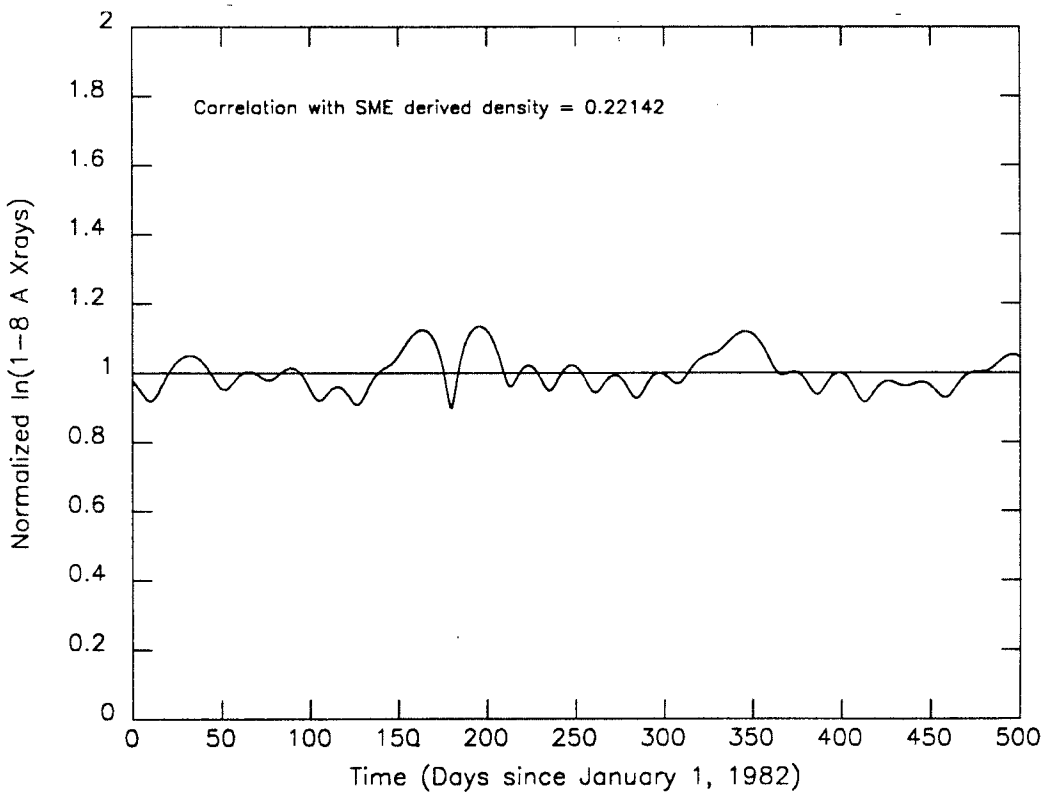

Figure 4.16 (f) **Normalized 24-day filtered ln(1-8 Å X-rays).**

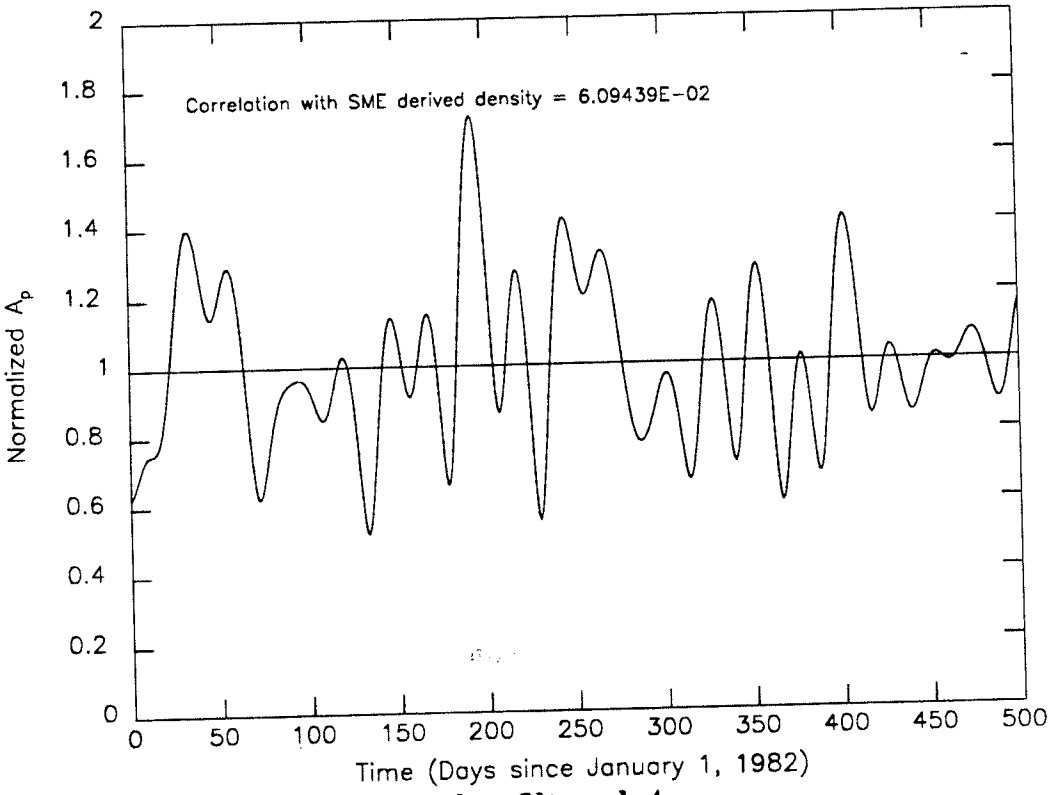

Figure 4.16 (g) **Normalized 22-day filtered A_p.**

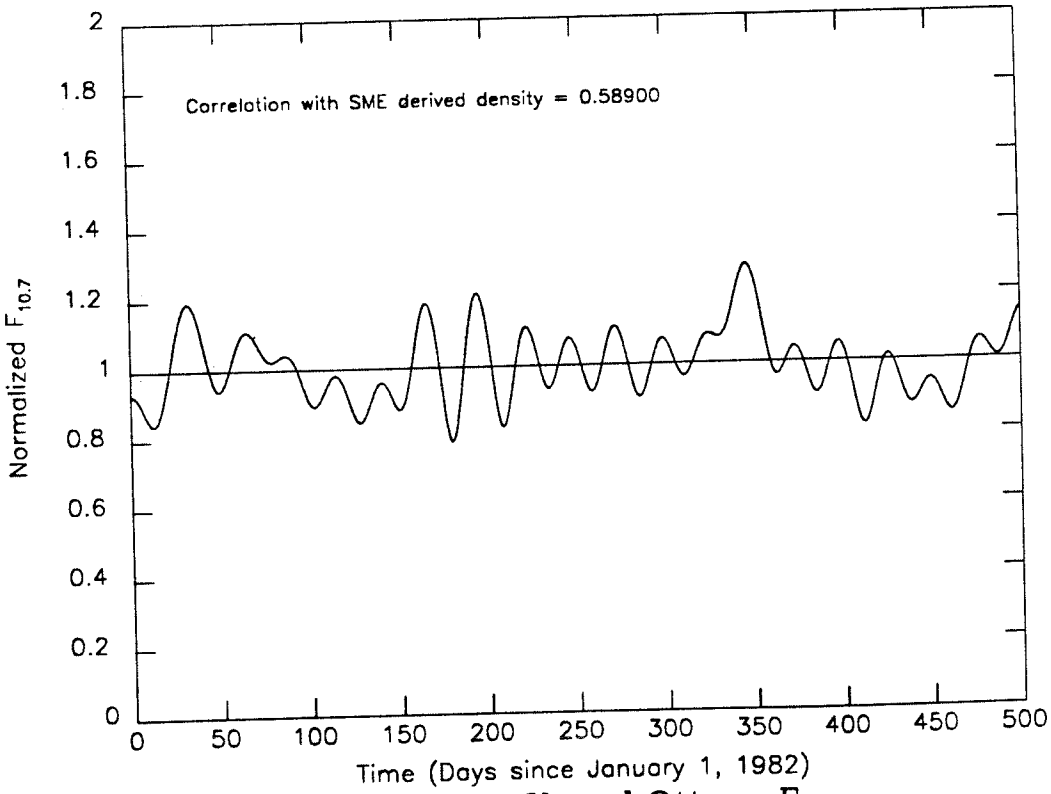

Figure 4.16 (h) Normalized 24-day filtered Ottawa $F_{10.7}$.

the chromospheric emission in this example while both models follow the coronal emissions. In the second case, March 1983, the normalized SME derived density in Figure 4.16a shows a solar rotational feature while neither MSIS 83 nor this model show an enhanced density feature. Normalized Lyman-α in Figure 4.16e does show an emission feature in this period and the SME derived density again follows chromospheric emissions rather than coronal or transition region emissions. This supports the general conclusion that, during high solar activity, derived density follows chromospheric emission variations better than coronal or transition region emission variations.

Other observations are made between the normalized time series of densities or indices and the normalized SME derived density. The normalized EUV model densities in Figure 4.16c have a low correlation, r = 0.27, where the influence of the 1-8 Å X-ray parameterized coronal emissions substantially overestimate that component of EUV heating. The normalized total EUV energy flux in Figure 4.16d also has a moderate correlation, r = 0.37, with the same overstated coronal influence. The normalized 10-day filtered SME Lyman-α in Figure 4.16e has a high correlation, r = 0.70, which supports the previous conclusion of a high correlation between chromospheric emissions and upper thermospheric densities. The normalized 24-day filtered natural logarithm of the 1-8 Å X-rays in Figure 4.16f has a low correlation, r = 0.22, and also supports the finding of a minimal correlation between purely coronal emissions and upper thermospheric densities. The normalized 22-day filtered A_p value in Figure 4.16g shows no correlation, r = 0.01, and, therefore, a constant auroral heating component parameterized by a constant A_p index is justified in this model. The normalized 24-day filtered Ottawa $F_{10.7}$ in Figure 4.16h shows a moderate correlation, r = 0.59, and gives general support to the EUV index as used in the empirical MSIS 83 model.

The time series of the exospheric temperature from this model over the January 1982 through May 1983 time period, shown in Figure 4.17, demonstrates the variation of modeled temperatures during high solar activity with a 27-day modulation. The range extends from the maximum value of 1289 °K to a minimum of 1111 °K. The modeled total EUV energy flux in Figure 4.18 is the solid line and shows the EUV variability with a 27-day periodicity. It is the sum of all the chromospheric and coronal components and it ranges between 5.3 ergs cm^{-2} sec^{-1} to 3.5 ergs cm^{-2} sec^{-1}. The dotted line shows the He II chromospheric emission and the dashed line shows the 150-200 Å cool coronal emissions. The He II and the 150-200 Å emissions are shown separately in Figures 4.19 and 4.20. They demonstrate the wide differences in the amplitudes of the chromospherically and coronally produced fluxes, respectively. In particular, it is observed that the He II chromospheric emission follows the Lyman-α variations in June 1982 and March 1983 while the 150-200 Å cool corona emissions follow the 1-8 Å X-ray variation during the same time periods. The range of He II variation is 0.41 ergs cm^{-2} sec^{-1} to 0.36 ergs cm^{-2} sec^{-1} and the 150-200 Å interval varies from 0.65 ergs cm^{-2} sec^{-1} to 0.42 ergs cm^{-2} sec^{-1}.

These results lay the groundwork for the next chapter in this thesis. It is possible to test of how well the EUV flux model mass densities may be used to represent the atmosphere. The density results from Figure 4.15a are used in a long-term orbit predictor for the SME case. From this, it is possible to compare the results of the actual SME orbit decay to the modeled decay over the same time period. This application of the modeled density is discussed in Chapter V.

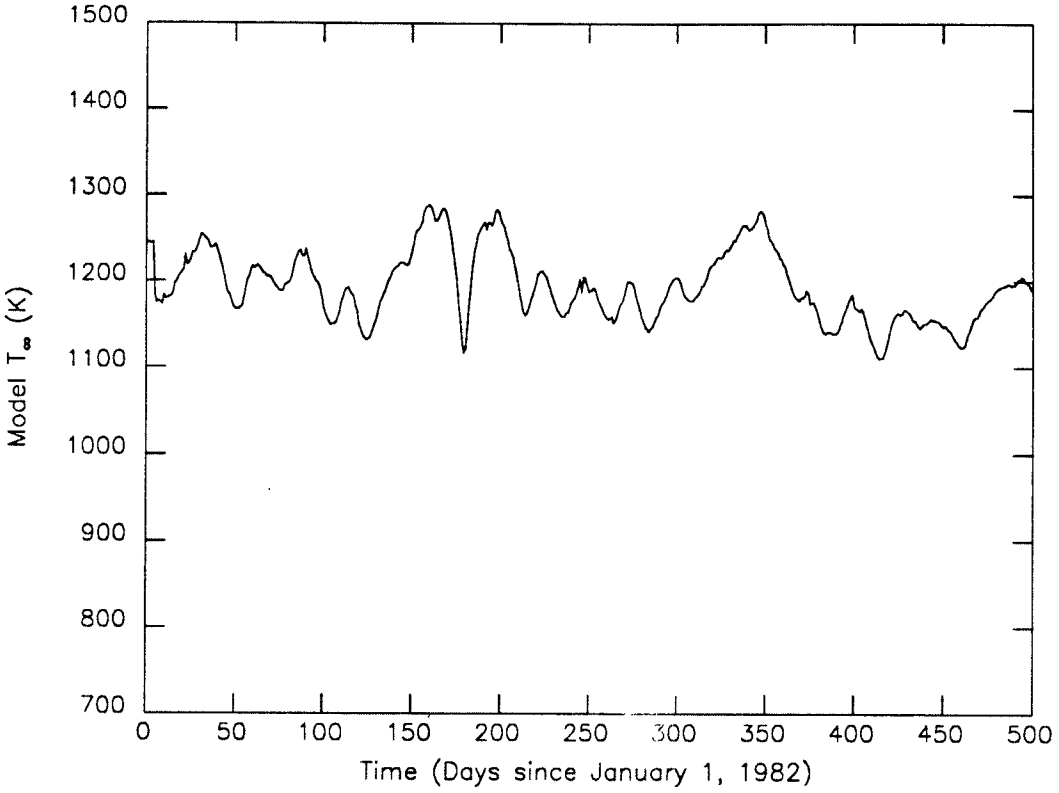

Figure 4.17 **Model exospheric temperature in 1982-83.**

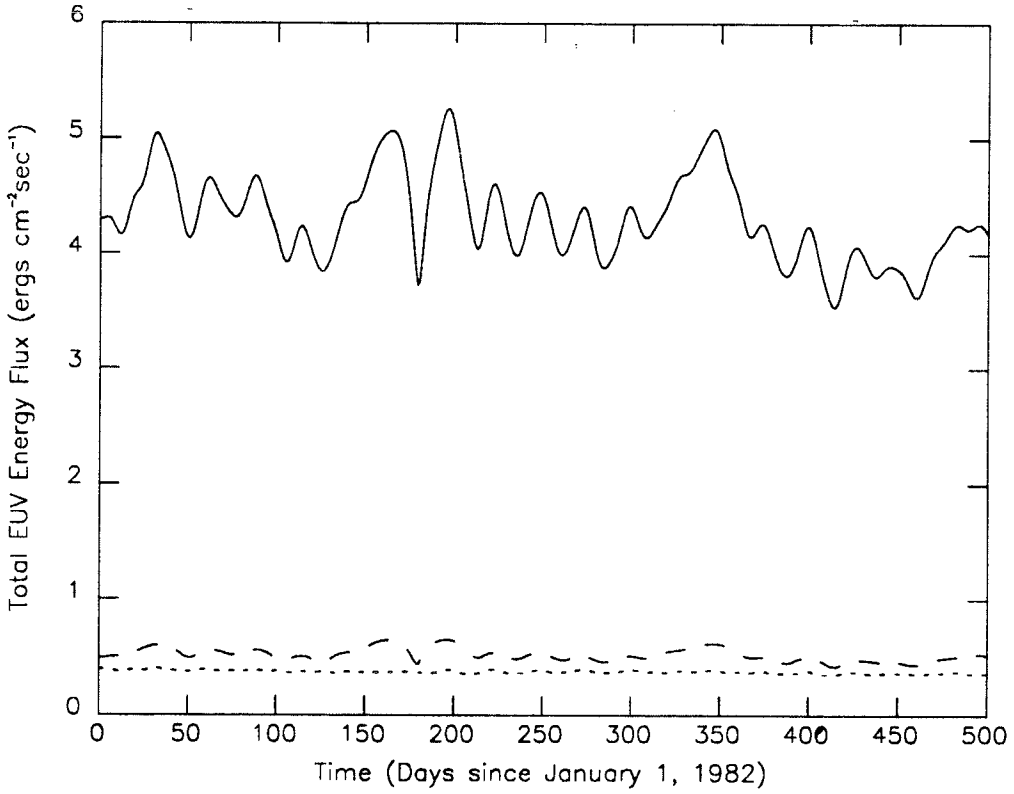

Figure 4.18 **Total EUV energy flux in 1982-83.**

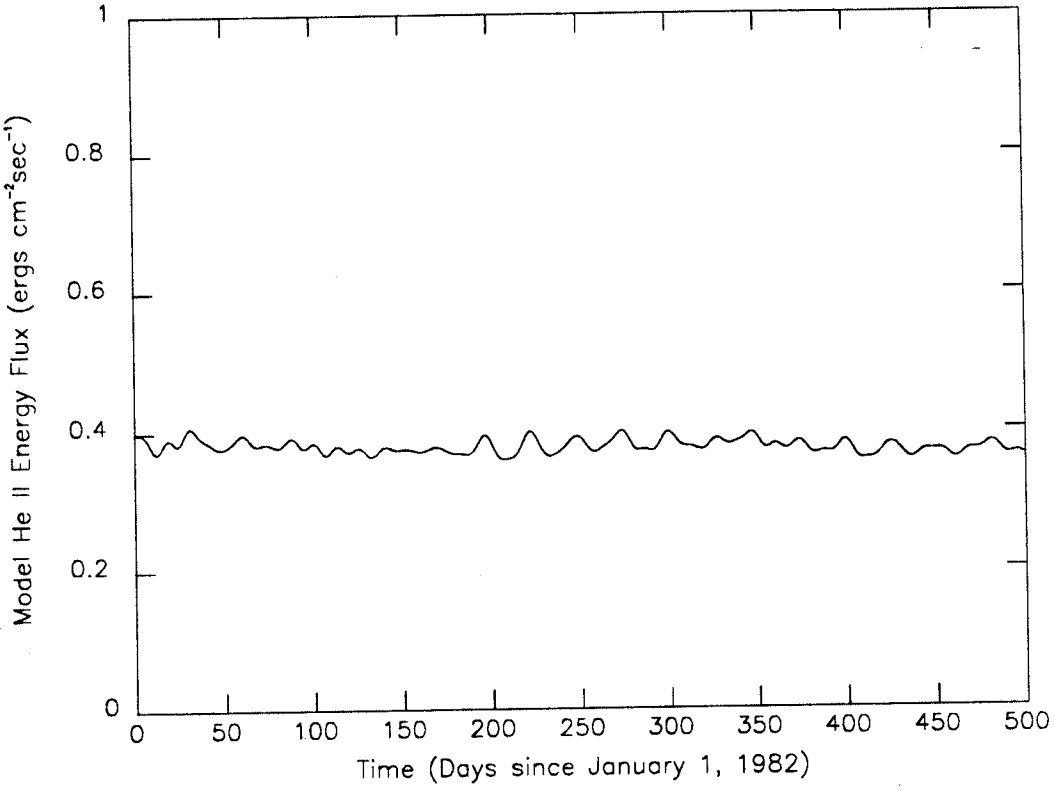

Figure 4.19 Model He II (304 Å) energy flux in 1982-83.

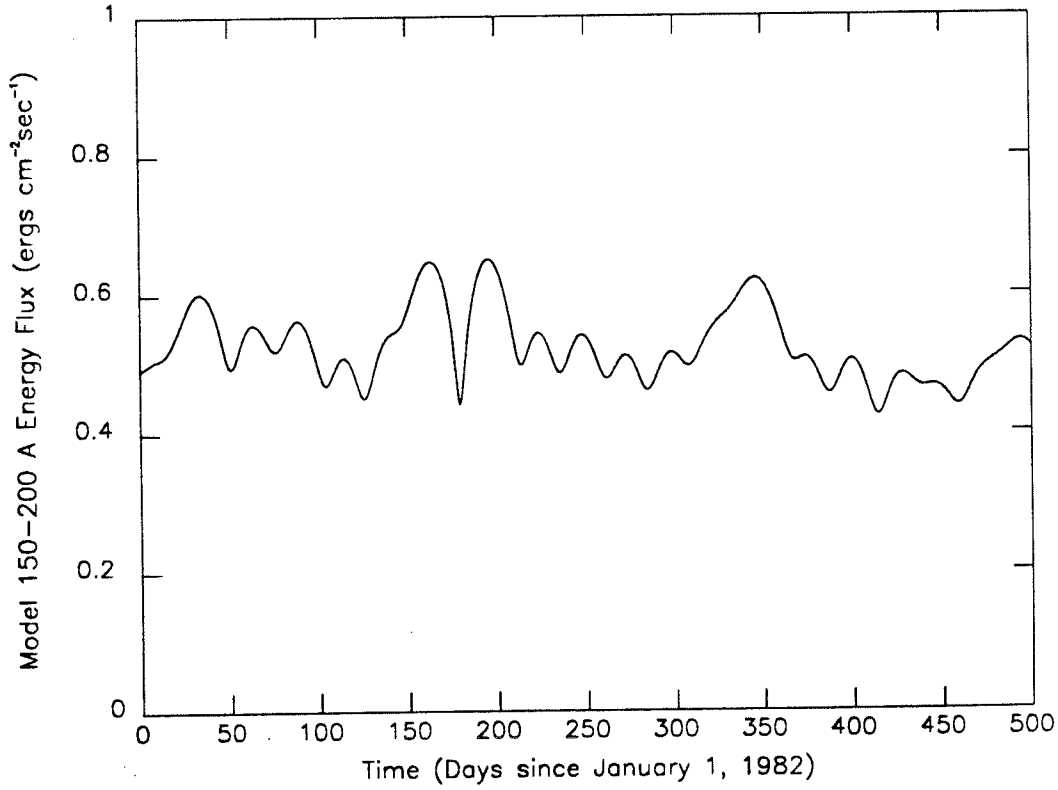

Figure 4.20 Model 150-200 Å energy flux in 1982-83.

4.3 Summary

Using a one-dimensional thermospheric model, which is validated by a comparison of its results to MSIS 83 for solar maximum and minimum conditions, the following conclusions can be drawn.

Auroral heating is a secondary but important component of the thermospheric heat budget and is empirically parameterized here for a constant low level heat input. Following a model run for 17 months during high solar activity, it is shown that the density time series model for the decline of cycle 21 has good 27-day solar rotational features comparable in phase to the MSIS 83 modeled densities and SME derived densities. The chromospheric and coronal EUV flux components have wide differences in their relative amplitudes of variation with the coronal fluxes having greater variation during high solar activity. Chromospheric emissions are primarily responsible for thermospheric density variations during highly active solar conditions. The modeling of chromospheric EUV energy flux by Lyman-α is demonstrated to be a valid method for estimating the EUV energy which heats the thermosphere and causes density and temperature variations. The $F_{10.7}$ is a moderate index for parameterizing EUV flux but is useful in the MSIS 83 model and 1-8 Å X-rays are a poor index for parameterizing EUV flux when used in this model.

CHAPTER V

MODELING THERMOSPHERE - SATELLITE ORBIT INTERACTIONS

The primary focus of Chapters II, III, and IV has been the modeling of EUV heating in the thermosphere and the subsequent densities and temperatures. These densities are now used as an input to an orbit propagator. In section 5.1, the Long-Term Orbit Predictor (LOP) program and its input parameters are discussed. It is the tool used in this study to model orbit decay. In section 5.2, the two-indices EUV flux model developed in Chapter III and validated in Chapter IV is now tested through use as an input which allows modeled orbit decay to be compared with actual orbit decay.

5.1 Long-Term Orbit Predictor (LOP)

5.1.1 Semi-Analytic Method

The LOP program by Kwok [1986] was developed in Fortran 77 as an analysis tool for long-term orbit studies using classical equations of motion combined with numerical integration. The Lagrange planetary equations of motion used in LOP are described by Kaula [1966] as

$$\frac{da}{dt} = \frac{2}{na}\frac{\partial R}{\partial M} \tag{5.1}$$

$$\frac{de}{dt} = \frac{1-e^2}{na^2 e}\frac{\partial R}{\partial M} - \frac{\sqrt{1-e^2}}{na^2 e}\frac{\partial R}{\partial \omega} \tag{5.2}$$

$$\frac{d\omega}{dt} = -\frac{\cos i}{na^2\sqrt{1-e^2}\sin i}\frac{\partial R}{\partial i} + \frac{\sqrt{1-e^2}}{na^2 e}\frac{\partial R}{\partial e} \tag{5.3}$$

$$\frac{di}{dt} = \frac{\cos i}{na^2\sqrt{1-e^2}\sin i}\frac{\partial R}{\partial \omega} - \frac{1}{na^2\sqrt{1-e^2}\sin i}\frac{\partial R}{\partial \Omega} \tag{5.4}$$

$$\frac{d\Omega}{dt} = \frac{1}{na^2\sqrt{1-e^2}\sin i}\frac{\partial R}{\partial i} \tag{5.5}$$

$$\frac{dM}{dt} = n - \frac{1-e^2}{na^2e}\frac{\partial R}{\partial e} - \frac{2}{na}\frac{\partial R}{\partial a}. \tag{5.6}$$

The classical orbital elements, i.e., the semi-major axis a, the eccentricity e, the argument of periapsis ω, the inclination i, the longitude of the ascending node Ω, and the mean anomaly M, are solved within a planet equator of epoch coordinate system. In this system, the $X-Y$ plane is defined at an epoch which is close to the initial propagation time. R is the disturbing function which contains all of the terms of the gravitational potential, V, except for the central term. n is the mean motion given by $n = \sqrt{\mu/a^3}$, where μ is the Earth's gravitational constant.

Prior to the numerical integration, the equations of motion are modified by using a singly averaged method of removing the fast time-varying element, M, from the geopotential expressions. The resulting differential equations are non-singular for zero eccentricity and singular for zero inclination. The numerical integration is then conducted using a multi-step, variable order, and variable step-size integrator. These features allow LOP to be used efficiently for long-term orbit propagation studies, especially when detailed information within one orbit is not necessary.

A particular characteristic of LOP which has been useful in this study is the modularity of the program. The main driver, the integrator, the derivative module, and the output module encompass the entire program. These units are supplemented by their sub-modules. Several of the sub-modules can be replaced without affecting other program components. This is true of the atmospheric density sub-module which is called within the derivative routine. It has been replaced in LOP with a set of subroutines which provide the user-supplied atmospheric densities.

5.1.2 Input Parameters

The list of input parameters in Table 5.1 allow for the initialization of the LOP program. Kwok describes the details and use of these parameters. Here, a brief description of the more important ones relative to this study are discussed.

The flags of IDRAG, IPRINT, NP, NQ, and NSEG1 all have non-zero values. The value of IDRAG may range from 0 to 8. The respective values, with their descriptive effect, are summarized in Table 5.2. For this study, the values of 6, 7, and 8 are used to compare the orbit decay results from the inputs of the SME derived density shown in Figures 3.29 and 4.15a, the density obtained with the two-indices EUV flux model shown in Figure 4.15a, and the MSIS 83 modeled density shown in Figure 4.15a, respectively. These flag values allow a subroutine to open a data file in order to retrieve the appropriate density time series. A value of 2 for IPRINT prints the density, date, and altitude information to the CRT screen during an interactive LOP run. NP is 15 and is the approximate integer number of nodal crossings per planet rotation resulting from SME's 15^{+} orbits per day. NQ is set to 1 and is a denominator used with NP as a numerator. NSEG1 is set to 4 and is the number of segments recommended by Kwok for applying quadrature in the atmospheric drag calculations.

The double precision floating point initialization values for LOP are given in the second page of Table 5.1. For the epoch of January 3, 1982, the listed values used for the classical orbital elements in ORB are $a = 6907.0568$ km, $e = .000259$, $i = 97.469°$, $\Omega = 328.2822°$, $\omega = 355.5519°$, and $M = 293.3501°$. These values were obtained from the GSFC definitive ephemeris for January 3, 1982. This date is referred to as 19820103 in the initial time, TINT. The relative and absolute accuracy for the integrator is set at 1×10^{-6}

TABLE 5.1. INPUT FLAGS FOR LOP

Flag Value	Description
0	L
0	M
0	ISUN
0	IMOON
0	IEPHEM
6	IDRAG
0	ISRP
0	IORB
2	IPRINT
0	IPLOT
15	NP
1	NQ
0	IQMAX
0	NK
0	ICASE
0	LSUN
0	NSUN(1)
0	(2)
0	(3)
0	(4)
0	(5)
0	(6)
0	(7)
0	(8)
0	(9)
0	LMOON
0	NMOON(1)
0	(2)
0	(3)
0	(4)
0	(5)
0	(6)
0	(7)
0	(8)
0	(9)
4	NSEG1
0	NSEG2

TABLE 5.1. INPUT VALUES FOR LOP
(continued)

Numerical Value	Description
6907.0568D0	ORB(1) A
.0002590D0	(2) E
97.4690D0	(3) I
328.2822D0	(4) NODE
355.5519D0	(5) W
293.3501D0	(6) M
1.0D-6	RELERR
1.0D-6	ABSERR
10.0D0	STEP
19820103.D0	TINT(1) YMD
0.0D0	TINT(2) HMS
19830531.D0	TFIN(1)
0.0D0	TFIN(2)
19820103.D0	TREF(1)
0.0D0	TREF(2)
3.9860045D5	GE
6378.140D0	RE
4.178074216D-3	RATE
0.0D0	PM
.08182D0	ELLIP
6468.140D0	RATM
0.0D0	RDENS
0.0D0	RHT
0.0D0	SHT
600.0D0	ALTMAX
3.5D-6	AREAD
0.0D0	AREAS
415.5D0	SCMASS
0.7D0	CDRAG
0.0D0	CSRP
0.0D0	GS
0.0D0	ES(1)
0.0D0	(2)
0.0D0	(3)
0.0D0	(4)
0.0D0	(5)
0.0D0	(6)
0.0D0	(7)
0.0D0	GM
0.0D0	EM(1)
0.0D0	(2)
0.0D0	(3)
0.0D0	(4)
0.0D0	(5)
0.0D0	(6)
0.0D0	(7)

TABLE 5.2. IDRAG VALUES IN LOP INPUT FILE

IDRAG	Effect of Flag on Drag Calculation
0	No Drag
1	Drag using simple exponential atmosphere
2	Drag with osculating altitude
3	Drag, osculating altitude, density from best estimate of $F_{10.7}$
4	Drag, osculating altitude, density from -1σ estimate of $F_{10.7}$
5	Drag, osculating altitude, density from $+1\sigma$ estimate of $F_{10.7}$
6	Drag, osculating altitude, SME-derived density
7	Drag, osculating altitude, two-indices EUV flux modeled density
8	Drag, osculating altitude, MSIS-83 modeled density

in RELERR and ABSERR and a 10-day time step value in STEP is used for printing the results to an output data file every tenth day. The run termination date is set for May 31, 1983, or 19830531, in TFIN for each case. The epoch reference date, TREF, is set to the initial orbit propagation epoch. A mean equatorial radius, RE, for the Earth of 6378.14 km is used for determining altitude information and the values of GE, RATE, ELLIP, and RATM are those recommended by Kwok. ALTMAX is the maximum altitude for considering atmospheric drag and is set to 600 km. SME never goes higher than this altitude. From Tobiska [1985], the SME area is shown to be 3.5 m^2 and this value is given in units of km^2 for the atmospheric drag parameter AREAD. Tobiska also indicates that SME has a mass of 415.5 kg, which is the value of SDMASS. CDRAG, the drag coefficient C_d, is set to 0.7 and is justified below in section 5.1.4.

5.1.3 J_2 and Other Coefficients

The J_2 and other higher degree and order spherical harmonic coefficients representing the gravitational field have been neglected in this study. J_2

gives the largest periodic geopotential perturbation according to Taff [1985]. This elimination of geopotential terms in the motion of a satellite around the Earth reduces the motion to a two-body Keplerian orbit. This is justified based on both the time resolution of the other datasets available in this study and on the results of a LOP sensitivity investigation.

In using seven datasets to conduct this modeling effort, the common time unit of one day was selected both to maximize computational efficiency and to retain as much time series information as possible. Thus, for comparative and modeling efforts, no time resolution of less than a day is used. Since the J_2 and the m-daily geopotential terms, where $m = 2, 3, ...$, are periodic on timescales of less than a day, a modeling and analysis tool with resolution less than a day is not justified for this particular study.

To further verify the decision to neglect J_2 and m-daily terms, a sensitivity test was conducted using LOP with and without the J_2 term which is the $-C_{20}$ spherical harmonic coefficient. In addition to the input values in Table 5.1, the input file included the following final line during the sensitivity study,

$$2 \quad 0 \quad -0.1082626999999999D-02 \quad 0.0000000000000000D+00.$$

The 2 and 0 indicate the degree, n, and order, m, of the $-C_{nm}$ coefficient, J_2. $-1082.6269 \times 10^{-6}$ is the J_{nm} value and 0.0D0 is the stroboscopic mean node, λ_{nm}, value required by LOP. After 17 months between January 1982 and May 1983, the mean altitude is 514.72 km using the J_2 term compared to 514.54 km without using J_2. The 180 m difference is negligible over this period of time. Thus, the assumption that gravity perturbations can be neglected when considering atmospheric drag on low Earth orbiting spacecraft is verified.

5.1.4 Drag Coefficient, C_d

The drag coefficient appears in the commonly used equation describing the drag force

$$F_d = \frac{1}{2} C_d A \rho v^2 \tag{5.7}$$

which is derived from the kinetic energy of a vehicle and relates the atmospheric drag force, F_d, to C_d, the vehicle area, A, the atmospheric mass density, ρ, and the vehicle velocity, v. Historically, the greatest uncertainty in solving this equation has been estimating ρ, determining A, and calculating C_d, roughly in that order. As a result, much effort has been expended toward developing time-dependent, empirical model atmospheres since the late 1950s. This was discussed in Chapter I. Satellite areas have been determined with more or less accuracy. Flat plate, spherical, or cylindrical satellite shapes have been assumed and an "effective" or projected area in the plane perpendicular to the vehicle direction of motion has often been used. This leads to a method of empirically setting C_d to a first order approximation. This method approximates or simplifies C_d by eliminating one independent variable and using a reduced area based on a maximum angle of attack where $\alpha = 90°$. This formulation is described by Cook [1965] and has yielded generally acceptable results which enable modeled and satellite derived atmospheric densities to be matched. This method differs from the empirical and contemporary use of a ballistic coefficient, $\frac{C_d A}{m}$ in units of $m^2\ kg^{-1}$, where C_d and A are described above and m is the spacecraft mass. This latter coefficient is also an empirical term which folds the uncertainties in all three variables into one term and allows a match between the theoretical atmospheric drag force on a satellite and the observed force obtained from the orbit decay rate. However, these methods of determining C_d are not appropriate for studying variations in or

the range of the drag coefficient.

The classical treatment of C_d is rigorously developed on the basis of geometry, conservation of energy, and conservation of momentum in gas dynamics. A gradual understanding of the atmospheric drag coefficient at satellite altitudes followed from the efforts of Millikan [1923], who analyzed spheres moving through a gas which had a large mean free path and where the dynamical interaction was considered mirror-like, or specular, reflection. Epstein [1924] showed that diffuse reflection of gas particles in a large mean free path gas plays an important role in momentum exchange and that this interaction has a gas temperature dependence.

A number of researchers subsequently evaluated C_d in free molecular flow, which is a rarefied gas flow. Free molecular flow differs from Newtonian flow in that the latter assumes the gas particles are at rest with respect to one another. Zahm [1934] noted that a free molecular flow becomes a Newtonian particle flow in the limit where an extremely large ratio exists for the mass velocity, v_{sc}, to the gas thermal velocity, v_{th}. This ratio is defined as the molecular speed ratio, S, where

$$S = \frac{v_{sc}}{v_{th}} \tag{5.8}$$

and $S \to \infty$ in the limiting case. In equation (5.8), if $S > 1$, then particles are assumed to strike only the forward face of a body. If $S \gg 1$, the thermal velocities of the particles can be neglected and there is an approximated Newtonian flow. However, as will be shown below, when $1 < S < 10$, gas particle thermal velocities may be accounted for in evaluating C_d.

The impinging gas particle velocities vary in magnitude as well as direction and assume a Maxwellian distribution, as do the reemitted particles which have been adsorbed onto the surface and come off with no "memory" of

their initial velocity magnitudes or directions. From the principle of equipartition, the Maxwellian distribution of velocities in a gas can be summarized as

$$v_{rms} = \sqrt{v_x^2 + v_y^2 + v_z^2} = \sqrt{\frac{3kT}{m}}. \tag{5.9}$$

Using SI units, k is Boltzmann's constant, T is the temperature in degrees Kelvin, and m is the mass of the particle. This analysis uses $v_{th} = v_{rms}$.

Sänger [1938] pioneered experimental work with extremely rarified gases by analyzing the air pressure on bodies of various shapes and outlining drag and lift coefficients. The regimes of gas kinetics, including rarified gases, and their differences as related to aerodynamics was explained by Tsien [1946], followed by the analytic and experimental work of Stalder and Jukoff [1948], Stalder *et al.* [1950], and Stalder and Zurick 1951]. Stalder and coworkers calculated surface temperatures in a rarified gas flow, experimentally determined drag coefficients and temperatures on bodies of various shapes, and noted that the drag coefficient C_d was dependent upon the molecular speed ratio, S, and the body surface temperature, T_w. The total C_d due to diffusive and specular reflections was summarized by Schaaf and Chambré [1958] while Hoerner [1958] simplified the expression for C_d in his work.

The physics describing gas particle interactions at and with spacecraft surfaces encompasses the concepts of body geometry, the conservation of energy in heat transfer and the conservation of momentum. In this thesis, the heat transfer between particle and surface "wall," which includes defining a thermal accommodation coefficient, is referenced only in comparison to other work. Its effect upon the magnitude of C_d is generally secondary compared to the momentum terms and is analyzed in depth by Stalder and Zurick and by Schaaf and Chambré. The conservation of momentum combined with geome-

try are discussed in detail below.

The diffuse reflection effect upon C_d is applicable to spacecraft flight conditions for two reasons. First, as noted by Sänger, and based on experimental observations, surfaces are often rough. The reflection from this type of surface is expected to be diffuse. Second, the impinging particles at altitudes above 200 km are predominantly O which is chemically reactive. Oxidizing surface reactions occur with some commonly used spacecraft metals such as aluminum. Subsequent reactions which release or replace chemically bonded O from surfaces are expected to give the released O atoms a thermal velocity distribution dissimilar to the ambient thermal velocities. The percentage of atoms which adhere to the surface is uncertain, however. In addition, laboratory experiments discussed by Herrero [1987] give data on the fractional momentum transfer of O^+ and N_2^+ as a result of impact with surfaces and as a function of incidence angle. The momentum fraction (reemitted/incident momentum) is small ($< \pm 0.25$) for angles less than 60° and high for higher incidence angles. Herrero interprets correctly that grazing collisions on engineering grade surfaces are strongly specular. However, momentum loss for low incidence angles does not rule out, and in fact may point to, diffuse reflection. While more experimental studies are needed, this thesis assumes that diffuse reflection from low incidence collisions is a major process occurring in an upper thermosphere flight regime. This is the assumption made for SME. Both diffuse and specular reflection C_d terms are described here in some detail.

The drag coefficient for diffuse reflection analytically described by Stalder and Zurick and summarized by Schaaf and Chambré, is

$$C_{d_{diff}} = \frac{2}{\sqrt{\pi}S}\left[e^{-(S\sin\alpha)^2} + \sqrt{\pi}S\sin\alpha\left(1+\frac{1}{2S^2}\right)erf(S\sin\alpha) + \frac{\pi S}{S_w}\sin^2\alpha\right]. \tag{5.10}$$

The specular reflection C_d described by the same authors is

$$C_{d_{spec}} = \frac{4\ sin\ \alpha}{\sqrt{\pi}S^2}\{(Ssin\ \alpha)e^{-(Ssin\ \alpha)^2} + \sqrt{\pi}\ [\frac{1}{2} + (Ssin\ \alpha)^2]\ erf(Ssin\ \alpha)\}. \tag{5.11}$$

These are expressions for a flat plate at an angle of attack, α, and are graphically shown in Figures 5.1 and 5.2. The flat plate approximation may be used in free molecular flow for a number of spacecraft surfaces since the vehicle dimensions "seen" by a particle, compared to its own size, are extremely large. S_w in equation (5.10) is the molecular speed ratio referenced to the temperature of the surface, T_w, where

$$S_w = \frac{v_{sc}}{\sqrt{\frac{3kT_w}{m}}}. \tag{5.12}$$

These equations do not use the ratio of specific heats, γ, and hence are valid for either monatomic or diatomic gases.

Equations (5.10) and (5.11) are two component formulations for C_d which include terms describing the impinging momentum related to the angle at which incident particles strike the surface and terms describing the diffuse or specular reflection of particles. These equations are derived from the conservation of momentum and geometry of the system detailed by Sänger and Stalder and Zurick. The 90° contour in Figure 5.1 may be compared to the flat plate drag coefficient given by Cook. His formulation for a diffuse reemission drag coefficient, plotted in Figure 5.3, is

$$C_{d_{diff}} = 2(1 + \frac{2}{3}r) \tag{5.13}$$

where r is related to the thermal accommodation coefficient, α_{th}, and is written as

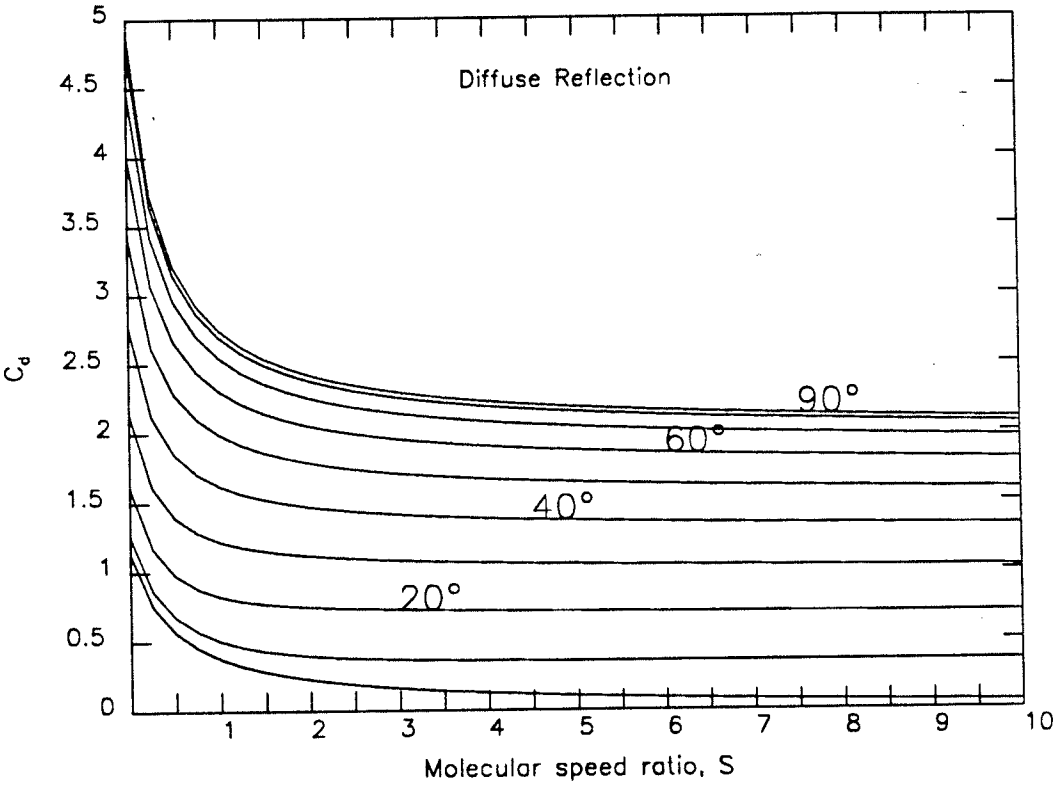

Figure 5.1 **Flat plate drag coefficient, $C_d(S, \alpha)$, with diffuse reflection.** This plot is based on equation (5.10).

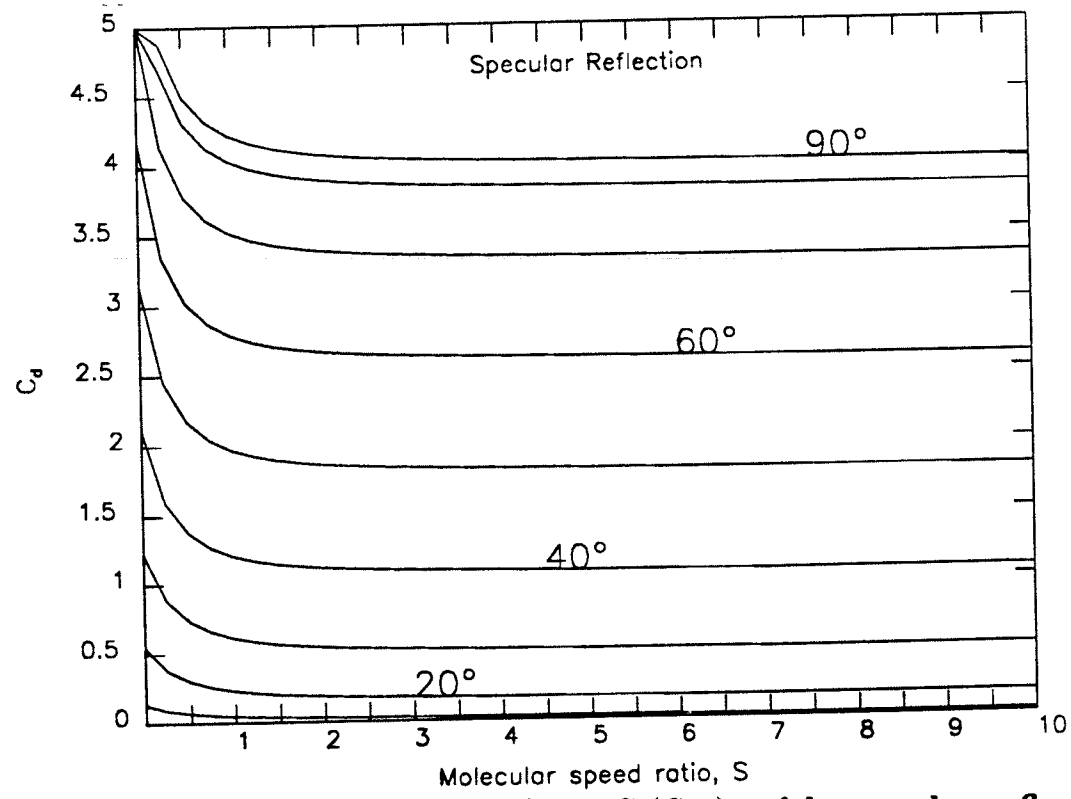

Figure 5.2 **Flat plate drag coefficient, $C_d(S, \alpha)$, with specular reflection.** This plot is based on equation (5.11).

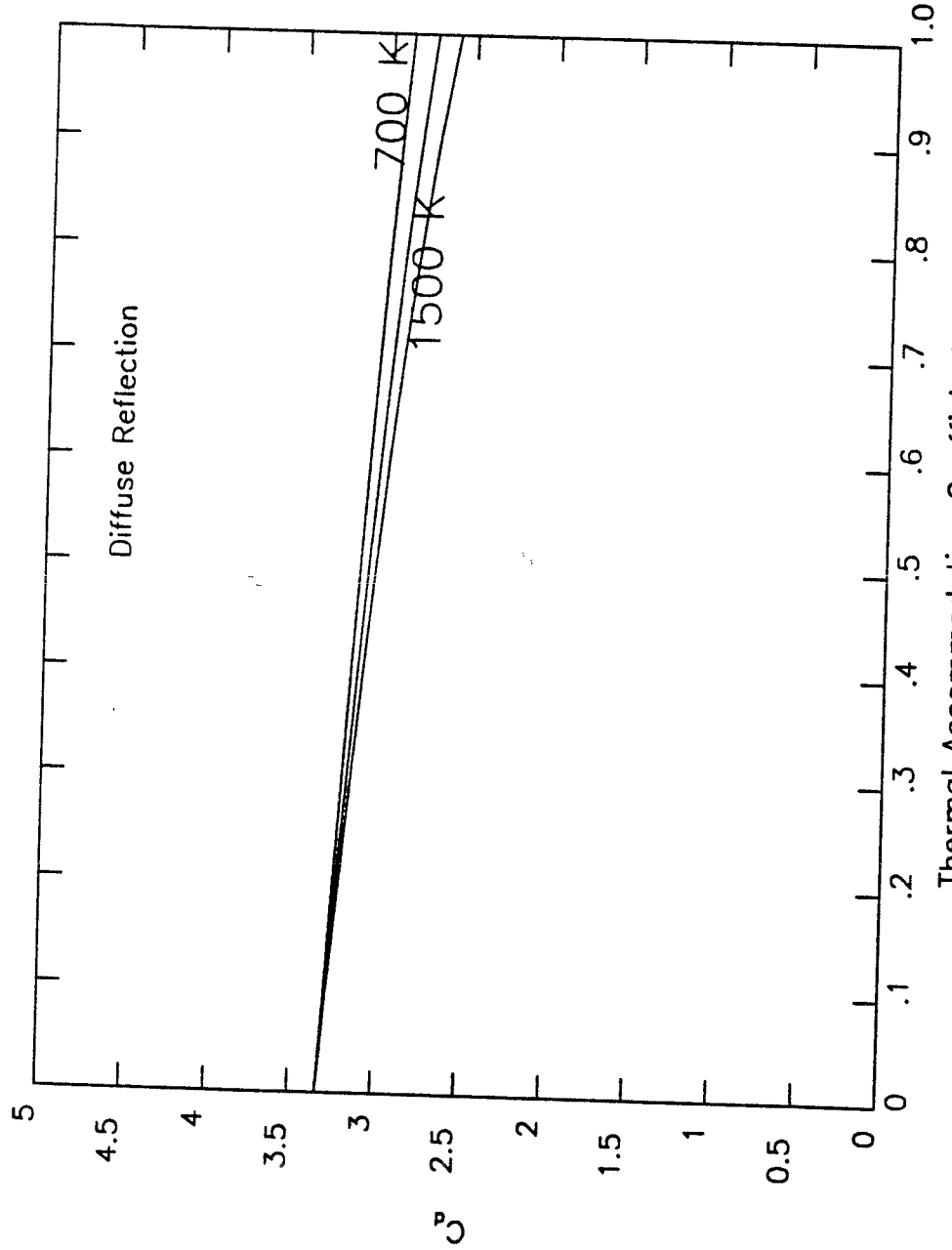

Figure 5.3 Flat plate drag coefficient, $C_d(\alpha)$, with diffuse reflection. This plot is based on equation (5.13).

$$r = \frac{v_r}{v_i} = \{1 + \alpha_{th}[\frac{T_w}{T_i} - 1]\}^{\frac{1}{2}}. \tag{5.14}$$

Cook defines v_r as the speed of the reemitted particle, v_i as the speed of the incident particle, T_w as the surface temperature, T_i as the kinetic temperature of the incident particle, and

$$\alpha_{th} = \frac{E_i - E_r}{E_i - E_w} \tag{5.15}$$

where the subscripts i, r, and w refer to the incident, reemitted, and surface "wall" average kinetic energies. In this comparison, T_i is varied between 700, 1000, and 1500 K while T_w is 300 K. Cook's equation (5.13) is a helpful simplification of equation (5.10) under certain conditions, although differences arise from the weighting of $\frac{T_w}{T_i}$ in each equation.

Equation (5.13) is based on a projected area whose plane is perpendicular to the direction of motion. This effective area is coupled with the drag coefficient since the angle of attack is set to 90°. Using equation (5.13), one notes that $C_d = 2$ for the impingement component which is the same as equation (5.10) when $S \rightarrow \infty$. It can be shown that for low Earth orbiting spacecraft, the contribution of the reemission term is between one-third and one-half for r equal to one-half to three-quarters in Cook's equation. Summing the impingement and reemission components, an empirical value between 2 and 2.5 has been commonly used. The equation is properly used as an approximation, where C_d is dependent upon a projected area, where skin temperature effects are considered, and where gas thermal velocities are neglected based on the Newtonian flow assumption.

The full C_d expression, equation (5.10), is properly used independently of surface area. The full surface area is used with an angle of attack while both gas thermal velocities and skin temperature effects are considered. The

range of C_d in these conditions falls between 5 and near 0 from Figures 5.1 and 5.2. The Cook equation (5.13), or Figure 5.3, is a subset of the full C_d range in equation (5.10) or Figure 5.1. An example similar to the SME conditions for an impingement plus diffuse reemission value ranges from C_d equal to 0.7 to 1.0 for a flat plate angle of attack between 20 and 30 degrees and a moderate speed ratio, S, between 5 and 7.25. From Tobiska [1985], SME may be modeled as a flat plate since the circular solar array, shown in Figure 5.4, is the primary structure facing the ram direction. An average angle of attack of 20°, representing an SME roll angle described by Tobiska, is used to give a $C_d = 0.7$. This value is used in the modeling effort here along with a 3.5 m^2 area and a 415.5 kg mass. This C_d value also enables a match between the observed and modeled orbit decay. However, it should be cautioned that the roll angle is a dynamic parameter, varying during an orbit and over longer timescales. The 20° value used here is an estimate in lieu of a full spacecraft dynamics analysis. The latter study is beyond the scope of this thesis.

There is a small variation in C_d due to thermospheric temperature changes which can be estimated by examining the cases of maximum, moderate, and minimum solar activity. Table 5.3 outlines this. T_∞ is the exospheric temperature and closely approximates the ambient temperature in an orbit near the top of the thermosphere. The actual range of S for a low Earth orbiter is 5 to 7.25 for high to low solar activity. It can be shown through the MSIS 83 thermospheric model that this also corresponds to high and low exospheric temperatures during 1982 through 1986. From equation (5.10), if $S = 5, \text{then } C_d = 0.707$; if $S = 6, \text{then } C_d = 0.703$; and if $S = 7.25, \text{then } C_d = 0.699$. For a ±20% change in S, C_d changes by ±0.5% as a result of the change in the v_{rms} of the gas particles. For 1500 K, $v_{rms} = 1.52$ km sec^{-1}; for 1000 K, $v_{rms} = 1.24$ km sec^{-1}; and for 700 K, $v_{rms} = 1.04$ km

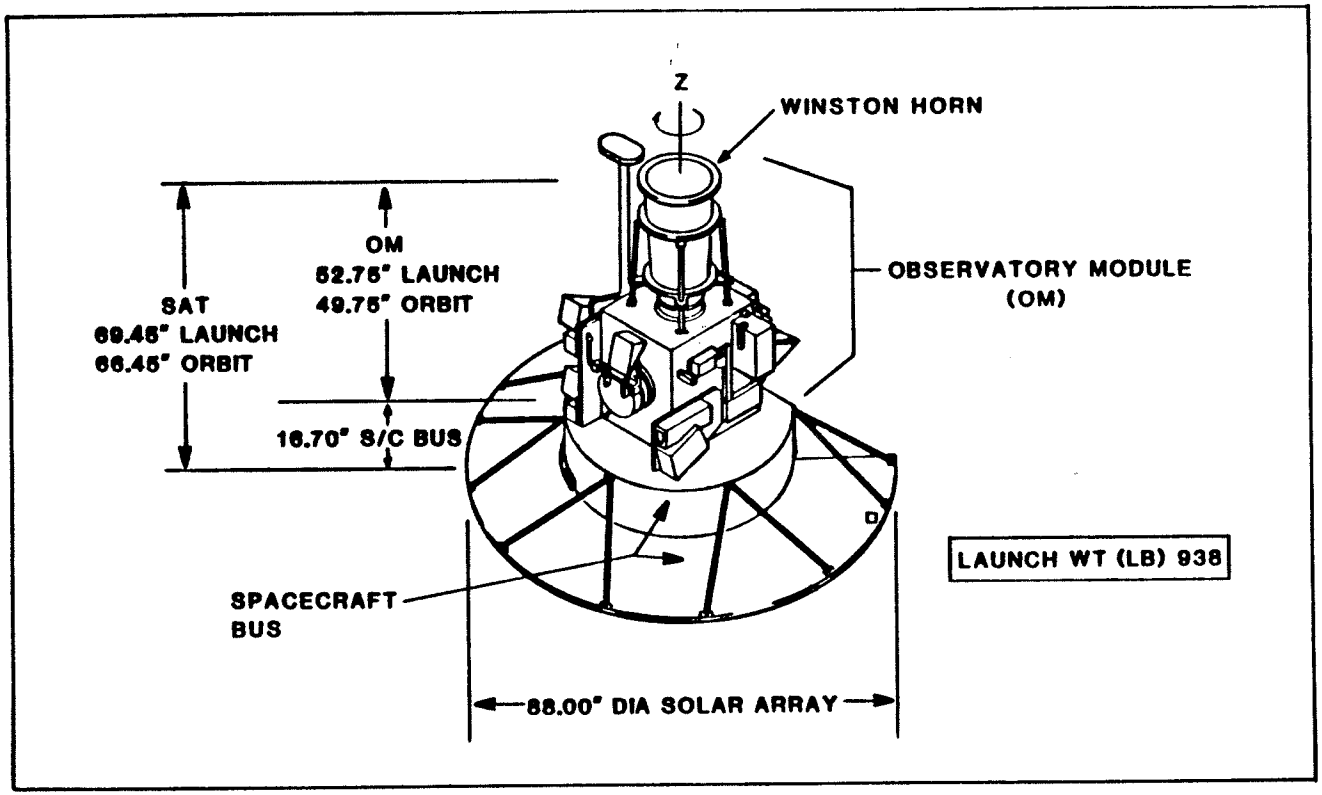

Figure 5.4 **Schematic of SME.** The back of the solar array, not shown here, faces the velocity vector. The on-orbit mass is 415 kg.

Table 5.3 C_d Variation with Solar Activity

Solar Activity [a]	T_∞ (K)	v_{rms} (km sec^{-1})	S	$C_{d_{diff}}$ [b]
high	1500	1.52	5	0.707
moderate	1000	1.24	6	0.703
low	700	1.04	7.25	0.699

[a] for solar cycle 21.
[b] C_d evaluated for $\alpha = 20°$, including a small S_w term from equation (5.10) where $T_w = 300$ K.

sec^{-1} using the example of O which has three degrees of freedom. Thus, there is also a ±20% variation around the $v_{rms} = 1.24$ km sec^{-1} value which is the basis for the change in S. This translates into a total 1% change in C_d due to thermospheric temperature changes over the course of a solar cycle from high-to-low activity and, for most applications, can be considered negligible.

In summary, by using the example of a flat plate spacecraft surface, the drag coefficient may vary due to changes in the spacecraft surface angle of attack and the gas temperature in rarified gas flows. C_d is independent of surface area and is a function of surface angle of attack, the molecular speed ratio referenced to the ambient gas particles, and the molecular speed ratio referenced to the spacecraft surface temperature. It is not a constant and may vary significantly from 2 over the range of near 0 to 5 primarily as a result of low-to-high angles of attack. Assuming that the spacecraft area, angle of attack, and atmospheric density are well known, the C_d variation due to gas temperature changes can be derived. This small variation is explained by changes in the kinetic energy of the gas particles over a solar cycle resulting from a variation in solar EUV energy input into the atmosphere at satellite altitudes. Angle of attack variations cause extremely large variations in C_d, i.e., up to 100%. Thermospheric temperature changes over the course of a solar cycle may cause variations on the order of 1% in C_d.

5.1.5 Modeled Thermospheric Density Time Series

As a final note on the use of LOP in this thesis, the program has been modified to include Fortran subroutines which allow modeled thermospheric density time series to be used. When the density at a particular altitude on a specific date is requested, the Julian date time format in LOP is converted to year and day-of-year format. Then, a file is opened containing the SME derived density, the two-indices EUV flux modeled density, and the MSIS 83 modeled density for the time period from January 3, 1982 through May 8, 1983. The appropriate record time series from the data file is read depending upon the value for IDRAG as noted above. Each of the record values, which are read into a one-dimensional array, are the derived or modeled density in kg km^{-3} at the mean altitude of SME on each date. The particular day is selected and that density value is returned to the main calling module in LOP.

5.2 Comparisons of SME Altitude Decay

LOP was run for the three cases of thermospheric density described above. The 10-day interval values of the classical orbital elements were returned by LOP and stored in a datafile. Figure 5.5 is a plot of the mean altitude calculated with LOP. This is the value obtained when the equatorial mean radius of 6378.14 km is subtracted from the semi-major axis value for the period from January 3, 1982 through May 8, 1983. The time axis is marked in increments of 20 days. The orbit decay results from the input SME derived density are shown as the light solid line, the results from the two-indices EUV flux model input are shown as the dotted line, and the results from the MSIS 83 model input are shown as the dashed line. The heavy solid line is the definitive ephemeris data provided by GSFC where missing day values are calculated by linear interpolation.

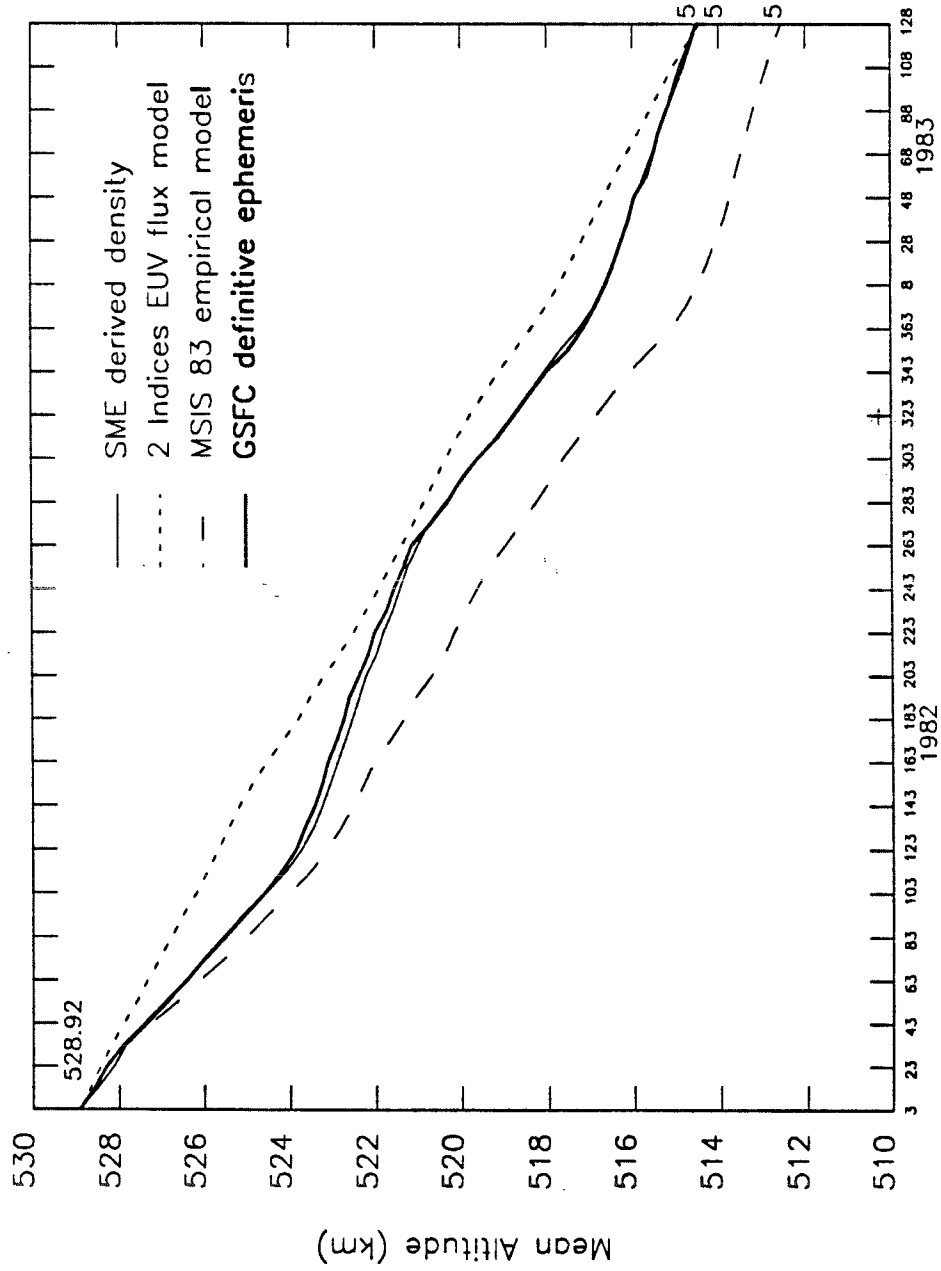

Figure 5.5 Comparison of orbit decay for January 3, 1982 through May 8, 1983. The LOP calculated altitude decay using the two modeled and one derived densities as inputs for atmospheric drag are compared to ephemeris data.

From the identical initial orbit elements on January 3, 1982 given to each LOP run, each time series of mean altitudes begin at 528.92 km. The SME derived density profile closely follows the GSFC ephemeris for the entire 17 months of high solar activity. This profile validates the use of LOP as an orbit predictor. The final mean altitude of the GSFC data and the SME derived density run is 514.54 km, or a total drop of 14.38 km mean altitude. The EUV flux model density profile follows a similar slope with a resulting 514.43 km mean altitude, or 14.49 km drop. This differs from the actual data by -0.11 km. The MSIS 83 density profile follows a steeper slope with a resulting 512.55 km mean altitude, or 16.37 km drop. This differs from the actual data by -1.99 km.

The time series themselves reveal high and low thermospheric density conditions when compared to Figure 4.15a, reproduced here as Figure 5.6 on a slightly shifted scale. The slope steepens in the mean altitude curve, which corresponds to periods of high density conditions. This is particularly noticeable in the GSFC and SME derived density profiles during days 23 through 103 and days 273 through 363 in 1982. Periods of lower relative density are apparent in days 123 through 263 in 1982 and days 8 through 128 in 1983. The EUV flux density model has slightly lower densities than the SME derived density dataset, as evident from Figure 5.6. With lower densities, there is less orbit decay as shown in Figure 5.5. The MSIS 83 density shows generally higher densities than the SME derived density dataset and this leads to greater orbit decay, which is also evident in Figure 5.5.

In conclusion, the orbit decay results of the input SME derived density time series validate LOP as an orbit propagator. The orbit decay results of the input EUV flux model density show reasonable long-term orbit decay with errors toward less decay. The orbit decay results of the input MSIS 83 mod-

eled density show reasonable long-term orbit decay with errors toward greater decay. Thus, the two-indices method of modeling EUV flux and calculating thermospheric density is a valid general method for determining EUV heating of the thermosphere which subsequently affects thermospheric density and satellite orbit histories.

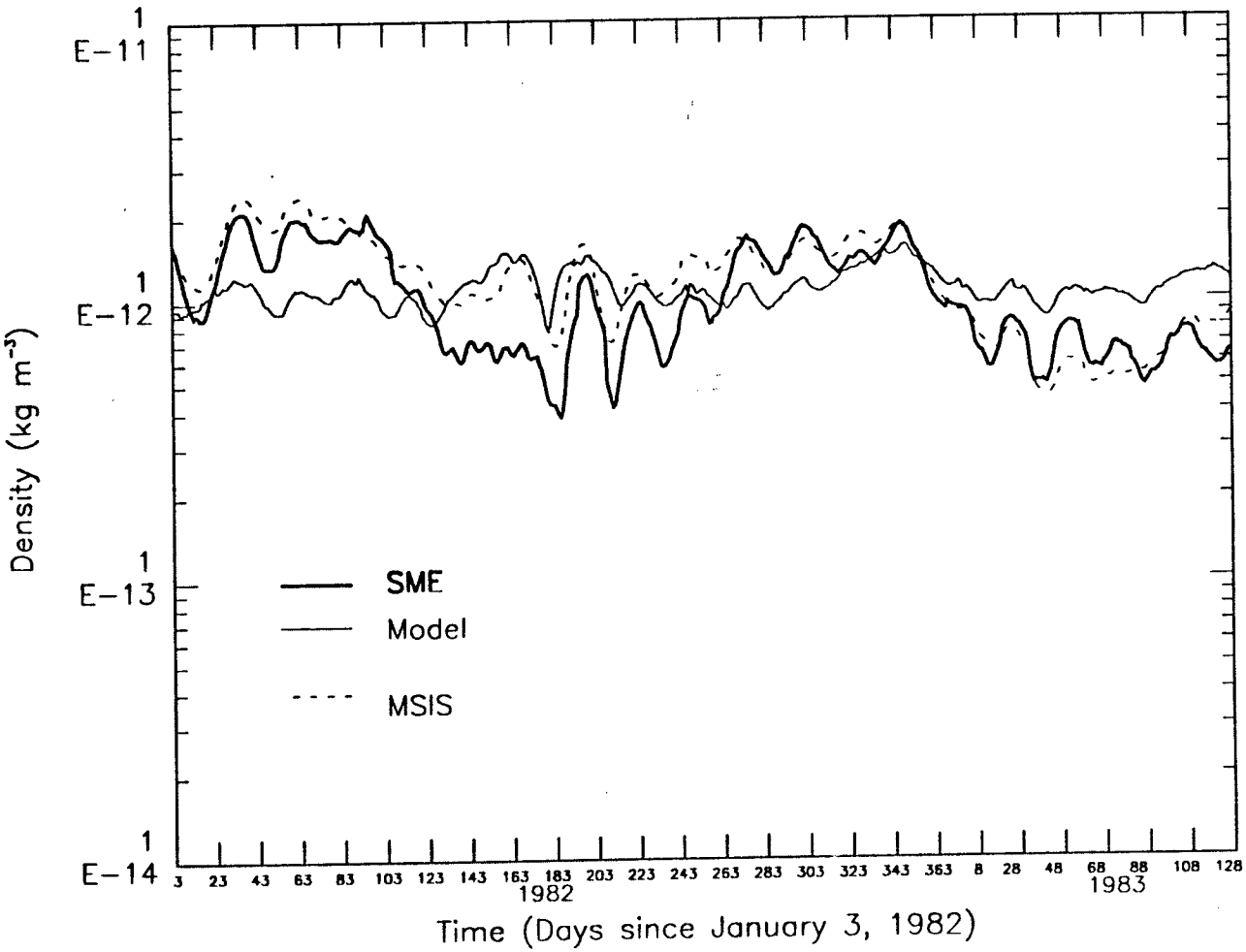

Figure 5.6 **Comparison of SME derived, model, and MSIS 83 mass densities.** This figure is on the same time scale as Figure 5.5 and is the same data as Figure 4.15a.

CHAPTER VI

SUMMARY

The final chapter covers a short review of the work in this dissertation, outlines the significant and new results of this work, and introduces a brief discussion of future work which may be conducted.

6.1 Review

The thesis describes seven datasets from four sources which provide the basis for correlations and lead to the results below. Of primary importance is the data from the AE-E, SME, and GOES satellites covering the solar EUV, Lyman-α, and 1-8 Å X-ray emissions, respectively.

Following an introductory discussion of the solar - terrestrial coupling in the thermosphere, which centers on the importance of and the mechanisms underlying the phenomena of EUV heating, an extensive number of correlations are shown. These are between solar EUV emissions and EUV flux indices of $F_{10.7}$, Lyman-α, and 1-8 Å X-rays. The dominant EUV emissions which heat the thermosphere are identified in this discussion and the indices which represent these emissions are detailed.

The primary contribution of this dissertation is in modeling the EUV flux using two solar indices of Lyman-α and 1-8 Å X-rays. Secondary features of the solar - terrestrial coupling are also reviewed, including auroral heating and its parameterization by the A_p geomagnetic index, satellite derived density from atmospheric drag observations, and the variation of the minor constituent

nitric oxide in the lower thermosphere. These discussions lay the basis for the thermospheric temperature and density modeling in Chapter IV.

The modeling of temperature and density is possible through the use of a one-dimensional, time-dependent model which numerically solves the conservation of energy equation and integrates the barometric equation. Energy is conserved in the system between 120 and 450 km, which is the main region of interest in this study. The model includes the major thermal and kinetic processes which occur in the thermosphere. The model is validated through a comparison to the MSIS 83 model outputs for solar maximum and minimum conditions. A time series of density values at the altitude of SME during solar cycle 21 decline is calculated with this model and is compared to similar time series of SME derived densities and MSIS 83 modeled densities. A secondary but important conclusion resulting from this modeling is that the 27-day variations in the magnitude of upper thermospheric density are predominantly due to chromospheric flux variations as opposed to coronal flux variations.

A further test of the modeled density from the two-indices method is conducted. The modeled density is used as an input for the atmospheric drag calculation in a long-term orbit propagator for the SME case. The resulting orbit decay over one and one-half years is compared to the actual decay from definitive ephemeris data. Within this orbit decay context, a detailed discussion is included on satellite drag coefficients. A secondary contribution is made with the postulation of a solar cycle variation in C_d.

6.2 Conclusions

This dissertation makes both primary and secondary significant and new contributions to the fields of atmospheric and astronautical sciences. These contributions, mentioned above, are supplemented by other new work

embodied in this thesis. The four areas in which contributions are made include observational data processing and analysis, EUV emission modeling, thermospheric temperature and density modeling, and satellite orbit lifetime modeling. They are described next.

6.2.1 Observational Data Processing and Analysis

Supplemental new work and conclusions which have aided the development of this thesis have been conducted with the processing and analysis of GOES, AE-E, and SME observational datasets.

The processing and analysis of the GOES 1-8 Å X-ray emissions during the period of January 1980 through May 1983 was carried out in support of this thesis work. The processing is described in Chapter II and the results made available in Figures 2.16, 2.17, 2.18, and 2.19. Appendix B lists the quantitative results of the daily mean and background flux values for that time period for the 1-8 Å flux as well as the 0.5-4 Å flux, the latter which was not used in this work but may be of interest to some readers. Analysis of this data indicates that the monthly means of the 1-8 Å background flux, which do not include flare activity, decline by a factor of 7 from high to low activity when a quadratic line fit to the data is made. The high and low monthly mean background values are separated by nearly a factor of 40 and the daily mean background high and low values have a ratio of at least 200:1 which compares with the order of magnitude variation of 492:1 in the Bouwer X-ray data.

In order to analyze and compare the data in the AE-E EUV dataset, the EUV emissions were retabulated in each of the 37 wavelength groups discussed by Torr *et al.* [1979] and revised by Torr and Torr [1985]. Small numerical corrections were made to the Torr and Torr values for the wavelengths at 787.71 and 790.15 Å (O IV) and the wavelength intervals of 750-800 and 1000-

1050 Å. The corrections slightly affect the reference values of the total EUV emissions for solar minimum and maximum. These corrections to the Torr and Torr data are a result of recalculating the sum of the flux in these intervals without overlapping the line emissions at interval boundaries. In addition, the Fe XVI emission (335 Å) is included separately since Hinteregger *et al.* [1981] considered it a key reference emission in ***EUV class*** modeling.

The dominant photon fluxes are analyzed in the AE-E dataset for solar maximum and minimum conditions with the conclusions drawn that 1) coronally-produced, shorter wavelength EUV emissions, vary more than chromospherically-produced, longer wavelength emissions, 2) the maximum high to low ratios for coronal flux ranges from 4 to 80 while the chromospheric flux ranges by no more than 2.5. These variations have important applications to the energetics of the atmosphere described below.

The SME orbit period rate change dataset results from an extension of the work of Tobiska [1985]. The newly processed data shows results which indicate that there is nearly an order of magnitude difference between high and low solar activity for the rate at which SME's average daily orbit period changes. Figure 2.11 confirms that the rate at which the orbit decays does decrease substantially from high to low solar activity, or conversely, the orbit decays faster at high solar activity than at low activity.

6.2.2 EUV Emission Modeling

The primary significant and new contribution to the atmospheric and astronautical sciences by this dissertation is the two-indices model of EUV flux based on Lyman-α, which models chromospheric emissions, and 1-8 Å X-rays, which model coronal emissions. Contributing and supporting new work is also found in the analysis of EUV thermospheric heating, the analysis of the $F_{10.7}$

solar index, the analysis of chromospheric fluxes and their effect upon lower thermospheric energy deposition, and the analysis of SME derived densities.

It is concluded in Chapter III that EUV emissions can be modeled by chromospheric and coronal fluxes, either separately or in combination. This is mainly based on high correlations found in the AE-E dataset when comparing Lyman-α, as a chromospheric emission, and the natural logarithm of the 1-8 Å X-rays, as coronal emissions, to the AE-E EUV chromospheric and coronal fluxes, respectively, during the rising cycle 21 time frame. These correlations are outlined in Tables 3.7 and 3.9. $F_{10.7}$ is found to correlate highly with transition region and cool corona emissions and is outlined in Table 3.8. The high correlations are valid for timescales over several solar rotations while short-term correlations are much weaker. It is noted that 1) Lyman-α and 1-8 Å X-rays bracket the EUV spectral range and themselves participate in mesospheric and lower thermospheric heating and 2) both emissions are created in the same general regions of the solar atmosphere as the dominant EUV fluxes which they model. Three assumptions are made which allow the correlations for Lyman-α to chromospheric EUV emissions and the natural logarithm of the 1-8 Å X-rays to coronal EUV emissions to be applied to modeling efforts outside of the time period of the correlated datasets. They are 1) an assumed general agreement between the calibrations of AE-E and SME spectrometers measuring Lyman-α, 2) an expected similarity in the rising slope of cycle 22 compared to cycle 21, and 3) an expected cycle 22 maximum variation similarity with cycle 21, even though the magnitudes may vary. These assumptions extend the correlations to 1) declining cycle 21 activity, 2) cycle 21 minimum, 3) cycle 22 rising activity, and 4) cycle 22 maximum. Table 3.14 summarizes the EUV flux model for the dominant chromospheric and coronal fluxes. The empirical relationship between chromospheric or coronal EUV fluxes and the

1-8 Å X-rays is non-linear, suggesting that the energy flux has an exponential temperature dependence.

Supporting analysis for the above EUV modeling conclusions comes from a review of the EUV heating processes using the AE-E solar minimum and maximum EUV data. Nine EUV emission lines or wavelength intervals are found to contribute nearly 50% of all available EUV energy flux for solar minimum and maximum conditions. This analysis supports similar recent results obtained by Roble [1987]. Among the nine dominant emissions are three primary ones including two chromospheric and one cool coronal, i.e., the He II (304 Å) line, the H Lyman continuum (850-900 Å), and the 150-200 Å interval. These energy emissions contribute the largest heating rates per unit mass to the thermospheric constituents of O, O_2, and N_2 for solar minimum and maximum conditions. They also deposit their maximum energy near 210 km for most solar activity. Tables 3.3 and 3.4 along with Figure 3.3 describe the details of these EUV heating rates.

Analysis of the $F_{10.7}$ solar EUV index indicates that it does not represent chromospheric solar emissions well during solar minimum conditions. $F_{10.7}$ reaches a threshold value below which it does not vary when compared to a purely chromospheric emission like Lyman-α which does show complex, decreasing solar minimum variation. This conclusion supports and extends the earlier observation of Vidal-Madjar and Phissamay [1980] who show a low correlation between $F_{10.7}$ and Lyman-α during the minimum of cycle 20.

The analysis of the 1-8 Å X-rays and their modeling of soft X-rays support the hypothesis of Barth *et al.* [1988] that solar variability in the 30 to 100 Å spectral range controls the production of equatorial lower thermospheric nitric oxide. Emissions in this range are predominantly produced in solar coronal regions and show a relatively high variation from solar minimum to

maximum. The magnitude of solar energy deposition at these altitudes is expected to vary as the natural logarithm of the 1-8 Å X-rays, i.e., following the pattern of the other coronal emissions in the EUV. Barth *et al.* claim that substantial variations in solar flux are needed to produce modeled NO in this region of the thermosphere which compares to the observed changes in NO from high to low solar activity. The modeled substantial changes in coronal soft X-ray emissions support the theoretically-needed substantial energy flux.

Analysis of the SME derived density, obtained from the rate change of the orbit period dataset and updated from Tobiska [1985], shows a decline in mass density at SME altitudes by a factor of 10 from high to low solar activity. SME also dropped approximately 30 km in its mean altitude during that same time period. Figure 3.29 shows these updated derived density results.

6.2.3 Thermospheric Modeling

An important secondary and new contribution from this work to both the atmospheric and astronautical sciences is that chromospheric fluxes significantly affect upper thermospheric densities more than coronal fluxes during periods of high solar activity. This follows from a comparison of the modeled densities with the satellite derived densities. Auroral heating and NO cooling are verified as important to the thermospheric thermal budget by analysis.

Analysis of the modeled densities resulting from the two-indices EUV modeled energy flux input into the one-dimensional thermospheric model was conducted by comparing the modeled density with the satellite derived density. Results indicate that, in the upper thermosphere, the chromospheric flux contributes the 27-day variation in the solar rotational density features rather than the coronal emissions. This conclusion is apparent when the Lyman-α, the 1-8 Å X-rays, and the $F_{10.7}$ indices are compared with the final density

results from both models and the derived densities from satellite data. An additional observation is that the modeled coronal and chromospheric emissions have wide differences in their time variations. Both solar energy components together sustain the overall magnitude of the density while auroral heating contributes finer time-varying detail which is not well correlated with the variations in the derived densities in this study. The modeled density has good phase agreement and moderate relative magnitude of variation agreement in the solar rotational features with the satellite derived density and the MSIS 83 density. These combined results generally validate the two-indices EUV model concept with the qualification that the EUV heating due to coronal emissions may be overstated by the 1-8 Å X-ray index.

Sensitivity to 1) auroral heating, and especially Joule heating, in the one-dimensional thermospheric model and 2) NO cooling from the 5.3 μm emission are verified.

6.2.4 Orbit Lifetime Modeling

The two-indices EUV flux model is further validated in a test of its use for orbit decay prediction compared to the actual orbit decay. A significant and new secondary contribution to the astronautical sciences is the hypothesis that the drag coefficient varies with solar cycle activity.

The method of modeling EUV flux with Lyman-α and 1-8 Å X-rays in order to parameterize chromospheric and coronal emissions for thermospheric density modeling is validated in this work by the successful use of the modeled density in a long-term orbit predictor. The modeled mean altitude change over one and one-half years during high solar activity compares favorably with the actual mean altitude change.

The use of a C_d value substantially less than is traditionally used fol-

lows from a detailed review of theoretical work on drag coefficients, a knowledge of the SME actual area, mass, and angle of attack, and a reasonable understanding of the gas temperatures through which the satellite was flying during the above time period. The theoretical C_d for SME of 0.7 was confirmed through its used in the long-term orbit predictor. Further analysis showed that C_d may vary by up to 100% as a result of changing angle of attack while the change in atmospheric gas thermal velocities from high to low solar activity will theoretically cause a change in C_d by 1%. This work extends previous theoretical work by Epstein [1924] and analytical and experimental work by Stalder and Zurick [1951]. It also clarifies and redirects the use of C_d as discussed by Cook [1965].

6.3 Future Work

There are four areas in which this work may be extended or improved in the foreseeable future. They include solar flux investigations, one-dimensional model improvement, aeronomical studies, and orbit lifetime applications.

Investigations into the variations and relations between different solar emissions can be further extended from the results in this thesis. Three important questions arose in the course of this study. First, what correlations exist between 1-8 Å X-rays and $F_{10.7}$ during solar minimum conditions? This could be resolved relatively soon with the processing of new GOES data. The answer to this question introduces a second one: what is the reason for $F_{10.7}$ reaching a threshold level during solar minimum conditions? Is is a result of coronal or transition region "quiet sun" thresholds? Do chromospheric emissions such as Lyman-α have similar threshold levels? A third question arises with respect to the Lyman-α measurements by AE-E and SME. There is a nine month gap between the datasets. What error exists in their comparative calibrations?

How can the datasets be merged into a single time series of Lyman-α over cycle 21? In addition, a useful question was raised to the author during the course of this study: do we want to develop a three-indices model, using $F_{10.7}$ to model transition region fluxes for example, or a two-indices Lyman-α and $F_{10.7}$ model, or do we want to simplify the EUV flux representation even more, given the lack of measurements?

The one-dimensional model needs improvement in the altitude range of 100 to 120 km. Not only does the lower boundary condition in the numerical solution of the energy equation need to be changed, and an upgrade to the eddy and turbulent conduction terms made, but more importantly, the accurate inclusion of auroral heating processes needs to be developed. An index different from A_p may be appropriate for this.

Two aeronomical applications of this work come to mind immediately. First, the time series modeling of nitric oxide, using the parameterized soft X-ray flux between 30 and 100 Å, would give a further verification of the Barth *et al.* hypothesis of NO equatorial control by this spectral range. These modeled results should then be compared to the SME NO dataset. Second, the inclusion of the modeled EUV flux during the decline of cycle 21 into the NCAR TGCM for a comparison to events such as the July 1982 solar activity would be useful to extend the application of this method.

Finally, the application of this method to the problem of orbit lifetime predictions is an unsolved question. This thesis steers clear of the problem of solar activity prediction, which was mentioned in Chapter I, and instead seeks to model solar activity in hindsight given the absence of measured EUV emissions. However, if a reasonable method of predicting near-term solar Lyman-α and 1-8 Å X-rays can be accomplished, say from 24-72 hours to 30 days ahead, then this method stands a better chance of predicting short-

term orbit perturbations than the present methods. The development of this capability would be tremendously enhanced from the use of a more sophisticated three-dimensional thermospheric model which includes winds. This is a project which would take considerable time and effort but would allow errors in short-term predicted atmospheric density to contract toward the 5 or 10% level.

BIBLIOGRAPHY

Alissandrakis, C.E., M.R. Kundu, and P. Lantos, A model for sunspot associated emission at 6 cm wavelength, *Astron. Astrophys.*, **82**, 30, 1980.

Banks, P.M. and G. Kockarts, *Aeronomy*, Academic Press, New York, 1973.

Bates, D.R., Some problems concerning the terrestrial atmosphere above about the 100 km level, *Proc. Roy. Soc. London,* **A**, **253**, 451, 1959.

Bartels, J., An attempt to standardize the daily international magnetic character figure, *IATME Bulletin*, **12e**, 109, 1951.

Barth, C.A., W.K. Tobiska, D.E. Siskind, and D.D. Cleary, Solar-terrestrial coupling: low-latitude thermospheric nitric oxide, *Geophys. Res. Lett.*, **15**, 92, 1988.

Bossy, L., Solar indices and solar U.V.-irradiances, *Planet. Space Sci.*, **31**, 977, 1983.

Bossy, L. and M. Nicolet, On the variability of Lyman-alpha with solar activity, *Planet. Space Sci.*, **29**, 907, 1981.

Bouwer, S.D, Intermediate-term epochs in solar soft X ray emission, *J. Geophys. Res.*, **88**, 7823, 1983.

Brasseur, G. and S. Solomon, *Aeronomy of the Middle Atmosphere*, D. Reidel Publ. Co., Dordrecht, Holland, 1984.

Brown, G.M., New methods for predicting the magnitude of sunspot maximum, in *Solar Terrestrial Prediction Proc.*, NOAA ERL, **II**, p. 264, 1979.

Chapman, R.D. and W.M. Neupert, Slowly varying component of extreme ultraviolet solar radiation and its relation to solar radio radiation, *J. Geophys. Res.*, **79**, 4138, 1974.

Cleary, D.D., Analysis of nitric oxide flourescence bands from high latitude rocket observations of the thermospheric dayglow, Ph.D. Thesis, University of Colorado, Boulder, 1985.

Cook, G.E., Satellite drag coefficients, *Planet. Space Sci.*, **13**, 929, 1965.

COSPAR International Reference Atmosphere 1965 (CIRA 65), compiled by the CO-SPAR Working Group IV, North-Holland Publishing Co., Amsterdam, 1965.

COSPAR International Reference Atmosphere 1972 (CIRA 72), compiled by the CO-SPAR Working Group IV, North-Holland Publishing Co., Amsterdam, 1972.

Covington, A.E., Solar noise observations on 10.7 centimeters, *Proc. of the I.R.E.*, **36**, 454, 1948.

Cravens, T.E., J.C. Gerard, M. LeCompte, A.I. Stewart, and D.W. Rusch, The global distribution of nitric oxide in the thermosphere as determined by the Atmosphere Explorer D satellite, *J. Geophys. Res.*, **90**, 9862, 1985.

Donnelly, R.F., Temporal trends of solar EUV and UV full-disk fluxes, *Solar Phys.*, **109**, 37, 1987a.

Donnelly, R.F., Solar X-ray, EUV and UV flux, paper presented at Workshop of Atmospheric Density, AFGL, Hanscom AFB, Mass., Oct. 20-22, 1987b.

Donnelly, R.F., H.E. Hinteregger, and D.F. Heath, Temporal variations of solar EUV, UV, and 10,830-Å radiations, *J. Geophys. Res.*, **91**, 5567, 1986a.

Donnelly, R.F., L.C. Puga, and W.S. Busby, Temporal characteristics of solar EUV, UV and 10830-A full-disk fluxes, *NOAA Technical Memorandum ERL ARL-146,* NOAA ERL, Boulder, 1986b.

Epstein, P.S., On the resistance experienced by spheres in their motion through gases, *Phys. Rev.*, **23**, 710, 1924.

Euler, H. and R. Holland, Solar activity statistical estimation technique, in *Proc. of a Workshop on Satellite Drag,* NOAA ERL, p. 151, Boulder, Mar. 18-19, 1982.

Felli, M., K.R. Lang, and R.F. Willson, VLA observations of solar active regions. I. The Slowly Varying Component, *Astrophys. J.*, **247**, 325, 1981.

Fukui, K., Unique increase of solar Lyman alpha flux observed by AE-E satellite during cycle 21, *Eos Trans. AGU,* **69**, 417, 1988.

Golshan, N. and C.F. Sechrist, Jr., Seasonal and solar cycle variation of E-region nitric oxide, *Radio Sci.*, **10**, 305, 1975.

Gordiets, B.F., Y.N. Kulikov, M.N. Markov, and M.Y. Marov, Numerical modelling of the thermospheric heat budget, *J. Geophys. Res.*, **87**, 4504, 1982.

Hall, L.A., and H.E. Hinteregger, Solar radiation in the extreme ultraviolet and its variation with solar rotation, *J. Geophys. Res.*, **75**, 6959, 1970.

Harris, I. and W. Priester, Theoretical models for the solar-cycle variation of the upper atmosphere, *J. Geophys. Res.*, **67**, 4585, 1962.

Hedin, A.E., A revised thermospheric model based on mass spectrometer and incoherent scatter data: MSIS-83, *J. Geophys. Res.*, **88**, 10170, 1983.

Hedin, A.E., Empirical modeling of the thermosphere, in *Workshop on Upper and Middle Atmospheric Density Modeling Requirements for Spacecraft Design and Operations,* NASA Conference Publication 2460, p. 111, Huntsville, Ala., Nov. 19-21, 1985.

Hedin, A.E., MSIS-86 thermospheric model, *J. Geophys. Res.*, **92**, 4649, 1987.

Hedin, A.E., J.E. Salah, J.V. Evans, C.A. Reber, G.P. Newton, N.W. Spencer, D.C. Kayser, D. Alcaydé. P. Bauer, L. Cogger, and J.P. McClure, A global thermospheric model based on mass spectrometer and incoherent scatter data MSIS 1. N_2 density and temperature, *J. Geophys. Res.*, **82**, 2139, 1977.

Herrero, F.A., Satellite drag coefficients and upper atmosphere densities: present status and future directions, paper AAS 87-551 presented at AAS/AIAA Astrodynamics Specialist Conference, Kalispell, Mont., Aug. 10-13, 1987.

Hinteregger, H.E., Preliminary data on solar extreme ultraviolet radiation in the upper atmosphere, *J. Geophys. Res.*, **66**, 2367, 1961.

Hinteregger, H.E., Effects of solar XUV radiation on the Earth's atmosphere, in *Annals of the IQSY*, edited by A.C. Strickland, **5**, p. 305, MIT Press, Cambridge, Mass., 1969.

Hinteregger, H.E., L.A. Hall, G. Schmidtke, Solar XUV radiation and neutral particle distribution in July 1963 thermosphere, *Space Res. V*, 1175, 1965.

Hinteregger, H.E., D.E. Bedo, and J.E. Manson, The EUV spectrophotometer on Atmosphere Explorer, *Radio Sci.*, **8**, 349, 1973.

Hinteregger, H.E., K. Fukui, and B.R. Gilson, Observational, reference and model data on solar EUV, from measurements on AE-E, *Geophys.*

Res. Lett., **8**, 1147, 1981.

Hoerner, S.F., *Fluid-Dynamic Drag*, sec. 18-17, published by the author, 1958.

Jacchia, L.G., Two atmospheric effects in the orbital acceleration of artificial satellites, *Nature*, **183**, 526, 1959.

Jacchia, L.G., Static diffusion models of the upper atmosphere with empirical temperature profiles, *Smith. Contr. Astrophys.*, **8**, 215, 1965.

Jacchia, L.G., Revised static models of the thermosphere and exosphere with empirical temperature profiles, *Spec. Rep. 332*, Smithson. Astrophys. Observ., Cambridge, Mass., 1971.

Kasting, J.F. and R.G. Roble, A zonally averaged chemical-dynamical model of the lower thermosphere, *J. Geophys. Res.*, **86**, 9641, 1981.

Kaula, W.M., *Theory of Satellite Geodesy*, Blaisdell Publishing Co., Waltham, Mass., 1966.

King-Hele, D., *Theory of Satellite Orbits in an Atmosphere*, Butterworths, London, 1964.

Kockarts, G., Nitric oxide cooling in the terrestrial thermosphere, *Geophys. Res. Lett.*, **7**, 137, 1980.

Kumer, J.B. and T.C. James, $CO_2(001)$ and N_2 vibrational temperatures in the $50 \leq z \leq 130$ km altitude range, *J. Geophys. Res.*, **79**, 638, 1974.

Kwok, J.H., The long-term orbit predictor (LOP), *EM 312/86-151*, Jet Propulsion Laboratory, Pasadena, Ca., 1986.

Lindzen, R.S. and S.S. Hong, Effects of mean winds and horizontal temperature gradients on solar and lunar semidiurnal tides in the atmosphere, *J. Atm. Sci.*, **31**, 1421, 1974.

Liu, J.J.F., Advances in orbit theory for an artificial satellite with drag, *J. Astronaut. Sci.*, **31**, 165, 1983.

Mayaud, P.N., *Derivation, Meaning, and Use of Geomagnetic Indices*, American Geophysical Union, Washington, 1980.

Millikan, R.A., The general law of fall of a small spherical body through a gas, and it's bearing upon the nature of molecular reflection from surfaces, *Phys. Rev.*, **22**, 1, 1923.

Neupert, W.M., W.E. Behring, and J.C. Lindsay, The solar spectrum from 50 Å to 400 Å, *Space Res. IV*, 719, 1964.

Ohl, A.I. and G.I. Ohl, A new method of very long-term prediction of solar activity, in *Solar Terrestrial Prediction Proc.*, NOAA ERL, II, 258, 1979.

Oster, L., Solar irradiance variations, 2: analysis of modeling techniques and intercomparison of ground-based data, *J. Geophys. Res.*, **88**, 9037, 1983.

Roble, R.G., Solar cycle variation of the global mean structure of the thermosphere, in *Solar Radiative Output Variation*, p. 1, NCAR, Boulder, Proceedings of a Workshop Nov. 9-11 1987.

Roble, R.G. and B.A. Emery, On the global mean temperature of the thermosphere, *Planet. Space Sci.*, **31**, 597, 1983.

Roble, R.G. and J.F. Kasting, The zonally averaged circulation, temperature, and compositional structure of the lower thermosphere and variations with geomagnetic activity, *J. Geophys. Res.*, **89**, 1711, 1984.

Roble, R.G., E.C. Ridley, and R.E. Dickinson, On the global mean structure of the thermosphere, *J. Geophys. Res.*, **92**, 8745, 1987.

Rottman, G.J., 27-day variations observed in solar U.V. (120-300 nm) irradiance, *Planet. Space Sci.*, **31**, 1001, 1983.

Rottman, G.J., Results from space measurements of solar UV and EUV flux, in *Solar Radiative Output Variation*, p. 71, NCAR, Boulder, Proceedings of a Workshop Nov. 9-11 1987.

Rottman, G.J., C.A. Barth, R.J. Thomas, G.H. Mount, G.M. Lawrence, D.W. Rusch, R.W. Sanders, G.E. Thomas, and J. London, Solar spectral irradiance, 120 to 190 nm, *Geophys. Res. Lett.*, **9**, 587, 1982.

Rusch, D.W., G.H. Mount, C.A. Barth, R.J. Thomas, and M.T. Callan, Solar Mesosphere Explorer ultraviolet spectrometer: measurements of ozone in the 1.0-0.1 mbar region, *J. Geophys. Res.*, **89**, 11677, 1984.

Sänger, E., The gas kinetics of very high flight speeds, *ZWB Forschungsbericht*, **972**, 1938, Engl. Trans. *NACA Tech. Mem. 1270*, 1950.

Sargent, H.H., A prediction of the next sunspot maximum, *Eos Trans. AGU*, **58**, 1220, 1977.

Sargent, H.H., An early forecast for sunspot cycle 22, paper presented at HAO Colloquium Series, NCAR HAO, Boulder, 1984.

Schaaf, S.A. and P.L. Chambré, Flow of rarefied gases, *Fundamentals of Gas Dynamics*, edited by H.W. Emmons, **III**, p. 687, Princeton University Press, Princeton, N.J., 1958.

Schatten, K.H., P.H. Scherrer, L. Svalgaard, and J.M. Wilcox, Using dynamo theory to predict the sunspot number during solar cycle 21, *Geophys. Res. Lett.*, **5**, 411, 1978.

Schatten, K. and A. Hedin, A dynamo theory prediction for solar cycle 22: sunspot number, radio flux, exospheric temperature, and total density at 400 km, *Geophys. Res. Lett.*, **11**, 873, 1984.

Schatten, K.H. and S. Sofia, Forecast of an exceptionally large even-numbered solar cycle, *Geophys. Res. Lett.*, **14**, 632, 1987.

Schmidtke, G., Todays knowledge of the solar EUV output and the future needs for more accurate measurements for aeronomy, *Planet. Space Sci.*, **26**, 347, 1978.

Schmidtke, G., Modelling of the solar extreme ultraviolet irradiance for aeronomic applications, *Handbuch der Physik (Encyclopedia of Physics)*, edited by S. Flügge, Vol. XLIX/7: Geophysics III, Part VII, p. 1, Springer-Verlag, Berlin, 1984.

Shimazaki, T., Effective eddy diffusion coefficient and atmospheric composition in the lower thermosphere, *Journ. Atmos. Terr. Phys.*, **33**, 1383, 1971.

Siskind, D.E., The response of thermospheric nitric oxide to an auroral storm, Ph.D. Thesis, University of Colorado, Boulder, 1988.

Smith, R.E., NASA/MSFC Prediction Techniques, *Workshop on Upper and Middle Atmospheric Density Modeling Requirements for Spacecraft Design and Operations*, NASA Conference Publication 2460, p. 151, Huntsville, Ala., Nov. 19-21, 1985.

Solar-Geophysical Data (Comprehensive Reports), National Geophysical Data Center, U.S. Department of Commerce, Boulder, CO., 1985-1986.

Stalder, J.R. and D. Jukoff, Heat transfer to bodies traveling at high speed in the upper atmosphere, *NACA Tech. Rep. 944*, 1948.

Stalder, J.R., G. Goodwin, and M.O. Creager, A comparison of theory and experiment for high-speed free-molecule flow, *NACA Tech. Note 2244*, 1950.

Stalder, J.R. and V.J. Zurick, Theoretical aerodynamic characteristics of bodies in a free-molecule-flow field, *NACA Tech. Note 2423*, 1951.

Sterne, T.E., *An Introduction to Celestial Mechanics*, Interscience Publications, Inc., New York, 1960.

Stolarski, R.S., P.B. Hays, and R.G. Roble, Atmospheric heating by solar EUV radiation, *J. Geophys. Res.*, **80**, 2266, 1975.

Taff, L.G., *Celestial Mechanics,* John Wiley and Sons, New York, 1985.

Thomas, G.E., C.A. Barth, E.R. Hansen, C.W. Hord, G.M. Lawrence, G.H. Mount, G.J. Rottman, D.W. Rusch, A.I. Stewart, R.J. Thomas, J. London, P.L. Bailey, P.J. Crutzen, R.E. Dickinson, J.C. Gille, S.C. Liu, J.F. Noxon, and C.B. Farmer, Scientific objectives of the Solar Mesosphere Explorer mission, *Pageoph*, **118**, 591, 1980.

Timothy, A.F. and J.G. Timothy, Long-term intensity variations in the solar Helium II Lyman alpha line, *J. Geophys. Res.*, **75**, 6950, 1970.

Tobiska, W.K., Predictive model of the orbit decay of the Solar Mesosphere Explorer, M.S. Thesis, University of Colorado, Boulder, 1985.

Tobiska, W.K., R.D. Culp, and C.A. Barth, Predicted solar cycle 22 10.7 cm flux and satellite orbit decay, *J. Astronaut. Sci.*, **35**, 419, 1987.

Torr, M.R., D.G. Torr, R.A. Ong, and H.E. Hinteregger, Ionization frequencies for major thermospheric constituents as a function of solar cycle 21, *Geophys. Res. Lett.*, **6**, 771, 1979.

Torr, M.R. and D.G. Torr, Ionization frequencies for solar cycle 21: revised, *J. Geophys. Res.*, **90**, 6675, 1985.

Tsien, H., Superaerodynamics, mechanics of rarefied gases, *J. Aeronaut. Sci.*, **13**, 653, 1946.

Vidal-Madjar, A., Evolution of the solar Lyman alpha flux during four consecutive years, *Solar Phys.*, **40**, 69, 1975.

Vidal-Madjar, A., The solar spectrum at Lyman-alpha 1216 Å, in *The Solar Output and Its Variation*, edited by O.R. White, p. 213, Colorado Associated University Press, Boulder, 1977.

Vidal-Madjar, A. and B. Phissamay, The solar L α flux near solar minimum, *Solar Phys.*, **66**, 259, 1980.

von Rosenberg, D.U., *Methods for the Numerical Solution of Partial Differential Equations*, American Elsevier Publishing Co., New York, 1969.

White, O.R., A generalized filter for numerical smoothing of measurements, *HAO Research Memorandum No. 182,* NCAR, Boulder, 1972.

Woodgate, B.E., D.E. Knight, R. Uribe, P. Sheather, P. Bowles, and R. Nettleship, Extreme ultraviolet line intensities from the sun, *Proc. Roy. Soc. London,* **A**, 291, 1973.

Zahm, A.F., Superaerodynamics, *J. Frank. Inst.,* **217**, 153, 1934.

APPENDIX A

THERMOSPHERIC TEMPERATURE SOLUTION

A.1 Conservation of Energy

The conservation of energy in an atmosphere has been formulated by Banks and Kockarts [1973] as

$$\rho c_v \frac{\partial T}{\partial t} + \nabla \cdot \mathbf{E} = P - L \qquad (A-1)$$

where the heat flow is

$$\mathbf{E} = -\lambda \nabla T. \qquad (A-2)$$

ρ is the total mass density, c_v is the specific heat at constant volume, T is the temperature in Kelvin, t is time, P is total heat production, and L is total heat loss. λ is the total thermal conductivity and includes only the molecular conductivity in this analysis.

$\nabla \cdot \mathbf{E}$ is evaluated in the vertical temperature change case only ($\frac{\partial T}{\partial z} \neq 0$). Globally, horizontal changes are assumed to be zero ($\frac{\partial T}{\partial x} = \frac{\partial T}{\partial y} = 0$). Thus,

$$\nabla \cdot \mathbf{E} = -\lambda \frac{\partial^2 T}{\partial z^2} \qquad (A-3)$$

and (A-1) then becomes the time-dependent energy equation

$$\frac{\partial T}{\partial t} = \frac{\lambda}{\rho c_v} \frac{\partial^2 T}{\partial z^2} + \frac{1}{\rho c_v}(P - L). \qquad (A-4)$$

The conservation of energy equation (A-4) is written in a simplified form which neglects the mass average velocity. It is assumed that there is diffusive equilibrium and hence there are no diffusion velocities. In addition,

the sum of all internal forces of the gas particles on each other is taken to be zero. These assumptions are made possible in a planetary thermosphere where the photolysis, chemical reaction, and thermal conduction processes occur on a relatively small timescale compared to molecular diffusion. It should be noted that this assumption is not useful for understanding dynamics resulting from winds and waves.

Equation (A-4) is a parabolic second order partial differential equation and may be solved with the Crank-Nicolson finite difference method outlined by von Rosenberg [1969]. The equation is first rewritten in a simplified linear form

$$\frac{\partial u}{\partial t} = A\frac{\partial^2 u}{\partial z^2} + B\frac{\partial u}{\partial z} + Cu + E \qquad (A-5)$$

where $u = T$ and

$$A = \frac{\lambda}{\rho c_v} \qquad (A-5a)$$

$$B = 0 \qquad (A-5b)$$

$$C = 0 \qquad (A-5c)$$

$$E = \frac{1}{\rho c_v}(P_t - L_t). \qquad (A-5d)$$

From Chapter IV, the total heating and cooling terms are composed of

$$P_t = q_{euv} + q_j + q_p + P + q_e \qquad (A-6)$$

$$L_t = L. \qquad (A-7)$$

q_e is composed of the eddy and turbulent heat conduction terms and is written as

$$q_e = q_{ec} + q_{eh} \quad \text{ergs cm}^{-3}\ \text{sec}^{-1} \qquad (A-8)$$

The eddy conduction rate is calculated from

$$q_{ec} = \frac{\partial}{\partial z}\left[\rho c_p K_h\left(\frac{\partial T}{\partial z} + \frac{g}{c_p}\right)\right] \cdot \text{ ergs cm}^{-3}\ \text{sec}^{-1} \qquad (A-9)$$

where ρ is the mass density, c_p is the specific heat at constant pressure, K_h is the eddy diffusion coefficient, and g is the local gravity. Gordiets *et al.* [1982] describe the formulation of K_h from experimental data where the maximum value, K_m, does not exceed 2×10^6 cm^{-2} sec^{-1}. The formulation of K_h follows the method of Shimazaki [1971]. Turbulent heating is a combination of the energy dissipation due to viscous and bouyancy forces. The resulting heating rate may be written as

$$q_{eh} = q_d + q_g. \quad \text{ergs cm}^{-3} \text{ sec}^{-1} \qquad (A-10)$$

The viscous force effect, described by Gordiets *et al.*, is

$$q_d = K_h \frac{\rho g}{T}\left(\frac{\partial T}{\partial z} + \frac{g}{c_p}\right)\frac{1 - R_f}{R_f} \quad \text{ergs cm}^{-3} \text{ sec}^{-1} \qquad (A-11)$$

and the bouyancy force is

$$q_g = K_h \frac{\rho g}{T}\left(\frac{\partial T}{\partial z} + \frac{g}{c_p}\right). \quad \text{ergs cm}^{-3} \text{ sec}^{-1} \qquad (A-12)$$

The turbulent heating is described by Gordiets *et al.* using the dynamic Richardson number, R_f, where the value represents a "quasi-stationary" thermospheric condition as if the wind shear values are obtained from averaging over a large number of measurements. It is used in a simplified form for this statistically steady turbulent motion which is representative of an average turbulence.

$$R_f = \frac{K_h}{K_m}\frac{g}{T}\left(\frac{\partial T}{\partial z} + \frac{g}{c_p}\right)\Big/\left(\frac{\partial u}{\partial z}\right)^2. \qquad (A-13)$$

It is dependent upon the velocity gradient of the horizontal winds, u. These winds have been estimated in this study based on the work of Lindzen and Hong [1974].

In order to simplify the numerical calculations, the EUV heating, q_{euv}, the molecular thermal conduction, q_{mol}, the auroral heating, q_j and q_p, the

dissociative heating, P, the eddy and turbulent heating, q_e, and the radiative cooling, L, are not functions of temperature at the time step being evaluated. The temperature term for each is evaluated at the previous time interval.

The specific heat at constant volume is

$$c_v = \sum_j \frac{N_j k}{2m_j} \qquad (A-14)$$

where N_j is the degrees of freedom for the gas particle, k is Boltzmann's constant, and m_j is the particle mass.

A.2 Finite Difference Analogs

Von Rosenberg indicates that the finite difference analogs of $\frac{\partial u}{\partial t}$ and $\frac{\partial^2 u}{\partial z^2}$ may be written in a second order correct form

$$(\frac{\partial u}{\partial t})_{i,n+\frac{1}{2}} = \frac{u_{i,n+1} - u_{i,n}}{\Delta t} \qquad (A-15)$$

and

$$(\frac{\partial^2 u}{\partial z^2})_{i,n+\frac{1}{2}} = \frac{1}{2}\left[\frac{u_{i+1,n} - 2u_{i,n} + u_{i-1,n}}{(\Delta z)^2} + \frac{u_{i+1,n+1} - 2u_{i,n+1} + u_{i-1,n+1}}{(\Delta z)^2}\right]. \qquad (A-16)$$

These are obtained from truncated Taylor series expressions for $\frac{\partial u}{\partial t}$ and $\frac{\partial^2 u}{\partial z^2}$. The truncation starts at the $(\Delta t)^2$ and $(\Delta z)^2$ terms and the second order correct definition comes from describing this order of accuracy. The subscripted values of i and n in (A-15) and (A-16) are the space and time steps, respectively. It can be shown that if the dependent variable u is solved at the $x_i, t_{n+\frac{1}{2}}$ point, then the equations (A-15) and (A-16) are second order correct. Figure A-1 illustrates the center of the analogs for the Crank-Nicolson equation.

The finite difference form of (A-5) may now be written as

$$\frac{u_{i,n+1} - u_{i,n}}{\Delta t} = \frac{1}{2} A \Delta_z^2 (u_{i,n} + u_{i,n+1}) + E \qquad (A-17)$$

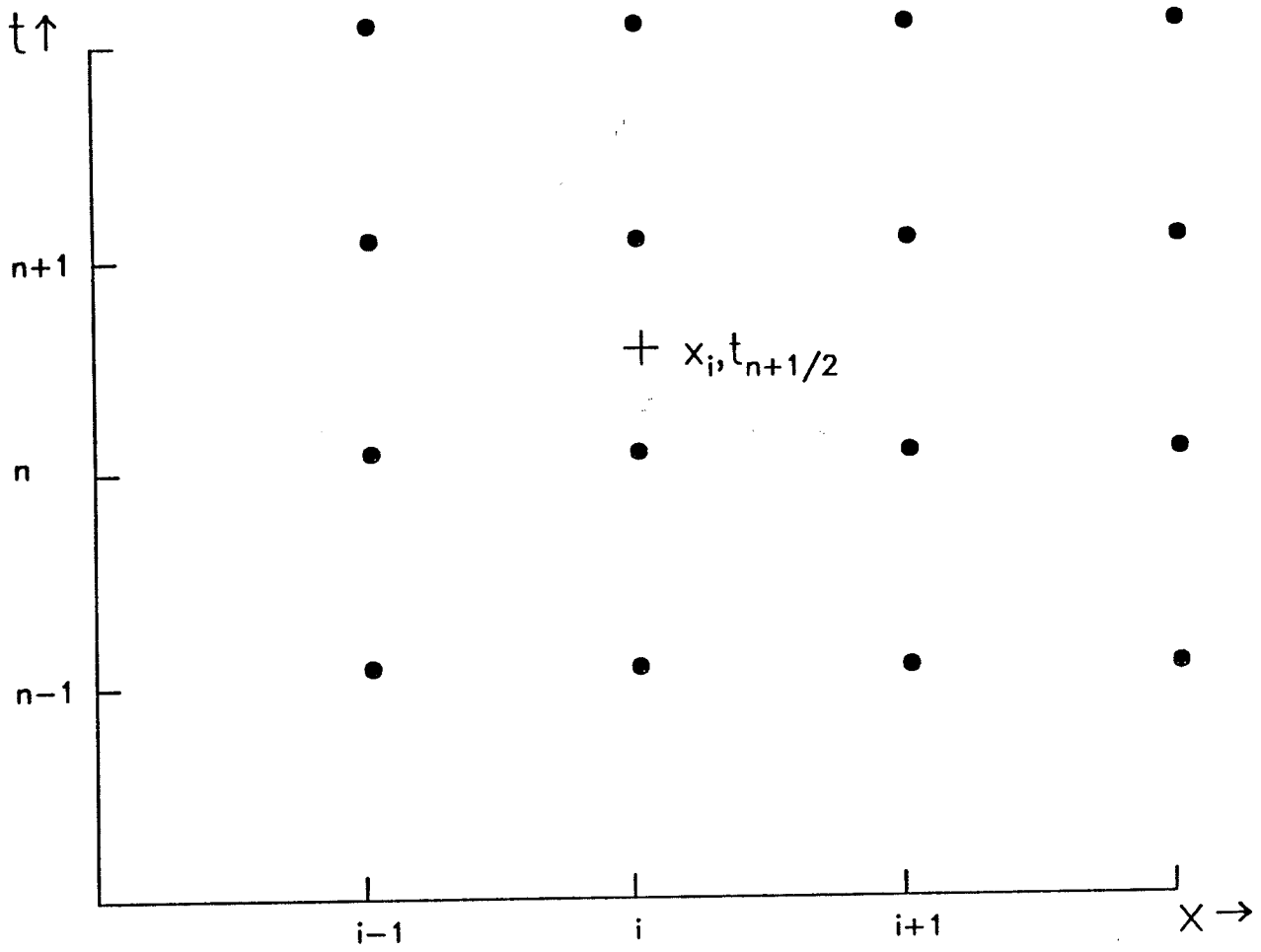

Figure A.1 **Center of analogs for finite difference solution.** x is the spatial dimension and n is the time dimension. The cross marks the point about which equation (A-17) is solved in the Crank-Nicolson algorithm.

where

$$\Delta_z^2(u_{i,n}+u_{i,n+1}) = \frac{u_{i+1,n}-2u_{i,n}+u_{i-1,n}}{(\Delta z)^2} + \frac{u_{i+1,n+1}-2u_{i,n+1}+u_{i-1,n+1}}{(\Delta z)^2}. \tag{A-18}$$

Equation (A-17) is rewritten as

$$a_i u_{i-1,n+1} + b_i u_{i,n+1} + c_i u_{i+1,n+1} = d_i. \tag{A-19}$$

where the $n+1$ time interval terms on the left hand side are grouped as a function of the nth time interval terms collected in d_i. The coefficients are

$$a_i = -\Delta t A \tag{A-19a}$$

$$b_i = 2(\Delta z)^2 + 2\Delta t A \tag{A-19b}$$

$$c_i = -\Delta t A \tag{A-19c}$$

$$d_i = \Delta t A u_{i-1,n} + [2(\Delta z)^2 - 2\Delta t A]u_{i,n} + \Delta t A u_{i+1,n} + 2(\Delta z)^2 \Delta t E. \tag{A-19d}$$

Equation (A-19) may be written as a matrix for more efficient computation

$$\begin{bmatrix} b_1 & c_1 & & & & & \\ a_2 & b_2 & c_2 & & & & \\ & a_3 & b_3 & c_3 & & & \\ & & \cdot & \cdot & \cdot & & \\ & & & a_i & b_i & c_i & \\ & & & & \cdot & \cdot & \cdot \\ & & & & & a_R & b_R \end{bmatrix} \begin{bmatrix} u_{1,n+1} \\ u_{2,n+1} \\ u_{3,n+1} \\ \cdot \\ u_{i,n+1} \\ \cdot \\ u_{R,n+1} \end{bmatrix} = \begin{bmatrix} d_1 \\ d_2 \\ d_3 \\ \cdot \\ d_i \\ \cdot \\ d_R \end{bmatrix} \tag{A-20}$$

A.3 Matrix Solution and Boundary Conditions

The Thomas algorithm is used to solve this tridiagonal matrix. Von Rosenberg notes that it is computationally efficient for digital computers. The equations solved are of the form (A-19) for $1 \le i \le R$ with $a_1 = c_R = 0$. Two temporary arrays are initially constructed, β_i and γ_i,

$$\beta_i = b_i - \frac{a_i c_{i-1}}{\beta_{i-1}} \qquad \text{with} \quad \beta_1 = b_1 \tag{A-21}$$

$$\gamma_i = \frac{d_i - a_i\gamma_{i-1}}{\beta_i} \qquad \text{with} \quad \gamma_1 = \frac{d_1}{b_1}. \tag{A-22}$$

Then, the dependent variable $u_{i,n+1}$ is iteratively solved at the ith space step for the $n+1$ time interval. Initially, $u_R = \gamma_R$ and is followed by

$$u_i = \gamma_i - \frac{c_i u_{i+1}}{\beta_i}. \tag{A-23}$$

This method is stable for round off error while $|b_i| \geq |a_i + c_i|$ for each equation.

The boundary conditions are solved from the equations in (A-20)

$$b_1 u_{1,n+1} + c_1 u_{2,n+1} = d_1 \tag{A-24}$$

$$a_R u_{R-1,n+1} + b_R u_{R,n+1} = d_R. \tag{A-25}$$

At the turbopause ($i = 1$), a steady state assumption is made. Thus,

$$\frac{\partial u}{\partial t} = \frac{u_{i,n+1} - u_{i,n}}{\Delta t} = 0 \tag{A-26}$$

and when (A-26) is compared to (A-24)

$$a_1 = 0 \tag{A-26a}$$

$$b_1 = 1 \tag{A-26b}$$

$$c_1 = 0 \tag{A-26c}$$

$$d_1 = u_0. \tag{A-26d}$$

At the exobase ($i = R$), the isothermal condition indicates that $\frac{\partial T}{\partial z} = 0$ by definition. Writing the first order correct derivative analog form to get the desired i and $i+1$ subscripts,

$$\frac{\partial u}{\partial z} = \frac{u_{i+1,n+1} - u_{i,n+1}}{\Delta z} = 0. \tag{A-27}$$

In comparison with (A-25),

$$a_R = -\frac{1}{\Delta z} \qquad (A-27a)$$

$$b_R = \frac{1}{\Delta z} \qquad (A-27b)$$

$$c_R = 0 \qquad (A-27c)$$

$$d_R = 0. \qquad (A-27d)$$

The initial conditions assume that a temperature profile exists where $u_{i,1} = u_{i,0}$ at the $n = 1$ time interval.

APPENDIX B

GOES 2 X-RAY DATA

The GOES 2 satellite X-ray data and its compilation is described in Chapter II, section 2.4. The following datasets are included as an appendix to this thesis and are the complete numerical values partially shown in Figures 2.16, 2.18, and 2.19. A short explanation of these tables is appropriate.

Each table is a set of X-ray values for one month in the time between January 1980 and May 1983. The dataset, which is available from NSSDC magnetic tapes, is time-tagged with the seconds into the year at 3-second intervals. Therefore, the time in seconds, at the end of the first day of each month of the compiled data, is also listed as a cross reference for any users who wish to compare this data to their own dataset.

Four general items are shown in each table. First, the day of the month is listed in column 1. Second, the daily averages of the short or long wavelength channels of the GOES instrument are listed in the second and third columns. The short channel in column 2 is the integrated flux between 0.5-4 Å in units of W m^{-2}. This daily average value is an arithmetic mean and is determined by summing the total flux during a day, including any flare contributions, and dividing by the number of data point values listed in column 4. The long channel value in column 3 is the integrated flux in the same units for the 1-8 Å range, divided by the number of data points in column 5. The background flux short and long channel values are in units of W m^{-2} and are listed in columns 6 and 7. They are the value of an 8-hour interval centered on 1200 UT and

determined from the lowest value of either 1) the 0800-1600 UT interval or 2) the interpolated value between 0000-0800 UT and 1600-2400 UT. This is described in section 2.4. The background values exclude solar flare activity.

On some dates there were gaps in the time series of the data and the total number of data values is considerably less than the total possible number of 28,800 values per day. In addition, on some dates there was no data available for the entire day. On those dates, all column values are zero. On a few days, the dataset contained an anomalous time which was not within one of the three 8-hour bin time intervals of 0000-0800, 0800-1600, and 1600-2400 UT and was discovered during the background averaging subroutine. In these cases, a "1" is printed in the Number of Values columns and the background data value is set to zero. The daily average value in columns 1 and 2 in these cases is the first data value read into the averaging array but occurs at the anomalous time. It should not be considered an average value but an available value.

On the next pages are the tables of data for January 1980 through May 1983.

Table B.1 January 1980 X-ray daily mean and background values
Time of end of first day (sec of yr) = 86400.
All daily average and background flux in units of W m^{-2}.

	— Daily Average —		Number of Values		— Background —	
Day	Short (0.5-4Å)	Long (1-8Å)	Short (0.5-4Å)	Long (1-8Å)	Short (0.5-4Å)	Long (1-8Å)
1	5.849E-08	1.816E-06	27904	27988	1.298E-08	1.273E-06
2	1.905E-08	1.529E-06	27145	27940	1.784E-08	1.472E-06
3	2.197E-08	1.642E-06	27954	28086	1.361E-08	1.436E-06
4	2.380E-08	1.726E-06	22997	23224	2.191E-08	1.701E-06
5	2.570E-08	1.691E-06	27905	28195	1.850E-08	1.615E-06
6	2.761E-07	3.480E-06	16426	16935	1.697E-07	2.984E-06
7	1.736E-07	3.348E-06	25976	26513	7.903E-08	2.573E-06
8	3.946E-07	4.205E-06	21045	21167	8.770E-08	2.341E-06
9	1.647E-07	2.763E-06	16295	19744	1.049E-08	1.806E-06
10	5.244E-07	5.609E-06	15903	17157	2.962E-08	2.522E-06
11	1.037E-07	3.474E-06	18925	20690	9.165E-08	3.371E-06
12	2.243E-07	4.853E-06	17944	18317	1.973E-07	4.399E-06
13	3.563E-07	5.314E-06	17525	18494	1.729E-07	4.394E-06
14	2.834E-07	4.128E-06	15338	17610	7.962E-08	2.477E-06
15	3.349E-08	1.986E-06	16783	17973	3.012E-08	1.802E-06
16	3.892E-08	1.586E-06	18270	18325	3.795E-08	1.586E-06
17	1.454E-08	1.122E-06	18625	18640	1.303E-08	1.086E-06
18	1.117E-08	9.493E-07	19060	19081	7.657E-09	8.336E-07
19	1.692E-08	1.002E-06	20640	20665	9.428E-09	6.746E-07
20	1.536E-08	8.936E-07	20905	20918	8.173E-09	7.424E-07
21	1.443E-07	2.262E-06	21026	21051	3.422E-08	1.431E-06
22	3.290E-08	1.167E-06	21022	21041	2.328E-08	1.117E-06
23	3.072E-08	1.506E-06	20997	21014	2.809E-08	1.354E-06
24	6.968E-08	2.375E-06	21251	21273	6.736E-08	2.382E-06
25	6.103E-07	6.362E-06	19480	19514	6.954E-08	2.358E-06
26	1.039E-07	4.049E-06	9603	9650	9.473E-08	2.567E-06
27	0.000E+00	0.000E+00	0	0	0.000E+00	0.000E+00
28	0.000E+00	0.000E+00	0	0	0.000E+00	0.000E+00
29	0.000E+00	0.000E+00	0	0	0.000E+00	0.000E+00
30	0.000E+00	0.000E+00	0	0	0.000E+00	0.000E+00
31	0.000E+00	0.000E+00	0	0	0.000E+00	0.000E+00

Table B.2 February 1980 X-ray daily mean and background values
Time of end of first day (sec of yr) = 3110400.
All daily average and background flux in units of W m^{-2}.

	— Daily Average —		Number of Values		— Background —	
Day	Short (0.5-4Å)	Long (1-8Å)	Short (0.5-4Å)	Long (1-8Å)	Short (0.5-4Å)	Long (1-8Å)
1	0.000E+00	0.000E+00	0	0	0.000E+00	0.000E+00
2	0.000E+00	0.000E+00	0	0	0.000E+00	0.000E+00
3	0.000E+00	0.000E+00	0	0	0.000E+00	0.000E+00
4	0.000E+00	0.000E+00	0	0	0.000E+00	0.000E+00
5	1.522E-07	3.109E-06	16277	16959	1.344E-07	2.635E-06
6	2.069E-07	3.588E-06	16611	17284	1.537E-07	3.507E-06
7	8.098E-08	2.159E-06	18795	18940	4.609E-08	1.562E-06
8	4.342E-07	3.619E-06	14132	15338	2.346E-08	1.547E-06
9	4.456E-08	1.778E-06	17865	18478	2.725E-08	1.634E-06
10	9.438E-08	2.776E-06	16126	18723	7.289E-08	2.614E-06
11	2.140E-07	3.966E-06	16646	21753	3.941E-08	2.515E-06
12	4.184E-08	2.231E-06	24458	28019	3.820E-08	2.225E-06
13	1.185E-07	3.189E-06	25639	28094	3.729E-08	2.211E-06
14	1.613E-08	1.459E-06	27976	28118	1.299E-08	1.244E-06
15	4.318E-08	2.224E-06	26705	28191	2.555E-08	1.769E-06
16	2.300E-08	1.523E-06	27004	27334	1.807E-08	1.437E-06
17	1.810E-08	1.335E-06	1	1	0.000E+00	0.000E+00
18	1.810E-08	1.335E-06	1	1	0.000E+00	0.000E+00
19	1.850E-08	1.335E-06	1	1	0.000E+00	0.000E+00
20	1.971E-08	1.335E-06	1	1	0.000E+00	0.000E+00
21	1.810E-08	1.335E-06	1	1	0.000E+00	0.000E+00
22	1.810E-08	1.335E-06	1	1	0.000E+00	0.000E+00
23	1.730E-08	1.335E-06	1	1	0.000E+00	0.000E+00
24	1.301E-08	1.182E-06	8194	8195	1.301E-08	1.182E-06
25	1.336E-07	2.703E-06	27698	27981	1.294E-08	1.149E-06
26	4.271E-08	1.733E-06	27715	27721	2.561E-08	1.442E-06
27	5.151E-08	1.573E-06	23893	23988	7.845E-09	9.961E-07
28	5.449E-08	1.367E-06	26801	26821	1.153E-08	1.003E-06
29	2.916E-08	1.370E-06	27256	27344	2.118E-08	1.301E-06

Table B.3 March 1980 X-ray daily mean and background values
Time of end of first day (sec of yr) = 5270400.
All daily average and background flux in units of W m^{-2}.

	— Daily Average —		Number of Values		— Background —	
Day	Short (0.5-4Å)	Long (1-8Å)	Short (0.5-4Å)	Long (1-8Å)	Short (0.5-4Å)	Long (1-8Å)
1	1.303E-08	1.055E-06	25815	25829	8.476E-09	9.051E-07
2	3.471E-08	1.113E-06	27231	27249	1.052E-08	8.360E-07
3	9.507E-08	1.696E-06	27098	27122	8.277E-09	7.544E-07
4	6.414E-08	1.855E-06	26738	26740	6.105E-08	1.702E-06
5	1.398E-08	9.334E-07	24633	24656	1.384E-08	9.274E-07
6	2.147E-08	1.163E-06	25493	25513	1.200E-08	9.654E-07
7	1.314E-08	9.356E-07	26890	26906	8.059E-09	8.263E-07
8	8.843E-09	8.923E-07	26918	26933	7.629E-09	8.349E-07
9	1.155E-08	9.055E-07	26851	26880	5.563E-09	7.480E-07
10	8.672E-08	1.521E-06	26656	26713	4.247E-09	5.976E-07
11	6.589E-09	6.849E-07	26456	26481	5.892E-09	6.617E-07
12	4.767E-09	4.654E-07	26497	26540	3.535E-09	4.133E-07
13	6.267E-09	4.735E-07	26445	26478	6.274E-09	4.657E-07
14	6.888E-09	5.393E-07	26639	26673	4.474E-09	4.962E-07
15	9.249E-09	6.767E-07	22420	22440	5.102E-09	5.547E-07
16	4.998E-08	7.660E-07	14213	14357	3.169E-09	4.812E-07
17	4.131E-08	9.255E-07	25661	25726	7.283E-09	6.182E-07
18	9.368E-09	6.976E-07	26770	26794	7.700E-09	6.564E-07
19	3.009E-08	1.254E-06	26688	26696	2.329E-08	1.124E-06
20	1.114E-08	9.165E-07	26579	26604	1.089E-08	8.653E-07
21	7.446E-09	8.725E-07	26161	26201	5.061E-09	7.288E-07
22	3.981E-08	1.698E-06	21276	21339	1.272E-08	1.193E-06
23	1.417E-08	1.198E-06	26821	26836	1.255E-08	1.168E-06
24	2.212E-08	1.349E-06	24163	24165	1.901E-08	1.306E-06
25	2.135E-08	1.323E-06	26833	26841	1.566E-08	1.259E-06
26	2.390E-08	1.227E-06	26874	26897	2.288E-08	1.053E-06
27	1.926E-07	3.901E-06	26082	26937	1.198E-07	2.635E-06
28	6.600E-08	1.774E-06	26936	26938	3.621E-08	1.533E-06
29	4.623E-08	1.671E-06	26988	26994	3.241E-08	1.551E-06
30	1.772E-08	1.253E-06	26996	27005	1.538E-08	1.245E-06
31	9.318E-08	1.658E-06	27005	27045	8.234E-09	8.122E-07

Table B.4 April 1980 X-ray daily mean and background values
Time of end of first day (sec of yr) = 7948800.
All daily average and background flux in units of W m^{-2}.

	— Daily Average —		Number of Values		— Background —	
Day	Short (0.5-4Å)	Long (1-8Å)	Short (0.5-4Å)	Long (1-8Å)	Short (0.5-4Å)	Long (1-8Å)
1	1.324E-08	9.595E-07	26896	26909	8.684E-09	8.199E-07
2	4.106E-08	1.456E-06	27139	27163	1.293E-08	1.005E-06
3	6.305E-08	2.032E-06	27018	27223	5.316E-08	1.980E-06
4	2.883E-07	4.714E-06	27206	27217	1.272E-07	3.632E-06
5	2.074E-07	4.253E-06	26994	27370	1.747E-07	4.225E-06
6	1.655E-07	4.446E-06	10575	10576	1.362E-07	4.046E-06
7	4.650E-07	6.754E-06	27321	27336	2.752E-07	5.057E-06
8	1.590E-07	3.648E-06	24609	25822	4.436E-08	2.385E-06
9	3.174E-08	2.048E-06	26375	27861	2.329E-08	1.830E-06
10	1.099E-07	2.780E-06	26710	28185	9.276E-08	2.542E-06
11	7.507E-08	3.110E-06	21660	24556	6.403E-08	3.002E-06
12	1.117E-07	3.296E-06	23693	27349	7.347E-08	3.031E-06
13	6.299E-08	2.716E-06	25492	28198	4.353E-08	2.350E-06
14	1.471E-07	3.083E-06	21575	28051	1.744E-08	2.062E-06
15	9.508E-08	2.106E-06	26979	27924	2.860E-08	1.656E-06
16	3.669E-08	1.757E-06	26256	26391	2.189E-08	1.529E-06
17	2.934E-08	1.818E-06	27604	28148	1.098E-08	1.336E-06
18	2.218E-08	1.661E-06	27047	28103	1.314E-08	1.398E-06
19	1.228E-08	1.546E-06	26383	28197	9.221E-09	1.469E-06
20	3.265E-08	1.777E-06	27695	28194	1.261E-08	1.547E-06
21	1.285E-07	2.793E-06	26945	27288	2.047E-08	1.574E-06
22	3.463E-08	1.773E-06	28016	28020	2.888E-08	1.523E-06
23	9.969E-09	9.434E-07	28165	28187	9.689E-09	9.240E-07
24	1.671E-08	1.112E-06	28142	28156	1.042E-08	9.953E-07
25	2.260E-08	1.134E-06	28114	28119	1.474E-08	9.831E-07
26	1.036E-07	2.314E-06	28174	28174	6.139E-08	2.029E-06
27	3.351E-08	1.729E-06	28194	28198	2.458E-08	1.545E-06
28	1.835E-07	3.890E-06	28083	28108	1.482E-07	3.857E-06
29	1.625E-07	4.160E-06	27770	27770	8.380E-08	3.106E-06
30	1.882E-07	4.348E-06	28187	28187	1.756E-07	4.263E-06

Table B.5 May 1980 X-ray daily mean and background values
Time of end of first day (sec of yr) = 10540800.
All daily average and background flux in units of W m^{-2}.

	— Daily Average —		Number of Values		— Background —	
Day	Short (0.5-4Å)	Long (1-8Å)	Short (0.5-4Å)	Long (1-8Å)	Short (0.5-4Å)	Long (1-8Å)
1	3.392E-08	2.466E-06	13510	13536	2.996E-08	2.345E-06
2	4.820E-08	2.179E-06	2569	2569	4.820E-08	2.179E-06
3	1.488E-07	3.480E-06	24372	24572	7.701E-08	2.752E-06
4	2.449E-08	1.739E-06	27985	28147	2.088E-08	1.601E-06
5	9.931E-08	2.258E-06	28019	28070	1.777E-08	1.542E-06
6	2.475E-08	1.622E-06	28158	28160	1.764E-08	1.486E-06
7	8.790E-08	1.745E-06	15941	15945	2.320E-08	1.484E-06
8	1.649E-08	1.154E-06	1	1	0.000E+00	0.000E+00
9	1.649E-08	1.154E-06	1	1	0.000E+00	0.000E+00
10	1.529E-08	1.154E-06	1	1	0.000E+00	0.000E+00
11	1.408E-08	1.154E-06	1	1	0.000E+00	0.000E+00
12	2.508E-07	3.317E-06	9868	9886	8.161E-09	1.023E-06
13	1.023E-08	1.131E-06	28170	28193	9.758E-09	1.124E-06
14	5.305E-08	1.847E-06	28092	28100	4.171E-08	1.748E-06
15	5.486E-08	1.815E-06	25377	25477	1.700E-08	1.314E-06
16	4.963E-08	2.043E-06	28048	28161	2.040E-08	1.499E-06
17	7.459E-08	2.400E-06	27773	28154	4.206E-08	2.300E-06
18	6.485E-08	2.301E-06	25556	28015	3.530E-08	2.129E-06
19	1.097E-07	2.666E-06	23329	28175	1.437E-08	1.881E-06
20	1.042E-07	3.006E-06	26146	27987	5.833E-08	2.623E-06
21	3.939E-07	3.970E-06	27350	28038	2.544E-08	1.653E-06
22	7.556E-08	2.866E-06	26757	28120	2.416E-08	2.099E-06
23	3.101E-08	2.212E-06	23153	28158	2.636E-08	2.066E-06
24	3.040E-08	2.219E-06	23794	28188	2.567E-08	2.211E-06
25	7.447E-08	3.150E-06	25396	28112	2.076E-08	2.277E-06
26	1.385E-07	3.221E-06	24176	28091	7.539E-08	2.892E-06
27	4.834E-08	2.384E-06	18632	25198	2.394E-08	1.923E-06
28	3.114E-07	4.723E-06	24536	26373	4.903E-08	2.431E-06
29	6.019E-08	2.503E-06	22623	27403	3.755E-08	2.120E-06
30	1.856E-08	1.493E-06	25828	28165	1.548E-08	1.443E-06
31	1.766E-08	1.257E-06	24104	28197	1.447E-08	1.132E-06

Table B.6 June 1980 X-ray daily mean and background values
Time of end of first day (sec of yr) = 13219200.
All daily average and background flux in units of W m^{-2}.

	— Daily Average —		Number of Values		— Background —	
Day	Short (0.5-4Å)	Long (1-8Å)	Short (0.5-4Å)	Long (1-8Å)	Short (0.5-4Å)	Long (1-8Å)
1	1.046E-07	2.514E-06	25734	28198	5.011E-08	2.001E-06
2	2.867E-07	5.465E-06	28072	28148	1.898E-07	5.112E-06
3	2.945E-07	5.053E-06	28165	28165	2.919E-07	5.034E-06
4	4.944E-07	6.544E-06	25719	25719	3.742E-07	4.831E-06
5	1.503E-07	4.161E-06	28161	28161	1.153E-07	3.532E-06
6	7.319E-08	2.303E-06	27074	27076	5.663E-08	2.119E-06
7	1.309E-07	2.419E-06	27957	27957	1.050E-07	1.898E-06
8	3.588E-08	2.003E-06	6717	6719	3.588E-08	2.003E-06
9	9.691E-08	1.986E-06	26779	26796	8.042E-09	1.007E-06
10	1.898E-08	1.295E-06	28085	28110	1.276E-08	1.173E-06
11	1.513E-08	1.244E-06	25062	25084	1.389E-08	1.154E-06
12	1.934E-08	1.502E-06	27898	28112	1.627E-08	1.320E-06
13	7.835E-08	1.904E-06	28077	28154	4.223E-08	1.835E-06
14	1.369E-07	2.844E-06	27999	28198	7.515E-08	2.573E-06
15	6.169E-08	2.145E-06	15907	16096	5.448E-08	2.000E-06
16	1.143E-07	2.238E-06	21349	22285	9.166E-09	1.217E-06
17	4.863E-08	1.792E-06	26313	28193	1.233E-08	1.158E-06
18	1.205E-08	1.286E-06	28119	28151	1.033E-08	1.265E-06
19	9.536E-08	3.199E-06	27606	28093	4.714E-08	2.592E-06
20	4.362E-08	2.658E-06	26746	28097	3.617E-08	2.507E-06
21	3.580E-07	4.141E-06	28009	28198	3.446E-08	1.722E-06
22	8.822E-08	3.360E-06	27138	27330	8.287E-08	3.330E-06
23	2.619E-07	4.863E-06	27353	27368	1.060E-07	3.379E-06
24	9.058E-08	3.089E-06	27399	27836	8.274E-08	3.068E-06
25	1.318E-07	3.177E-06	26884	28116	1.126E-07	3.059E-06
26	3.126E-08	2.202E-06	26991	28198	2.817E-08	2.122E-06
27	1.146E-07	2.508E-06	27414	28022	1.828E-08	1.700E-06
28	7.044E-08	2.201E-06	28152	28195	6.233E-08	2.005E-06
29	1.830E-07	3.132E-06	28160	28195	1.370E-07	2.504E-06
30	1.464E-07	4.194E-06	16559	16558	1.359E-07	3.799E-06

Table B.7 July 1980 X-ray daily mean and background values
Time of end of first day (sec of yr) = 15811200.
All daily average and background flux in units of W m^{-2}.

	— Daily Average —		Number of Values		— Background —	
Day	Short (0.5-4Å)	Long (1-8Å)	Short (0.5-4Å)	Long (1-8Å)	Short (0.5-4Å)	Long (1-8Å)
1	1.634E-07	2.247E-06	28159	28163	1.254E-08	1.155E-06
2	9.767E-09	8.542E-07	28158	28188	6.048E-09	7.413E-07
3	1.034E-08	8.286E-07	28145	28174	6.394E-09	6.869E-07
4	7.543E-09	7.262E-07	28143	28188	4.171E-09	6.172E-07
5	4.128E-07	3.394E-06	27982	27994	3.531E-08	1.268E-06
6	4.879E-08	1.262E-06	28175	28183	1.087E-08	8.654E-07
7	1.214E-07	2.710E-06	26777	26790	7.952E-08	2.137E-06
8	1.980E-08	1.343E-06	27682	27733	1.434E-08	1.133E-06
9	1.729E-08	1.363E-06	27861	28196	1.631E-08	1.180E-06
10	3.487E-08	1.682E-06	28142	28143	2.861E-08	1.646E-06
11	3.176E-07	4.421E-06	27634	27635	7.923E-08	2.609E-06
12	2.262E-07	4.392E-06	26995	26997	1.188E-07	3.351E-06
13	8.212E-08	2.473E-06	26406	26465	4.870E-08	2.154E-06
14	2.112E-07	3.277E-06	27622	28175	1.992E-07	3.243E-06
15	1.926E-08	1.777E-06	27312	28177	1.601E-08	1.596E-06
16	1.303E-08	1.815E-06	24027	28198	1.052E-08	1.691E-06
17	9.467E-08	2.826E-06	25090	28191	2.581E-08	2.227E-06
18	1.762E-08	1.746E-06	25302	27310	1.015E-08	1.464E-06
19	2.191E-08	1.816E-06	26068	28176	9.943E-09	1.376E-06
20	2.874E-08	1.711E-06	26647	28125	1.837E-08	1.689E-06
21	1.932E-07	3.299E-06	23681	28155	9.608E-09	1.740E-06
22	3.540E-08	2.268E-06	23906	28196	1.517E-08	1.994E-06
23	2.984E-07	4.615E-06	24398	28154	1.648E-08	2.072E-06
24	2.136E-08	1.897E-06	23725	28041	1.278E-08	1.764E-06
25	1.779E-08	1.505E-06	28046	28080	1.579E-08	1.446E-06
26	2.091E-08	1.465E-06	28051	28056	1.591E-08	1.323E-06
27	2.052E-08	1.504E-06	28152	28189	1.701E-08	1.405E-06
28	1.406E-07	2.331E-06	27505	28032	8.798E-09	1.057E-06
29	2.908E-08	1.381E-06	26989	28152	1.105E-08	8.711E-07
30	7.058E-09	5.565E-07	11175	13494	5.055E-09	5.893E-07
31	7.781E-09	5.122E-07	24711	28190	6.629E-09	4.371E-07

Table B.8 August 1980 X-ray daily mean and background values
Time of end of first day (sec of yr) = 18489600.
All daily average and background flux in units of W m^{-2}.

	— Daily Average —		Number of Values		— Background —	
Day	Short (0.5-4Å)	Long (1-8Å)	Short (0.5-4Å)	Long (1-8Å)	Short (0.5-4Å)	Long (1-8Å)
1	4.911E-09	3.426E-07	22748	28169	3.594E-09	3.168E-07
2	9.256E-09	3.408E-07	18164	28136	9.032E-09	3.363E-07
3	6.526E-09	3.707E-07	21657	28198	5.986E-09	3.420E-07
4	1.794E-07	1.541E-06	20405	28102	5.613E-09	3.077E-07
5	1.116E-08	5.563E-07	24379	27327	4.997E-09	3.877E-07
6	2.326E-08	1.043E-06	26068	26782	1.191E-08	8.130E-07
7	2.821E-08	9.321E-07	23014	25304	1.217E-08	7.308E-07
8	9.621E-09	6.608E-07	24857	28171	5.974E-09	5.189E-07
9	1.704E-08	9.334E-07	26661	28174	1.101E-08	8.255E-07
10	8.943E-08	1.732E-06	26326	28147	1.000E-08	9.132E-07
11	1.307E-07	2.415E-06	27273	27501	2.615E-08	1.386E-06
12	2.738E-08	1.238E-06	27952	28076	1.144E-08	1.030E-06
13	1.465E-07	2.329E-06	25927	27028	1.664E-08	1.127E-06
14	1.309E-08	1.117E-06	27640	28159	1.277E-08	1.083E-06
15	1.952E-08	1.272E-06	27716	28178	1.537E-08	1.167E-06
16	1.889E-08	1.239E-06	27936	28193	1.681E-08	1.173E-06
17	2.211E-08	1.476E-06	27884	28190	1.741E-08	1.368E-06
18	8.872E-08	2.019E-06	27671	28172	1.939E-08	1.453E-06
19	1.600E-08	1.255E-06	22559	25532	1.312E-08	1.146E-06
20	1.639E-08	1.223E-06	26600	28175	1.483E-08	1.163E-06
21	1.740E-07	2.476E-06	28043	28194	1.005E-07	2.275E-06
22	7.609E-08	1.952E-06	28016	28117	4.433E-08	1.564E-06
23	8.410E-08	1.846E-06	28086	28198	8.387E-08	1.755E-06
24	1.382E-07	2.520E-06	28144	28174	6.623E-08	1.826E-06
25	2.364E-07	3.794E-06	28124	28175	1.402E-07	2.768E-06
26	6.524E-08	2.081E-06	27788	27806	5.621E-08	2.055E-06
27	7.149E-08	2.059E-06	28078	28109	3.951E-08	1.802E-06
28	3.612E-08	1.930E-06	27979	27982	2.172E-08	1.566E-06
29	2.724E-08	1.659E-06	27036	27111	1.824E-08	1.429E-06
30	4.506E-08	1.994E-06	28102	28194	3.787E-08	1.890E-06
31	1.450E-07	2.834E-06	17919	18080	2.137E-08	1.732E-06

Table B.9 September 1980 X-ray daily mean and background values
Time of end of first day (sec of yr) = 21168000.
All daily average and background flux in units of W m^{-2}.

	— Daily Average —		Number of Values		— Background —	
Day	Short (0.5-4Å)	Long (1-8Å)	Short (0.5-4Å)	Long (1-8Å)	Short (0.5-4Å)	Long (1-8Å)
1	1.063E-07	2.331E-06	27643	27707	2.948E-08	1.676E-06
2	3.204E-08	1.785E-06	27557	27587	2.982E-08	1.715E-06
3	9.891E-08	2.521E-06	25283	25308	5.835E-08	2.189E-06
4	2.787E-07	3.881E-06	27313	27360	1.660E-08	1.573E-06
5	2.216E-08	1.473E-06	12882	12980	8.264E-09	1.073E-06
6	1.560E-08	1.308E-06	27231	27242	1.264E-08	1.255E-06
7	2.109E-08	1.788E-06	26547	26673	1.630E-08	1.624E-06
8	3.767E-07	4.754E-06	21601	21615	2.102E-08	1.408E-06
9	3.397E-08	1.862E-06	12768	12822	1.250E-08	1.196E-06
10	2.614E-08	1.334E-06	27018	27024	1.192E-08	1.140E-06
11	2.471E-08	1.476E-06	21656	21668	2.114E-08	1.315E-06
12	2.044E-08	1.160E-06	26857	26883	1.301E-08	9.936E-07
13	1.064E-08	9.351E-07	25267	25300	9.066E-09	9.266E-07
14	8.892E-09	7.248E-07	26839	26865	5.037E-09	6.148E-07
15	1.077E-08	6.886E-07	26371	26837	1.055E-08	6.763E-07
16	8.476E-09	6.540E-07	26821	26856	5.435E-09	5.319E-07
17	1.577E-08	9.071E-07	24268	24284	9.127E-09	8.243E-07
18	1.089E-08	7.283E-07	21649	21674	4.756E-09	5.878E-07
19	1.165E-08	8.282E-07	6820	6823	8.116E-09	7.610E-07
20	9.656E-09	8.951E-07	1	1	0.000E+00	0.000E+00
21	1.359E-08	9.038E-07	26807	26819	1.306E-08	9.084E-07
22	1.552E-07	2.670E-06	26712	26730	5.212E-08	1.924E-06
23	1.185E-07	2.633E-06	26629	26640	4.097E-08	1.551E-06
24	2.435E-08	1.471E-06	22877	22879	2.401E-08	1.456E-06
25	2.332E-08	1.227E-06	25987	25991	1.770E-08	1.172E-06
26	2.086E-08	1.369E-06	26469	26468	1.907E-08	1.368E-06
27	2.040E-08	1.408E-06	26629	26637	1.526E-08	1.288E-06
28	3.696E-08	1.906E-06	26333	26335	3.512E-08	1.887E-06
29	1.068E-07	2.313E-06	26467	26480	1.446E-08	1.299E-06
30	9.519E-08	2.093E-06	26807	26812	1.397E-08	1.167E-06

Table B.10 October 1980 X-ray daily mean and background values
Time of end of first day (sec of yr) = 23760000.
All daily average and background flux in units of W m^{-2}.

	— Daily Average —		Number of Values		— Background —	
Day	Short (0.5-4Å)	Long (1-8Å)	Short (0.5-4Å)	Long (1-8Å)	Short (0.5-4Å)	Long (1-8Å)
1	1.991E-08	1.046E-06	26814	26826	1.366E-08	9.479E-07
2	2.014E-08	8.980E-07	26780	26790	7.700E-09	7.403E-07
3	3.247E-08	1.391E-06	26880	26883	2.056E-08	1.129E-06
4	1.738E-08	1.375E-06	26962	26962	1.119E-08	1.234E-06
5	1.939E-08	1.664E-06	25476	25960	1.751E-08	1.600E-06
6	1.201E-07	2.896E-06	26532	27022	3.675E-08	1.873E-06
7	2.765E-07	3.852E-06	25661	25941	1.847E-07	3.259E-06
8	1.883E-07	3.489E-06	26481	26638	6.900E-08	1.997E-06
9	2.380E-07	3.269E-06	26520	27204	4.510E-08	1.908E-06
10	5.839E-08	2.424E-06	26209	27281	4.478E-08	2.289E-06
11	1.441E-07	3.249E-06	26375	27320	5.850E-08	2.563E-06
12	8.906E-08	3.280E-06	27164	27447	7.980E-08	3.038E-06
13	2.245E-07	4.363E-06	27401	27567	2.222E-07	4.277E-06
14	1.231E-06	7.416E-06	26319	27738	1.263E-07	3.968E-06
15	2.223E-07	5.099E-06	27330	27811	2.189E-07	4.975E-06
16	6.286E-08	2.836E-06	27849	27951	5.947E-08	2.795E-06
17	7.249E-08	2.873E-06	25702	25920	6.677E-08	2.911E-06
18	1.256E-07	3.094E-06	28147	28166	8.608E-08	2.697E-06
19	6.882E-08	1.957E-06	24792	24792	4.771E-08	1.782E-06
20	2.093E-07	3.219E-06	12085	12103	2.162E-08	1.549E-06
21	1.619E-08	1.128E-06	27919	27925	1.497E-08	1.119E-06
22	1.667E-08	1.123E-06	28187	28193	1.506E-08	1.052E-06
23	1.316E-07	1.849E-06	28085	28132	3.599E-08	1.232E-06
24	1.299E-08	1.066E-06	28114	28198	1.023E-08	1.043E-06
25	8.038E-07	3.917E-06	27334	28198	6.365E-08	1.512E-06
26	2.684E-08	1.272E-06	27955	27960	2.400E-08	1.231E-06
27	1.136E-07	2.414E-06	28086	28140	1.542E-08	1.224E-06
28	8.476E-08	2.415E-06	28192	28192	2.921E-08	1.412E-06
29	1.863E-07	4.495E-06	27843	28083	7.728E-08	3.145E-06
30	2.822E-08	1.909E-06	25716	28111	1.817E-08	1.909E-06
31	3.351E-08	2.034E-06	13291	13631	2.283E-08	1.685E-06

Table B.11 November 1980 X-ray daily mean and background values
Time of end of first day (sec of yr) = 26524800.
All daily average and background flux in units of W m^{-2}.

	— Daily Average —		Number of Values		— Background —	
Day	Short (0.5-4Å)	Long (1-8Å)	Short (0.5-4Å)	Long (1-8Å)	Short (0.5-4Å)	Long (1-8Å)
1	0.000E+00	0.000E+00	0	0	0.000E+00	0.000E+00
2	2.407E-08	1.779E-06	27073	28186	2.045E-08	1.732E-06
3	2.299E-07	3.469E-06	24013	28169	6.499E-08	2.073E-06
4	2.061E-07	3.961E-06	26211	28127	2.035E-07	3.690E-06
5	2.348E-06	1.332E-05	27342	27342	2.952E-07	6.014E-06
6	6.630E-06	3.538E-05	28188	28188	3.257E-06	2.021E-05
7	1.990E-06	1.296E-05	26739	26739	7.360E-07	7.324E-06
8	6.735E-07	5.937E-06	27754	28178	1.676E-07	3.531E-06
9	1.042E-07	3.121E-06	27182	28100	4.469E-08	2.439E-06
10	5.579E-07	6.724E-06	28075	28113	2.274E-07	4.375E-06
11	6.579E-07	7.483E-06	27494	28186	4.879E-07	6.707E-06
12	5.660E-07	6.886E-06	28176	28176	1.613E-07	4.574E-06
13	1.069E-06	1.090E-05	28189	28189	9.862E-07	9.436E-06
14	1.225E-06	1.344E-05	28189	28189	6.739E-07	7.784E-06
15	1.563E-06	1.117E-05	26952	26958	1.480E-06	9.845E-06
16	4.871E-07	5.938E-06	28091	28172	4.082E-07	5.506E-06
17	4.447E-07	5.746E-06	26852	28175	3.133E-07	4.788E-06
18	2.252E-07	4.517E-06	25319	27077	1.293E-07	3.467E-06
19	5.566E-07	5.403E-06	25415	27928	6.751E-08	2.269E-06
20	1.286E-07	1.888E-06	27523	28194	6.315E-08	1.333E-06
21	4.051E-08	1.129E-06	27905	27926	2.776E-08	1.004E-06
22	4.975E-08	1.832E-06	27931	28198	1.877E-08	1.594E-06
23	8.674E-08	2.072E-06	28119	28125	1.043E-08	9.346E-07
24	1.102E-07	2.195E-06	28033	28053	3.938E-08	1.471E-06
25	2.968E-08	1.941E-06	27404	28198	2.885E-08	1.937E-06
26	2.577E-08	1.829E-06	24613	28162	1.945E-08	1.769E-06
27	1.401E-08	1.653E-06	25938	28197	1.081E-08	1.610E-06
28	2.088E-07	3.507E-06	26572	28139	1.754E-08	1.634E-06
29	2.331E-08	1.669E-06	26953	28152	8.663E-09	1.299E-06
30	3.506E-08	1.782E-06	15340	15345	1.139E-08	1.140E-06

Table B.12 December 1980 X-ray daily mean and background values
Time of end of first day (sec of yr) = 29030400.
All daily average and background flux in units of W m^{-2}.

	— Daily Average —		Number of Values		— Background —	
Day	Short (0.5-4Å)	Long (1-8Å)	Short (0.5-4Å)	Long (1-8Å)	Short (0.5-4Å)	Long (1-8Å)
1	1.038E-07	2.480E-06	27956	28172	1.788E-08	1.640E-06
2	2.843E-07	3.408E-06	28045	28177	5.256E-08	1.938E-06
3	2.340E-08	1.401E-06	28156	28172	1.269E-08	1.240E-06
4	1.824E-08	1.486E-06	28065	28181	1.706E-08	1.334E-06
5	1.260E-08	1.117E-06	28171	28186	1.064E-08	1.008E-06
6	3.289E-08	1.254E-06	28190	28198	1.455E-08	1.069E-06
7	3.519E-08	1.298E-06	28192	28196	1.639E-08	1.165E-06
8	9.041E-08	1.811E-06	28110	28131	8.501E-09	9.489E-07
9	4.395E-08	2.223E-06	27609	28196	3.476E-08	1.769E-06
10	5.073E-08	1.811E-06	27399	27575	2.259E-08	1.537E-06
11	8.814E-08	2.850E-06	27242	28196	4.455E-08	2.398E-06
12	3.013E-07	4.791E-06	26876	28147	8.439E-08	2.772E-06
13	7.669E-08	2.846E-06	22539	24951	5.602E-08	2.592E-06
14	9.831E-08	2.750E-06	24215	28165	6.271E-08	2.562E-06
15	3.291E-07	4.756E-06	24487	28169	1.841E-07	3.821E-06
16	4.223E-07	6.246E-06	27229	28175	8.815E-08	3.585E-06
17	1.386E-07	3.246E-06	22860	28176	8.076E-08	2.956E-06
18	4.993E-08	2.035E-06	24099	28151	1.149E-08	1.735E-06
19	1.802E-08	1.479E-06	28100	28173	1.244E-08	1.386E-06
20	2.339E-08	1.791E-06	27598	28198	2.138E-08	1.757E-06
21	1.400E-08	1.498E-06	27606	28194	1.346E-08	1.375E-06
22	1.138E-07	2.589E-06	24770	28170	2.129E-08	1.829E-06
23	3.942E-08	1.964E-06	19362	28028	9.547E-09	1.703E-06
24	1.357E-08	1.763E-06	13057	21151	9.900E-09	1.751E-06
25	3.411E-08	1.856E-06	24332	25752	1.836E-08	1.585E-06
26	4.598E-08	1.741E-06	27941	28147	1.333E-08	1.610E-06
27	3.017E-08	1.408E-06	28193	28194	1.632E-08	1.326E-06
28	3.240E-08	1.755E-06	28119	28134	1.763E-08	1.739E-06
29	1.605E-07	2.941E-06	27772	28161	1.443E-07	2.791E-06
30	1.650E-08	1.546E-06	14162	14224	1.684E-08	1.621E-06
31	1.160E-08	1.152E-06	28151	28156	1.114E-08	1.142E-06

Table B.13 January 1981 X-ray daily mean and background values
Time of end of first day (sec of yr) = 86400.
All daily average and background flux in units of W m^{-2}.

	— Daily Average —		Number of Values		— Background —	
Day	Short (0.5-4Å)	Long (1-8Å)	Short (0.5-4Å)	Long (1-8Å)	Short (0.5-4Å)	Long (1-8Å)
1	9.552E-09	1.063E-06	28029	28118	7.965E-09	1.010E-06
2	8.050E-09	9.541E-07	28085	28136	6.896E-09	9.006E-07
3	1.083E-08	9.559E-07	28141	28146	9.152E-09	9.111E-07
4	1.187E-08	1.018E-06	28154	28162	1.000E-08	9.560E-07
5	2.216E-07	3.082E-06	28123	28170	1.853E-08	1.222E-06
6	3.299E-08	1.387E-06	28131	28153	2.531E-08	1.303E-06
7	2.838E-08	1.639E-06	28000	28063	2.138E-08	1.474E-06
8	4.692E-08	1.721E-06	22212	22569	5.077E-08	1.329E-06
9	2.345E-08	1.056E-06	28188	28198	2.342E-08	1.035E-06
10	1.816E-08	9.435E-07	28178	28184	1.711E-08	9.165E-07
11	1.097E-08	8.466E-07	28109	28168	7.585E-09	7.406E-07
12	1.907E-08	6.791E-07	27611	27643	7.904E-09	6.375E-07
13	7.646E-09	7.434E-07	28165	28176	6.605E-09	7.299E-07
14	1.049E-08	8.076E-07	28032	28193	7.580E-09	8.055E-07
15	8.845E-09	7.454E-07	28048	28085	5.225E-09	6.464E-07
16	9.915E-09	7.892E-07	27971	28158	5.652E-09	7.204E-07
17	7.100E-09	7.308E-07	28165	28198	6.379E-09	6.729E-07
18	7.235E-09	8.547E-07	28173	28185	5.744E-09	8.226E-07
19	8.562E-08	1.628E-06	28133	28157	7.687E-09	9.138E-07
20	7.848E-09	7.979E-07	28160	28168	7.647E-09	7.877E-07
21	5.088E-09	6.212E-07	28133	28159	4.400E-09	5.966E-07
22	4.855E-09	5.859E-07	26678	26714	3.781E-09	5.257E-07
23	5.638E-09	5.999E-07	28106	28193	4.782E-09	5.763E-07
24	3.254E-08	1.247E-06	28195	28196	9.715E-09	8.394E-07
25	1.011E-06	8.759E-06	28099	28118	7.349E-07	6.204E-06
26	3.454E-07	5.418E-06	28129	28142	2.200E-07	4.284E-06
27	1.425E-07	2.575E-06	27974	28116	9.149E-08	2.338E-06
28	3.515E-07	4.448E-06	25813	28164	8.661E-08	2.386E-06
29	3.563E-08	1.683E-06	27935	28166	2.763E-08	1.599E-06
30	2.100E-08	1.377E-06	28039	28039	1.617E-08	1.212E-06
31	2.649E-08	1.302E-06	28193	28196	1.648E-08	1.261E-06

Table B.14 February 1981 X-ray daily mean and background values
Time of end of first day (sec of yr) = 2764800.
All daily average and background flux in units of W m^{-2}.

	— Daily Average —		Number of Values		— Background —	
Day	Short (0.5-4Å)	Long (1-8Å)	Short (0.5-4Å)	Long (1-8Å)	Short (0.5-4Å)	Long (1-8Å)
1	2.650E-07	1.771E-06	9395	9396	8.334E-09	1.169E-06
2	6.189E-07	4.182E-06	11730	12305	4.454E-07	2.478E-06
3	2.839E-08	1.903E-06	15889	16292	2.266E-08	1.872E-06
4	9.209E-08	3.499E-06	1	1	0.000E+00	0.000E+00
5	9.168E-08	3.499E-06	1	1	0.000E+00	0.000E+00
6	9.128E-08	3.499E-06	1	1	0.000E+00	0.000E+00
7	7.104E-08	3.181E-06	425	425	7.104E-08	3.181E-06
8	9.855E-08	2.344E-06	28048	28196	2.962E-08	1.633E-06
9	6.387E-08	2.491E-06	27158	27978	4.763E-08	2.316E-06
10	2.051E-07	3.561E-06	25825	28147	3.807E-08	2.020E-06
11	6.264E-08	2.329E-06	27935	28148	3.406E-08	1.885E-06
12	6.447E-08	2.329E-06	27355	28151	4.248E-08	2.010E-06
13	7.716E-08	2.173E-06	28043	28194	5.619E-08	2.043E-06
14	2.863E-08	1.514E-06	28127	28178	2.131E-08	1.354E-06
15	2.921E-08	1.542E-06	27791	28194	1.398E-08	1.275E-06
16	2.161E-08	1.493E-06	22010	22137	2.097E-08	1.476E-06
17	7.600E-08	3.535E-06	1	1	0.000E+00	0.000E+00
18	7.640E-08	3.499E-06	1	1	0.000E+00	0.000E+00
19	7.560E-08	3.535E-06	1	1	0.000E+00	0.000E+00
20	1.100E-07	3.692E-06	3202	3709	1.100E-07	3.692E-06
21	3.309E-08	1.920E-06	27519	28185	2.025E-08	1.782E-06
22	5.066E-08	2.440E-06	26434	28143	2.729E-08	2.085E-06
23	2.844E-07	5.123E-06	26109	26180	9.464E-08	3.886E-06
24	1.173E-06	9.167E-06	28122	28124	8.592E-07	7.682E-06
25	6.995E-08	2.445E-06	25408	28054	3.338E-08	2.061E-06
26	1.358E-06	9.140E-06	19287	20400	7.680E-07	5.081E-06
27	9.165E-08	2.883E-06	25417	27218	1.598E-08	2.035E-06
28	2.280E-08	1.756E-06	24509	27270	1.586E-08	1.595E-06

Table B.15 March 1981 X-ray daily mean and background values
Time of end of first day (sec of yr) = 5184000.
All daily average and background flux in units of W m^{-2}.

	— Daily Average —		Number of Values		— Background —	
Day	Short (0.5-4Å)	Long (1-8Å)	Short (0.5-4Å)	Long (1-8Å)	Short (0.5-4Å)	Long (1-8Å)
1	2.892E-08	1.772E-06	25251	26276	2.652E-08	1.719E-06
2	1.647E-07	3.721E-06	23834	24979	8.878E-08	3.275E-06
3	1.620E-07	4.581E-06	25833	26285	4.668E-08	2.675E-06
4	6.894E-08	2.483E-06	12771	13992	5.837E-08	2.450E-06
5	9.106E-08	2.863E-06	25359	27057	2.671E-08	2.090E-06
6	7.483E-08	2.062E-06	22498	26351	1.456E-08	1.362E-06
7	6.216E-08	2.023E-06	25627	26966	2.684E-08	1.802E-06
8	3.653E-08	1.979E-06	25506	26784	2.564E-08	1.809E-06
9	1.308E-07	3.032E-06	26597	26773	4.344E-08	2.165E-06
10	1.866E-08	1.405E-06	26880	26884	1.584E-08	1.383E-06
11	4.094E-08	1.821E-06	26606	26920	1.723E-08	1.363E-06
12	2.094E-08	1.433E-06	26655	26691	1.460E-08	1.270E-06
13	8.642E-08	2.189E-06	26808	26808	1.907E-08	1.363E-06
14	5.992E-08	2.425E-06	26121	26819	4.880E-08	2.265E-06
15	3.860E-07	6.131E-06	26814	26838	3.459E-07	5.958E-06
16	1.544E-07	3.471E-06	25054	26771	8.988E-08	3.155E-06
17	2.604E-08	1.717E-06	26398	26762	2.657E-08	1.712E-06
18	6.126E-08	2.082E-06	26771	26774	4.214E-08	1.759E-06
19	3.178E-08	1.698E-06	26803	26802	2.074E-08	1.546E-06
20	3.511E-08	1.634E-06	26701	26704	3.129E-08	1.599E-06
21	7.693E-08	2.388E-06	26485	26799	7.590E-08	2.040E-06
22	1.372E-07	2.212E-06	26665	26795	2.645E-08	1.515E-06
23	1.747E-07	3.194E-06	26399	26748	1.597E-07	3.090E-06
24	4.275E-08	1.700E-06	26804	26834	2.343E-08	1.458E-06
25	2.731E-07	3.857E-06	26048	26833	2.598E-08	1.710E-06
26	5.793E-08	2.075E-06	26499	26847	3.454E-08	1.767E-06
27	6.445E-08	2.193E-06	26467	26881	1.092E-08	1.207E-06
28	5.101E-08	2.062E-06	26594	26929	2.717E-08	1.547E-06
29	4.344E-08	2.021E-06	26575	26886	2.163E-08	1.559E-06
30	4.534E-07	6.691E-06	26648	26847	4.078E-08	2.227E-06
31	7.375E-08	3.000E-06	26549	26994	4.233E-08	2.379E-06

Table B.16 April 1981 X-ray daily mean and background values
Time of end of first day (sec of yr) = 7862400.
All daily average and background flux in units of W m^{-2}.

	— Daily Average —		Number of Values		— Background —	
Day	Short (0.5-4Å)	Long (1-8Å)	Short (0.5-4Å)	Long (1-8Å)	Short (0.5-4Å)	Long (1-8Å)
1	3.087E-07	5.859E-06	22134	22340	1.420E-07	4.514E-06
2	2.984E-07	3.343E-06	23405	26170	7.314E-08	2.786E-06
3	5.777E-07	7.730E-06	26295	27099	1.761E-07	4.229E-06
4	4.289E-07	5.614E-06	23566	27210	2.823E-07	4.511E-06
5	7.111E-08	2.903E-06	25420	27264	2.949E-08	2.120E-06
6	2.545E-07	4.460E-06	23028	27252	1.407E-07	4.341E-06
7	8.910E-08	3.130E-06	24962	27218	3.892E-08	2.505E-06
8	3.780E-07	7.340E-06	27168	27467	1.315E-07	4.278E-06
9	4.095E-07	7.608E-06	27625	27626	2.106E-07	5.245E-06
10	1.239E-06	1.229E-05	27343	27343	1.209E-06	1.101E-05
11	1.213E-07	4.115E-06	27860	28177	7.409E-08	3.336E-06
12	2.361E-07	5.389E-06	26853	28183	1.342E-07	4.200E-06
13	2.072E-07	5.689E-06	27861	27887	9.799E-08	4.386E-06
14	1.363E-07	3.900E-06	27955	28130	4.378E-08	2.826E-06
15	2.154E-07	5.354E-06	27117	27117	9.931E-08	3.889E-06
16	1.525E-07	3.859E-06	26955	28177	1.341E-07	3.197E-06
17	1.624E-07	3.898E-06	25149	28187	1.147E-07	3.266E-06
18	6.343E-07	6.881E-06	28067	28188	6.232E-07	6.676E-06
19	1.396E-07	3.047E-06	27683	28191	1.256E-07	2.843E-06
20	4.204E-07	4.656E-06	25620	25913	2.319E-08	1.592E-06
21	4.679E-08	2.251E-06	27886	28017	4.015E-08	2.073E-06
22	1.515E-07	3.175E-06	27881	28132	1.953E-08	1.713E-06
23	7.673E-08	2.784E-06	26872	27003	3.852E-08	2.125E-06
24	3.938E-06	2.278E-05	28077	28078	1.203E-06	9.767E-06
25	2.372E-07	4.365E-06	28015	28170	1.218E-07	2.621E-06
26	1.563E-06	1.285E-05	27969	28069	2.908E-07	4.406E-06
27	5.412E-06	2.479E-05	27962	28005	7.315E-07	6.083E-06
28	1.485E-06	9.099E-06	27889	27937	1.558E-08	1.294E-06
29	1.453E-07	3.393E-06	28047	28046	3.417E-08	1.932E-06
30	1.980E-08	1.156E-06	19590	19676	1.106E-08	1.047E-06

Table B.17 May 1981 X-ray daily mean and background values
Time of end of first day (sec of yr) = 10454400.
All daily average and background flux in units of W m^{-2}.

	— Daily Average —		Number of Values		— Background —	
Day	Short (0.5-4Å)	Long (1-8Å)	Short (0.5-4Å)	Long (1-8Å)	Short (0.5-4Å)	Long (1-8Å)
1	1.909E-08	1.472E-06	27539	27553	1.489E-08	1.366E-06
2	1.042E-08	1.078E-06	28169	28181	8.901E-09	1.033E-06
3	2.066E-08	1.658E-06	27896	27967	1.499E-08	1.453E-06
4	2.632E-07	3.962E-06	25729	27150	1.516E-07	3.287E-06
5	2.860E-07	3.952E-06	26073	28184	1.610E-07	3.244E-06
6	2.367E-08	1.959E-06	26808	28055	1.340E-08	1.622E-06
7	1.928E-08	1.764E-06	27470	28152	1.563E-08	1.710E-06
8	5.900E-07	5.289E-06	28167	28169	2.195E-08	1.585E-06
9	3.494E-07	6.279E-06	27968	28176	7.823E-08	3.062E-06
10	2.607E-07	5.497E-06	22858	22979	1.115E-07	3.638E-06
11	1.764E-07	3.854E-06	27570	27797	6.018E-08	2.719E-06
12	3.453E-08	2.281E-06	26365	28083	1.660E-08	2.045E-06
13	1.606E-06	1.396E-05	27862	27866	2.327E-07	6.123E-06
14	1.181E-07	3.106E-06	25118	28163	4.533E-08	2.148E-06
15	3.176E-08	1.782E-06	26155	26194	2.174E-08	1.546E-06
16	1.021E-06	9.100E-06	26437	26446	2.923E-08	1.739E-06
17	1.946E-08	1.401E-06	27986	28179	1.110E-08	1.236E-06
18	1.013E-07	2.085E-06	28095	28173	2.650E-08	1.437E-06
19	1.563E-08	1.218E-06	27352	28198	1.353E-08	1.156E-06
20	3.639E-08	1.412E-06	28139	28175	9.339E-09	1.021E-06
21	1.769E-08	1.255E-06	27605	27882	8.117E-09	1.049E-06
22	2.344E-08	9.751E-07	26920	28191	8.204E-09	8.723E-07
23	2.201E-08	1.190E-06	27755	28179	8.233E-09	8.688E-07
24	5.144E-08	2.119E-06	14861	14879	4.212E-08	1.791E-06
25	2.081E-07	3.338E-06	11854	11955	1.558E-08	1.871E-06
26	1.820E-08	1.124E-06	26914	27136	1.209E-08	9.812E-07
27	1.494E-08	9.157E-07	26156	28146	1.251E-08	8.536E-07
28	1.436E-08	9.342E-07	26008	28190	1.378E-08	9.137E-07
29	1.372E-08	8.712E-07	25176	28016	1.088E-08	8.459E-07
30	9.300E-09	7.275E-07	23284	28169	8.321E-09	6.806E-07
31	9.001E-09	6.816E-07	20233	24789	6.979E-09	6.080E-07

Table B.18 June 1981 X-ray daily mean and background values
Time of end of first day (sec of yr) = 13132800.
All daily average and background flux in units of W m^{-2}.

	— Daily Average —		Number of Values		— Background —	
Day	Short (0.5-4Å)	Long (1-8Å)	Short (0.5-4Å)	Long (1-8Å)	Short (0.5-4Å)	Long (1-8Å)
1	1.250E-07	1.650E-06	23061	27777	1.218E-08	7.704E-07
2	2.297E-08	6.249E-07	22550	27687	1.002E-08	5.977E-07
3	1.173E-08	5.743E-07	23834	27200	1.167E-08	4.278E-07
4	2.823E-08	9.176E-07	25507	28196	9.999E-09	6.073E-07
5	9.269E-09	6.730E-07	24487	28196	9.157E-09	6.706E-07
6	9.417E-09	6.334E-07	22387	28174	8.901E-09	6.009E-07
7	1.482E-08	8.340E-07	22725	28160	1.153E-08	7.928E-07
8	1.427E-07	1.935E-06	23719	28139	1.610E-08	8.085E-07
9	2.656E-08	1.152E-06	25615	28172	2.606E-08	1.062E-06
10	2.807E-08	8.443E-07	22964	28198	1.697E-08	8.100E-07
11	5.364E-08	1.243E-06	21002	28154	1.768E-08	6.477E-07
12	1.528E-08	6.983E-07	21526	28066	1.312E-08	6.229E-07
13	1.495E-08	6.474E-07	19325	26664	1.410E-08	6.417E-07
14	2.097E-08	8.401E-07	21550	28196	1.285E-08	6.693E-07
15	1.145E-07	1.583E-06	21211	28031	1.554E-08	7.206E-07
16	2.115E-08	9.899E-07	23731	28185	1.668E-08	9.844E-07
17	5.032E-08	1.348E-06	25292	28126	4.906E-08	1.341E-06
18	6.442E-08	1.896E-06	26369	28125	1.689E-08	1.134E-06
19	2.099E-08	1.109E-06	24100	28184	2.030E-08	1.045E-06
20	2.260E-08	1.135E-06	25468	28165	2.040E-08	1.118E-06
21	1.444E-08	8.304E-07	25054	28198	1.215E-08	7.439E-07
22	2.242E-07	2.960E-06	27226	28105	2.218E-07	2.685E-06
23	2.019E-07	3.252E-06	27472	28176	1.536E-07	2.794E-06
24	1.164E-07	2.731E-06	27511	28177	1.074E-07	2.589E-06
25	2.274E-07	3.315E-06	26910	28182	9.708E-08	2.066E-06
26	1.992E-07	4.075E-06	27942	28156	1.181E-07	3.270E-06
27	2.323E-07	3.868E-06	27699	28169	1.013E-07	2.592E-06
28	3.521E-08	1.414E-06	26721	28186	2.794E-08	1.365E-06
29	3.370E-07	3.487E-06	25311	28175	3.141E-08	1.201E-06
30	3.064E-08	1.164E-06	23894	28181	2.805E-08	1.141E-06

Table B.19 July 1981 X-ray daily mean and background values
Time of end of first day (sec of yr) = 15724800.
All daily average and background flux in units of W m^{-2}.

	— Daily Average —		Number of Values		— Background —	
Day	Short (0.5-4Å)	Long (1-8Å)	Short (0.5-4Å)	Long (1-8Å)	Short (0.5-4Å)	Long (1-8Å)
1	1.624E-08	8.611E-07	21410	26587	1.536E-08	8.269E-07
2	1.031E-07	1.528E-06	25214	27946	3.462E-08	1.008E-06
3	1.234E-07	2.034E-06	25387	28187	5.052E-08	1.314E-06
4	2.734E-08	1.327E-06	25537	28198	2.352E-08	1.189E-06
5	2.747E-08	1.177E-06	22911	28096	2.456E-08	1.173E-06
6	1.133E-07	1.906E-06	23921	26975	2.510E-08	1.091E-06
7	8.090E-08	1.725E-06	25170	27736	4.968E-08	1.711E-06
8	5.572E-08	1.777E-06	25987	28196	3.721E-08	1.474E-06
9	9.343E-08	1.844E-06	23612	27684	7.478E-08	1.658E-06
10	4.359E-08	1.412E-06	23598	27279	2.643E-08	1.343E-06
11	3.554E-08	1.260E-06	28058	28193	2.890E-08	1.174E-06
12	5.325E-08	1.528E-06	25185	25223	3.295E-08	1.205E-06
13	1.960E-07	2.634E-06	20041	21820	1.846E-08	1.094E-06
14	1.955E-08	1.114E-06	24653	27436	1.548E-08	1.103E-06
15	1.598E-07	2.326E-06	27295	27697	1.154E-07	2.057E-06
16	1.598E-07	2.789E-06	27112	27664	1.571E-07	2.483E-06
17	1.717E-06	9.896E-06	27352	27613	1.982E-07	3.307E-06
18	3.080E-07	3.728E-06	25179	25273	3.005E-07	3.774E-06
19	2.088E-06	1.373E-05	28178	28183	2.772E-07	6.513E-06
20	6.849E-07	8.416E-06	25143	25195	4.395E-07	6.372E-06
21	1.965E-07	4.388E-06	28029	28048	1.545E-07	3.689E-06
22	1.811E-07	3.952E-06	28185	28191	1.736E-07	3.645E-06
23	3.704E-07	5.858E-06	28196	28196	2.587E-07	4.539E-06
24	1.550E-07	3.947E-06	27885	28188	1.330E-07	3.628E-06
25	1.722E-07	3.357E-06	26156	26718	5.434E-08	2.569E-06
26	9.420E-07	8.196E-06	28065	28070	3.971E-07	5.662E-06
27	5.545E-07	5.872E-06	27710	28173	1.292E-07	3.202E-06
28	5.905E-08	1.785E-06	27558	28196	2.719E-08	1.574E-06
29	3.802E-08	1.917E-06	27721	28112	3.776E-08	1.748E-06
30	1.520E-07	2.739E-06	28139	28186	7.096E-08	2.051E-06
31	6.602E-08	2.391E-06	27982	28191	3.683E-08	1.963E-06

Table B.20 August 1981 X-ray daily mean and background values
Time of end of first day (sec of yr) = 18403200.
All daily average and background flux in units of W m^{-2}.

	— Daily Average —		Number of Values		— Background —	
Day	Short (0.5-4Å)	Long (1-8Å)	Short (0.5-4Å)	Long (1-8Å)	Short (0.5-4Å)	Long (1-8Å)
1	4.077E-08	1.797E-06	16997	17022	1.144E-08	1.088E-06
2	6.956E-08	2.464E-06	8003	8004	6.956E-08	2.464E-06
3	5.347E-07	6.249E-06	26594	26630	1.849E-07	3.868E-06
4	1.992E-07	4.632E-06	27108	27108	1.969E-07	4.560E-06
5	4.612E-08	2.040E-06	28186	28196	3.342E-08	1.830E-06
6	5.481E-08	1.756E-06	27604	28192	2.669E-08	1.496E-06
7	1.008E-06	9.697E-06	12994	13075	4.798E-08	1.828E-06
8	7.256E-08	2.506E-06	27834	27905	2.054E-08	1.384E-06
9	3.391E-08	1.609E-06	28155	28191	3.276E-08	1.577E-06
10	1.507E-07	2.576E-06	27980	28125	2.358E-08	1.729E-06
11	2.249E-07	3.866E-06	28031	28050	2.167E-07	3.493E-06
12	6.518E-07	6.128E-06	27783	28194	7.335E-08	2.913E-06
13	4.562E-07	5.837E-06	26494	26702	3.483E-07	5.163E-06
14	1.157E-07	3.115E-06	27599	28184	2.300E-08	1.939E-06
15	1.806E-07	3.531E-06	26427	28132	1.786E-07	3.339E-06
16	6.373E-08	2.374E-06	26840	28198	6.035E-08	2.359E-06
17	1.503E-07	3.063E-06	25060	28132	4.038E-08	2.031E-06
18	2.856E-08	1.913E-06	24222	28198	2.293E-08	1.863E-06
19	1.365E-07	2.714E-06	23085	28180	1.533E-08	1.830E-06
20	3.836E-08	2.348E-06	24117	28089	3.520E-08	2.228E-06
21	2.223E-07	3.972E-06	27466	28170	8.780E-08	3.175E-06
22	5.255E-08	2.643E-06	22411	26612	4.644E-08	2.565E-06
23	2.937E-08	2.027E-06	16367	28198	2.270E-08	1.926E-06
24	2.003E-07	3.435E-06	21574	28132	3.742E-08	2.078E-06
25	4.711E-08	2.437E-06	21661	28142	2.539E-08	2.219E-06
26	1.039E-07	3.526E-06	27035	28166	6.389E-08	2.904E-06
27	6.513E-07	8.146E-06	28013	28132	1.265E-07	4.581E-06
28	1.565E-07	3.773E-06	27409	28169	1.013E-07	3.613E-06
29	2.392E-07	5.183E-06	27714	28198	1.506E-07	4.313E-06
30	2.472E-07	4.801E-06	26740	28153	2.153E-07	4.572E-06
31	4.735E-07	7.022E-06	20002	21469	4.448E-07	6.686E-06

Table B.21 September 1981 X-ray daily mean and background values
Time of end of first day (sec of yr) = 21081600.
All daily average and background flux in units of W m^{-2}.

	— Daily Average —		Number of Values		— Background —	
Day	Short (0.5-4Å)	Long (1-8Å)	Short (0.5-4Å)	Long (1-8Å)	Short (0.5-4Å)	Long (1-8Å)
1	6.575E-08	2.425E-06	21945	27665	5.837E-08	2.431E-06
2	1.926E-08	1.773E-06	23613	27529	1.405E-08	1.684E-06
3	2.575E-07	3.403E-06	27003	27380	3.270E-08	1.962E-06
4	4.835E-08	2.605E-06	24928	27324	2.835E-08	2.087E-06
5	2.571E-07	4.693E-06	19364	19364	6.940E-08	3.064E-06
6	2.051E-08	1.984E-06	1	1	0.000E+00	0.000E+00
7	2.051E-08	1.984E-06	1	1	0.000E+00	0.000E+00
8	1.380E-07	3.437E-06	11573	12241	5.715E-08	2.359E-06
9	1.591E-07	3.233E-06	26565	26916	1.211E-07	2.971E-06
10	2.347E-07	3.573E-06	26702	27020	8.131E-08	2.648E-06
11	1.758E-07	3.639E-06	26834	23938	1.516E-07	3.551E-06
12	8.269E-08	3.084E-06	26767	26907	7.789E-08	3.038E-06
13	2.273E-07	3.791E-06	25847	26865	3.276E-08	1.988E-06
14	6.728E-08	2.513E-06	24047	25759	4.728E-08	2.199E-06
15	4.017E-07	4.941E-06	26637	26879	4.726E-08	2.211E-06
16	5.039E-08	2.224E-06	26687	26821	3.608E-08	2.074E-06
17	5.609E-08	2.208E-06	26687	26763	2.023E-08	1.667E-06
18	2.505E-08	1.543E-06	26824	26830	2.061E-08	1.382E-06
19	1.465E-07	2.533E-06	26674	26693	1.886E-08	1.346E-06
20	1.256E-08	1.098E-06	26691	26704	1.137E-08	1.064E-06
21	2.322E-08	1.328E-06	26711	26746	2.348E-08	1.205E-06
22	4.357E-08	1.303E-06	26736	26741	7.723E-09	8.988E-07
23	1.716E-08	1.004E-06	12495	12498	1.314E-08	8.889E-07
24	2.345E-08	1.617E-06	3227	3227	2.345E-08	1.617E-06
25	1.005E-08	1.158E-06	26710	26717	1.009E-08	1.162E-06
26	1.495E-07	2.524E-06	15509	15524	1.302E-07	2.339E-06
27	1.495E-08	1.365E-06	26850	26855	1.158E-08	1.275E-06
28	2.130E-08	1.410E-06	26678	26682	1.555E-08	1.339E-06
29	6.659E-08	2.098E-06	26197	26449	2.035E-08	1.542E-06
30	2.935E-08	1.815E-06	26871	26880	2.185E-08	1.731E-06

Table B.22 October 1981 X-ray daily mean and background values
Time of end of first day (sec of yr) = 23673600.
All daily average and background flux in units of W m^{-2}.

	— Daily Average —		Number of Values		— Background —	
Day	Short (0.5-4Å)	Long (1-8Å)	Short (0.5-4Å)	Long (1-8Å)	Short (0.5-4Å)	Long (1-8Å)
1	8.097E-09	1.817E-06	4033	4600	8.097E-09	1.817E-06
2	1.872E-08	1.601E-06	3446	3446	1.872E-08	1.601E-06
3	6.787E-08	2.092E-06	28747	28800	2.944E-08	1.651E-06
4	8.167E-08	2.242E-06	28353	28800	7.476E-08	2.210E-06
5	9.304E-08	1.890E-06	28753	28776	1.610E-08	1.108E-06
6	2.108E-08	1.327E-06	26972	26976	1.711E-08	1.236E-06
7	2.411E-06	1.054E-05	26941	27018	1.064E-07	2.675E-06
8	3.793E-07	5.131E-06	26486	26714	1.099E-07	3.838E-06
9	3.032E-08	1.452E-06	26092	26098	2.815E-08	1.414E-06
10	2.297E-07	3.577E-06	27164	27188	2.016E-07	3.265E-06
11	1.124E-07	2.737E-06	27322	27322	1.035E-07	2.661E-06
12	2.747E-06	1.228E-05	27405	27405	2.515E-06	1.144E-05
13	3.391E-07	4.557E-06	27603	27604	1.061E-07	3.613E-06
14	7.689E-07	6.165E-06	27711	27730	1.832E-07	4.148E-06
15	2.279E-07	3.691E-06	28196	28198	1.321E-07	3.478E-06
16	3.003E-07	3.739E-06	28192	28192	2.192E-07	3.028E-06
17	2.009E-07	3.214E-06	28148	28173	1.250E-07	2.489E-06
18	4.592E-07	2.937E-06	28198	28198	8.509E-08	1.465E-06
19	1.110E-07	1.431E-06	26058	28098	5.583E-08	8.752E-07
20	1.076E-07	3.282E-06	27240	28166	9.134E-08	3.103E-06
21	1.052E-07	2.332E-06	27778	27780	9.752E-08	2.323E-06
22	3.884E-08	1.291E-06	26999	27002	2.885E-08	1.030E-06
23	2.450E-08	1.508E-06	13464	13465	8.354E-09	1.081E-06
24	1.677E-07	2.956E-06	27178	28173	1.201E-08	1.599E-06
25	4.411E-08	1.946E-06	27495	27809	1.841E-08	1.392E-06
26	1.643E-08	1.183E-06	28184	28196	1.337E-08	1.079E-06
27	2.821E-08	1.167E-06	28143	28152	2.558E-08	1.122E-06
28	3.427E-08	1.534E-06	28126	28186	1.066E-08	1.206E-06
29	2.107E-08	1.303E-06	28189	28194	1.856E-08	1.285E-06
30	1.487E-08	1.220E-06	28166	28168	1.249E-08	1.140E-06
31	1.569E-07	2.658E-06	28141	28176	1.873E-08	1.198E-06

Table B.23 November 1981 X-ray daily mean and background values
Time of end of first day (sec of yr) = 26352000.
All daily average and background flux in units of W m^{-2}.

	— Daily Average —		Number of Values		— Background —	
Day	Short (0.5-4Å)	Long (1-8Å)	Short (0.5-4Å)	Long (1-8Å)	Short (0.5-4Å)	Long (1-8Å)
1	5.981E-08	1.657E-06	28156	28198	5.251E-08	1.522E-06
2	3.768E-08	1.614E-06	28191	28194	2.425E-08	1.418E-06
3	1.732E-07	2.730E-06	9767	9767	1.319E-07	2.333E-06
4	1.328E-08	2.020E-06	1	1	0.000E+00	0.000E+00
5	1.368E-08	2.020E-06	1	1	0.000E+00	0.000E+00
6	1.247E-08	2.020E-06	1	1	0.000E+00	0.000E+00
7	1.207E-08	1.984E-06	1	1	0.000E+00	0.000E+00
8	6.646E-08	2.509E-06	8549	11427	8.040E-09	1.619E-06
9	3.054E-07	4.745E-06	25904	28192	9.989E-08	3.099E-06
10	8.351E-08	2.538E-06	27095	28168	3.814E-08	1.861E-06
11	7.550E-08	2.072E-06	28168	28168	6.201E-08	2.022E-06
12	5.924E-07	5.903E-06	28198	28198	3.345E-07	5.217E-06
13	2.387E-07	3.740E-06	27327	28149	2.245E-07	3.157E-06
14	3.484E-07	5.095E-06	28003	28174	5.097E-08	2.246E-06
15	6.332E-08	1.911E-06	28097	28198	4.575E-08	1.849E-06
16	2.979E-08	1.370E-06	28157	28164	2.625E-08	1.317E-06
17	2.784E-08	1.241E-06	28192	28194	2.094E-08	1.167E-06
18	7.957E-08	1.978E-06	28189	28192	4.867E-08	1.561E-06
19	5.480E-08	1.536E-06	27850	27872	2.755E-08	1.316E-06
20	1.551E-08	9.353E-07	28176	28183	1.157E-08	8.755E-07
21	9.104E-08	1.854E-06	28129	28171	1.680E-08	1.248E-06
22	8.808E-08	2.364E-06	27522	27732	8.027E-08	1.776E-06
23	2.549E-08	1.334E-06	28114	28156	2.390E-08	1.257E-06
24	1.714E-08	1.018E-06	28177	28193	1.665E-08	9.738E-07
25	2.792E-08	1.171E-06	26867	26871	1.733E-08	1.079E-06
26	1.995E-08	1.088E-06	16418	16422	1.567E-08	1.204E-06
27	2.232E-08	1.507E-06	19082	19163	1.599E-08	1.403E-06
28	9.555E-08	2.097E-06	28162	28175	2.496E-08	1.412E-06
29	1.461E-07	3.305E-06	27853	28195	3.259E-08	1.904E-06
30	3.241E-08	2.003E-06	23800	27817	1.560E-08	1.752E-06

Table B.24 December 1981 X-ray daily mean and background values
Time of end of first day (sec of yr) = 28944000.
All daily average and background flux in units of W m^{-2}.

	— Daily Average —		Number of Values		— Background —	
Day	Short (0.5-4Å)	Long (1-8Å)	Short (0.5-4Å)	Long (1-8Å)	Short (0.5-4Å)	Long (1-8Å)
1	1.560E-07	3.129E-06	24217	28061	1.460E-07	3.082E-06
2	2.641E-08	1.927E-06	21691	28157	1.190E-08	1.737E-06
3	4.594E-08	2.438E-06	21820	28175	1.437E-08	2.159E-06
4	6.107E-08	2.882E-06	22456	28142	5.651E-08	2.793E-06
5	1.645E-07	3.951E-06	26298	28171	5.458E-08	3.048E-06
6	6.136E-08	2.666E-06	20576	28175	1.638E-08	2.216E-06
7	1.728E-07	3.828E-06	24606	28159	1.282E-07	3.316E-06
8	9.479E-08	3.398E-06	27426	27867	7.087E-08	3.150E-06
9	4.705E-07	6.084E-06	26923	28192	5.143E-08	2.957E-06
10	5.406E-08	2.450E-06	24348	28196	3.839E-08	2.235E-06
11	2.620E-08	2.003E-06	25156	28178	1.970E-08	1.968E-06
12	3.430E-07	5.218E-06	25750	28165	6.689E-08	3.002E-06
13	5.349E-08	1.939E-06	26371	28151	4.492E-08	1.834E-06
14	1.263E-08	1.388E-06	26717	27649	1.207E-08	1.280E-06
15	9.050E-08	2.102E-06	28099	28136	9.020E-08	1.804E-06
16	2.967E-08	1.370E-06	27982	28198	9.222E-09	9.693E-07
17	1.785E-08	9.931E-07	28131	28141	1.024E-08	8.918E-07
18	6.604E-09	6.616E-07	28017	28066	6.328E-09	6.323E-07
19	7.884E-08	1.196E-06	27588	28072	3.259E-09	4.858E-07
20	4.891E-09	5.264E-07	28013	28132	4.254E-09	5.223E-07
21	5.725E-09	5.696E-07	22455	22488	4.154E-09	5.696E-07
22	5.169E-09	5.528E-07	27884	27919	5.031E-09	5.431E-07
23	7.245E-09	7.087E-07	28165	28183	5.806E-09	6.189E-07
24	1.372E-08	8.190E-07	25796	25807	6.881E-09	6.684E-07
25	1.317E-08	8.887E-07	28182	28197	8.462E-09	7.673E-07
26	9.411E-08	1.787E-06	28113	28133	8.359E-09	8.186E-07
27	4.589E-08	2.159E-06	27740	28198	2.386E-08	1.743E-06
28	8.805E-08	2.800E-06	28036	28185	6.076E-08	2.296E-06
29	1.559E-08	1.423E-06	27971	28102	9.365E-09	1.113E-06
30	1.852E-08	1.235E-06	27756	28198	9.704E-09	1.071E-06
31	1.281E-08	1.171E-06	17759	17780	1.048E-08	1.170E-06

Table B.25 January 1982 X-ray daily mean and background values
Time of end of first day (sec of yr) = 172800.
All daily average and background flux in units of W m^{-2}.

	— Daily Average —		Number of Values		— Background —	
Day	Short (0.5-4Å)	Long (1-8Å)	Short (0.5-4Å)	Long (1-8Å)	Short (0.5-4Å)	Long (1-8Å)
1	0.000E+00	0.000E+00	0	0	0.000E+00	0.000E+00
2	3.898E-07	3.728E-06	28099	28168	1.294E-08	1.296E-06
3	6.481E-08	1.819E-06	27957	28194	3.240E-08	1.515E-06
4	1.419E-08	1.010E-06	28034	28175	1.320E-08	9.987E-07
5	8.482E-09	7.865E-07	28182	28198	8.069E-09	7.572E-07
6	1.427E-08	9.426E-07	28157	28191	8.172E-09	7.868E-07
7	2.424E-08	1.067E-06	28190	28193	2.381E-08	1.036E-06
8	8.153E-08	1.519E-06	28147	28161	3.308E-08	1.110E-06
9	2.136E-07	3.326E-06	28086	28159	2.018E-07	3.093E-06
10	3.421E-08	1.294E-06	28168	28173	1.600E-08	1.052E-06
11	3.314E-08	1.237E-06	28193	28198	1.630E-08	1 054E-06
12	1.031E-08	7.339E-07	28191	28196	9.272E-09	7.251E-07
13	4.185E-08	1.009E-06	28152	28171	6.938E-09	5.974E-07
14	6.632E-09	5.381E-07	27904	27927	6.418E-09	5.298E-07
15	1.788E-08	9.891E-07	28099	28104	1.696E-08	9.598E-07
16	1.001E-07	1.668E-06	28079	28107	1.766E-08	9.196E-07
17	1.254E-08	8.026E-07	22697	22711	9.113E-09	7.963E-07
18	2.950E-08	1.404E-06	28146	28151	2.627E-08	1.281E-06
19	4.989E-08	1.631E-06	28170	28170	3.679E-08	1.505E-06
20	2.433E-08	1.223E-06	28189	28196	2.429E-08	1.200E-06
21	3.021E-08	1.501E-06	27923	27946	1.852E-08	1.263E-06
22	5.343E-08	1.518E-06	28155	28164	1.739E-08	1.253E-06
23	1.060E-07	2.090E-06	28085	28146	1.540E-08	1.194E-06
24	2.222E-07	2.790E-06	26340	26928	3.991E-08	1.617E-06
25	3.797E-08	1.987E-06	6357	6360	3.797E-08	1.987E-06
26	3.357E-08	1.914E-06	26720	28033	3.178E-08	1.806E-06
27	4.609E-08	2.284E-06	25655	28187	1.749E-08	2.073E-06
28	3.357E-07	4.984E-06	27255	28190	1.024E-07	3.775E-06
29	1.094E-07	3.787E-06	28152	28189	1.059E-07	3.645E-06
30	5.375E-07	6.560E-06	27918	28173	3.682E-07	5.705E-06
31	4.136E-07	6.809E-06	28183	28192	3.556E-07	5.794E-06

Table B.26 February 1982 X-ray daily mean and background values
Time of end of first day (sec of yr) = 2764800.
All daily average and background flux in units of W m^{-2}.

	— Daily Average —		Number of Values		— Background —	
Day	Short (0.5-4Å)	Long (1-8Å)	Short (0.5-4Å)	Long (1-8Å)	Short (0.5-4Å)	Long (1-8Å)
1	1.014E-06	9.110E-06	27278	28194	1.695E-07	4.468E-06
2	1.071E-07	3.918E-06	9771	9771	2.843E-08	2.776E-06
3	1.126E-07	4.256E-06	1	1	0.000E+00	0.000E+00
4	1.126E-07	4.292E-06	1	1	0.000E+00	0.000E+00
5	1.114E-07	4.256E-06	1	1	0.000E+00	0.000E+00
6	1.122E-07	4.292E-06	1	1	0.000E+00	0.000E+00
7	5.201E-07	4.849E-06	18772	21220	1.487E-07	3.287E-06
8	4.226E-07	5.746E-06	24016	25741	1.569E-07	4.578E-06
9	8.366E-07	6.092E-06	23688	27861	7.275E-07	5.762E-06
10	2.620E-07	4.819E-06	27395	27685	8.929E-08	3.494E-06
11	7.711E-08	2.846E-06	24849	28040	7.193E-08	2.673E-06
12	1.584E-07	2.866E-06	26938	27907	1.898E-08	1.390E-06
13	1.287E-07	2.618E-06	25735	28169	2.417E-08	1.534E-06
14	7.854E-08	2.043E-06	22378	22593	6.790E-08	1.520E-06
15	2.749E-08	1.367E-06	28136	28196	1.366E-08	1.114E-06
16	4.185E-08	1.513E-06	28176	28177	2.077E-08	1.366E-06
17	5.508E-08	1.387E-06	28058	28062	3.498E-08	1.114E-06
18	9.612E-08	1.596E-06	27772	27831	4.220E-08	1.222E-06
19	8.434E-08	1.904E-06	27936	27945	3.474E-08	1.464E-06
20	2.317E-07	3.215E-06	27837	28172	1.873E-07	2.959E-06
21	2.098E-08	1.062E-06	28095	28180	1.481E-08	9.907E-07
22	1.887E-08	1.091E-06	28181	28192	1.257E-08	9.820E-07
23	4.728E-08	1.942E-06	26369	28198	3.503E-08	1.580E-06
24	1.088E-07	2.733E-06	24307	28173	5.365E-08	2.200E-06
25	3.385E-08	1.841E-06	27712	28051	1.980E-08	1.417E-06
26	8.526E-08	2.427E-06	27498	27753	2.834E-08	1.756E-06
27	1.170E-07	2.839E-06	24152	27583	3.410E-08	2.321E-06
28	5.607E-08	2.288E-06	26486	27486	3.444E-08	2.058E-06

Table B.27 March 1982 X-ray daily mean and background values
Time of end of first day (sec of yr) = 5184000.
All daily average and background flux in units of W m^{-2}.

	— Daily Average —		Number of Values		— Background —	
Day	Short (0.5-4Å)	Long (1-8Å)	Short (0.5-4Å)	Long (1-8Å)	Short (0.5-4Å)	Long (1-8Å)
1	1.703E-08	1.692E-06	26267	27377	1.680E-08	1.667E-06
2	3.339E-08	1.830E-06	26794	27259	2.305E-08	1.566E-06
3	3.185E-08	1.752E-06	26527	27230	2.155E-08	1.710E-06
4	2.827E-08	2.069E-06	24664	27169	2.120E-08	1.988E-06
5	1.739E-07	3.711E-06	24483	26740	7.203E-08	2.777E-06
6	1.385E-07	2.938E-06	25564	26989	4.483E-08	1.937E-06
7	1.021E-06	7.886E-06	25454	26995	8.370E-08	3.058E-06
8	3.327E-07	4.409E-06	18106	20056	1.000E-07	3.577E-06
9	2.962E-08	1.712E-06	26045	26886	1.575E-08	1.504E-06
10	9.153E-08	2.308E-06	23132	23148	2.134E-08	1.488E-06
11	1.662E-08	1.432E-06	26739	26845	1.547E-08	1.401E-06
12	1.267E-08	1.332E-06	25660	25776	1.105E-08	1.292E-06
13	2.412E-08	1.539E-06	26739	26744	1.984E-08	1.515E-06
14	3.798E-08	2.128E-06	26241	26246	3.372E-08	2.016E-06
15	4.540E-08	1.920E-06	26373	26373	2.512E-08	1.668E-06
16	7.494E-08	2.889E-06	25680	26224	3.865E-08	2.309E-06
17	3.808E-08	2.034E-06	26015	26771	2.632E-08	1.854E-06
18	7.637E-08	2.381E-06	26176	26374	5.345E-08	2.085E-06
19	1.677E-07	3.101E-06	26724	26738	1.584E-07	3.072E-06
20	1.472E-07	2.705E-06	26278	26320	1.836E-08	1.322E-06
21	3.977E-08	1.974E-06	25955	26216	3.855E-08	1.939E-06
22	6.890E-08	2.501E-06	25066	25600	6.429E-08	2.360E-06
23	5.672E-08	2.418E-06	25794	26792	5.052E-08	2.422E-06
24	1.130E-07	2.589E-06	26268	26748	5.215E-08	2.118E-06
25	6.297E-08	1.773E-06	26316	26353	2.164E-08	1.312E-06
26	3.309E-08	1.388E-06	26810	26817	1.987E-08	1.296E-06
27	3.776E-07	4.883E-06	26680	26764	3.280E-07	4.208E-06
28	4.927E-08	1.844E-06	26646	26873	3.382E-08	1.460E-06
29	4.170E-08	1.953E-06	26818	26943	4.070E-08	1.589E-06
30	1.014E-06	7.627E-06	26702	26838	1.580E-07	3.748E-06
31	2.435E-07	4.074E-06	26657	26667	2.017E-07	3.540E-06

Table B.28 April 1982 X-ray daily mean and background values
Time of end of first day (sec of yr) = 7862400.
All daily average and background flux in units of W m^{-2}.

	— Daily Average —		Number of Values		— Background —	
Day	Short (0.5-4Å)	Long (1-8Å)	Short (0.5-4Å)	Long (1-8Å)	Short (0.5-4Å)	Long (1-8Å)
1	1.177E-07	2.624E-06	26160	27053	8.724E-08	2.416E-06
2	1.126E-07	2.268E-06	26008	26044	1.845E-08	1.515E-06
3	1.308E-07	2.585E-06	27068	27103	5.358E-08	1.821E-06
4	3.918E-08	1.806E-06	25807	27173	2.940E-08	1.660E-06
5	7.899E-08	2.790E-06	27075	27220	6.593E-08	2.173E-06
6	1.165E-08	1.195E-06	26901	27322	9.190E-09	1.181E-06
7	1.967E-08	1.449E-06	27376	27430	1.711E-08	1.351E-06
8	9.521E-09	9.872E-07	27358	27405	9.279E-09	9.467E-07
9	2.873E-08	1.449E-06	27440	27528	2.645E-08	1.289E-06
10	1.117E-07	2.376E-06	27799	27815	2.074E-08	1.384E-06
11	5.679E-08	2.029E-06	28059	28122	4.289E-08	1.904E-06
12	3.244E-08	1.721E-06	27992	28165	1.686E-08	1.501E-06
13	1.388E-08	1.054E-06	28050	28114	1.013E-08	1.031E-06
14	4.752E-08	1.799E-06	28134	28161	1.203E-08	1.094E-06
15	1.659E-08	9.016E-07	28072	28097	1.384E-08	8.359E-07
16	1.805E-08	7.485E-07	27902	28102	1.010E-08	7.386E-07
17	9.241E-08	1.623E-06	28120	28146	7.653E-09	7.060E-07
18	1.458E-08	8.518E-07	28125	28141	7.357E-09	7.601E-07
19	4.468E-08	1.177E-06	27924	27992	3.315E-08	1.159E-06
20	4.692E-09	5.669E-07	28094	28167	4.276E-09	5.651E-07
21	7.200E-09	6.762E-07	27898	28159	5.445E-09	6.433E-07
22	1.099E-07	2.169E-06	27844	28174	1.570E-08	1.091E-06
23	2.242E-08	1.305E-06	28021	28028	1.850E-08	1.196E-06
24	9.203E-08	1.764E-06	28055	28082	1.539E-08	1.062E-06
25	1.273E-08	9.845E-07	28146	28152	9.798E-09	9.789E-07
26	7.677E-09	7.450E-07	27972	27990	6.265E-09	7.216E-07
27	1.275E-08	8.796E-07	28131	28177	1.040E-08	8.729E-07
28	1.247E-08	9.224E-07	28076	28118	1.164E-08	9.009E-07
29	2.839E-08	1.235E-06	28126	28139	1.361E-08	1.007E-06
30	1.308E-08	9.195E-07	27792	28180	1.154E-08	8.769E-07

Table B.29 May 1982 X-ray daily mean and background values
Time of end of first day (sec of yr) = 10454400.
All daily average and background flux in units of W m^{-2}.

	— Daily Average —		Number of Values		— Background —	
Day	Short (0.5-4Å)	Long (1-8Å)	Short (0.5-4Å)	Long (1-8Å)	Short (0.5-4Å)	Long (1-8Å)
1	1.384E-07	2.194E-06	27990	28121	1.248E-08	9.193E-07
2	3.944E-08	1.158E-06	27347	28176	1.321E-08	9.057E-07
3	3.282E-08	1.231E-06	26450	26625	1.783E-08	1.017E-06
4	2.452E-08	8.636E-07	25350	28177	4.496E-09	5.007E-07
5	5.798E-09	5.217E-07	26359	28100	5.624E-09	4.994E-07
6	9.570E-09	7.278E-07	26881	28141	6.048E-09	7.115E-07
7	1.341E-08	6.767E-07	27516	28087	9.355E-09	6.503E-07
8	8.890E-08	1.416E-06	27881	28132	7.467E-09	6.364E-07
9	1.539E-08	6.712E-07	28131	28160	5.405E-09	5.184E-07
10	1.264E-08	7.144E-07	28090	28113	5.952E-09	5.343E-07
11	4.921E-09	4.548E-07	28057	28103	4.898E-09	4.489E-07
12	1.911E-08	6.658E-07	28000	28047	4.118E-09	4.353E-07
13	9.901E-09	7.102E-07	8347	8354	9.901E-09	7.102E-07
14	5.380E-09	5.780E-07	8482	8498	5.380E-09	5.780E-07
15	1.964E-07	2.335E-06	26313	26538	2.655E-09	3.987E-07
16	1.750E-08	8.604E-07	27639	27685	7.111E-09	6.472E-07
17	1.479E-08	8.843E-07	28086	28109	1.300E-08	8.714E-07
18	1.247E-07	1.753E-06	27334	27346	4.757E-08	1.279E-06
19	4.414E-08	1.392E-06	28170	28173	1.320E-08	9.244E-07
20	1.522E-07	2.158E-06	28127	28131	4.475E-08	1.520E-06
21	1.538E-07	2.785E-06	27973	28133	8.589E-08	2.112E-06
22	2.932E-07	3.713E-06	28087	28151	3.092E-08	1.211E-06
23	4.793E-08	1.293E-06	28052	28057	2.758E-08	1.054E-06
24	1.194E-08	8.088E-07	28168	28180	1.001E-08	7.033E-07
25	1.564E-08	8.500E-07	27903	27914	1.370E-08	8.093E-07
26	4.061E-08	1.639E-06	27943	27946	3.812E-08	1.565E-06
27	5.056E-08	2.111E-06	27633	27633	3.988E-08	1.856E-06
28	1.455E-07	2.818E-06	27424	27424	1.136E-07	2.547E-06
29	8.184E-07	7.841E-06	28089	28174	1.161E-07	3.727E-06
30	3.390E-07	3.461E-06	27797	28192	1.772E-07	2.379E-06
31	4.124E-08	1.217E-06	27388	27916	1.174E-08	8.390E-07

Table B.30 June 1982 X-ray daily mean and background values
Time of end of first day (sec of yr) = 13132800.
All daily average and background flux in units of W m^{-2}.

	— Daily Average —		Number of Values		— Background —	
Day	Short (0.5-4Å)	Long (1-8Å)	Short (0.5-4Å)	Long (1-8Å)	Short (0.5-4Å)	Long (1-8Å)
1	3.704E-08	1.204E-06	27528	27631	2.535E-08	1.108E-06
2	2.852E-07	2.618E-06	28198	28198	1.168E-07	2.164E-06
3	1.470E-06	8.042E-06	27413	27406	8.755E-08	2.073E-06
4	3.390E-06	1.861E-05	28193	28193	1.287E-06	1.091E-05
5	1.492E-06	1.139E-05	28131	28171	8.171E-07	6.816E-06
6	3.518E-06	2.079E-05	28042	28043	5.856E-07	5.422E-06
7	2.775E-07	3.745E-06	28157	28156	1.522E-07	2.617E-06
8	1.083E-07	2.510E-06	28175	28174	3.989E-08	1.655E-06
9	1.942E-07	3.747E-06	28161	28161	1.611E-07	3.737E-06
10	4.124E-07	6.042E-06	28196	28196	5.635E-08	2.461E-06
11	4.649E-07	7.189E-06	28154	28154	4.251E-07	6.542E-06
12	2.573E-06	1.766E-05	28067	28106	6.091E-07	8.135E-06
13	1.763E-06	1.281E-05	28144	28143	4.578E-07	6.693E-06
14	9.492E-07	1.032E-05	28190	28190	3.729E-07	7.055E-06
15	3.263E-06	2.065E-05	27884	27885	2.160E-06	1.349E-05
16	6.554E-07	5.609E-06	28155	28155	3.997E-08	1.973E-06
17	1.713E-07	2.420E-06	28175	28177	1.035E-07	1.965E-06
18	6.542E-08	1.872E-06	28163	28164	5.839E-08	1.840E-06
19	1.638E-07	3.458E-06	27922	28161	8.881E-08	3.285E-06
20	3.074E-07	4.920E-06	28090	28122	1.194E-07	3.146E-06
21	5.584E-07	7.182E-06	28013	28169	1.713E-07	4.940E-06
22	2.813E-07	4.835E-06	27942	28165	2.421E-07	4.541E-06
23	4.363E-07	5.380E-06	25358	26131	4.181E-07	5.167E-06
24	1.285E-07	2.410E-06	25349	27868	2.385E-08	1.243E-06
25	2.661E-07	3.314E-06	26332	27782	5.340E-08	1.623E-06
26	1.003E-06	8.022E-06	25337	26998	8.200E-08	2.038E-06
27	5.837E-07	6.782E-06	26504	28187	1.035E-07	1.916E-06
28	1.450E-07	3.935E-06	28119	28152	1.201E-07	3.369E-06
29	2.113E-08	8.136E-07	25614	28132	1.465E-08	6.636E-07
30	6.263E-09	3.078E-07	21368	27981	5.813E-09	2.789E-07

Table B.31 July 1982 X-ray daily mean and background values
Time of end of first day (sec of yr) = 15724800.
All daily average and background flux in units of W m^{-2}.

	— Daily Average —		Number of Values		— Background —	
Day	Short (0.5-4Å)	Long (1-8Å)	Short (0.5-4Å)	Long (1-8Å)	Short (0.5-4Å)	Long (1-8Å)
1	8.391E-09	2.925E-07	20197	27984	8.347E-09	2.590E-07
2	5.742E-09	2.657E-07	20013	28136	5.317E-09	2.479E-07
3	1.129E-07	1.212E-06	23450	28140	1.945E-08	4.699E-07
4	6.358E-08	1.003E-06	24174	28105	4.846E-09	4.200E-07
5	5.554E-09	3.323E-07	12263	15078	3.533E-09	3.297E-07
6	3.099E-08	8.420E-07	15772	16492	8.390E-09	4.485E-07
7	3.185E-08	1.197E-06	26843	28800	2.148E-08	1.020E-06
8	1.019E-07	2.392E-06	28600	28800	3.875E-08	1.726E-06
9	5.558E-07	5.976E-06	28761	28800	1.124E-07	2.669E-06
10	3.947E-06	2.631E-05	28492	28539	3.738E-07	7.118E-06
11	6.071E-07	7.414E-06	28184	28186	3.521E-07	5.379E-06
12	9.184E-06	5.218E-05	28189	28189	7.984E-07	1.115E-05
13	3.397E-07	6.358E-06	27954	28189	2.362E-07	5.518E-06
14	6.355E-07	9.167E-06	25419	25454	6.740E-07	9.302E-06
15	5.699E-07	8.480E-06	24772	24779	2.163E-07	4.954E-06
16	2.154E-07	4.667E-06	24051	24146	1.613E-07	4.280E-06
17	1.233E-06	1.226E-05	28073	28134	8.113E-07	9.980E-06
18	1.582E-07	4.212E-06	28158	28172	1.148E-07	3.834E-06
19	1.512E-06	1.556E-05	28136	28136	6.320E-07	1.071E-05
20	4.985E-07	8.197E-06	27879	27949	4.359E-07	7.558E-06
21	3.808E-07	5.532E-06	27051	28155	1.774E-07	4.081E-06
22	3.687E-07	5.802E-06	26666	28122	6.140E-08	2.235E-06
23	3.203E-08	1.711E-06	24548	28060	2.716E-08	1.666E-06
24	1.150E-07	1.601E-06	22498	28081	1.298E-08	8.497E-07
25	4.528E-08	1.165E-06	23852	28055	4.031E-08	1.034E-06
26	2.139E-08	4.276E-07	20375	28059	1.720E-08	4.229E-07
27	1.849E-08	2.323E-07	16680	27860	1.456E-08	2.203E-07
28	1.077E-08	2.531E-07	17330	27868	9.336E-09	1.847E-07
29	1.265E-08	2.110E-07	17847	27784	1.092E-08	1.976E-07
30	1.585E-08	4.611E-07	20470	27579	1.255E-08	3.472E-07
31	1.042E-07	1.575E-06	25533	27363	1.859E-08	8.691E-07

Table B.32 August 1982 X-ray daily mean and background values
Time of end of first day (sec of yr) = 18403200.
All daily average and background flux in units of W m^{-2}.

	— Daily Average —		Number of Values		— Background —	
Day	Short (0.5-4Å)	Long (1-8Å)	Short (0.5-4Å)	Long (1-8Å)	Short (0.5-4Å)	Long (1-8Å)
1	5.364E-08	1.116E-06	22728	27313	2.215E-08	8.626E-07
2	1.607E-07	2.518E-06	25551	26483	9.636E-08	2.069E-06
3	8.550E-08	2.252E-06	26147	26974	6.140E-08	1.728E-06
4	6.415E-08	2.046E-06	25920	26298	6.077E-08	2.013E-06
5	5.694E-08	1.585E-06	20438	21119	6.008E-08	1.431E-06
6	4.946E-08	2.015E-06	25106	26161	4.912E-08	1.875E-06
7	1.936E-07	3.520E-06	23814	25827	1.940E-07	3.605E-06
8	2.584E-07	3.932E-06	18697	19674	9.779E-08	2.705E-06
9	7.492E-08	2.004E-06	24855	26258	1.709E-08	1.397E-06
10	1.035E-07	2.481E-06	15789	17001	8.807E-08	2.243E-06
11	4.214E-08	1.614E-06	19714	21562	1.731E-08	1.378E-06
12	2.505E-08	1.260E-06	26575	28147	2.361E-08	1.247E-06
13	3.981E-08	1.268E-06	26855	28196	3.723E-08	1.256E-06
14	1.459E-07	2.462E-06	27292	28174	1.943E-08	1.333E-06
15	1.894E-08	1.246E-06	26763	28190	1.844E-08	1.223E-06
16	2.147E-08	1.224E-06	27700	28198	1.652E-08	1.206E-06
17	3.065E-08	1.333E-06	27611	28140	2.333E-08	1.267E-06
18	5.856E-08	1.811E-06	28074	28192	5.538E-08	1.723E-06
19	3.474E-08	1.362E-06	27490	28191	3.143E-08	1.355E-06
20	1.547E-08	8.224E-07	26219	27858	1.489E-08	8.162E-07
21	1.014E-07	1.698E-06	27410	28071	2.384E-08	1.009E-06
22	1.875E-08	7.464E-07	19091	20763	1.358E-08	6.396E-07
23	1.192E-08	6.057E-07	9485	10748	1.007E-08	5.416E-07
24	1.120E-08	4.433E-07	22039	28198	1.019E-08	4.176E-07
25	1.357E-08	6.195E-07	23573	28026	1.055E-08	5.772E-07
26	3.589E-08	9.656E-07	25213	28187	1.287E-08	6.626E-07
27	1.034E-07	1.821E-06	27449	28085	8.097E-08	1.675E-06
28	9.411E-08	1.892E-06	26376	27693	1.474E-08	1.099E-06
29	3.319E-08	1.427E-06	25631	27639	1.047E-08	1.070E-06
30	2.596E-08	1.381E-06	24135	26496	1.858E-08	1.343E-06
31	1.544E-07	3.960E-06	19256	19440	5.097E-08	2.509E-06

Table B.33 September 1982 X-ray daily mean and background values
Time of end of first day (sec of yr) = 21081600.
All daily average and background flux in units of W m^{-2}.

	— Daily Average —		Number of Values		— Background —	
Day	Short (0.5-4Å)	Long (1-8Å)	Short (0.5-4Å)	Long (1-8Å)	Short (0.5-4Å)	Long (1-8Å)
1	2.813E-07	5.071E-06	26781	27424	1.431E-07	3.265E-06
2	4.142E-08	1.651E-06	25573	27370	3.413E-08	1.608E-06
3	2.067E-08	1.327E-06	27181	27288	1.924E-08	1.183E-06
4	8.343E-07	1.138E-05	27144	27190	1.354E-07	5.088E-06
5	3.630E-08	1.648E-06	26827	27137	1.591E-08	1.391E-06
6	8.658E-09	1.022E-06	25007	25100	7.652E-09	9.735E-07
7	2.040E-08	1.321E-06	24926	27053	1.090E-08	1.128E-06
8	1.730E-08	1.348E-06	27040	27049	1.365E-08	1.197E-06
9	8.334E-08	2.442E-06	26959	27012	6.781E-08	2.128E-06
10	3.190E-08	1.323E-06	26921	26940	2.825E-08	1.284E-06
11	1.048E-07	1.812E-06	25574	26879	1.551E-08	1.097E-06
12	3.793E-08	1.406E-06	26858	26914	2.217E-08	1.106E-06
13	1.638E-08	1.106E-06	24048	24054	1.519E-08	1.094E-06
14	1.445E-08	9.157E-07	26836	26851	1.092E-08	8.860E-07
15	3.499E-08	1.100E-06	26552	26566	1.746E-08	1.017E-06
16	6.505E-09	6.614E-07	26361	26380	5.592E-09	6.363E-07
17	9.327E-09	6.791E-07	26526	26573	5.443E-09	5.959E-07
18	8.461E-08	1.335E-06	26603	26698	5.464E-09	6.257E-07
19	5.496E-08	1.623E-06	26755	26800	4.273E-08	1.563E-06
20	6.858E-09	6.437E-07	24842	26787	5.792E-09	6.338E-07
21	7.417E-09	6.607E-07	25584	26089	6.798E-09	6.309E-07
22	1.441E-08	8.173E-07	25285	26549	1.064E-08	7.900E-07
23	1.314E-08	9.125E-07	20558	26808	1.315E-08	9.136E-07
24	1.488E-08	1.200E-06	26792	26801	1.475E-08	1.154E-06
25	9.393E-08	1.858E-06	26440	26793	1.026E-08	1.038E-06
26	6.193E-08	1.932E-06	26760	26774	4.590E-08	1.865E-06
27	2.808E-08	1.274E-06	26513	26833	2.012E-08	1.149E-06
28	1.743E-08	1.073E-06	26861	26865	1.131E-08	8.957E-07
29	4.479E-08	1.419E-06	26879	26884	4.227E-08	1.366E-06
30	9.626E-08	1.758E-06	26866	26872	4.986E-08	1.415E-06

Table B.34 October 1982 X-ray daily mean and background values
Time of end of first day (sec of yr) = 23673600.
All daily average and background flux in units of W m^{-2}.

	— Daily Average —		Number of Values		— Background —	
Day	Short (0.5-4Å)	Long (1-8Å)	Short (0.5-4Å)	Long (1-8Å)	Short (0.5-4Å)	Long (1-8Å)
1	1.727E-08	1.214E-06	26923	26940	1.560E-08	1.142E-06
2	1.490E-07	2.581E-06	26926	26966	1.917E-08	1.285E-06
3	1.729E-08	1.218E-06	26735	26739	1.098E-08	1.101E-06
4	3.972E-08	1.408E-06	27024	27023	3.105E-08	1.274E-06
5	5.564E-08	2.224E-06	27048	27071	2.537E-08	1.644E-06
6	4.933E-08	1.342E-06	27138	27147	9.883E-09	9.356E-07
7	2.122E-08	8.753E-07	27139	27173	1.080E-08	8.555E-07
8	7.207E-09	7.024E-07	26028	26544	4.910E-09	6.001E-07
9	8.495E-08	1.317E-06	26865	26979	4.428E-09	4.624E-07
10	6.187E-09	5.048E-07	26999	27040	5.485E-09	4.656E-07
11	8.050E-09	5.146E-07	26834	26859	8.057E-09	5.077E-07
12	4.988E-09	4.110E-07	26237	26885	3.627E-09	4.101E-07
13	5.384E-09	4.737E-07	27130	27515	5.143E-09	4.243E-07
14	7.540E-09	4.066E-07	25533	27282	5.973E-09	3.788E-07
15	1.224E-08	4.413E-07	25285	26695	9.832E-09	4.260E-07
16	7.606E-08	9.797E-07	25994	27486	1.559E-08	4.241E-07
17	5.084E-09	4.656E-07	27734	27782	5.047E-09	4.599E-07
18	1.368E-08	6.982E-07	27348	27429	1.251E-08	6.813E-07
19	1.860E-08	7.849E-07	26534	26954	1.685E-08	7.667E-07
20	1.118E-08	8.067E-07	27278	27320	1.062E-08	7.979E-07
21	3.674E-08	1.423E-06	27381	27439	3.193E-08	1.354E-06
22	2.756E-08	1.320E-06	26723	26750	1.460E-08	9.916E-07
23	1.350E-07	2.332E-06	26614	26669	7.496E-08	1.676E-06
24	7.005E-08	1.785E-06	19572	19572	2.729E-08	2.112E-06
25	3.026E-07	3.911E-06	6982	7015	3.026E-07	3.911E-06
26	2.794E-08	1.455E-06	28186	28189	1.405E-08	1.043E-06
27	1.152E-07	1.923E-06	28125	28128	1.474E-08	1.057E-06
28	1.782E-08	1.094E-06	28165	28166	1.679E-08	1.045E-06
29	3.510E-08	1.399E-06	28139	28146	3.437E-08	1.193E-06
30	7.748E-09	9.122E-07	5342	5345	7.748E-09	9.122E-07
31	0.000E+00	0.000E+00	0	0	0.000E+00	0.000E+00

Table B.35 November 1982 X-ray daily mean and background values
Time of end of first day (sec of yr) = 26352000.
All daily average and background flux in units of W m^{-2}.

	— Daily Average —		Number of Values		— Background —	
Day	Short (0.5-4Å)	Long (1-8Å)	Short (0.5-4Å)	Long (1-8Å)	Short (0.5-4Å)	Long (1-8Å)
1	2.910E-08	1.374E-06	27035	27725	1.668E-08	1.214E-06
2	3.425E-08	1.454E-06	28038	28194	1.206E-08	1.017E-06
3	1.890E-08	1.068E-06	28120	28181	1.800E-08	9.719E-07
4	1.227E-08	8.078E-07	28169	28191	9.474E-09	7.280E-07
5	6.412E-09	5.952E-07	27818	28195	4.843E-09	5.633E-07
6	1.400E-07	2.116E-06	28117	28167	1.043E-08	9.001E-07
7	1.721E-08	9.485E-07	28169	28175	1.225E-08	8.398E-07
8	3.875E-08	1.396E-06	28182	28184	3.753E-08	1.336E-06
9	9.677E-08	1.919E-06	28197	28197	1.717E-08	1.033E-06
10	7.959E-08	1.574E-06	28196	28198	2.666E-08	1.023E-06
11	3.907E-08	1.256E-06	28072	28073	1.916E-08	9.855E-07
12	5.680E-07	5.418E-06	27924	27929	1.828E-07	3.384E-06
13	3.410E-07	5.028E-06	28116	28163	1.644E-07	2.986E-06
14	5.699E-08	1.237E-06	28060	28198	1.046E-08	7.430E-07
15	2.541E-07	2.488E-06	28131	28198	9.548E-09	6.715E-07
16	1.892E-07	2.911E-06	28197	28198	3.324E-08	1.416E-06
17	1.219E-07	2.177E-06	28167	28192	2.495E-08	1.378E-06
18	4.842E-08	1.659E-06	28189	28194	2.701E-08	1.304E-06
19	4.897E-08	1.750E-06	28046	28053	3.808E-08	1.612E-06
20	1.969E-07	3.279E-06	28151	28172	6.646E-08	1.976E-06
21	2.691E-07	5.092E-06	28171	28171	2.246E-07	4.687E-06
22	9.722E-07	1.009E-05	28142	28141	2.257E-07	4.088E-06
23	1.827E-07	4.450E-06	28141	28140	1.782E-07	4.208E-06
24	8.058E-08	2.638E-06	27423	27423	7.315E-08	2.544E-06
25	8.266E-08	2.251E-06	28172	28186	6.589E-08	2.164E-06
26	5.400E-06	2.993E-05	28178	28177	5.794E-07	8.587E-06
27	1.799E-07	3.381E-06	28055	28136	8.889E-08	2.541E-06
28	4.432E-08	1.521E-06	28164	28168	2.667E-08	1.171E-06
29	3.790E-08	1.405E-06	27951	28194	3.572E-08	1.372E-06
30	2.094E-08	1.079E-06	28184	28190	2.060E-08	1.020E-06

Table B.36 December 1982 X-ray daily mean and background values
Time of end of first day (sec of yr) = 28944000.
All daily average and background flux in units of W m^{-2}.

	— Daily Average —		Number of Values		— Background —	
Day	Short (0.5-4Å)	Long (1-8Å)	Short (0.5-4Å)	Long (1-8Å)	Short (0.5-4Å)	Long (1-8Å)
1	1.473E-08	9.864E-07	28143	28149	8.666E-09	7.935E-07
2	8.613E-08	2.122E-06	28191	28190	2.018E-08	1.073E-06
3	9.213E-08	2.215E-06	28108	28196	8.255E-08	2.192E-06
4	1.711E-07	3.603E-06	28127	28168	1.259E-07	3.453E-06
5	1.026E-07	2.711E-06	27665	28196	7.518E-08	2.710E-06
6	1.419E-07	3.046E-06	27286	28185	1.306E-07	2.952E-06
7	9.984E-07	7.613E-06	28032	28193	3.545E-07	6.115E-06
8	1.979E-06	1.688E-05	28177	28184	1.828E-06	1.676E-05
9	7.487E-07	7.441E-06	28192	28191	3.364E-07	5.990E-06
10	1.099E-06	1.270E-05	28155	28155	3.230E-07	6.812E-06
11	4.735E-07	6.384E-06	27168	28170	1.856E-07	5.711E-06
12	3.515E-08	2.147E-06	18268	28194	3.537E-08	2.106E-06
13	4.035E-07	4.343E-06	22328	24726	3.632E-07	4.139E-06
14	6.031E-08	2.214E-06	20464	22625	1.921E-08	1.764E-06
15	2.772E-06	1.406E-05	25321	27089	7.714E-08	3.373E-06
16	4.636E-07	5.700E-06	14664	15434	1.557E-07	4.503E-06
17	2.908E-06	1.538E-05	25125	27937	9.587E-08	2.313E-06
18	5.036E-07	4.714E-06	24925	28175	2.173E-07	4.154E-06
19	1.146E-06	1.120E-05	26585	28136	1.151E-07	2.875E-06
20	1.233E-07	3.456E-06	25647	26328	5.286E-08	2.632E-06
21	1.935E-07	3.399E-06	28073	28158	3.774E-08	2.366E-06
22	6.513E-07	4.467E-06	27041	28157	2.392E-08	1.455E-06
23	2.849E-08	1.459E-06	28129	28165	2.719E-08	1.366E-06
24	4.536E-08	1.594E-06	28099	28105	1.925E-08	1.143E-06
25	6.009E-07	6.835E-06	27921	28113	4.736E-07	6.283E-06
26	5.715E-08	1.545E-06	9629	9629	1.072E-08	7.740E-07
27	3.548E-08	1.305E-06	10060	10068	1.230E-08	1.029E-06
28	3.966E-08	1.221E-06	28051	28192	3.003E-08	1.139E-06
29	2.248E-07	1.988E-06	28039	28189	1.251E-08	1.208E-06
30	2.205E-07	2.178E-06	27142	28192	1.589E-08	9.384E-07
31	2.203E-08	7.887E-07	26683	28052	7.397E-09	6.534E-07

Table B.37 January 1983 X-ray daily mean and background values
Time of end of first day (sec of yr) = 86400.
All daily average and background flux in units of W m^{-2}.

	— Daily Average —		Number of Values		— Background —	
Day	Short (0.5-4Å)	Long (1-8Å)	Short (0.5-4Å)	Long (1-8Å)	Short (0.5-4Å)	Long (1-8Å)
1	9.933E-08	1.501E-06	27227	28097	1.977E-08	7.754E-07
2	2.511E-08	7.754E-07	16274	16305	2.605E-08	7.864E-07
3	5.467E-09	5.639E-07	28058	28190	5.011E-09	5.534E-07
4	5.847E-09	6.072E-07	27763	28198	4.267E-09	5.805E-07
5	1.931E-08	1.090E-06	28188	28189	1.551E-08	1.042E-06
6	1.237E-08	9.192E-07	28187	28194	1.184E-08	8.875E-07
7	2.367E-08	1.343E-06	28186	28193	1.103E-08	8.287E-07
8	1.953E-07	2.688E-06	28093	28134	3.285E-08	1.278E-06
9	1.126E-08	7.766E-07	28194	28198	8.902E-09	7.230E-07
10	1.102E-08	8.016E-07	28187	28194	9.404E-09	7.457E-07
11	8.353E-09	6.917E-07	28175	28181	8.208E-09	6.856E-07
12	1.439E-08	7.522E-07	26829	27040	1.255E-08	7.100E-07
13	1.217E-08	7.764E-07	27359	28193	4.000E-09	4.544E-07
14	5.091E-09	5.002E-07	27608	28183	4.080E-09	4.835E-07
15	8.551E-08	1.382E-06	28149	28170	7.910E-09	6.023E-07
16	1.312E-08	8.085E-07	27932	28182	6.622E-09	6.613E-07
17	1.039E-08	6.725E-07	26460	28150	7.627E-09	6.249E-07
18	6.892E-09	5.542E-07	25962	28198	6.581E-09	5.257E-07
19	7.453E-09	4.886E-07	21121	22226	5.687E-09	3.830E-07
20	4.379E-09	2.998E-07	23777	28198	3.173E-09	2.836E-07
21	4.308E-09	2.491E-07	15058	18878	2.007E-09	2.181E-07
22	1.078E-07	1.141E-06	23250	28108	2.648E-09	2.606E-07
23	7.417E-09	4.478E-07	27167	28198	6.738E-09	4.388E-07
24	1.110E-08	5.841E-07	28093	28162	9.996E-09	5.564E-07
25	8.179E-09	5.633E-07	25757	28198	6.710E-09	5.508E-07
26	1.176E-08	7.766E-07	26621	27085	1.010E-08	7.654E-07
27	2.993E-08	9.945E-07	27930	28198	9.339E-09	7.482E-07
28	6.532E-09	5.097E-07	27778	28148	5.422E-09	4.672E-07
29	2.386E-07	2.933E-06	28079	28139	8.314E-09	7.055E-07
30	7.930E-09	7.123E-07	27675	28173	6.180E-09	6.594E-07
31	9.208E-09	7.230E-07	27790	28113	5.990E-09	5.710E-07

Table B.38 February 1983 X-ray daily mean and background values
Time of end of first day (sec of yr) = 2764800.
All daily average and background flux in units of W m^{-2}.

	— Daily Average —		Number of Values		— Background —	
Day	Short (0.5-4Å)	Long (1-8Å)	Short (0.5-4Å)	Long (1-8Å)	Short (0.5-4Å)	Long (1-8Å)
1	2.233E-05	1.367E-06	28198	28198	2.833E-08	1.218E-06
2	1.662E-08	8.661E-07	28190	28198	1.243E-08	8.048E-07
3	1.892E-06	9.024E-06	28160	28161	1.031E-07	2.681E-06
4	2.433E-08	1.163E-06	28039	28188	1.771E-08	1.069E-06
5	1.368E-07	2.138E-06	28134	28172	7.943E-08	1.611E-06
6	2.377E-08	9.474E-07	14741	15420	1.527E-08	9.276E-07
7	5.132E-09	4.924E-07	9093	10562	2.806E-09	4.521E-07
8	3.406E-08	7.945E-07	25417	28189	3.169E-09	4.571E-07
9	4.377E-08	1.307E-06	26828	28174	1.124E-08	7.454E-07
10	4.109E-09	3.545E-07	27723	28186	3.616E-09	3.4[illegible]E-07
11	6.928E-09	3.429E-07	28104	28196	5.148E-09	3.272E-07
12	9.076E-08	1.002E-06	23713	28134	4.083E-09	2.615E-07
13	7.646E-09	2.129E-07	1	1	0.000E+00	0.000E+00
14	4.262E-09	1.552E-07	2718	2725	4.262E-09	1.552E-07
15	3.320E-09	1.125E-07	20597	27547	2.384E-09	9.991E-08
16	4.655E-09	1.233E-07	17964	27637	2.295E-09	1.012E-07
17	4.299E-09	1.367E-07	19984	28120	2.832E-09	1.221E-07
18	6.087E-09	2.438E-07	22696	28063	3.428E-09	1.888E-07
19	9.568E-08	9.442E-07	25192	28160	1.977E-09	1.286E-07
20	3.713E-09	2.071E-07	21952	28197	2.461E-09	1.569E-07
21	4.615E-09	2.716E-07	15089	21233	2.897E-09	2.414E-07
22	1.512E-07	1.643E-06	23817	25904	3.637E-09	3.967E-07
23	5.886E-09	4.077E-07	24914	28093	3.583E-09	3.797E-07
24	1.378E-08	5.118E-07	20485	27793	3.498E-09	3.722E-07
25	1.275E-08	5.604E-07	23157	27624	2.879E-09	3.327E-07
26	9.031E-08	1.306E-06	26691	27444	8.722E-09	5.755E-07
27	1.207E-08	6.878E-07	26769	27407	9.172E-09	6.183E-07
28	1.290E-08	6.966E-07	22878	22892	1.292E-08	7.024E-07

Table B.39 March 1983 X-ray daily mean and background values
Time of end of first day (sec of yr) = 5184000.
All daily average and background flux in units of W m^{-2}.

	— Daily Average —		Number of Values		— Background —	
Day	Short (0.5-4Å)	Long (1-8Å)	Short (0.5-4Å)	Long (1-8Å)	Short (0.5-4Å)	Long (1-8Å)
1	4.392E-03	1.300E-06	27250	27255	3.811E-08	1.258E-06
2	1.916E-08	6.493E-07	25322	25926	1.255E-08	6.246E-07
3	5.443E-09	4.347E-07	19669	25441	4.848E-09	4.326E-07
4	1.018E-08	5.898E-07	2099	2100	1.018E-08	5.898E-07
5	1.465E-07	1.810E-06	25118	26987	6.162E-09	5.587E-07
6	7.522E-09	5.826E-07	26869	26889	7.302E-09	5.557E-07
7	6.358E-09	5.304E-07	18781	18798	4.439E-09	5.308E-07
8	1.185E-08	7.108E-07	26586	26607	1.010E-08	6.763E-07
9	1.373E-08	6.417E-07	26851	26863	1.102E-08	5.032E-07
10	4.989E-08	1.186E-06	14062	14063	1.282E-08	7.699E-07
11	5.892E-09	4.296E-07	25158	25334	3.461E-09	3.438E-07
12	1.429E-07	1.819E-06	24024	24150	1.282E-07	1.379E-06
13	1.593E-08	7.434E-07	22375	22863	7.466E-09	5.887E-07
14	2.389E-08	7.372E-07	20326	21810	1.175E-08	5.388E-07
15	1.173E-08	5.484E-07	22925	24838	8.971E-09	4.815E-07
16	1.800E-08	5.647E-07	20171	21066	2.900E-09	3.138E-07
17	2.049E-07	2.491E-06	24197	24498	1.824E-07	2.221E-06
18	4.677E-08	1.315E-06	22020	23043	1.974E-08	1.187E-06
19	1.260E-07	1.519E-06	19722	21467	1.449E-08	6.140E-07
20	8.069E-09	4.597E-07	18877	22946	4.763E-09	4.352E-07
21	7.131E-09	3.839E-07	17497	24365	4.982E-09	3.721E-07
22	9.058E-09	5.310E-07	25333	26562	5.116E-09	4.971E-07
23	1.293E-08	5.021E-07	21330	26808	2.796E-09	3.606E-07
24	4.300E-09	3.785E-07	24562	26821	2.821E-09	3.733E-07
25	1.169E-08	6.509E-07	25275	25505	7.111E-09	6.263E-07
26	9.195E-08	1.416E-06	26776	26800	1.629E-08	7.217E-07
27	4.241E-09	3.415E-07	15063	15091	3.200E-09	3.143E-07
28	3.513E-09	3.371E-07	9845	10278	2.845E-09	3.213E-07
29	4.350E-09	1.986E-07	21303	26463	4.206E-09	1.979E-07
30	3.126E-09	1.795E-07	19486	25538	2.055E-09	1.745E-07
31	4.020E-09	1.521E-07	9671	14121	1.645E-09	1.168E-07

Table B.40 April 1983 X-ray daily mean and background values
Time of end of first day (sec of yr) = 7862400.
All daily average and background flux in units of W m^{-2}.

	— Daily Average —		Number of Values		— Background —	
Day	Short (0.5-4Å)	Long (1-8Å)	Short (0.5-4Å)	Long (1-8Å)	Short (0.5-4Å)	Long (1-8Å)
1	5.114E-09	2.178E-07	18140	25921	1.825E-09	1.698E-07
2	2.100E-07	1.461E-06	17171	26953	1.811E-09	1.612E-07
3	4.770E-09	2.746E-07	13305	15670	4.666E-09	2.669E-07
4	7.120E-09	2.589E-07	8566	10038	5.350E-09	2.580E-07
5	8.191E-09	3.592E-07	26362	26445	4.559E-09	2.750E-07
6	3.176E-09	2.573E-07	25173	27045	2.826E-09	2.515E-07
7	8.350E-09	3.627E-07	22022	27504	3.175E-09	3.099E-07
8	1.458E-08	5.095E-07	22376	27732	1.205E-08	4.590E-07
9	1.278E-07	1.503E-06	25497	28032	1.057E-08	4.818E-07
10	6.353E-09	2.929E-07	19685	28081	3.099E-09	2.582E-07
11	5.628E-09	3.067E-07	22802	27698	3.579E-09	2.884E-07
12	5.699E-09	3.495E-07	22377	28107	4.862E-09	2.837E-07
13	3.847E-09	3.073E-07	26060	27838	3.748E-09	3.045E-07
14	1.665E-08	7.020E-07	25980	27931	1.279E-08	5.039E-07
15	2.674E-08	5.809E-07	22042	27942	9.002E-09	3.852E-07
16	1.398E-07	1.058E-06	16699	27762	8.798E-09	3.470E-07
17	7.710E-09	4.194E-07	19890	27966	5.951E-09	3.543E-07
18	3.694E-07	3.439E-06	27573	27825	1.221E-08	9.307E-07
19	1.349E-08	7.710E-07	28133	28178	1.014E-08	7.335E-07
20	2.651E-08	1.141E-06	28143	28152	2.457E-08	1.122E-06
21	2.917E-08	1.314E-06	27886	27891	2.331E-08	1.231E-06
22	2.244E-08	1.126E-06	28108	28120	1.794E-08	1.105E-06
23	1.034E-07	1.908E-06	28112	28127	1.962E-08	1.123E-06
24	2.802E-08	1.028E-06	28133	28144	7.623E-09	6.923E-07
25	2.507E-08	1.062E-06	27542	28116	1.083E-08	7.776E-07
26	1.304E-08	8.072E-07	26027	28083	1.176E-08	7.928E-07
27	2.469E-08	1.053E-06	27543	28074	2.403E-08	9.456E-07
28	3.591E-08	1.684E-06	27952	27986	1.715E-08	1.154E-06
29	1.582E-08	9.021E-07	27766	28155	8.784E-09	7.204E-07
30	1.991E-07	2.741E-06	27074	28093	1.645E-07	2.214E-06

Table B.41 May 1983 X-ray daily mean and background values
Time of end of first day (sec of yr) = 10454400.
All daily average and background flux in units of W m^{-2}.

	— Daily Average —		Number of Values		— Background —	
Day	Short (0.5-4Å)	Long (1-8Å)	Short (0.5-4Å)	Long (1-8Å)	Short (0.5-4Å)	Long (1-8Å)
1	1.375E-07	2.414E-06	28015	28051	5.066E-08	1.382E-06
2	3.985E-08	1.481E-06	28094	28103	3.561E-08	1.169E-06
3	1.692E-08	9.173E-07	28102	28104	1.266E-08	9.101E-07
4	1.152E-08	7.852E-07	27318	27496	9.230E-09	7.326E-07
5	5.619E-08	1.526E-06	26250	26524	3.278E-08	1.150E-06
6	3.634E-08	1.613E-06	26166	26172	3.452E-08	1.465E-06
7	4.761E-07	3.165E-06	27839	28123	5.138E-08	1.204E-06
8	1.030E-06	9.709E-06	27739	27744	1.338E-07	3.523E-06
9	3.240E-07	2.674E-06	28074	28076	5.838E-08	1.401E-06
10	6.551E-08	1.524E-06	28042	28041	4.180E-08	1.383E-06
11	3.383E-07	3.865E-06	28022	28022	2.799E-07	3.209E-06
12	1.867E-07	2.850E-06	26451	26445	1.494E-07	2.623E-06
13	3.291E-08	1.186E-06	28036	28107	2.527E-08	1.105E-06
14	1.785E-07	3.173E-06	27981	28018	9.764E-08	2.733E-06
15	1.477E-06	9.661E-06	23198	23199	9.922E-08	2.215E-06
16	6.112E-08	1.776E-06	9246	9245	6.112E-08	1.776E-06
17	9.583E-09	7.465E-07	17148	17166	9.401E-09	7.186E-07
18	9.254E-09	7.924E-07	1	1	0.000E+00	0.000E+00
19	1.287E-08	9.715E-07	13234	13237	1.163E-08	8.743E-07
20	0.000E+00	0.000E+00	0	0	0.000E+00	0.000E+00
21	0.000E+00	0.000E+00	0	0	0.000E+00	0.000E+00
22	0.000E+00	0.000E+00	0	0	0.000E+00	0.000E+00
23	0.000E+00	0.000E+00	0	0	0.000E+00	0.000E+00
24	0.000E+00	0.000E+00	0	0	0.000E+00	0.000E+00
25	0.000E+00	0.000E+00	0	0	0.000E+00	0.000E+00
26	0.000E+00	0.000E+00	0	0	0.000E+00	0.000E+00
27	0.000E+00	0.000E+00	0	0	0.000E+00	0.000E+00
28	0.000E+00	0.000E+00	0	0	0.000E+00	0.000E+00
29	0.000E+00	0.000E+00	0	0	0.000E+00	0.000E+00
30	0.000E+00	0.000E+00	0	0	0.000E+00	0.000E+00
31	0.000E+00	0.000E+00	0	0	0.000E+00	0.000E+00